Contribution to the Study of Transfer Processes from the Surface to the Deep Ocean in the Mediterranean Sea using in situ Measurements

Loïc Houpert

Collège Doctoral du Languedoc-Roussillon

THÈSE

Pour obtenir le grade de

Docteur

Délivré par

UNIVERSITE DE PERPIGNAN VIA DOMITIA

Préparée au sein de l'école doctorale
Energie et Environnement (ED 305)
Et de l'unité de recherche CEFREM UMR 5110

Spécialité : **Océanologie**

Présentée par

Loïc Houpert

Contribution to the Study of Transfer Processes from the Surface to the Deep Ocean in the Mediterranean Sea using *in situ* Measurements.

Soutenue le 12/12/2013 devant le jury composé de

A. CRISE, Directeur de Recherche, OGS (Trieste)	*Rapporteur*
G. REVERDIN, Directeur de Recherche CNRS, LOCEAN	*Rapporteur*
F. D'ORTENZIO, Chargé de Recherche CNRS, LOV	*Examinateur*
C. ESTOURNEL, Directeur de Recherche CNRS, LA	*Examinateur*
P. RAIMBAULT, Directeur de Recherche CNRS, MIO	*Examinateur*
C. NAHUM, Chargé de Recherche, DGA/DS/MRIS	*Examinateur*
X. DURRIEU DE MADRON, Directeur de Recherche, CEFREM	*Directeur de thèse*
P. TESTOR, Chargé de Recherche CNRS, LOCEAN	*Co-directeur de thèse*

Remerciements

Je remercie les membres du jury qui ont accepté de juger cette thèse, et tout spécialement Gilles Reverdin et Alessandro Crise pour avoir accepté de rapporter cette thèse, et surtout pour leurs remarques et judicieux conseils. Merci à Patrick Raimbault de m'avoir fait l'honneur de présider ce jury, merci à Claude Estournel, Carole Nahum et Fabrizio d'Ortenzio d'avoir accepté d'examiner mon travail.

Je tiens à remercier sincèrement toutes les personnes qui m'ont entouré au cours de cette thèse. Tout d'abord un grand merci à Laurent Mortier pour m'avoir guidé et conseillé dans mes choix de jeune étudiant en Océanographie. Merci à Jacqueline et Gilles de m'avoir fait découvrir l'océanographie expérimentale au cours mon stage de Master 1. J'exprime aussi ma profonde gratitude à mes deux directeurs de thèse Xavier et Pierre, qui m'ont accueilli en master 2 pour faire un stage et qui m'ont fait confiance pour continuer en thèse. Vous avez su être disponible pour partager vos expériences et vos connaissances de l'océanographie. Tout au cours de ma thèse j'ai vraiment eu beaucoup de plaisir à travailler avec vous, tout en disposant d'une précieuse liberté riche d'enseignements et de découvertes.

De nombreuses personnes ont également joué un rôle important tout au long de cette thèse, je vais essayer de n'oublier personne, mais j'ai tellement de personnes à remercier...

Commençons par le CEFREM, merci à tous de m'avoir si bien accueilli durant toutes ces années. J'ai toujours été motivé pour venir travailler au laboratoire, ce n'est pas seulement grâce au sujet mais aussi grâce à la bonne ambiance qui a toujours régné dans les bureaux... Merci à Marion, François, Philippe, Dominique, Wolfgang, Christophe, Olivier, Serge H. d'avoir su apporter un peu de biogéochimie dans ma vie... merci aussi aux "surfeurs" (Nico R., Olivier R., Raph.) et aux "géologues" (Maria-Angela, Serge B., Lies, Thierry) pour les nombreuses discussions scientifiques, culturelles, naturelles, autour d'un café, d'un pot, ou d'un apéro ... Un grand merci aussi à Nicole, Sophie, Marie-France, Stéphane, Christine et Bertil pour votre bonne humeur et votre aide précieuse. Merci beaucoup aussi à Marion, Nicolas, France (et Marc), Chloé, Marina, Charlie, Marie, Julie, Cédric, Gaël M. et Gaël L., mes amis doctorants avec qui on a partagé de très bon moments.

Merci aussi à tous les gens que j'ai pu rencontrer tout au long de mon parcours pour leurs conseils, leur bonne humeur, leur sympathie, qu'ils soient de Paris (Thomas, Anthony, Pierre, JB, Hervé, Denis, Matthieu), de Toulouse (Claude, Samuel, Marine, Hervé, Pierre, Faycal, Robin, Lars, Romain), de Villefranche (Fabrizio, Vincent, Laurent, Héloïse), de Barcelone (Pere, Jacobo).

Cette thèse n'aurait pas été possible sans la participation de nombreuses équipes, tant dans la collecte d'un grand nombre de données, qu'à leur mise en forme et leur analyse à terre. Je tiens notamment à associer à ces remerciements toute la communauté MOOSE, les équipes "techniques marines", la cellule glider, ainsi que le commandement et les équipages des navires océanographiques de l'Atalante, du Suroît et du Thetys II.

Enfin je voudrais exprimer toute ma reconnaissance à mes parents ainsi qu'à toute ma famille qui m'ont toujours soutenu dans mes choix tout au long de ces années. Un grand merci aussi à tous mes amis de longues date qui ont toujours été là. Un merci particulier à Mickaël et Raymond, ça a été un grand plaisir de vous voir à ma soutenance.

Merci à Kathy pour tout ...

Résumé

La Méditerranée a été reconnue comme particulièrement sensible au changement climatique. De nombreuses interactions et rétroactions entre l'océan, l'atmosphère et les surfaces continentales jouent un rôle proéminent dans le climat et les écosystèmes, et qui font de cette mer semi-fermée un système unique et complexe, où la réponse des écosystèmes marins aux changements climatiques et anthropiques est plus manifeste que dans l'Océan planétaire.

Cette thèse porte plus particulièrement sur la variabilité de la structure verticale de l'océan de surface et sur les processus de formation d'eau profonde. Les différents résultats présentés sont issus de nombreuses plateformes de mesure in-situ : navires, flotteurs-profileurs, «gliders» (planeurs sous-marins), mouillages et bouée de surface.

Dans une première partie, nous nous sommes intéressé à caractériser la variabilité de la couche mélangée océanique en Méditerranée. Ceci nous a permis de constituer la première climatologie en Méditerranée (0.5° latitude x 0.5° longitude x 12 mois) de la pente de la thermocline et du taux de stockage de chaleur associé, à partir de plus de 190 000 profils recueillis entre 1969 et 2012. En plus de mettre en évidence des régions à la dynamique particulière (comme les zones de convection profonde), cette climatologie du taux de stockage de chaleur dans l'océan de surface a conduit à la construction d'un estimateur indépendant du cycle saisonnier du flux net de chaleur de surface, en moyenne sur la méditerranée. À travers ce travail nous avons pu fournir la première climatologie du cycle saisonnier du flux net de chaleur calculé en moyenne sur la Méditerranée.

Cette climatologie a permis de mettre en évidence en Méditerranée, une grande variabilité temporelle et spatiale de la couche mélangée et de la thermocline saisonnière. En Méditerranée Nord-Occidentale, le mélange vertical de l'océan de surface peut se faire sur de très grandes profondeurs, atteignant le fond (2300m) lors d'hivers particulièrement froids et secs. À partir d'un très grand nombre de nouvelles observations multi-plateformes intégrées au sein du système d'observation MOOSE (Mediterranean Ocean Observing System on Environment), ce travail de thèse a permis de caractériser la variabilité saisonnière et interannuelle du processus de convection profonde, ainsi que les échelles de temps associées à ce processus, l'évolution du contenu en chaleur et en sel de la colonne d'eau, le rôle de l'atmosphère, l'évolution des eaux profondes, mais aussi l'activité tourbillonnaire de méso- et sous méso-échelle très active dans cette zone.

Abstract

The Mediterranean Sea was recognized as being particularly sensitive to climate change. Numerous interactions and feedback between ocean-atmosphere-land processes, that play a prominent role in climate and ecosystems, make the Mediterranean area a unique highly coupled system, where the response of the marine ecosystems to both climate and anthropic changes is expected to be much faster than in the rest of the world's oceans. This thesis is mainly focused on the variability of the vertical structure of the ocean surface and the processes of deep water formation. Results are based on many platforms measuring in-situ: ships, profiling floats, "gliders" (unmanned autonomous underwater vehicle), and surface buoy moorings.

In the first part, we characterize the variability of the ocean mixed layer in the Mediterranean. We present the first Mediterranean climatology (1°x1°x12 months) of the thermocline based on a comprehensive collection of temperature profiles of the last 44 years (1969-2012), including more than 190,000 profiles. This data set is first used to describe the seasonal cycle of the thermocline depth and averaged temperature on the whole Mediterranean on a monthly climatological basis. Our analysis discriminates several regions with coherent behaviors, in particular the deep water formation sites, characterized by significant differences in the winter mixing intensity. We used our new climatology to calculate the seasonal cycle of the upper ocean heat rate and we propose a new independent estimate of the seasonal cycle of the Net surface Heat Flux (NHF). This estimate is calculated on average over the Mediterranean Sea for the 1969-2012 period.

This climatology highlights the high temporal and spatial variability of the mixed layer and of the seasonal thermocline in the Mediterranean Sea. In the Northwestern Mediterranean, the oceanic mixed layer can reach the bottom (2300m depth) in winter, this phenomenon is known as deep convection. Recently a multi-platforms and integrated monitoring system in the framework of the Mediterranean Ocean Observing System on Environment (MOOSE) enables to monitor the deep water formation processes. For the first time, the deep convection process was monitored in the Northwestern Mediterranean on a pluriannual basis, improving our understanding of the seasonal and interannual variability of the deep convection process, together with the timescale associated to this process, the evolution of heat and salt content of the water column, the influence of surface buoyancy forcing, the thermohaline evolution of Western Mediterranean Deep Waters, and the meso- / submeso-scale eddy activity in the deep convection area.

Table of Contents

List of Figures

List of tables

Acronymes

ADCP	Acoustic Doppler Current Profiler
AW	Atlantic Water
CIW	Cretan Intermediate Water
CTD	Conductivity-Temperature-Depth
DSWC	Dense Shelf Water Cascading
DWF	Dense Water Formation
ECMWF	European Centre for Medium-Range Weather Forecasts
EMED	Eastern Mediterranean
HSR	Heat Storage Rate
LIW	Levantine Intermediate Water
MLD	Mixed Layer Depth
MOOSE	Mediterranean Ocean Observing System for the Environment
NHF	Net Heat Flux
NWMED	Northwestern Mediterranean Sea
OODC	Open-Ocean Deep Convection
RCM	Regional Climate Model
TDW	Tyrrhenian Deep Water
WIW	Winter Intermediate Water
WMDW	Western Mediterranean Deep Water
WMED	Western Mediterranean

Introduction

Notre compréhension de l'Océan a constamment évolué grâce au développement de nouvelles techniques de mesure permettant de mettre en lumière de nouveaux processus physiques. Les deux guerres mondiales ont considérablement contribué au développement de nouveaux instruments avec l'apparition des sonars et des chaînes de thermistances. Le développement des méthodes de détections acoustiques a notamment conduit à la mise en place et au suivi de mouillages profonds et de flotteurs, permettant de découvrir que dans une grande partie des océans, l'énergie cinétique est dominée par des tourbillons de méso-échelle, dont les échelles spatiales sont de l'ordre de plusieurs dizaines de kilomètres et les périodes temporelles de plusieurs mois. Les chaînes de thermistances ont, quant à elles, permis de mieux comprendre ces tourbillons, la structure des océans et ses petites variations liées à la propagation d'ondes internes.

Le développement des satellites d'observation depuis les années 1970 est un autre exemple de l'impact des nouveaux instruments sur notre compréhension de la dynamique de l'Océan et de ses propriétés. Ce nouvel outil a permis de réaliser de grandes avancées notamment dans notre compréhension de la distribution du phytoplancton à la surface des océans, de la variabilité spatiale et temporelle de la température de surface, de l'amplitude des vagues, des tourbillons, des courants de surface, et récemment de la salinité de surface.

Dans les années 2000, un nouveau tournant dans l'observation de l'Océan a été pris à travers l'essor des plateformes autonomes avec le déploiement d'un réseau mondial de flotteurs profileurs (Argo). Avec plus de 3500 flotteurs actifs, il permet pour la première fois de connaître en continu la température, la salinité et la vitesse des 2000 premiers mètres de l'océan, et d'accéder aux données disponibles publiquement dans les heures qui suivent chaque cycle de mesures. Un des objectifs principaux du réseau Argo est de surveiller l'Océan, et notamment son évolution liée au changement climatique.

De nos jours, le développement des planeurs sous-marins (ou *gliders*) constitue la nouvelle révolution technologique de l'océanographie. Ces petits engins sous-marins autonomes sont téléguidés et capables d'échantillonner l'Océan à haute résolution généralement jusqu'à une profondeur de 1000m (voire 6000m) en étant équipés de différents capteurs physiques, biogéochimiques et acoustiques. L'idée de cette nouvelle plateforme d'observation fut déjà évoquée en 1989 par Henry Stommel, soulignant sa facilité d'utilisation, son coût relativement faible et son utilité scientifique. La grande utilité des *gliders* vient du fait qu'ils comblent des vides laissés par les autres plateformes utilisées dans l'observation de l'océan (satellites, navires,

mouillages, flotteurs profileurs ou bouées dérivantes). Une des principales futures applications sera notamment leurs utilisations simultanées sous forme d'une flotte de *gliders*. Ces déploiements permettront ainsi des observations multidisciplinaires et en quatre dimensions de l'intérieur de l'Océan.

Toutefois, à l'échelle du globe, les observations de l'Océan sont dispersées géographiquement et temporellement. Elles ne fournissent qu'une description sommaire de l'écoulement moyen et de nombreux processus sont mal observés. Ces lacunes peuvent être comblées en combinant les observations à la théorie[1] dans des modèles numériques[2]. La puissance de calcul qui a grandi exponentiellement ces dernières décennies a permis le développement considérable de la modélisation numérique. Conjointement les plateformes d'observations se sont multipliées et diversifiées, ce qui a permis d'améliorer notre compréhension des processus physiques qui régissent la dynamique océanique et notre capacité à prévoir l'évolution de l'Océan.

Les océans sont responsables de l'absorption d'environ 1/3 des émissions anthropiques de dioxyde de carbone (CO_2), entraînant leur acidification (IPCC [2013]). Dû à la grande capacité thermique de l'eau et à l'énorme volume des océans (97% de l'eau présente sur Terre est salée), le réchauffement océanique constitue l'essentiel de l'augmentation de la quantité d'énergie emmagasinée au sein du système climatique et représente plus de 90% de l'énergie accumulée entre 1971 et 2010 (IPCC [2013]). L'absorption de chaleur par les océans a, par conséquent, réduit les effets associés à ce réchauffement sur l'atmosphère, mais implique un réchauffement océanique sur le long terme même si le taux des émissions de gaz à effet de serre était réduit à zéro, car leur temps de résidence dans l'atmosphère est très long (de 4 ans pour le méthane à 5-200 ans pour le CO_2, responsable de plus de 50% du réchauffement anthropique, voire 50 000 ans pour le Perfluorométhane CF_4, IPCC [2013]).

Les océans séquestrent la chaleur et la transportent, avec le sel et une multitude d'autres molécules, au grès des courants océaniques, qui les relâchent ultérieurement en différents endroits de la planète. Une des grandes questions est de savoir comment la circulation océanique est affectée par le changement climatique. À cause de la grande masse des océans (270 fois celle de l'atmosphère), de leur grande étendue (le globe terrestre est recouvert à 70% par les océans) et de leur grande capacité thermique, les interactions océan-atmosphère et les réponses de l'océan à ces interactions impliquent des processus lents agissant à diverses échelles de temps. Ainsi, dans le cadre des prévisions à long terme du climat, une grande partie des projections indique une diminution de la capacité des océans à absorber le carbone.

Notre compréhension du rôle de l'Océan dans la variabilité et le changement climatique, et sa capacité à absorber et stocker le carbone, a évolué au fil de nombreux projets de recherche comme CLIVAR (CLImate VARiability and predictability), SOLAS (Surface Ocean Lower Atmosphere Study), ou encore IMBER (Integrated Marine Biogeochemistry and Ecosystem Research).

[1] La théorie repose sur la dynamique des fluides géophysiques qui est l'étude des écoulements de moyenne et grande échelle dans l'océan et l'atmosphère, milieux stratifiés sur une planète en rotation.

[2] Les modèles numériques sont crés à partir d'équations numériques qui sont des approximations des équations théoriques. Dans les modèles, l'information n'est connue qu'en certains points de l'espace et du temps.

La Méditerranée joue un rôle important dans la circulation océanique mondiale. La "langue" méditerranéenne d'eau salée s'échappe du détroit de Gibraltar et se répand dans tout l'Océan Atlantique Nord à une profondeur intermédiaire. Ces eaux salées méditerranéennes sont un des facteurs agissant sur les cellules de convection profonde de l'Atlantique Nord, à la fois par un transfert direct vers les régions atlantiques polaires et par des processus indirects de mélange.

De par sa localisation dans des régions relativement tempérées et ses dimensions, la Méditerranée constitue un réel bassin de "laboratoire" pour l'étude des processus qui ont une importance à l'échelle mondiale. Chacun des bassins Ouest et Est possède sa propre circulation thermohaline. Ces deux bassins sont connectés par la branche supérieure d'une cellule thermohaline, ayant pour origine l'Atlantique Nord. Les eaux intermédiaires et profondes de la Méditerranée sont formées en différents sites, qui sont, relativement, "facilement" accessible et observable, par leur proximité des côtes, comparés aux sites de formation d'eau profonde des régions polaires.

En plus de sa propre circulation thermohaline à l'échelle du bassin, la Méditerranée est aussi caractérisée par deux autres échelles de mouvement (une échelle liée aux sous-bassins, incluant de nombreux gyres, et une activité tourbillonnaire de méso- et de subméso- échelle énergétique et omniprésente). Ces trois échelles (bassin, sous-bassin et méso/subméso) sont imbriquées les unes dans les autres et sont responsables de nombreuses interactions que l'ont peut retrouver dans l'Océan planétaire.

En dépit de sa taille relativement petite (0.82% de la surface des océans), la Méditerranée concentre de 4 à 18% de la diversité marine, et a été reconnue comme particulièrement sensible au changement climatique (Giorgi [2006]; Somot et al. [2006]). Cette mer semi-fermée est bordée par des littoraux très urbanisés et par de multiples chaînes de montagne qui donnent naissance à de nombreux fleuves. Ses plateaux continentaux (larges ou étroits) sont séparés de l'océan profond par d'abruptes pentes continentales. Tout ceci résulte en de multiples interactions et rétro-actions entre les processus océan - atmosphère - surface continentale, qui jouent un rôle prépondérant dans le climat et les écosystèmes, et qui font de la région Méditerranée un système couplé unique et complexe, où la réponse des écosystèmes marins aux changements climatiques et anthropiques est attendue comme étant plus manifeste que dans l'Océan planétaire.

Le travail présenté dans ce manuscrit a été financé en partie par la Direction Générale de l'Armement et par le projet européen HERMIONE (Hotspot Ecosystem Research and Man's Impact On European Seas, http://www.eu-hermione.net/). Il s'inscrit aussi dans le cadre de deux projets de recherche français : HyMeX (Hydrological cycle in the Mediterranean Experiment, http://www.hymex.org) et MERMeX (Marine Ecosystems Response in the Mediterranean Experiment, http://mermex.pytheas.univ-amu.fr), qui font partie du programme MISTRALS (Mediterranean Integrated STudies at Regional And Local Scales). Ce programme est dédié à l' étude du bassin Méditerranéen avec l'objectif de "mieux comprendre l'impact des facteurs globaux sur cette région et d'anticiper l'évolution, sur un siècle, de ses conditions

d'habitabilité". La majorité des données utilisées dans ce travail de thèse est issue du service d'observation Mediterranean Ocean Observing System for the Environment (MOOSE), une initiative qui a mis en place un système d'observation intégré et multi-sites en Méditerranée Nord-Occidentale, dans le but de surveiller son évolution à long terme dans le contexte du changement climatique et de fortes pressions anthropiques.

Différentes questions scientifiques relient ce travail de thèse au projet HyMeX :

- *Quelle est la variabilité du bilan en eau de la Méditerranée à l'échelle saisonnière, interannuelle et décennale ?*
- *Comment des évènements intenses, localisés temporellement ou/et spatialement peuvent affecter le bilan en eau de la Méditerranée ?*
- *Comment la Méditerranée répond aux forçages de l'atmosphère ?*

Les processus étudiés dans ce travail de thèse constituent aussi des forçages importants qui influencent l'évolution des écosystèmes méditerranéens, en plus de ceux liés aux activités humaines. Cette étude est donc aussi inscrite dans différents axes de recherche de MERMeX :

- *Comment les changements dans les mécanismes de stratification et déstratification, ainsi que dans la circulation thermohaline vont modifier la répartition spatio-temporelle des nutriments et leurs bilans ? Plus précisément, quel est l'influence de la formation d'eau dense sur la variabilité spatiale et temporelle des éléments biogènes, le déclenchement des "blooms" planctoniques et la séquestration des éléments biogéniques (notamment de carbone)* ?
- *Est-ce que le fonctionnement des écosystèmes méditerranéens mésopélagiques et profonds va être fortement affecté par les changements provenant de la production des écosystèmes de surface et des flux verticaux ou par les changements dans l'hydrodynamique des eaux intermédiaires et profondes ?*

Les principaux objectifs de cette thèse sont d'améliorer notre compréhension des processus de formation d'eaux denses. En effet, la couche de surface de l'océan est le siège d'échanges océan-atmosphère nombreux et intenses, en particulier à cause du mélange, du refroidissement/réchauffement et de l'évaporation/précipitation qui sont liés à de nombreux phénomènes tels que le vent, l'ensoleillement ou les conditions atmosphériques. Cette couche de surface homogène, aussi appelée couche de mélange océanique, présente un cycle saisonnier caractéristique dans les régions tempérées (profonde en hiver, proche de la surface en été). Dans le Golfe du Lion ce mélange peut atteindre le fond de l'océan (2300m), à travers le phénomène de convection profonde. La convection profonde en haute mer, mais aussi les plongées d'eau dense côtière liées à la convection hivernale qui a lieu sur le plateau continental, sont des processus clés qui relient l'océan de surface à l'océan profond. Ils peuvent transférer de la chaleur, du sel, mais également des éléments biogéochimiques à l'océan profond, comme de l'oxygène et de la matière inorganique et organique. Ces processus contribuent donc à la

ventilation et l' alimentation des écosystèmes pélagiques[3] et benthiques[4] profonds.

Ce travail est essentiellement basé sur des observations océaniques. J'ai eu l'opportunité de participer à quatre campagnes de mesures océanographiques où j'ai pris part au déploiement et à l'acquisition des données de différents instruments (stations CTD, Lower-ADCP, ADCP de coque, gliders, mouillage profond LION), dont une grande partie est maintenue dans le cadre du service d'observation MOOSE. Le traitement et l'analyse de ces données ont été faits conjointement avec les données provenant d'autres plateformes de mesures, comme la bouée Météo-France Lion, les flotteurs profileurs Argo, les images satellites de couleur de l'océan, ou les réanalyses des modèles atmosphériques.

Tout au long de ma thèse, j'ai pu rencontrer des personnes de différents domaines (physiciens, biogéochimistes , biologistes) avec qui j'ai eu souvent l'occasion de travailler. Certains des résultats découlant de ces collaborations sont présentés au début des principaux chapitres.

Cette thèse est composée de cinq chapitres. La zone d'étude et les processus physiques intervenant dans l'océan de surface et la formation d'eaux denses sont présentés dans le premier chapitre. Le deuxième chapitre présente un aperçu des principales données utilisées. Le troisième chapitre permet de caractériser la variabilité de la couche mélangée océanique en mer Méditerranée et de mieux comprendre les bilans 'grande échelle' associés de chaleur. L'utilisation de données historiques et récentes acquises sur l'ensemble de la Méditerranée entre 1969 et 2012 a permis la construction d'une climatologie de la couche de mélange, de la thermocline et du taux de stockage de chaleur dans la couche de surface. Ce travail a permis d'établir la première climatologie du cycle saisonnier du flux net de chaleur calculé en moyenne sur la Méditerranée et basée uniquement sur des données océaniques in-situ, ce qui a permis de mettre en évidence une grande variabilité temporelle et spatiale de la couche de mélange et de la thermocline saisonnière. Les chapitres 4 et 5 sont consacrées à l'étude approfondie d'un chantier particulier (le Golfe du Lion), où la couche de mélange peut atteindre de très grande profondeur (>2000m) lors d'hivers particulièrement froids et secs. À partir d'un très grand nombre de nouvelles observations multi-plateformes intégrées au sein du système d'observation MOOSE (Mediterranean Ocean Observing System on Environment), ce travail de thèse a permis de caractériser les échelles de temps associées au processus de convection profonde (chapitre 4), ainsi que sa variabilité saisonnière et interannuelle, l'évolution du contenu en chaleur et en sel de la colonne d'eau, l'influence des pertes de flottabilités à la surface, l'évolution des eaux profondes, mais aussi l'activité tourbillonnaire de méso- et sous méso-échelle très active dans cette zone. De nouvelles observations de plongées d'eau profonde côtière et les résultats récents issus de l'interaction entre les eaux formées par ces plongées d'eau dense et par la convection profonde en haute mer durant l'hiver 2012 sont présentés dans le chapitre 5.

[3] Relatif au milieu marin loin des côtes, à la haute mer.
[4] Relatif aux grandes profondeurs, au fond des mers.

Introduction

Our understanding of the oceans has constantly evolved due to the development of new measurement techniques that have highlighted new physical processes. The two World Wars have contributed significantly to the development of new instruments including underwater sonar and thermistor chain. The development of acoustic methods improved the ability to track and detect floats or deep moorings , which led to the discovery that in most parts of the oceans the kinetic energy is dominated by mesoscale eddies with scales of many tens of kilometers and periods of several months. The development of thermistor chain has led to much better understanding of these eddies and of the structure of the ocean and its shorter term variations such as internal waves.

Another example of the impact of new instruments on our understanding of the dynamics of the ocean and its properties is the development of satellite observations since the 1970s has radically extended knowledge of the oceans, both of the surface and also of some aspects of its motion at depth. Major progress has been achieved with this new tool especially in our understanding of the distribution of plankton in the upper ocean, of the seasonal and area variations in sea-surface properties, temperature, wave amplitude, mesoscale eddies, surface currents and recently surface salinity.

In the 2000s, a new milestone in the observation of the oceans has been achieved through the development of autonomous platforms and the deployment of a global network of profiling floats (Argo). With more than 3500 active floats, This allows, for the first time, continuous monitoring of the temperature, salinity, and velocity of the upper ocean, with all data being relayed and made publicly available within hours after collection. For the first time, the physical state of the upper ocean is being systematically measured and the data assimilated in near real-time into computer models.

Nowadays the development of underwater gliders is the new technological revolution in oceanography. These small autonomous underwater vehicles are unmanned and able to sample the oceans in high resolution usually to a depth of 1000m (even 6000m) and can be equipped with various physical, biogeochemical and acoustic sensors. The idea of this new platform of measurement was mentioned in 1989 by Henry Stommel, evoking its ease of use, relatively low cost and its scientific value. The great utility of gliders comes from the fact that they fill the gaps left by the other platforms presently used for the observation of the oceans (satellites, ships, moorings, profiling floats, drifting buoys). One of the main future applications will include in particular the simultaneous use of a fleet of gliders. These

deployments will enable novel multidisciplinary 3-dimensional surveys of the upper ocean interior.

However the global observations of the oceans are dispersed spatially and temporally, they provide only a brief description of the mean flow and many processes are not properly observed. These gaps can be filled by combining theory and observations in numerical models. The exponential growth of computing power in recent decades has led to the extensive development of numerical modeling, jointly observation platforms have become more numerous and more diversified, which has allowed to improve our understanding of the physical processes that govern the ocean dynamics and our ability to predict the evolution of the oceans.

The oceans absorb approximately one-third of the emitted anthropogenic carbon dioxide, causing ocean acidification (IPCC [2013]), observed in the oceans globally. As a result of the high thermal capacity of the water and the huge mass of the oceans, ocean warming dominates the increase in energy stored in the climate system, accounting for more than 90% of the energy accumulated between 1971 and 2010 (IPCC [2013]). This has correspondingly reduced the associated heating effect on the atmosphere, but implies a long-term warming commitment even if the rate of emission of greenhouse gases were reduced to zero.

The oceans sequesters heat and moves heat, salt, and chemicals through the ocean currents, releasing them in different places and times. How ocean circulation is affected as the climate changes is a key issue. Because of the large mass of oceans (270 times the mass of the atmosphere), their large area (70% of the Earth is covered by oceans), and their high thermal capacity, ocean-atmosphere interactions and ocean responses involve slow processes that are predictable over a variety of timescales. In the framework of predictions of future climate on secular timescales, most future climate projections expect that the capacity of the oceans to absorb carbon will diminish.

Our understanding of the oceans (role in the climate variability and change, capacity to absorb and store carbon) has evolved due to activities of several research projects, such as CLIVAR (CLImate VARiability and predictability), SOLAS (Surface Ocean Lower Atmosphere Study), and IMBER (Integrated Marine Biogeochemistry and Ecosystem Research).

The Mediterranean Sea plays a significant role in the world ocean circulation. The Mediterranean salty water tongue exits from the Gibraltar strait at intermediate depths and spreads throughout the Atlantic interior. The salty Mediterranean water preconditions the deep convection cells of the north Atlantic, through direct pathways to the Atlantic polar regions or through indirect mixing processes.

With its location in relatively temperate regions and its dimensions, the Mediterranean is a real “laboratory” basin for study processes of global importance. Each of the western and the eastern basin possess closed thermohaline circulations. These two basins are connected to each other by a upper thermohaline cell, which has its origin in the north Atlantic. Deep and intermediate water masses are formed in different sites of the Mediterranean. These convection cells are relatively more simple to monitor by direct observational surveys and mooring arrays due to their relatively easily accessible locations, compared to the (sub-) polar

regions.

In addition to its thermohaline circulation, the Mediterranean circulation is characterized by two other scales of motion (a sub-basin scale and an energetic meso- and submeso- scale eddy field). These three scales are therefore superimposed producing numerous kinds of interactions processes, typical of the ones found in the global ocean.

Despite its relatively small size (0.82% of the world ocean surface), the Mediterranean Sea concentrates from 4 to 18% of the world marine diversity, and was recognized as being particularly sensitive to climate change (Giorgi [2006]; Somot et al. [2006]). This semi-enclosed sea is surrounded by very urbanized littorals and mountains from which numerous rivers originate. The deep sea interiors are separated by steep continental slopes from wide and narrow shelves. This results in many interactions and feedback between ocean-atmosphere-land processes that play a prominent role in climate and ecosystems and make the Mediterranean area a unique highly coupled system, where the response of the marine ecosystems to both climate and anthropic changes is expected to be much faster than in the rest of the world's oceans.

The work presented in this PhD thesis has got the financial support from the Direction Générale de l'Armement and from the European project HERMIONE (Hotspot Ecosystem Research and Man's Impact On European Seas, http://www.eu-hermione.net/). It was also done in the framework of two French research projects: HyMeX (Hydrological cycle in the Mediterranean Experiment, http://www.hymex.org) and MERMeX (Marine Ecosystems Response in the Mediterranean Experiment, http://mermex.pytheas.univ-amu.fr), part of MISTRALS program (Mediterranean Integrated STudies at Regional And Local Scales). MISTRALS is a research program dedicated to the study of the Mediterranean basin and its surroundings, with the aim to "better understand the impact of global factors on this region and to anticipate changes over a century of living conditions". A significant number of the data used in this work, originate from the observing system MOOSE (Mediterranean Ocean Observing System for the Environment), an initiative for building an efficient integrated observation network in the Northwestern Mediterranean Sea in order to observe its long-term evolution in the context of climate change and anthropogenic forcing.

This work is connected to several key scientific questions within the framework of HyMeX:

- *What is the variability of the Mediterranean Sea Water Budget at seasonal, interannual and decadal time-scales?*
- *How do spatially and/or temporally localized intense events affect the Mediterranean Sea Water Budget?*
- *How does the Mediterranean Sea response to the atmosphere?*

The processes studied in this work constitute also majors pressures acting on the evolution of Mediterranean ecosystems, in addition to those related to human activity. This study is also part of several main research axes of MERMeX:

- *How would changes in stratification and destratification mechanisms and in the overall thermohaline circulation alter the spatio-temporal distribution of nutrients and their*

budgets? More specifically, what is the influence of dense water formation on the spatial and temporal variability of biogenic elements, the triggering of planktonic blooms, and the sequestration of biogenic elements, particularly carbon?

- *Will the functioning of mesopelagic and deep sea Mediterranean ecosystems be strongly affected by changes originating from surface ecosystem production and vertical fluxes or by changes in the hydrodynamics of the intermediate and deep waters?*

The main aims of this PhD thesis are to improve our understanding of dense water formation processes. The surface layer of the ocean is the site of active ocean-atmosphere exchanges, due to wind mixing and heat and fresh water fluxes across the air–sea interface. This homogeneous surface layer, also called the oceanic mixed layer, presents a typical seasonal cycle in temperate regions (deep in winter, close to the surface in summer). In the Gulf of Lions, the oceanic mixed layer can reach the bottom (2300m depth) in winter, this phenomenon is known as deep convection. Open-ocean deep convection and dense shelf water cascading (cascades into the continental shelf canyons of dense water formed by convection on the shelf in winter) are key processes that connect the surface ocean to the deep ocean. They may transfer heat, salt, but also biogeochemical components to the deep ocean, like oxygen and inorganic and organic matter. These processes contribute therefore to the ventilation and the "feeding" of the deep pelagic and benthic ecosystems.

This work is essentially based on ocean observations. I had the opportunity to participate in four oceanographic cruises, where I took part in the deployment and the data acquisition of several instruments (CTD-stations, Lower-ADCP, Vessel-Mount ADCP, gliders, deep mooring), whose an important part are maintained by the MOOSE project. The processing and the analysis of these data were made mainly together with data from other measurement platforms, like the French Lion Buoy, Argo profiling floats, Ocean Color satellite data or atmospheric reanalysis.

Throughout my thesis I met people of different backgrounds (physicists, biogeochemists, biologists) with whom I often had the opportunity to collaborate. Some of the results arising from these studies are presented in the header of the main chapters.

This thesis is composed by 5 chapters. The general background of this work is presented in the first chapter, where the processes and the region studied are introduced. The second chapter presents an overview of the principal data used. The third chapter is dedicated to the seasonal cycle of the upper ocean heat rate, based on historical and recent data (1969-2012), in the whole Mediterranean. The chapter 4 focuses on the Gulf of Lions to study the seasonal and the interannual variability of open ocean deep convection, mainly through the deep LION mooring deployed since 2007 and equipped with numerous sensors. Finally, the chapter 5 describes new observations of dense shelf water cascading, particularly we show recent results from the interaction of dense shelf water cascading and open-ocean deep convection during winter 2012.

1 General Background

Contents

1.1 The Upper Ocean

The upper ocean can be considered as a buffer zone between the deep ocean and the atmosphere. The surface forcing from winds, heat and evaporation (precipitation) have first a local impact on this layer. Then, heat and fresh water are transferred and sequestered in the "quiescent" deeper ocean where they are released on longer time- and larger scales.

1.1.1 Vertical Structure

The surface layer includes both an upper mixed layer that is subject to the direct influence of the atmosphere, and also a highly stratified zone below the mixed layer where vertical gradients are strong.

The vertical structure of the upper ocean is mainly controlled by the temperature and salinity, which together determine the density structure of the water column. Within the ocean surface layer, a number of distinct layers can be distinguished that are formed by different processes over different timescales: the upper mixed layer, the seasonal pycnocline, and the main (or permanent) pycnocline (figure 1.1).

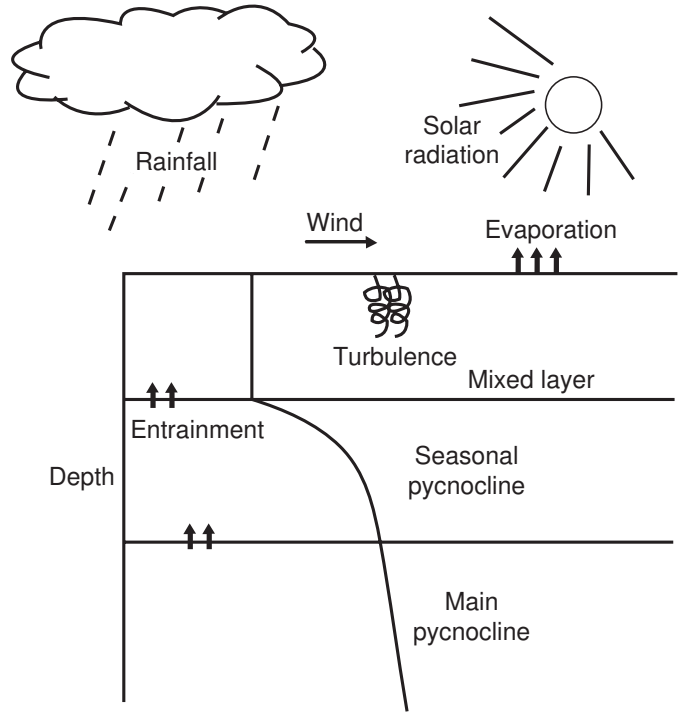

Figure 1.1: Conceptual diagram of the vertical structure in the surface layer, and the forcing and physics that govern its existence. The depth of the mixed layer, the seasonal pycnocline, and the main pycnocline are indicated, from Sprintall and Cronin [2009].

The upper mixed layer is the site of active ocean-atmosphere exchanges, due to wind mixing and surface buoyancy flux (figure 1.2, left panel). If the wind is one of main drivers of the ocean circulation at the global scale (Sverdrup showed in 1947 that the circulation in the upper kilometer or so of the ocean is directly related to the curl of the wind stress), it also has a direct influence on the vertical structure of the ocean surface layer. Wind forcing results in vertical turbulence through waves and by entrainment of cooler water through the bottom of the mixed layer, but also results in advection by upper ocean currents that can change the vertical structure of the mixed layer.

Surface buoyancy forcing is due to heat and fresh water fluxes across the air–sea interface. Convective mixing and overturning is induced by cooling and evaporation, whereas heating and rainfall cause the mixed layer to restratify. If the wind and buoyancy fluxes are strong enough, they can generate a thick and well-mixed (in temperature, salinity, and density) surface layer.

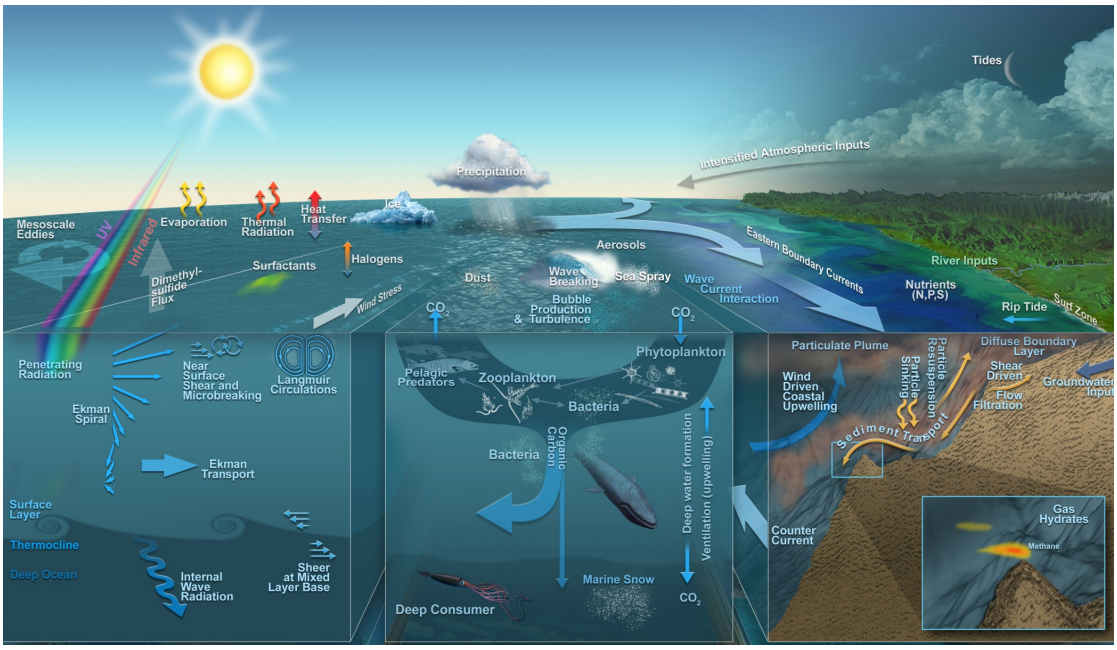

Figure 1.2: Upper Ocean physical and biogeochemical main processes. Illustration designed by John Delaney and Mark Stoermer; created by the Center for Environmental Visualization (CEV) for the NEPTUNE Program, University of Washington, Seattle.

The deep ocean is separated from the upper mixed layer by substantial vertical gradients in temperature (the thermocline), salinity (the halocline) and density (the pycnocline). The stability of the water column is maintained by lighter water lying above heavier water, the pycnocline is a region where density increases rapidly with depth. The thermocline and the halocline may not always exactly coincide in their depth range, they together determine the density structure and the the pycnocline. In mid-latitudes mainly during summer, surface heating from the sun can cause a shallow seasonal thermocline/pycnocline that connect the upper mixed layer to the deeper more permanent thermocline or “main pycnocline” (figure 1.1).

The turbulence and buoyancy changes within the upper mixed layer induced by the air–sea exchanges of wind and heat cannot overcome the great stability of the main pycnocline to penetrate into the deeper ocean. Beneath this depth the water remains isolated from the surface for a very long time. Therefore the main pycnocline marks the depth limit of the upper ocean.

Large temporal variation of the thickness of the upper mixed layer can occur on daily and seasonal timescales due to changes in the solar radiation. Similarly, the mixed layer structure can exhibit significant horizontal variations between different regions, due to contrasting atmospheric forcing, large-scale circulation, mesoscale activities and/or topography influence.

In extreme case, the mixed layer can undergo strong deepening, this phenomenon known as the open-ocean deep convection will be discussed in details at the end of this chapter in

section 1.3. In that kind of regions, no stable permanent pycnocline exists and dense water are sinking to great depths. In addition to polar regions as the Labrador (Lazier [1973]; Clarke and Gascard [1983]) , the Greenland (Schott et al. [1993]), the Weddell and Ross Seas (Killworth [1983]), open-ocean deep convection takes place in more temperate regions as the East/Japan Sea (Kim et al. [2008]) and the Mediterranean (Gulf of Lions, Adriatic Sea, Aegean Sea, CIESM [2009]).

Although the vertical structure is primarily defined by the stratification in the water properties of temperature, salinity, and density, in some regions dissolved oxygen and nutrients (e.g., phosphates, silica, and nitrates), can also vary in structure in the upper ocean. Even if these properties are considered to be non-conservative, they play an important biogeochemical role.

1.1.2 Biogeochemical Implications

The upper ocean is also the place where the marine trophic chain begins (mid-panel, figure 1.2). Below the ocean-atmosphere interface, the first chain link is composed by the phytoplankton. Its growth is controlled by light and nutrients (Mann and Lazier [2005]). The seawater rapidly attenuates the solar light in the visible portion of the spectrum (in the clearest ocean water, only 10% of the light transmitted below the sea surface reaches a depth of 90m), the concentration of phytoplankton has the potential to be more elevated at the surface than in

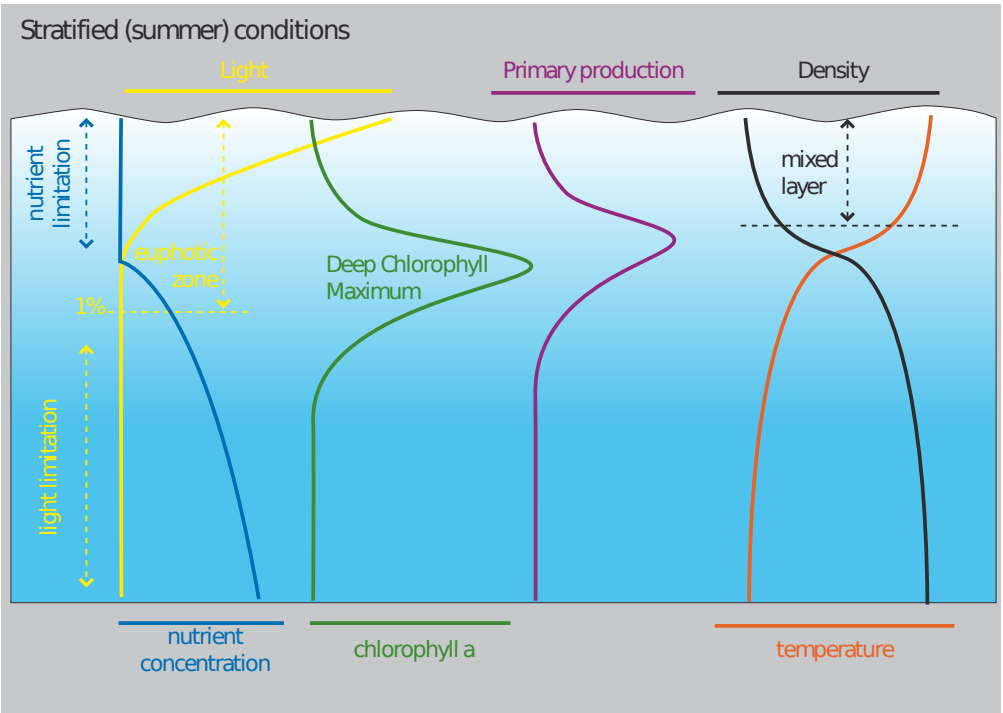

Figure 1.3: Schematic diagram showing typical vertical structure of the water column in temperate regions in summer.

depth. Close to the surface, the nutrient concentration is generally low (Longhurst [1995]) due to a rapid consumption by phytoplankton. The concentration of nutrients is higher below the euphotic zone, where excretion and losses accumulate and are remineralized by viruses and bacteria. In the open ocean, the principal way to inject important nutrients in the surface layer is by vertical exchanges and mixing of the water column (Williams and Follows [2003]), thus the mixed layer dynamic play an important role in the availability of nutrients in surface layers. In temperate regions in summer, the upper layers of the euphotic zone are nutrient-depleted, the lower levels are light-limited, and a deep chlorophyll maximum occurs within the layer of density stratification, at the same depth than the nutricline (fig. 1.3). Although in the ocean the physical conditions of living organisms are very little affected by the biology, the chlorophyll maximum constitutes one example of how the biological processes can modify the effects of physical processes. As an example, with a chlorophyll maximum sufficiently strong, the heat absorbed from the solar downwelling radiation might caused a local heating of the water, which could increased the vertical mixing and the deepening of the mixed layer.

Phytoplankton account for half of all photosynthetic activity on Earth, thus phytoplankton are responsible for much of the oxygen present in the Earth's atmosphere and play a key role in the biogeochemical cycle that transport carbon from the surface to the deep ocean. The process by which CO_2 fixed in photosynthesis is transferred to the interior of the ocean resulting in a temporary or permanent sequestration of carbon is named "biological" pump. The organic carbon is transported primarily by sinking particulate material (dead organisms or faecal pellets), but some carbon reaches the deep ocean by physical transport processes such as downwelling. The physico-chemical counterpart of the "biological pump" is the solubility pump, that transport dissolved inorganic carbon from the surface to the deep ocean.

1.2 The Mediterranean Sea

The Mediterranean Sea extends from 6° W to 36° E and 30° N to 46° N, with an average depth of 1500m and a maximum depth of 5000m. This semi-enclosed basin is connected with the Atlantic (the Gibraltar Strait, ≈300m depth) and with the Black Sea (the Dardanelles Strait, ≈100m depth). It is composed of two main basins, so-called the Western Mediterranean (WMED) and Eastern Mediterranean (EMED) separated by the strait of Sicily (≈400m depth), and eight sub-basins. The Alboran Sea (ALB), the Algerian Basin (ALG), the Northwestern Mediterranean Sea (NWMED) and the Tyrrhenian Sea (TY) compose the WMED, while the Ionian Sea (IO), the Adriatic Sea (AD), the Aegean Sea (AG) and the Levantine Basin (LE) compose the EMED (figure 1.4).

Besides wind, the main drivers of the Mediterranean Sea circulation and of the water mass properties evolution are the surface heat and freshwater exchanges between the sea and the atmosphere. Other fundamental forcings are composed by the river influx, the exchanges through the Strait of Gibraltar and the exchanges with the Black Sea (see Schroeder et al. [2012] for a review).

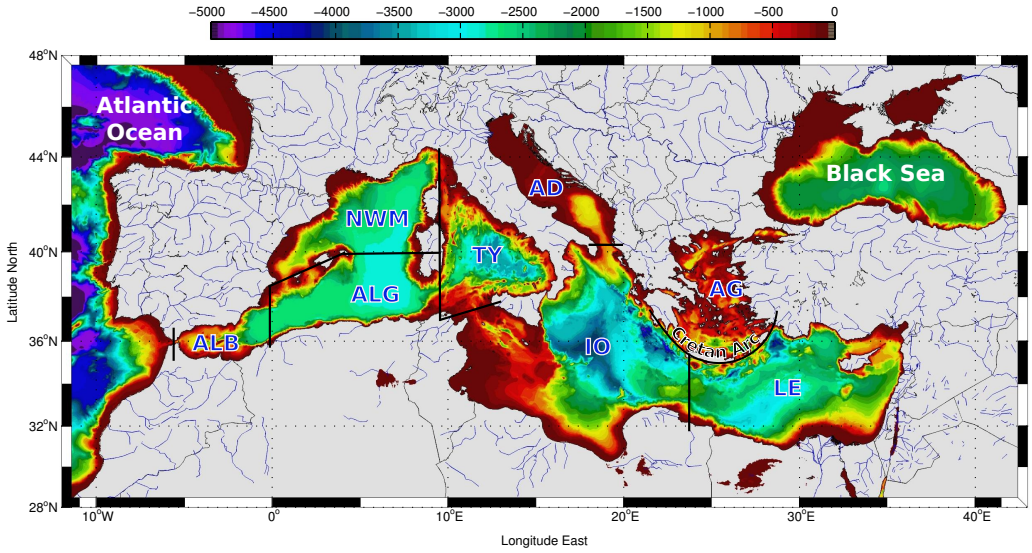

Figure 1.4: Bathymetry of the Mediterranean Sea, with its main sub-basins: the Alboran Sea (ALB), the Algerian Basin (ALG), the Northwestern Mediterranean Sea (NWMED), the Tyrrhenian Sea (TY), the Ionian Sea (IO), the Adriatic Sea (AD), the Aegean Sea (AG) and the Levantine Basin (LE)

The Mediterranean is a concentration basin, it shows an excess of evaporation over freshwater inputs and a heat loss through air-sea interaction. The freshwater loss to the atmosphere by evaporation is larger than the gains by precipitation and runoff from the main rivers and input from the Black Sea. The total heat budget is negative, that is, the Mediterranean Sea looses more energy than it gains. These deficits of freshwater and heat are compensated by exchanges through the Strait of Gibraltar (positive net water and heat transports), where the inflow is composed by a relatively warm and fresh (15.4°C, 36.2‰) upper water, and the outflow to the Atlantic is relatively cooler and saltier (13°C, 38.4‰) (Bryden et al. [1994]; Tsimplis and Bryden [2000]; Soto-Navarro et al. [2010]; Criado-Aldeanueva et al. [2012]). This circulation of heat and salt is maintained through deep and intermediate water formation. The well-defined overturning circulation (Wüst [1961]; Robinson et al. [2001]) has different deep convection zones (fig. 1.5), which produce distinct intermediate and deep water masses.

1.2.1 The Eastern Basin

The Atlantic Water (AW) that entered by the Strait of Gibraltar is identified by a subsurface salinity minimum close to 36.2‰. The overturn period of this water, between 20–50 years, is relatively short. AW is warmer and fresher than the residing waters (for a detailed review of the horizontal circulation of the water masses in the Mediterranean Sea, see Malanotte-Rizzoli et al. [1997]; Millot and Taupier-Letage [2005]; Pinardi et al. [2006]).

Being less dense, AW constitutes the surface circulation (fig. 1.5a), which describes a

cyclonic (counter-clockwise) circuit along the continental slopes through both basins. Having undergone a lot of evaporation since their entry through the strait of Gibraltar, AW is identified by a salinity close to 38.9‰ in the Levantine subbasin, where it is transformed into Levantine Intermediate Water (LIW, ≈15.5°C, ≈39.1‰) mainly close to the Rhodes Gyre (Ovchinnikov [1984]; Lascaratos [1993]). Some occasional formations were detected in the northwestern Levantine by cascading along isopycnals from shelf regions (Zodiatis et al. [1998]). Other studies report that LIW formation is not localized but rather ubiquitous in the whole Levantine (Nittis and Lascaratos [1998]; Robinson et al. [1992]). The formation of Levantine Deep Water (LDW) was also observed in that basin during severe winters (Ozsoy et al. [1993]; Gertman et al. [1994]).

Traditionally, the Aegean Sea was recognized as a source of dense waters (Nielsen [1910]), but not dense enough to contribute to the Eastern Mediterranean Deep Water (EMDW, Pollak [1951]; Wüst [1961]; Schlitzer et al. [1991]). The major sites of dense water formation are the North Aegean shelves (Theocharis et al. [1993]) and the Creatan Sea (Lascaratos [1993]). Dense waters outflow through the Cretan Straits (Zodiatis [1993]) and periodically form lenses of Cretan Intermediate Water (CIW), lying below LIW in the eastern basin (Schlitzer et al. [1991]; Theocharis et al. [1993]).

The AW, LIW and CIW flow into the Adriatic (figs. 1.5a,b) where they are involved in the formation of the Adriatic Deep Water (AdDW). They constitute traditionally the main source of the EMDW (Pollak [1951]; Wüst [1961]; Schlitzer et al. [1991]). A striking change in the main Dense Water Formation (DWF) areas occurred at the end of the 80s / beginning of the 90s, with a shift of the formation of the deep water, from the Adriatic to the Aegean (Klein et al. [1999]; Malanotte-Rizzoli et al. [1999]; Lascaratos et al. [1999]), called the Eastern Mediterranean Transient (EMT). Between 1987 and 1995 the Cretan Deep Water (CDW) became warmer, saltier and denser than EMDW, and overflowed above the sills in the Cretan Arc into the Levantine and the Ionian.

Recently, Gačić et al. [2010] showed a bi-modal oscillation of the upper circulation in the Ionian Sea. This process can shed light on the decadal variability of the AW and of a number of physical and chemical properties in the Adriatic-Ionian system.

1.2.2 The Western Basin

The LIW/CIW reaches the Tyrrhenian Sea (fig. 1.5b), where its salinity decreases close to 38.6‰ (Sparnocchia et al. [1999]) due to mixing with resident waters after crossing the Sicily Channel (≈38.75‰). Recently Millot [2013] suggested that, from the Channel of Sicily downstream, LIW should be renamed Eastern Intermediate Water (EIW). Since the traditionally called LIW in the western basin represents in fact all intermediate waters formed in all zones of dense water formation in the eastern basin, not only Levantine waters but also in particular Aegean/Cretan waters. The reader should keep in mind that the use of the LIW acronym in the WMED throughout this manuscript, refers to all eastern intermediate water flowing through

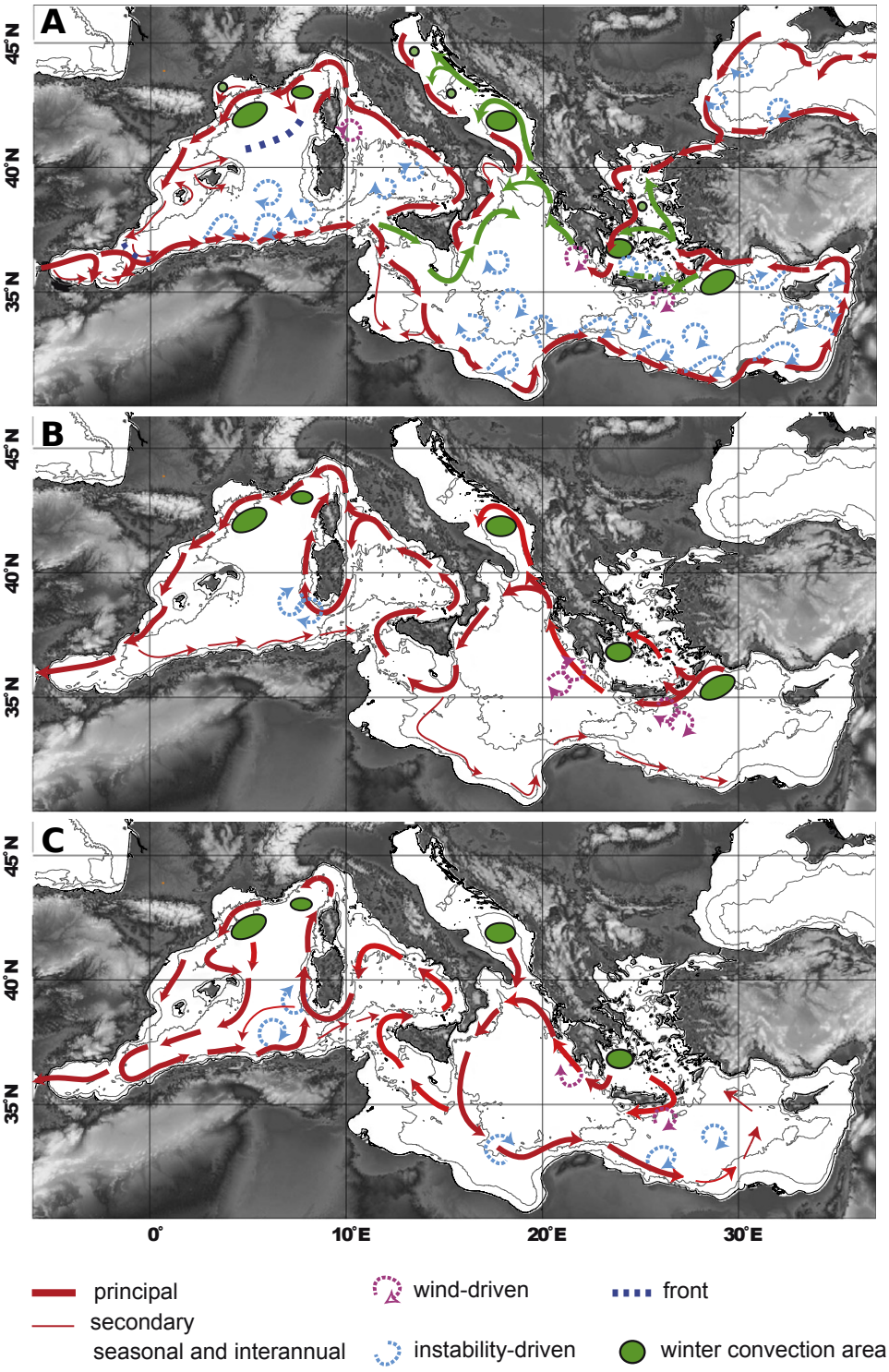

Figure 1.5: Circulation of main Mediterranean Waters from The MerMex Group [2011]: (A) surface water masses, (B) intermediate water masses, and (C) deep water masses. The thin lines represent the 1000-m and 2000-m isobaths.

the Channel of Sicily to the Tyrrhenian.

In the Northwestern Mediterranean Sea intense winter cooling and evaporation leads to the mixing of the LIW with the AW (salinities between 38.0‰ and 38.3‰), and Western Mediterranean Deep Water (WMDW) is formed by deep convection (a more detailed description is made in section 1.3). The WMDW export from the Gulf of Lions might be done by an incorporation to the boundary Northern Current (Send et al. [1996]) and by submesoscale coherent eddies (Testor and Gascard [2003, 2006]). The WMDW spreads into the Algerian and Alboran Basins mainly along the east margin of the Balearic Islands (fig. 1.5c). While a part of the WMDW mixes with the LIW and composes the Mediterranean outflow (Gascard and Richez [1985]; Kinder and Parrilla [1987]; Millot [2009]), another part join the north african coast and recirculate in the WMED (fig. 1.5c). According to Hopkins [1988], a part of this WMDW enters in the Tyrrhenian by the Sardina-Tunisia Channel and it mixes with LIW, forming the Tyrrhenian Deep Water (TDW) which circulates cyclonically in the Tyrrhenian Sea before flowing back in the western basin through the Sardinia-Tunisia Channel below the LIW. Millot [1999] argues that the mixing might be induce by cascading of the inflow from Sicily channel composed by LIW and EMDW, while Fuda et al. [2002] suggest that TDW might result from a dense water formation process occurring within the Tyrrhenian itself, east of the Bonifacio Strait. Although the formation mechanisms are not clear, this water mass was clearly identified on chlorofluorocarbon (CFC) measurements (Rhein et al. [1999]).

The main formation zones of dense water in the WMED is the Northwestern Mediterranean. If the atmospheric forcing is not intense enough or if the ocean stratification is too strong, the winter convection might not reach the LIW, and then would form Winter Intermediate Water (WIW, 12 -13°C, 38.0‰-38.3‰; Salat and Font [1987]). Its main formation area is the Gulf of Lions (Fuda et al. [2000]) and the Ligurian Sea (Sparnocchia et al. [1995]; Gasparini et al. [1999]), and WIW can be found sporadically everywhere in the WMED (Millot [1999]): in the Alboran (Gascard and Richez [1985]; Vargas-Yanez et al. [2002]), in the Algerian basin (Benzohra and Millot [1995]; Allen et al. [2008]) and close to the Sardina and Sicily Straits (Sammari et al. [1999]). The WIW seems to follow the general circulation of the AW (fig. 1.5a) from its formation area (Perkins and Pistek [1990]; Benzohra and Millot [1995]), but plays a role in the dramatic and frequent changes of the circulation around the Balearic Islands in summer (Monserrat et al. [2008]). The Northern Current may be blocked when reaching the Channel of Ibiza by anticyclonic channel-size eddies and then recirculates with a cyclonic way in the Balearic Sea without significant transport of water through the Ibiza Chanel (Castellón et al. [1990]). These channel-size eddies are composed of cold and relative fresh water (Pinot et al. [2002]) corresponding to WIW characteristics.

1.2.3 The Mediterranean Outflow

Mediterranean Waters flow out the Strait of Gibraltar as an overflow of dense saline water that spread in the North Atlantic, at a neutral buoyancy level of 1000m (Potter [2004]). This subsurface heat and salt source might play a substantial role in the heat content and dense water formation processes in the northern Atlantic and hence in the density driven circulation of the World's Oceans (Johnson [1997]; Candela [2001]). Moreover the shorter residential time for Mediterranean Waters (between 20 and 125 years according to the water mass, Robinson et al. [2001]) compared to the global ocean make the Mediterranean acting as a quick indicative of local climate anomalies, that might transmit it to the Atlantic (Bethoux et al. [1998]).

The water exiting the Strait of Gibraltar is a mixing of Mediterranean Waters: WMDW, TDW, WIW and LIW (Millot [2009]). Warming and salinification of the outflowing waters were detected by Millot et al. [2006] in the early 2000s, while a significant salinity increase of the inflowing water was reported between 2003 and 2007 by Millot [2007].

Recently Millot and Garcia-Lafuente [2011] highlighted the spatial heterogeneity and longterm temporal variabilities of outflowing waters entering the strait, that might prevent an accurate prediction of the characteristics of the Mediterranean outflow into the North Atlantic Ocean.

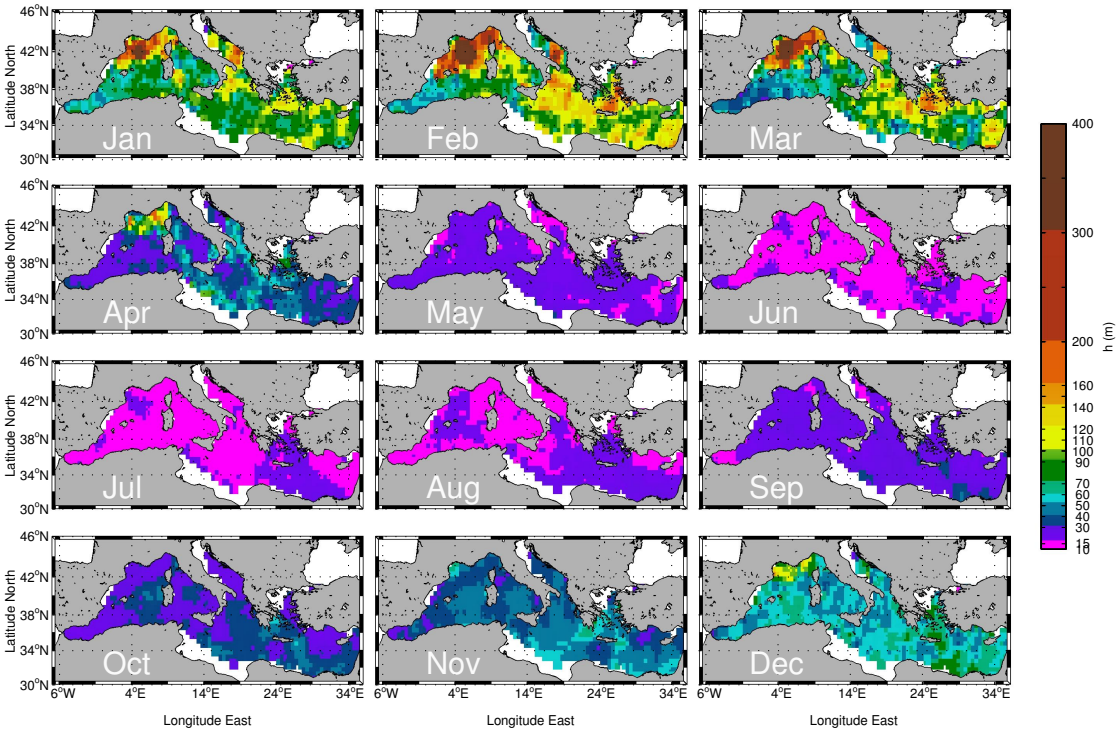

Figure 1.6: Seasonal cycle of the mean mixed layer depth in the Mediterranean from in-situ measurements collected between 1969 to 2012. MLD was calculated from each single profile using a $\Delta T = 0.2$°C criterion with a reference level at 10m depth

1.2.4 The Mediterranean Upper Mixed Layer

The Mediterranean Sea is also a region where mesoscale processes (meanders, eddies, filaments) play a key role in determining the characteristics of the large-scale circulation, the distribution and mixing of water masses, with important consequences on the whole ecosystem functioning (CIESM [2005]). Mesoscale features are set primarily by the internal properties of the ocean. In the Mediterranean, the internal Rossby radius does not exceed 15 km, about four times smaller than the typical values found in the world oceans (Chelton et al. [1998]).

The interaction between atmospheric forcings (heat and freshwater flux, wind stress), large-scale circulation, mesoscale activities and a tortuous basin topography makes the dynamics of the upper mixed layer in the Mediterranean extremely complex (D'Ortenzio and Prieur [2012]). However due to the intensive sampling of the Mediterranean during the last decades, D'Ortenzio et al. [2005] performed a climatological analysis of the seasonal cycle of the upper mixed layer. The figure 1.6 is an updated version of this climatology and the data used are presented in chapter 2, section 2.4. A discussion of the differences with the climatology made by D'Ortenzio et al. [2005] can be found in chapter 3, section 3.3.2.

The Mediterranean Mixed Layer Depth (MLD) climatology presented figure 1.6 shows similar remarkable features than in D'Ortenzio et al. [2005]:

- A seasonal variability, characterized by a basin scale deepening from November to February–March and an abrupt restratification in April
- The EMED displays MLD values generally higher than the WMED, with the important exception of the Northwestern Mediterranean region
- The maximum values of the MLD are observed in February–March in the Gulf of Lions and in the Southern Adriatic Sea, which are known regions of deep convection.

1.3 Dense Water Formation in the Gulf of Lions

The prevailing winds in the northwestern Mediterranean are the Mistral (north) and Tramontane (north-west). They are channeled by the surrounding topography, namely the Alps, the Massif Central and the Pyrenees. These winds are particularly strong in winter, bringing cold and dry polar air over the Gulf of Lions. Heat losses in the Gulf of Lions in winter can then reach very high values, sometimes exceeding 1000 $W.m^{-2}$ (Mertens and Schott [1998]). Evaporation and cooling of the surface waters due to the northern wind bursts, are responsible of dense water formation in the open-ocean during the Open-Ocean Deep Convection (OODC) process, but also on the continental shelf. The dense water formation on the shelf can also participate in the formation of intermediate waters (WIW) and even occasionally in the deep water renewal (fig 1.7b) .

1.3.1 The Open-Ocean Deep Convection

The northwestern Mediterranean is one of the few regions of the world ocean where deep convection occured (Marshall and Schott [1999]). The other main areas are in North Atlantic (Labrador Sea and Irminger), in the subpolar regions of the northern hemisphere (Norway and Greenland Seas) and in the southern hemisphere (Weddell and Ross Seas). In these regions, the surface water becomes denser by evaporation and cooling, which causes the vertical mixing of the water column. This thermohaline circulation plays a key role in the ocean circulation (see Wunsch [2002] for a discussion on the definition of the thermohaline circulation). Its understanding is therefore an important issue in physical oceanography. The deep convection processes studied in the Gulf of Lions might improve our knowledge of the physical phenomenon, but also better understand the deep water circulation in Mediterranean.

The intense and deep vertical mixing of deep convection might also have major impacts on biology, since the intensity of the spring phytoplankton blooms and their interannual variability may be largely determined by the amount of nutrients injected from the deep ocean to the photic zone during winter episodes.

Since the first experiment (MEDOC Group [1970]) took place in 1969, the open-ocean deep convection can be decomposed in three phases that can overlap (figure 1.8).

The preconditioning phase involves a local weakening of the ocean stratification. In the Northwestern Mediterranean the global circulation is cyclonic (figs 1.7a and 1.5). The gyre is

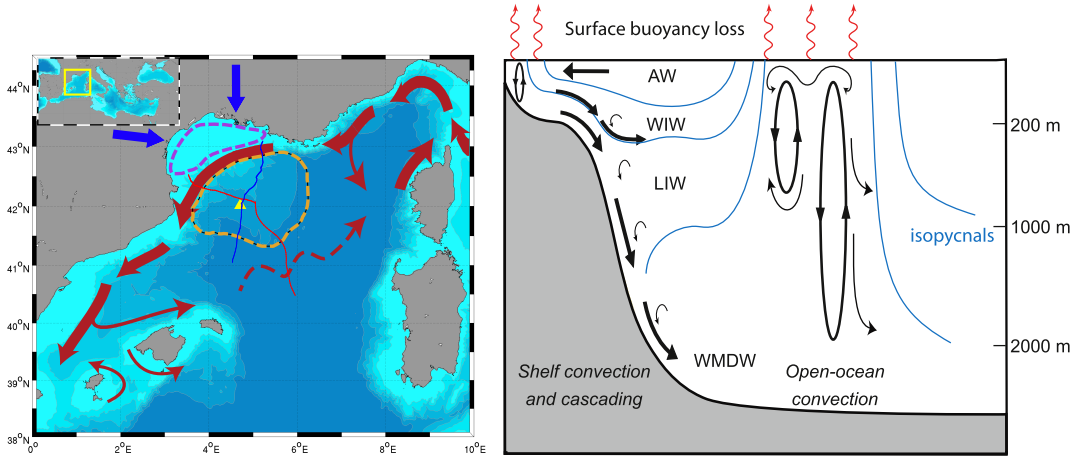

Figure 1.7: On the left panel, map of the Northwestern Mediterranean showing the dense water formation on the shelf (purple dashed line) and in the open-ocean (orange dashed line) with the major continental winds (blue arrows) and the basin-scale surface circulation (red arrows). The thin dotted lines correspond to glider Campe sections presented on figure 1.9, the red one corresponds to the Mistrals T02 deployment in October 2012 and the blue one represents a section of the ASICSMED deployment. On the right, a schematic diagram showing the dense shelf water cascading and open-ocean convection processes, with the water masses involved (from Puig et al. [2012])

bounded on the north by the Northern Current, while a eastward current poorly defined and marked by the North-Balearic Front seems to define the southern boundary (Millot [1999]; Testor and Gascard [2006]). This global cyclonic circulation produces a doming of isopycnals (left panel on fig. 1.9) that exposes a lot of weakly stratified water to the atmospheric forcings, in the central part of the gyre.

The Rhone deep-sea fan may also play a role in setting up a Taylor column. This feature is due to the Coriolis effect. Rotating fluids that are perturbed by a topographic obstacle will tend to form columns parallel to the axis of rotation. Thus in the Gulf of Lions, water parcels will tend to stay longer in the area, and will be more exposed to the atmospheric forcing (Hogg [1973]; Madec et al. [1996]).

The Gulf of Lions is also characterized by a large mesoscale activity (Gaillard et al. [2000]; Escudier et al. [2013]), especially through instabilities of the Northern Current (Crepon et al. [1982]; Sammari et al. [1995]; Flexas et al. [2005]). Mesoscale eddies which may present a weakly stratified subsurface core, can also act as agents of local preconditioning (Killworth [1979]; Legg and Marshall [1998]; Lherminier et al. [1999]; Straneo and Kawase [1999]; Legg and McWilliams [2001]; Steffen and D'Asaro [2004]).

Vigorous buoyancy loss during the cooling and evaporation event, such as the strong wind outburst of continental air, initiates the deep convection of the very weakly stratified water (fig.

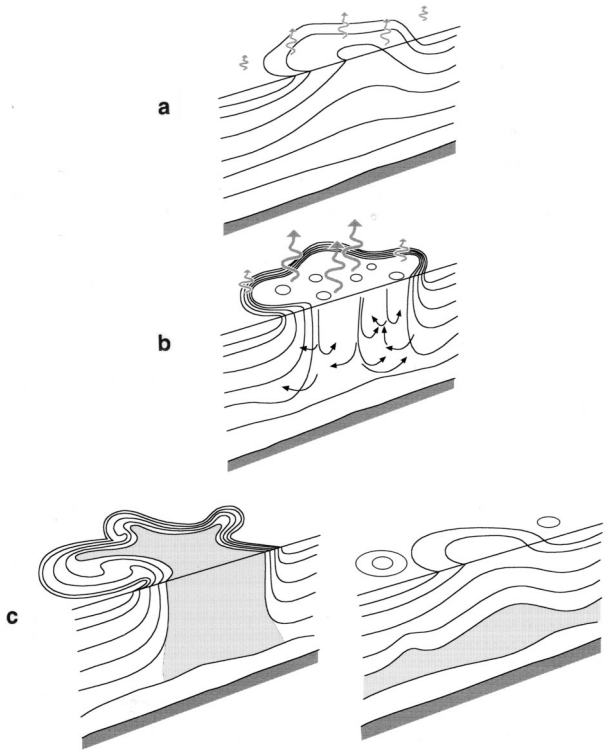

Figure 1.8: Schematic diagram of the three phases of ocean deep convection: (a) preconditioning, (b) deep vertical mixing, (c) lateral exchange leading to spreading and restratification, from Marshall and Schott [1999]

1.8b) in the core of the cyclonic gyre. The vertical mixing occurs in plumes of horizontal scale of O(1km), at vertical speeds up to 10cm.s^{-1}. These small scale features were first observed by Voorhis and Webb [1970] using isobaric floats, then by Schott and Leaman [1991] and Schott et al. [1996] using moored ADCPs. More recently, downward vertical velocities measurements up to 10cm.s^{-1} were observed using gliders (Merckelbach et al. [2010]). These plumes mix properties over the preconditioned site, forming a deep "mixed patch" (right panel on fig. 1.9) ranging in scale from several tens of kilometers to >100 km in diameter. The characteristics of the newly formed water mass can be linked to the frequency and the intensity of the surface forcing (Artale et al. [2002]; Grignon [2009]) and to the heat and salt content of the "preconditioned" state (Schroeder et al. [2010]; Herrmann et al. [2010]).

The density contrast between the mixed patch and the surrounding would establish a rim current at the edge of the mixed patch which would be baroclinically unstable and shed eddies of scale O(5-10km). These eddies would be geostrophic considering the low stratification of the area. The spreading of dense water is made through the action of these eddies (Testor and Gascard [2003, 2006]; Demirov and Pinardi [2007]; Herrmann et al. [2008]) and by their incorporation into the northern boundary current (Send et al. [1996]; Herrmann et al. [2008]). Restratification of the deep convection zone starts as soon as the intense vertical mixing

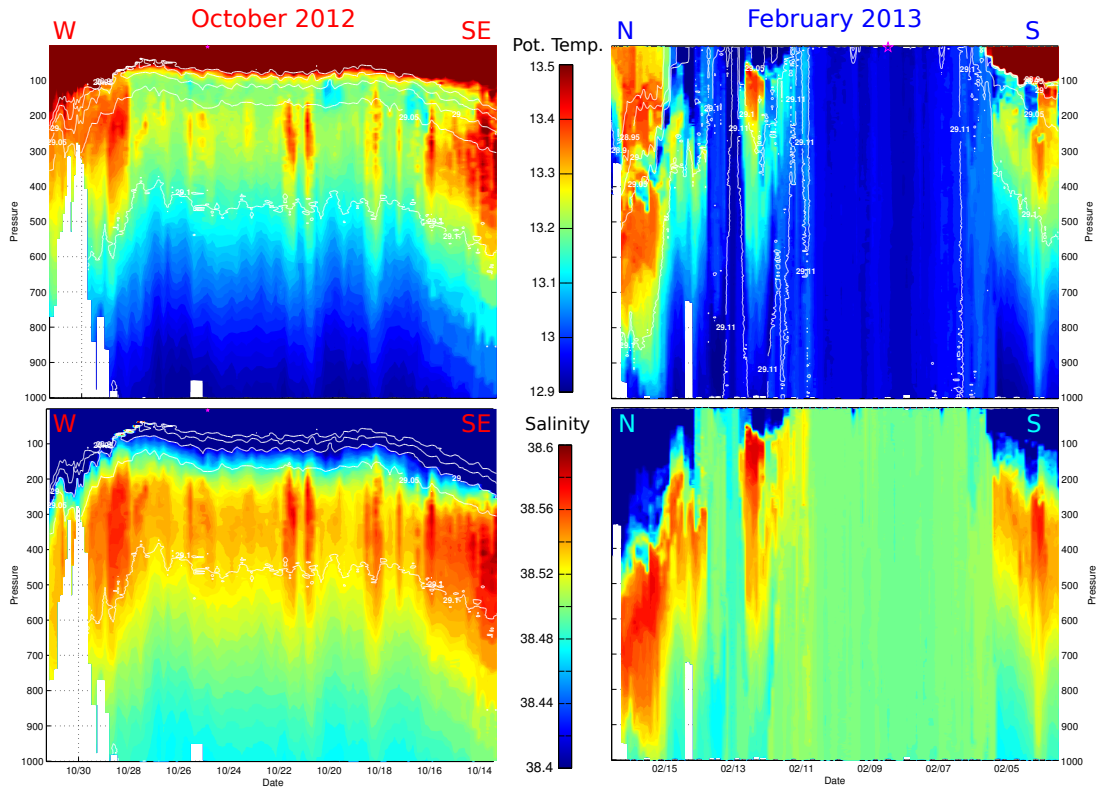

Figure 1.9: Temperature (top) and salinity (bottom) sections in the Gulf of Lions from the glider Campe (courtesy of A. Bosse), in October 2012 (left) and February 2013 (right). The glider sections are indicated on figure 1.7a.

stopped. After the end of the deep convection, the restratification of the upper ocean is mainly due to both the boundary current and the mesoscale structures that advect surface light water (Leaman and Schott [1991]; Schott et al. [1996]; Herrmann et al. [2008]).

1.3.2 The Dense Shelf Water Cascading

Dense Shelf Water Cascading (DSWC) is a climate-driven oceanographic phenomenon on high latitude continental margins, but also on mid latitude and tropical margins (Ivanov et al. [2004]; Durrieu de Madron et al. [2005]). These regions are generally characterized by a shallow depth and a steep slope separating them from the deep ocean. The dense water is formed by cooling, evaporation or during the ice formation. The buoyancy driven current in the surface layer over the continental shelf descends down the continental slope to a greater depth.

The cascades of dense shelf water and the associated strong currents can induce erosion and resuspension of surface sediments, promoting exchanges between the shelf and the deep ocean. This process plays therefore a role in the export of particulate and organic matter from the shelf, contributing to the carbon sequestration in the ocean deep.

Shapiro et al. [2003] distinguish four phases in the process of DSWC. During the preconditioning phase, dense water accumulates on the shelf, which gives rise to a density front. During the active phase, this density front propagates down the slope. Then, the main phase is the development of an almost steady flow of dense water along the slope, associated with a strong downward current. Finally, in the final phase, the dense water reaches it neutral buoyancy level, stabilizes and then spreads leaving the slope.

The continental slope of the Gulf of Lions is incised by numerous canyons (fig. 1.10). They are natural corridors for the dense water formed on the shelf during episodes of strong continental wind bursts, where a part of it escapes towards the open ocean by cascading along these canyons. Several episodes of DSWC have been observed, in this region characterized by large continental inputs and high biological productivity, particularly due to the presence of the Rhone River (Durrieu de Madron et al. [2005]; Heussner et al. [2006]; Canals et al. [2006]).

The dense water cascading down the canyons to the deep ocean carries large masses of sediment and organic matter affecting the functioning of deep sea ecosystems and the geological characteristics of these canyons (Palanques et al. [2006]; Gaudin et al. [2006]; Heussner et al. [2006]; Canals et al. [2006]; Puig et al. [2008]; Pusceddu et al. [2013]).

1.3.3 The Western Mediterranean Deep Water(s)

The deep layers of the WMED were first considered as relatively constant in temperature and salinity. However, in certain years, an “occasional bottom water” was also detected in the northwestern Mediterranean, in addition to the typical water masses (fig. 1.11), especially in

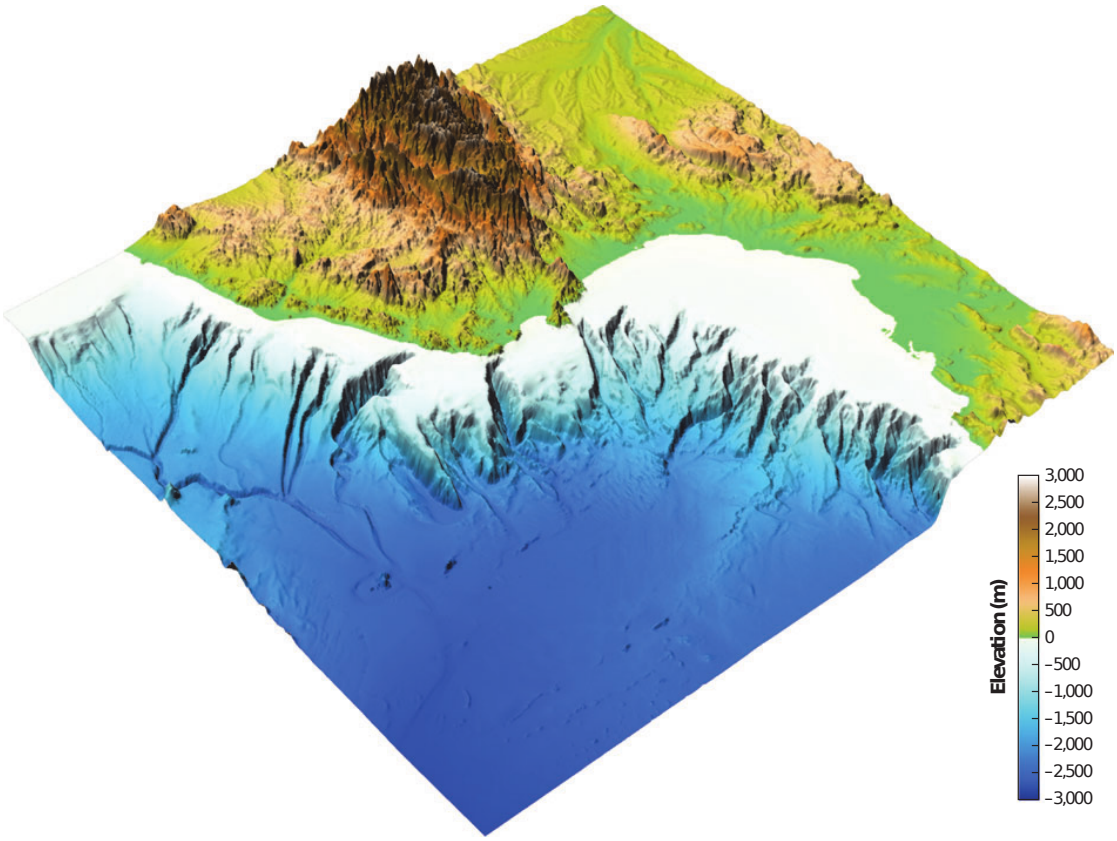

Figure 1.10: Perspective view from the Gulf of Lions showing the numerous submarine incising canyons, from Puig et al. [2013] (10 times vertical exaggeration)

.

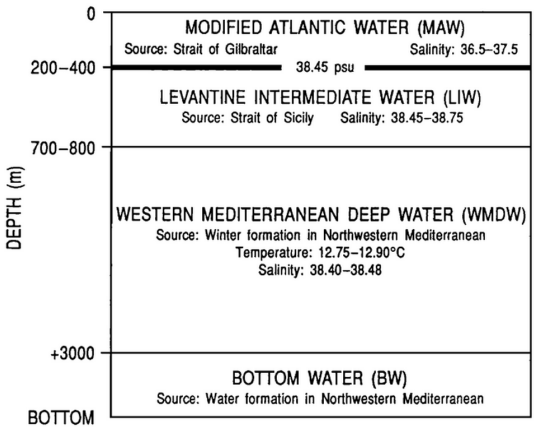

Figure 1.11: Scheme of the main water masses in the Western Mediterranean and their approximate location in the water column, from La Violette [1994]

.

1972–1973 and in 1981–1982 (Lacombe et al. [1985]). The mechanism of formation of this new bottom water has seemed to be likely a result of open ocean convection. Significant changes

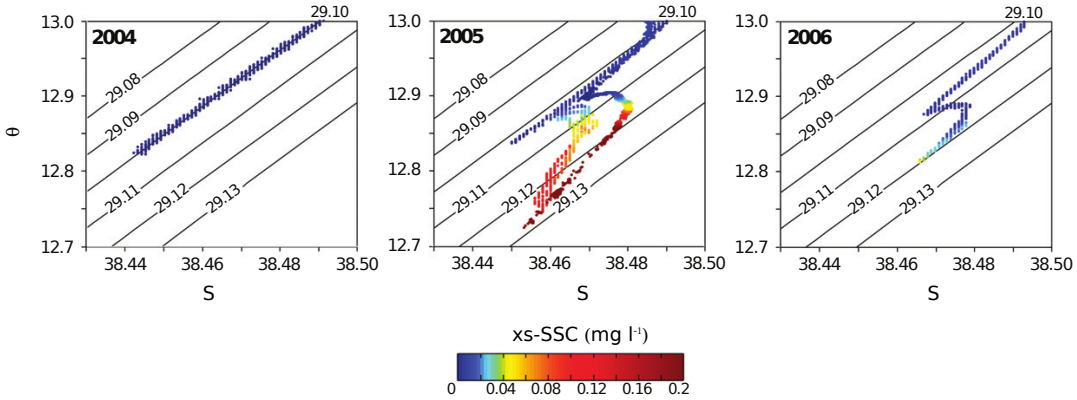

Figure 1.12: Deepest part of θ-S diagrams ($\approx$ 600/800m to the bottom) made in the Northwestern Mediterranean during different oceanographic surveys (2004:EFLUBIO; 2005:MEDOCC-05 and STRATA-3; 2006:MEDOCC-06). The color code corresponds to the excess suspended sediment concentration, from Puig et al. [2012]

.

in deep water θ and S characteristics were also found by Leaman and Schott [1991], which have detected an increase in deep-water (>2000m) salinities and temperature after the severe winter 1986/1987.

The interannual variability of convection activity in the Gulf of Lions (Mertens and Schott [1998]; L'Hévéder et al. [2012]) leads also to an interannual variability in thermohaline characteristics of WMDW. During severe winter, the strong surface buoyancy losses might lead to an active mixing of the whole water column. The deeper layers of the water column are subjected to an input of heat and salt coming from the mixing of the upper and intermediate layer, modulated by the surface heat losses and evaporation responsible for the deepening of the mixed layer.

Thus, the evolution of WMDW thermohaline characteristics through deep convection events might explain the long-term warming and salting trends observed in the deep layers of the WMED by several authors (Bethoux et al. [1990, 1998]; Rohling and Bryden [1992]; Leaman and Schott [1991]; Krahmann and Schott [1998]; Rixen et al. [2005]; Vargas-Yanez et al. [2010a,b]). Recently, Bethoux et al. [2002] hypothesized the contribution of DSWC in the formation of WMDW after the observation of a bottom anomaly in 1999, that rapidly spread throughout the western Mediterranean basin.

Very intense events of dense water formation have been reported since 2005 in the Northwestern Mediterranean Sea, in winter 2004/05 as well as in winter 2005/06 (Lopez-Jurado et al. [2005]; Salat et al. [2006]; Canals et al. [2006]; Schroeder et al. [2006, 2008]; Font et al. [2007]; Smith et al. [2008]), involving both OODC and DSWC. The DSWC event was exceptionally intense, lasting for more than three months. These dense shelf waters propagated along and across the continental slope (Font et al. [2007]), reaching depths >2000 m where they merged with dense waters formed off-shelf, by the OODC process. This intense event was well monitored (Canals et al. [2006]; Puig et al. [2008]) and modeled (Ulses et al. [2008b]). In winter

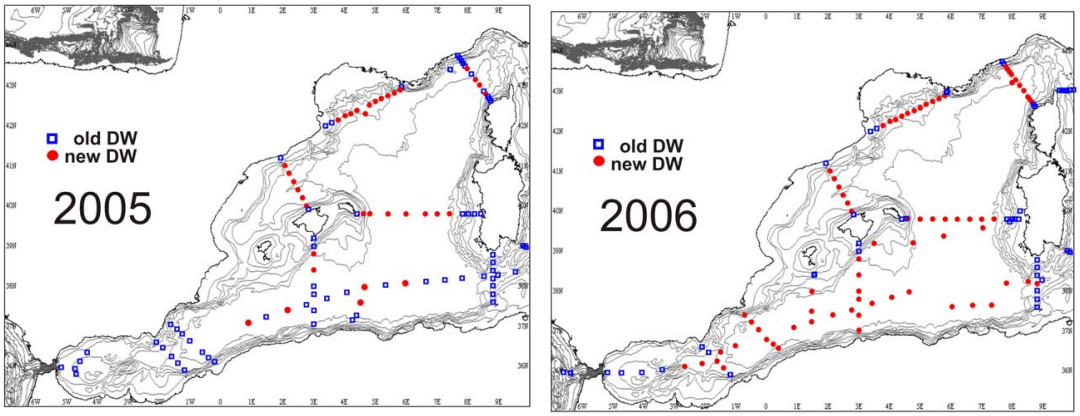

Figure 1.13: Spreading of the newly-formed WMDW (red dots) in 2005 and 2006, from Schroeder et al. [2008]

2006, another deep DSWC event occurred which could be also traced down to 1900 m depth by a large network of instrumented moorings deployed in the south-western end of the Gulf of Lions margin (Sanchez-Vidal et al. [2008]; Palanques et al. [2012]).

There is also new indications of dense water formation in winter 2008/09 (CIESM [2009]). Since winter 2004/05 the deep waters of the WMED have experienced significant physical changes (Lopez-Jurado et al. [2005]; Schroeder et al. [2006, 2008]; Smith et al. [2008]), with an abrupt increase in the deep heat and salt contents, and a change in the deep stratification, with the appearance of a sharp inversion in the temperature-salinity diagrams (fig. 1.12). This anomaly has been significantly enhanced by the huge amount of new deep water formed in winters 2004/05 and 2005/06 (fig. 1.13a), which induced a basin- wide propagation of the new WMDW and thus of the abrupt increase in deep heat/salt contents (Schroeder et al. [2008]).

From 2004 to 2006, the deep layer of the WMED experienced a warming of about 0.038°C and a salinity increase of 0.016‰(Schroeder et al. [2012]). These increases are five to seven times greater than the increasing trends indicated by Bethoux et al. [1998] and about four times greater than the estimates given by Rixen et al. [2005] for the 1985-2000 period. This anomaly has also been found at the Camarinal sill and on the Moroccan shelf in the Strait of Gibraltar, where Millot [2009] reported significant changes of the outflow in spring 2005, no LIW was recorded in the outflow and WMDW was detected at both locations. Millot [2009] attributed these observations to the large amount of WMDW formed during winter 2004/05 in the Northwestern Mediterranean.

Several causes responsible for this intense event of deep convection were discussed. First, winter 2004-2005 was one of the coldest and driest winter of the last 40 years (Lopez-Jurado et al. [2005]). Second, Gasparini et al. [2005] showed that the Eastern Mediterranean Transient (EMT, Malanotte-Rizzoli et al. [1999]; Lascaratos et al. [1999]; Klein et al. [1999]) induced a remarkable injection of heat and salt in the eastern waters flowing westward through the Sicily channel to the deep Tyrrhenian sub-basin. The propagation of this θ-S increase from the Eastern Mediterranean basin could have induced a warming and salting of the intermediate

layer of the NWMED (Schroeder et al. [2010]). Results from modeling studies (Herrmann et al. [2010]) assess the role of the EMT, by deepening the heat and salt maxima, in the high volume of WMDW formed in 2005. Grignon et al. [2010] showed that even a normal winter would have led to deep convection in 2004/05 due to low pre-winter stratification.

2 Measurement platforms

Contents

This thesis is based on a large number of oceanographic data which are presented in this chapter. The LION mooring line, together with Conductivity-Temperature-Depth (CTD) stations and autonomous platforms, deployments carried out in the Gulf of Lions since 2007, compose the core of the dataset used in this thesis.

A database combining all available hydrological data in the Mediterranean was established during this work in order to achieve a climatology of the mixed layer depth, of the thermocline and of the upper ocean heat rate. We also present in detail the database (data description, quality control procedures, user operations).

Finally additional data used in this thesis will be presented: shipboard (or vessel-mount) Acoustic Doppler Current Profiler (ADCP), ocean color from satellite data and atmospheric reanalysis.

2.1 LION Mooring Line

The mooring site was chosen in the center of the convection zone described by MEDOC Group [1970], Leaman and Schott [1991] and The THETIS Group [1994] at 42°02.4'N, 4°41.0'E. There were six deployments (LION1 to LION6) during which the line was equipped with 8 to 26 instruments between September 2007 and July 2012. Since 2010, the mooring line is maintained within the observing system MOOSE (Mediterranean Ocean Observing System on Environment). The evolution of the instrumented line over the years is presented in detail in table 4.2, in the chapter 4. The configuration of the mooring line deployed during the July 2012 - July 2013 period is showed on figure 2.1.

2.1.1 Description

RBR (temperature recorders), SeaBird Microcat SBE37-SMP (conductivity-temperature-pressure recorders) were used until June 2011. Since then, the 10 RBR were replaced by SeaBird Temperature Logger SBE56. Nortek Aquadopp were deployed since LION 3 (September 2008) at 5 levels measuring horizontal and vertical currents, while there were only 2 Aanderaa RCM9 at 1000m and 2300m depth during LION1 (Sep. 2007 / Mar. 2008) and 1 Aanderaa RCM9 at 1000m LION2 (Sep. 2008). During these two first deployments, we get only the horizontal currents. The vertical sampling was better since LION 3 with 20 temperature records, 10 salinity records and 5 current records spanning depths from 150 m to the bottom (2300 m). Here we did not use the Aquadopp temperature data because of the low resolution and accuracy of the sensor (0.1°), and because for each current meter there was another much more accurate temperature sensor available nearby (a few meters).

The severe environmental conditions imposed us the use of a subsurface mooring, this prevent us from recording the upper 150m heat content. This lack of data could be filled by close glider profiles and by temperature records from the meteorologial surface buoy LION deployed by Météo-France close to the deep mooring. RBR were set up with a 15 seconds sampling, while Microcat and current meters had a sampling of respectively 6 minutes and 30 minutes. In order to have a consistent data set, we undersampled RBR and Microcat to get 30-minutes time-series.

In general all the mooring instruments returned good data, except for some periods. During LION 3, the 500m depth Aquadopp seemed to have encountered writing problems. Due to a breaking of the base of the line during the recovery (April 2009), we lost the bottom Aquadopp and no current data were obtained at 2300m for the period from September 2008 to March 2009. During LION 5, there were some battery issues on five Microcat (165m, 1100m, 1300m, 1780m and 200m) which stopped recording in February 2011. A delayed recovery of the mooring in July 2012 caused battery issues for most of the current meters (the 150m and the 2300m depth current meter stopped on 11 June 2012, while the 250m and the 500m depth stopped on 14 July 2012.

2.1.2 Calibration

Since the recovery of LION 4 (in June 2010), inter-calibration of the moored instruments after and before each deployment are done. Niskin bottles are removed from the shipboard Rosette, and replaced by Microcat and RBR (or SBE56). We perform an hydrographical cast with a 20 minutes stop at 1000m depth, thus we can have a relative calibration of the moored instruments with the CTD probe SBE 19plus. Post- and/or pre- cruise calibrations, together with in-lab analysis of salinity bottles with a Salinometer (Guideline Autosal) calibrated using standard water at 38‰ give us an absolute accuracy, for all records used in this study, better than 0.005‰ for S, and 0.001°C for θ. From September 2007 to April 2009, no inter-calibration was done. Comparisons with gliders and CTD stations was the only solution to detect some biases in the conductivity measurements. The conductivity corrections applied to the Microcat correspond to equivalent salinity corrections ranging from 0.000‰ to 0.012‰.

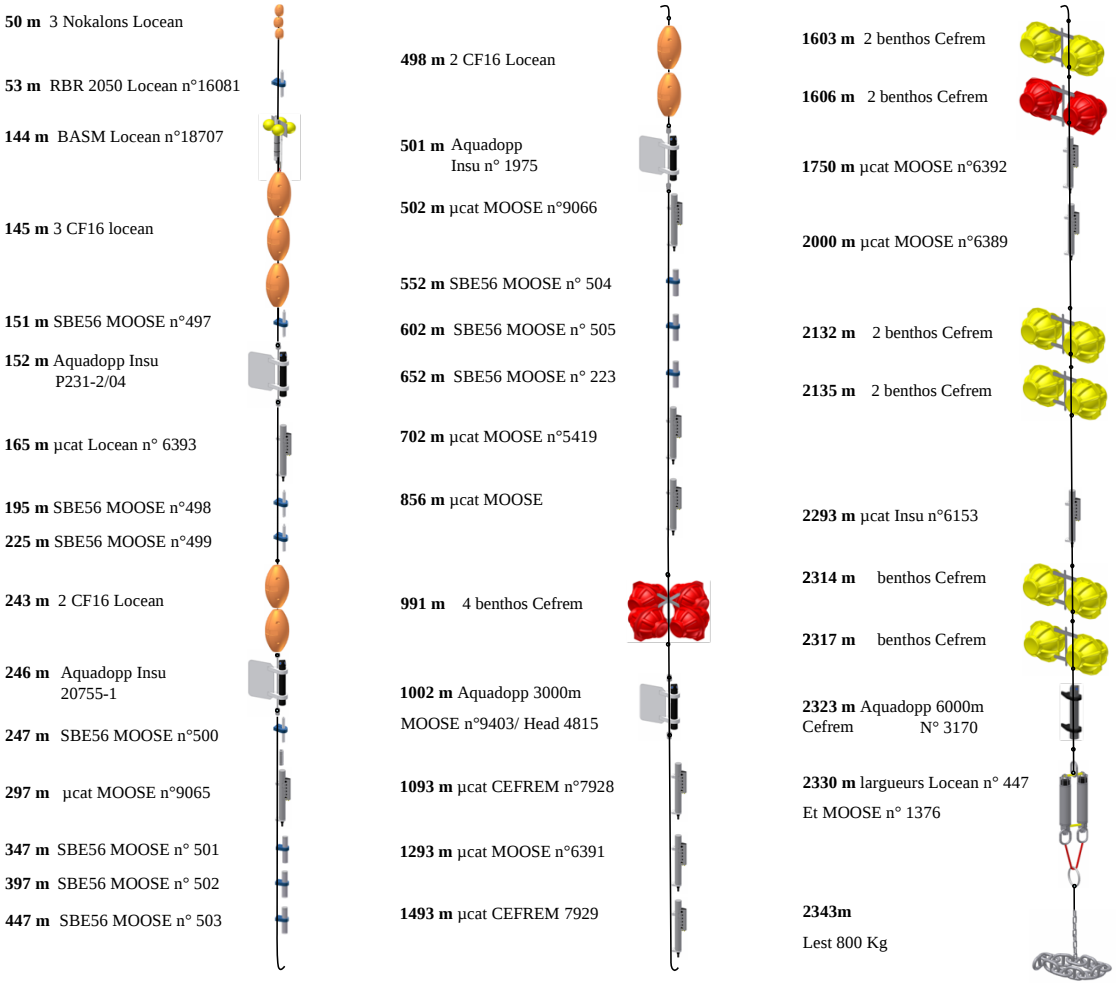

Figure 2.1: Detailed plan of the deep LION mooring line deployed in July 2012 in the framework of the observing system MOOSE.

2.1.3 Météo-France Meteorological Buoy LION

A useful complementary dataset to the deep LION mooring is the instrumented Météo-France buoy MF-LION. This meteorological buoy is located at 42.0637°N 4.6482°E, 4-4.5 kilometers from the deep mooring location. In addition to the atmospheric sensors and to the sea surface temperature sensor, a 250m mooring line was fixed below the surface buoy since November 2009 (table 4.2). This line is currently equipped by 20 temperature sensors NKE SP2T installed between 5 to 250 meters below the sea surface. An additional SeaBird Microcat SBE37-SMP was installed at 2m depth in September 2011. Since 2012 maintenance operations, surface salinity is also available.

2.2 CTD stations

The CTD (Conductivity, Temperature, and Depth) probe is the primary tool that has been used during the last four decades, for determining essential physical properties of sea water. This device has supplanted the traditional hydrocast using Nansen bottles and reversing thermometers that was standard physical oceanographic practice from about 1910 to 1970.

The shipboard CTD is made up of a set of small probes attached to a large metal rosette wheel which is lowered on a cable down to the seafloor. The CTD and the rosette can also be a host of other accessories and instruments (fig 2.3a), as the Niskin bottles that collect water samples at different depths, Acoustic Doppler Current Profilers (ADCP) that measure

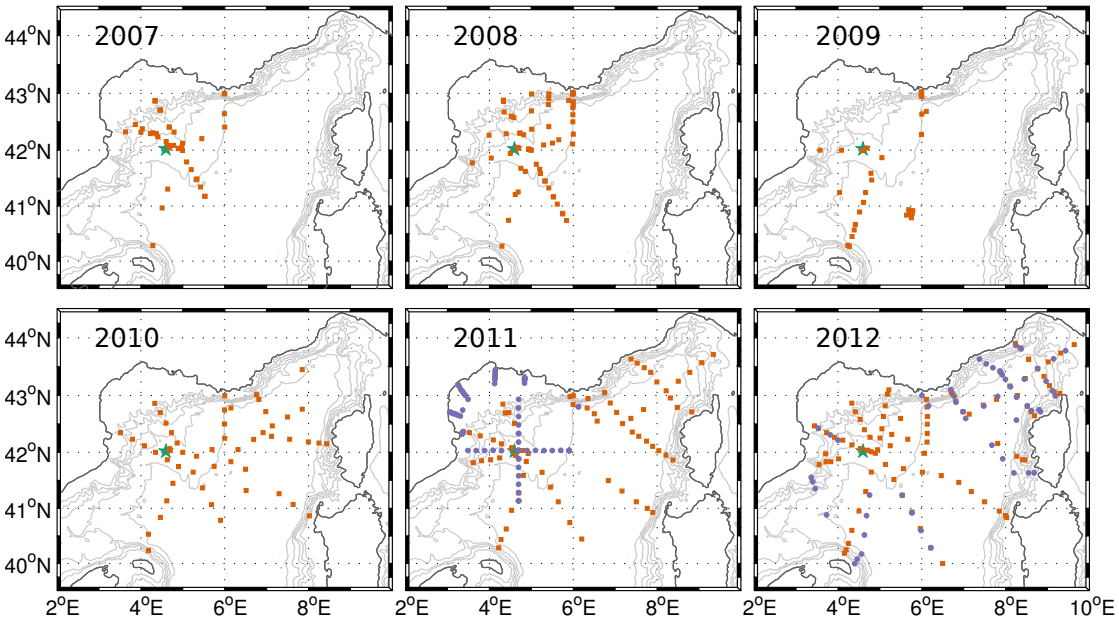

Figure 2.2: Maps of CTD stations carried out from 2007 to 2012 in the NWMED (2007: DOCONUG2007, 2008: DOCONUG2008, 2008: 42N5E, 2010: MOOSE-GE2010, 2011: in blue CASCADE and in orange MOOSE-GE2011, 2012: in blue DOWEX2012 and in orange MOOSE-GE2012) with the LION mooring line indicated by the green star

the horizontal velocity, oxygen or other biogeochemical sensors.

520 CTD profiles were carried out during several oceanographic cruises (DOCONUG2007, DOCONUG2008, 42N5E, MOOSE-GE2010, CASCADE, MOOSE-GE2011 and MOOSE-GE2012) in the Northwestern Mediterranean (fig. 2.2).

At least at all stations, pressure, temperature and conductivity were measured with a CTD Sea-Bird SBE 911+. Water samples were collected and analyzed on a salinometer to calibrate the conductivity sensor. The accuracy is estimated to be ± 0.004 for salinity and ± 0.001° for temperature.

2.3 Gliders data

Gliders are relatively new oceanographic platforms (Testor et al. [2010]). These autonomous underwater vehicles are capable of moving to specific locations and depths. The glider can move vertically by varying its buoyancy using a ballast system. It converts this vertical movement into an horizontal one thanks to a fixed and symmetrical pair of wings. The position of its center of gravity can move relative to its center of buoyancy by moving internal mass (battery packs) and this can control the pitch angle of the vehicle. They can dive and ascent

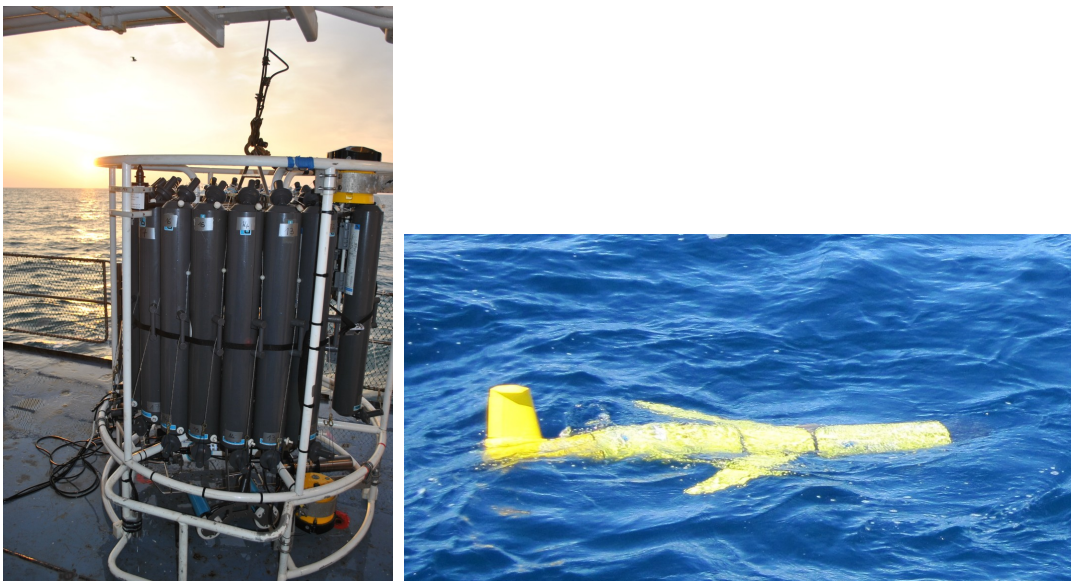

Figure 2.3: *Left panel*: CTD rosette onboard R/V Atalante in the Northwestern Mediterranean during the CASCADE cruise in March 2011. The CTD package was the host of a number of other instruments dedicated to monitor biogeochemical parameters like dissolved oxygen, light attenuation, turbidity, fluorescence, photo-synthetically active radiation, colored dissolved organic matter, and altimetry probes. A Lowered ADCP (L-ADCP) system with two (upward and downward looking) ADCPs, together with an Underwater Video Profiler (UVP) and a Laser In-Situ Scattering and Transmissiometry sensor were setup on the rosette. The carrousel holds 22 Niskin bottles of 12L.
Right panel: Slocum Glider "Tenuse" off Banyuls just before its recovery on 2010/09/29 by R/V Nereis

with angles between 15° and 30° relative to the sea surface with a horizontal speed of about 30-40 cm.s^{-1} and a vertical speed of 10-20 cm.s^{-1}. This propulsion system allows the glider to collect oceanographic measurements along a sawtooth trajectory between the surface and a prescribed depth (typically 1000m depth) or the bottom, its onboard altimeter allowing him to avoid the bottom and to be operated in relatively shallow waters.

Considering the dive/ascent angles and the typical slopes of oceanic variables (shallow water framework), the profiles can be considered as vertical. The time (spatial) resolution is a profile every 1-5 hours (1-5 km), depending on the depth of diving. It travels at a speed of 20-25 km per day. With an autonomy of 1.5 to 4 months depending on the onboard instruments, it can cover a distance comprised between 1100 and 3000 km during a deployment.

The long-range and duration capabilities of gliders make them ideally suited for subsurface sampling at the regional scale. Carrying a wide variety of sensors, they can be programmed to patrol for weeks, surfacing to transmit their data to shore while downloading new instructions at regular intervals. These small, lightweight devices (2m long and about 50kg) can be launched and recovered from small ships. All these advantages make gliders a useful complementary measurement platform to the large scale and synoptic basin sampling operated by surface ships.

Quality control and calibration of gliders profiles (particularly the conductivity sensor) can be made using other measurement platforms. First, if a glider is passing near the LION mooring line, its θ-S values will be compared with those measured at different depths by the mooring instruments. Only the nearer glider profiles are kept (less than 2.5km from the mooring line). Second, the DYFAMED time-series in the Ligurian Sea, can be used as another "calibration station", especially for gliders which would not passed by the LION mooring, however only two instruments (700db 1000db) can be use to calibrate gliders data. Third, one can use shipboard CTD measurements acquired in the vicinity of gliders.

Gliders with an unpumped CTD sensors, can be the source of salinity errors when gliders move through temperature gradients (like the thermocline). Because temperature sensors are located outside the conductivity cell, the temperature reported by the CTD will be slightly different from the actual temperature inside the conductivity cell. The thermal inertia and time responses can be corrected by aligning temperature and conductivity data for the computation of salinity (Garau et al. [2011]).

Once gliders data have been compared with another correct source of data (like the LION mooring line), the accuracy on gliders measurements is certainly better than 0.01°C and 0.01‰. Thus permanent mooring lines are very useful for glider calibrations because unlike shipboard CTD measurements, it is (almost) certain that they will always be in the same location, whatever the time of year.

Since 2007, gliders were deployed in the NWMED in the framework of several European and national projects (see Everyone's Gliding Observatories (EGO), http://www.ego-network.org, EU FP6 MERSEA, ANR LIVINGSTONE, NERC DOCONUG, SOERE MOOSE, HyMeX/MerMeX). 77 deployments were carried out between 2007 and 2012 (fig. 2.4a) corresponding to a total of

36513 profiles.

With the development of the observing system MOOSE in 2010, there is almost always an active glider (fig. 2.4b). Whereas before 2010, glider deployments were not continuous but instead integrated into large experiments (from the end of January to April in 2007 and in 2008, for example).

The gliders represents a real step forward in ocean observing. The large number of measurements made by each unit has enabled the observation of small-scale physical processes that were not necessarily accessible to traditional measurement platforms. Since the use of gliders, the number of oceanographic profiles has exploded. On figure 2.5, one can clearly see the evolution of the oceanographic measurement platforms used in the NWMED, with the apparition of the CTD sensors at the beginning of the 70s, the development of the Argo profiling floats in the beginning of the 2000s, and the democratization of the gliders since 2006.

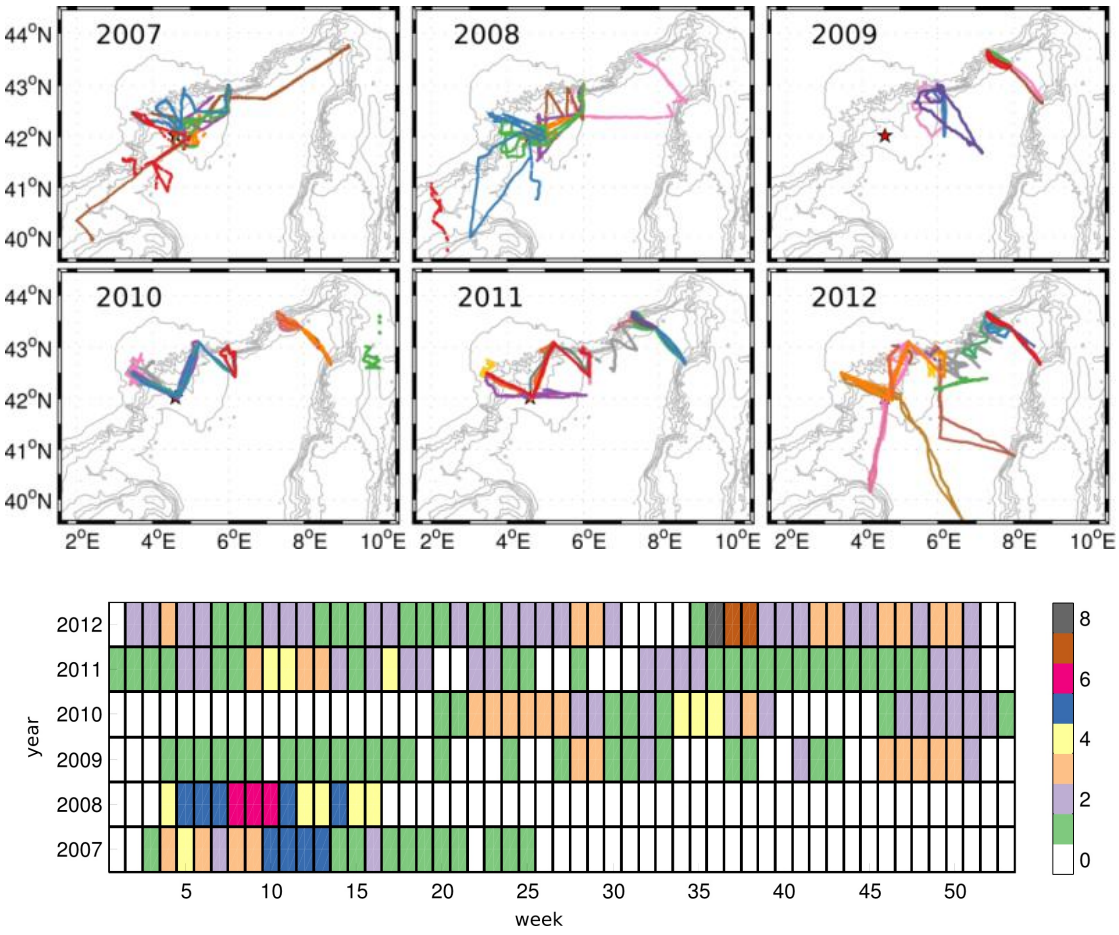

Figure 2.4: *Top panel*: Maps of glider deployments in the NWMED from 2007 to 2012, colors correspond to different deployments. *Bottom panel*: Number of active glider deployments week by week in the NWMED from 2007 to 2012

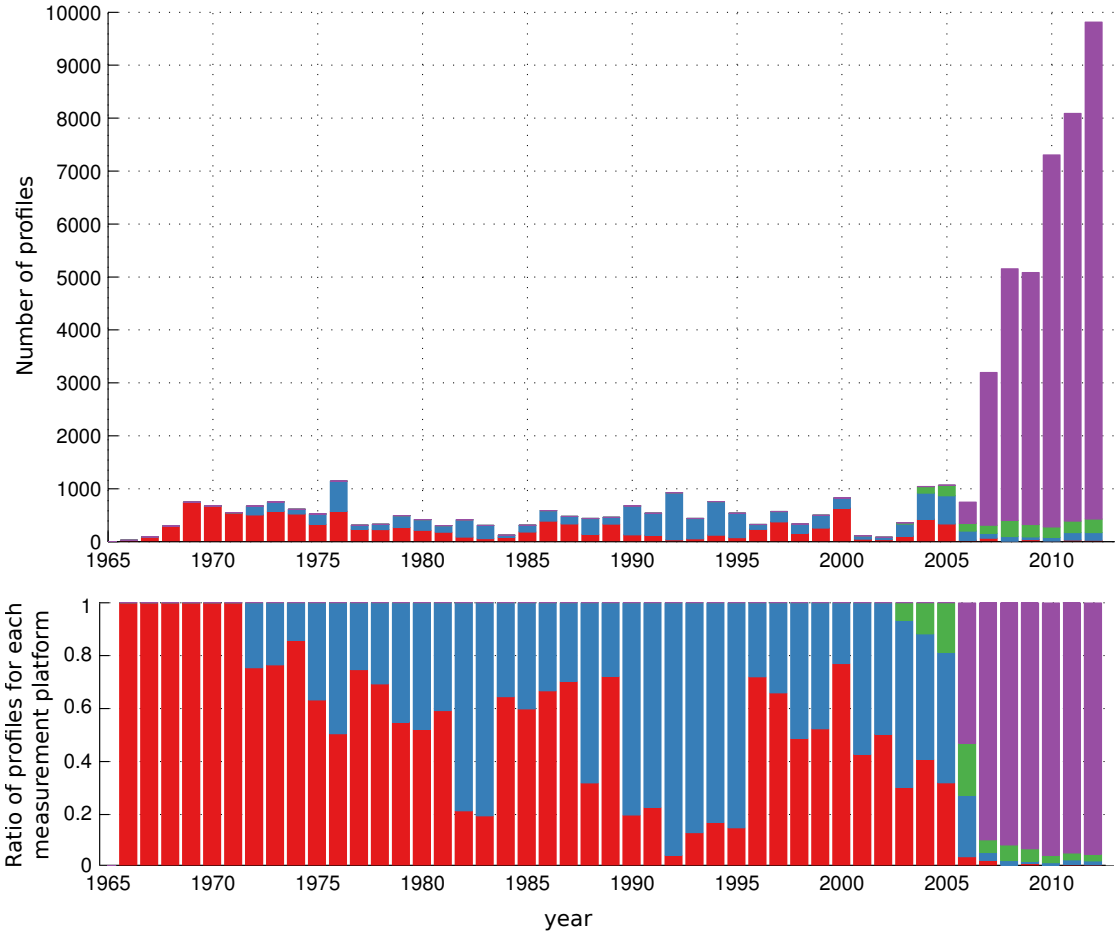

Figure 2.5: Top: Number of profiles by platforms in the NWMED from 1965 to 2012. Bottom: Ratio of profiles for each measurement platforms. Red: BT/XBT, blue: CTD stations, green: Argo, purple: gliders

At the end of 2012, 18.5% of temperature profiles collected since 1965 were carried out using bathythermograph (BT) and expandable bathythermograph (XBT/XCTD), 16.4% using shipboard CTD, 3.1% using Argo profiling floats and 62.0% using gliders. While salinity profiles were collected at 0.1% by XCTD, 19.8% by shipboard CTD, 3.9% by Argo profiling floats and 75.7 % by gliders.

2.4 Database of Mediterranean Data

In order to better quantify the seasonal cycle of surface net heat flux in the Gulf of Lions, we have wanted to produce a Mediterranean climatology of the thermocline and of the upper-ocean heat storage rate over an annual cycle and a grid of 0.5° longitude x 0.5° latitude (see chap. 3). As this climatology could be useful to other areas of the Mediterranean, we have generalized our study to the whole Mediterranean.

The first source of data for this study was the Medar-MEDATLAS project (MEDAR Group [2002]). We also used data from the World Ocean Database (Conkright et al. [2002]), from

additional Italian (D'Ortenzio et al. [2005]) and Spanish cruises (Puig et al. [2012]), from the CORIOLIS data center (see Coriolis, http://www.coriolis.eu.org) and from the MOOSE data base.

2.4.1 Description of additional measurement platforms

In addition to CTD stations (section 2.2) and glider data (section 2.3), this database is also composed by Bathythermograph and expandable Bathythermograph data, and by Argo profiling float data.

Bathythermograph and Expandable Bathythermograph

The (mechanical) Bathythermograph (MBT) was the principal operational naval device from the 1940s up to the mid-1970s. The MBT was lowered into the water from a vessel, and it inscribed a temperature-depth trace, with a sharp stylus on a small coated glass slide. The temperature-sensing element was a xylene-filled copper tube, whose (temperature- dependent) pressure moved the stylus across the slide via a Bourdon tube. Stylus movement along the slide was determined by a copper bellows, compressed by the increasing water pressure. Data were read from the trace using an optical projector and scale.

The XBT was originally intended to improve on the (non-expendable) mechanical bathythermograph. It was a major advance, allowing operation while under way and dispensing with the intricate measurement routine of the MBT, with the need for a deployment/recovery winch and with the need for calibration. It uses a pre-calibrated thermistor measurement, read onboard in real time. Inference of its depth uses knowledge of its rate of fall through the water.

Recently Domingues et al. [2008]; Wijffels et al. [2008]; Levitus et al. [2009]; Ishii and Kimoto [2009]; Gouretski and Reseghetti [2010]; Hamon et al. [2012] have shown that bathythermographs dominate the upper ocean temperature record since the mid-1960s and both mechanical and expendable bathythermographs seem to be positively biased. XBT biases are mainly caused by errors in the fall rate equation and have changed with depth and time along the observational record, with averaged biases ranging between 0.2°C and 0.4°C.

Argo profiling floats

Since 2000, the global network of temperature/salinity floating profilers known as Argo (Array for real-time geostrophic oceanography) has grown considerably, becoming a major component of the ocean observing system with more than 3500 active free-drifting profiling floats. This allows, for the first time, continuous monitoring of the temperature, salinity, and velocity of the upper ocean. The primary motivation of these floats was for operational oceanography in addition to altimetry satellites, but they are also a powerful tool for the study of the ocean and climate, especially thanks to their long lifetime (>3 years).

In the Mediterranean, 113 floats deployments (fig. 2.6) were collected mainly through MedArgo (http://nettuno.ogs.trieste.it/sire/medargo) from 2001 to 2012. Each float descents from the surface to a programmed parking depth of 350 m, where it remains for about 4.5

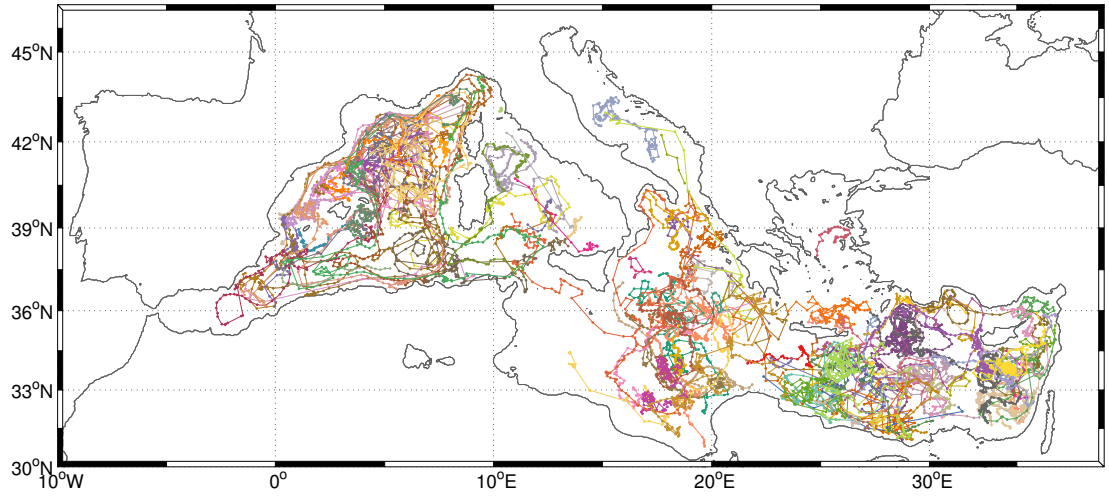

Figure 2.6: Argo profiling floats deployments in the Mediterranean since the 2000s

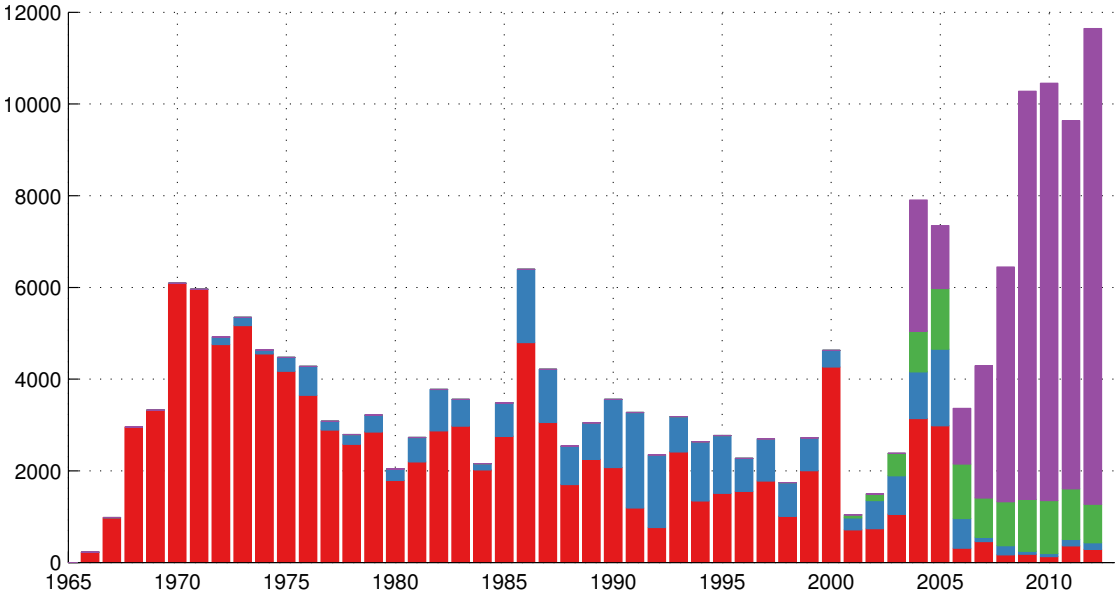

Figure 2.7: Number of profiles collected by platforms in the MED from 1965 to 2012. Red: BT/XBT, blue: CTD stations, green: Argo, purple: gliders

days before reaching the profile depth, that is generally 700 m but extends to 2000 m every ten cycles. At the end of each cycle the float remains for about 5–7 h at the sea surface, where it is localised by, and transmit the data to satellite system.

Floats are equipped with CTD sensors, and can also be a host of other accessories and instruments to monitor oxygen, chlorophyll or turbidity, for example.

2.4.2 Description of the multi-platform database

After removal of duplicates, the merged database is composed by more than 194 000 temperature profiles (fig. 2.7) from 1965 to 2012 (55.1% of BT and XBT, 14.1% of shipboard CTD, 5.2% of Argo profiling floats and 25.6% of gliders). This database is also composed of 87 293 salinity profiles (1.2% of XCTD, 30.7% of CTD, 11.5% of Argo profiling floats data and 56.1% of EGO gliders data).

The data are aggregated in a grid of 0.5° of longitude x 0.5° of latitude and stored in matlab files. One can easily access the data through a matlab function that runs through the database and extract the desired data:

dataDB = DBhisto_loaddata(*pathdb* , *arealimit* , *timeselect* ,*minp* , *instrtyp* , *qcselec* , *qlvl*)

where *pathdb* is the path of the database, *arealimit* is a polygon indicating the selection area, *timeselect* is the min and max value for a timeselection, *minp* is the minimal depth of the desired profiles (for example minp=1200 will return only profiles going deeper than 1200m, *instrtyp* is a string where the user can specify the kind of measurement platforms desired (exemple: 'ALL', 'CTD', 'ARGO', 'XBT', 'GLIDER'), *qcselec* is equal to 1 if quality checked data are needed otherwise it is 0, *qlvl* is used if *qselec* is equal to 1 and corresponds to quality flag level desired. We keep the same quality flags than CORIOLIS (1: good, 2: probably good, 3: probably bad, 4: bad, 0: no QC, 7: error in time or position, 8: no data) and we added also our personal quality flag (10: good raw data, 11: good raw data controlled by the Principal Investigator, 20: probably good data).

Then the user gets back a matlab structure aggregating all the profiles corresponding to its criteria selection. The structure includes different fields like the time, the latitude, the longitude, the 'name' of the profile, the cruise name, the platform type, the ID of the platform, the operator name (who has provided the data), the datasource, the depth level of the profile, the temperature profile, the salinity profile and quality flags on temperature and salinity profiles.

2.5 Complementary datasets

In this PhD thesis, other complementary data were used and are presented in this section.

2.5.1 Shipboard ADCP

An Acoustic Doppler Current Profiler, is deployed to measure how fast water is moving across an entire water column. It uses the Doppler frequency shift of an acoustic ping to infer water velocity. ADCPs can be attached to moorings, lowered on CTD rosette packages, and mounted on ship hulls. During this thesis, I mainly worked on shipboard ADCP (SACDP, also known as Vessel-Mounted ADCP, VMADCP).

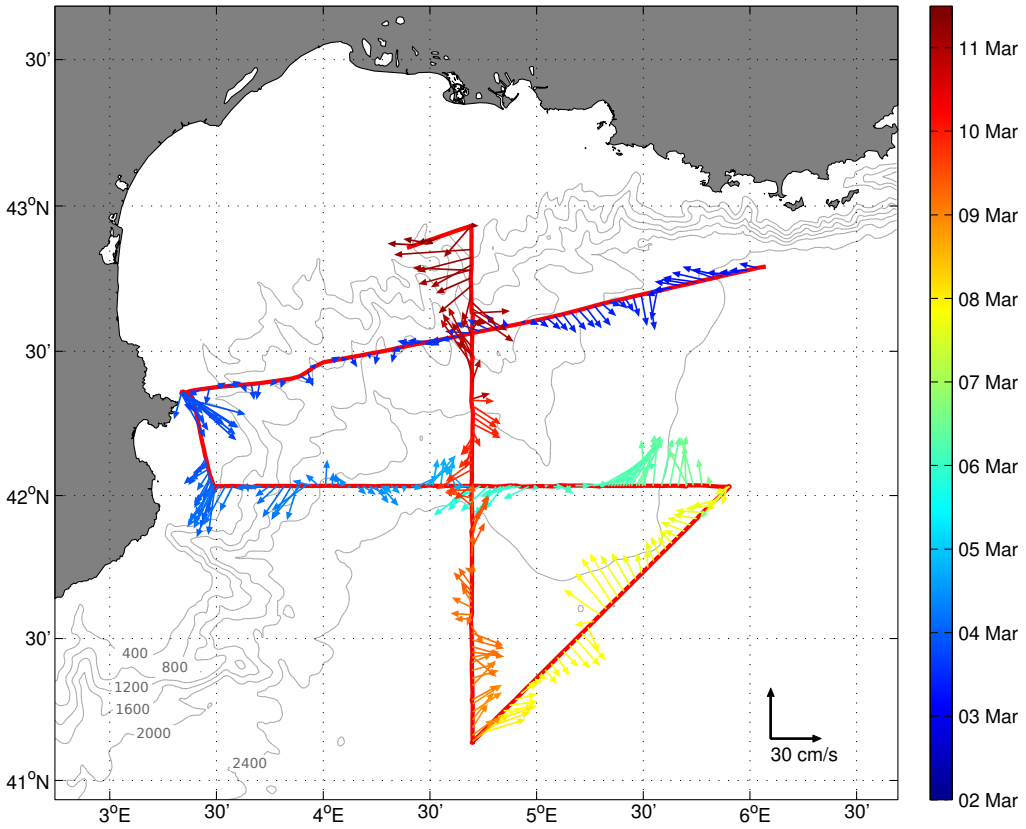

Figure 2.8: Shipboard ADCP data from the first leg of the CASCADE oceanographic cruise, that took place in March 2011 in the Gulf of Lions. Data come from a 38 Khz RDI-Ocean Surveyor, profiling the upper 700 meters of the water column in 16m-wide cells. Arrows indicate the mean horizontal currents of the upper 700 meters of the water column. The red line indicate the ship track.

An overview of shipboard ADCP systems was written for the GO_SHIP (Global Ocean Ship-Based Hydrographic Investigation Program) Repeat Hydrography Manual (http://www.go-ship.org/HydroMan.html) by Firing and Hummon [2010]. SADCP data are stored and accessed using a CODAS (Common Ocean Data Access System) database, developed in the late 1980's as a portable, self-describing format for ADCP data, by the University of Hawaii (Firing et al. [1995]). The CODAS processing is composed of a processing software and procedures that were developed around the CODAS format (http://currents.soest.hawaii.edu/docs/adcp_doc/index.html). Although the processing steps are automated, human judgment is still required for the final product. The high flexibility of CODAS makes it useful for near real-time processing at sea, with processed, corrected and edited data available for onboard scientists.

Four processing steps for ADCP data are performed by the CODAS routines:

1. An ocean reference layer is used to remove the speed of the ship from the measured velocities.

2. A GPS-derived heading source may provide a more accurate heading source than a gyro.

3. Calibration routines are available to estimate the heading misalignment from either "bottom track" or "water track" data. Watertrack calibration routines use sudden accelerations (such as stopping and starting of the ship when doing station-work) to derive an estimate if there is a heading misalignment.

4. Bad data can be edited out prior to use (to screen out interference from other instruments or bubbles).

Once the data are averaged and the above steps are applied, it is still often necessary to further edit the data (for example: remove data when the ship is in harbor or remove velocities below the bottom). This can be automated but for final processing, a person must visually inspect all the dataset.

SADCP data were mainly used during the CASCADE cruise (figs. 2.2 and 2.8) that took place in the Gulf of Lions in March 2011, and are presented in chapter 5. .

2.5.2 Atmospheric reanalyses

During this PhD thesis, atmospheric reanalysis were investigated in order to explain the influence of atmospheric forcing on the ocean dynamic. We used two different products, the ERA-Interim reanalysis and a dynamical downscaling of the ERA-Interim reanalysis performed with the Regional Climate Model (RCM) ALADIN-Climate developed at Météo-France/CNRM.

Era-Interim

The ERA-Interim reanalysis data (http://www.ecmwf.int/research/era/do/get/era-interim) contains consistent atmosphere and surface analyses for the period from 1979 until real time based on the European Centre for Medium-Range Weather Forecasts (ECMWF) numerical weather prediction model. The reanalysis makes use of the ECMWF Integrated Forecast System at T255 spectral resolution (80 km horizontal resolution) with 91 vertical levels. We considered in this work the daily fields of the air-sea fluxes (downward and upward short-wave radiation, downward and upward long-wave radiation, latent heat flux, sensible heat flux, total precipitation and evaporation) in order to compute the daily net heat flux and the net freshwater flux out of the ocean.

Era-Interim data were used in different parts of this thesis (chapters 4 and 5).

RCM ALADIN-Climate

A description of ALADIN-Climate, version 5 (dynamics and physics) can be found in Colin et al. [2010] and Herrmann et al. [2011]. The version 5 is used in the framework of the international CORDEX exercise over various domains (Mediterranean, Africa, North America) and is close to the ARPEGE-Climate version. Different configurations of this model can be used. They are obtained by varying the spatial resolution, the size and position of the domain, and the dataset used for the large scale forcing. The model version has 31 vertical levels. The time step used is 600s. This geographical set- up allows to fully include the Med-CORDEX (http://www.medcordex.eu) official domain in the model central zone.

One of the main advantage of using the dynamical downscalling of ERA-Interim reanalysis with the regional climate model ALADIN, is to obtain a jet-like structure of the most intense latent heat loss, that better reflects orographic control of the wind (Herrmann et al. [2011]). This behavior is mostly seen in the Aegean Sea (the Etesian wind or Meltem), in the North-Western Mediterranean Sea (Mistral, Tramontane), in the Adriatic Sea (Bora area).

From this simulation provided by Samuel Somot (CNRM Toulouse), we extracted the daily fields of the air-sea fluxes (downward and upward short-wave radiation, downward and upward long-wave radiation, latent heat flux and sensible heat flux) in order to compute the monthly mean time series of the neat heat flux for the whole available period (1979 to 2011). We used this dataset in the chapter 3 of this manuscript.

2.5.3 Ocean color images

Ocean color images are a useful tool to get estimates of geophysical quantities at the sea surface, as the chlorophyll *a* concentration. These high-resolution spatial measurements can be studied on regional or global scales for addressing both research and operational requirements related to marine primary production, ecosystem dynamics, fisheries management, ocean dynamics, coastal sedimentation and pollution.

The term 'ocean color' refers to the spectral composition of the visible light field that emanates from the ocean, determined by the interactions of incident light with substances or particles present in the water. The color of the ocean depends on the solar irradiance spectra, atmospheric conditions, solar and viewing geometries, and the absorption and scattering properties of water and the substances that are dissolved and suspended in the water column, for example, phytoplankton and suspended particles.

Clear open-ocean have a 'color' that peak at blue wavelengths because its reflects the color of the sky, but also because water absorbs strongly in the near-infrared and scatters blue light more effectively than at longer wavelengths. As the concentrations of microscopic green plants (phytoplankton) and suspended materials increase, absorption and scattering change and the color shifts from blue to green and brown.

Thanks to the analysis of the satellite images that estimate the 'ocean color' (= the water-leaving radiance spectra), other geophysical quantities can be derived, in our case we will focus on the chlorophyll *a* concentration. In this work we will use the 1-day Level 3 standard mapped images of MODIS Aqua surface chlorophyll at 9 km resolution, obtained from the NASA web site (http://oceancolor.gsfc.nasa.gov/) for the 2007-2012 period.

3 Mixed Layer, Seasonal Thermocline and Upper-Ocean Heat Rate in the Mediterranean Sea

Contents

In this chapter, we mainly investigate the seasonal cycle of the upper ocean heat rate in the Mediterranean Sea. The active turbulence in the upper ocean is responsible for the onset of an oceanic mixed layer, where the temperature, the salinity and the density are almost vertically uniform. It is through this buffer zone, that mass, momentum and energy, are transferred between the atmosphere and the deep ocean. In addition to the important role that the oceanic mixed layer may play in the physical climate, this layer has also a major influence on biological and chemical processes.

The upper ocean is also a place where marine trophic chain begins with the first element of this chain, phytoplankton, finds all the elements required for growth (light and nutrients). Characterizing the oceanic phytoplankton phenology[1] is a necessary step to better understand functioning of oceanic ecosystems and their possible alterations in response to global or local changes. The phytoplankton phenology is driven by biotic[2] (eg: zooplankton controls of phytoplankton accumulation) and abiotic[3] forcings. The mixed layer depth, considered as the main physical abiotic factor in influencing phytoplankton dynamics, governs both nutrient and light availability for phytoplankton growth (Mann and Lazier [2005]).

The database presented in section 2.4 was intended for studies on the upper ocean heat rate in the Mediterranean Sea. However I also had the opportunity to use it through collaborations with biogeochemists and physicists in order to study the influence of the mixed layer on the phenology of phytoplankton. One of the main results of this study is the confirmation of the coexistence in the Mediterranean Sea of two dominant phenological regimes, named "Bloom" and "No Bloom". The "No Bloom" regime is characterized by concomitant MLD and surface chlorophyll peaks, whereas, in the "Bloom" regime, MLD peaks precede surface chlorophyll peaks by about 30 days. Moreover for the "No Bloom" regime, observations indicate that phytoplankton would never be limited by light, whatever the MLD, and would even grow during the winter period thanks to small nutrient inputs. For the "Bloom" regime, the important supplies of nutrients in surface waters by deep mixing and the low uptake rate by phytoplankton (episodically limited by a deficit of light), lead to the hypothesis that the nutrients accumulate in surface waters during winter, which could explain the 30 days time-lag between MLD and surface chlorophyll peaks, characteristic of the "Bloom" regime.

My contribution to this study was done mainly through the MLD database and the discussion related to dynamics of deep water formation regions. This study is available in the appendix B, and is published in Journal of Geophysical Research: Oceans under the reference :

Lavigne H. , F. D Ortenzio, C. Migon, H. Claustre, P. Testor, M. Ribera D Alcalà, R. Lavezza, L. Houpert, L. Prieur (2013): Enhancing the comprehension of mixed layer depth control on the Mediterranean phytoplankton phenology, Journal of Geophysical Research: Oceans, doi: 10.1002/jgrc.20251

[1] The relationship between a periodic biological phenomenon and climatic conditions
[2] Any living component that affects another organism
[3] Non-living chemical and physical factors in the environment, which affect ecosystems

In the following, we present an article in revision in Progress in Oceanography, in which we have constructed the first Mediterranean climatology of the seasonal thermocline based on a comprehensive collection of temperature profiles of the last 44 years (1969-2012), using the database presented in section 2.4. This climatology of the seasonal thermocline together with the climatology of the upper mixed layer depth have led to the calculation of the upper-ocean heat storage rate. In addition to discriminate particular dynamical regions in the Mediterranean, this climatology of the upper ocean heat rate has led to the construction of an independent estimate of the seasonal cycle of the surface Net Heat Flux (NHF) on average over the Mediterranean, based only on oceanic in-situ measurements. Although there is a good agreement between our estimation of NHF from observations with NHF from atmosphere-ocean regional climate models, some differences may be noticed during specific periods. A part of these differences may be explained by the high temporal and spatial variability of the mixed layer and of the seasonal thermocline, responsible for very localized heat transfer in the ocean. The reference of the article in revision is:

Houpert L., P. Testor, X. Durrieu de Madron, S. Somot, F. D Ortenzio, C. Estournel, H. Lavigne (2013): Observations of the Mixed Layer, the Seasonal Thermocline and the upper-ocean Heat Storage Rate to estimate the seasonal cycle of the Net Heat Flux over the Mediterranean Sea, Progress in Oceanography, SI: North Atlantic and Arctic Oceans' State and Variability.

Abstract

We present a Mediterranean climatology (1°x1°x12 months) of the mixed layer and of the seasonal thermocline, based on a comprehensive collection of temperature profiles spanning 44 years (1969-2012). The database includes more than 190,000 profiles, merging CTD, MBT/XBT, profiling floats, and gliders observations. This data set is first used to describe the seasonal cycle of the mixed layer depth and temperature, together with the seasonal thermocline depth and averaged temperature, on the whole Mediterranean on a monthly climatological basis. Our analysis discriminates several regions with coherent behaviors, in particular the deep water formation sites, characterized by significant differences in the winter mixing intensity.

Heat Storage Rate (HSR) is calculated as the time rate of change of the heat content due to variations in the temperature integrated from the surface down to the base of the seasonal thermocline. We propose a new independent estimate of the seasonal cycle of the mean Net surface Heat Flux (NHF), calculated on average over the Mediterranean Sea for the 1969-2012 period, based only on in-situ observations. We use our new climatologies of HSR, combined to existing climatology of the horizontal net heat flux at Gibraltar Strait. NHF is calculated from ocean observations has an annual mean value of -4.7±4.4 $W.m^{-2}$ over the Mediterranean Sea, and presents a clear seasonal signal with minimal and maximal values being about -169.3±4.7$W.m^{-2}$ in December and +125.2±3.9$W.m^{-2}$ in June respectively. Although there is a good agreement between the seasonal cycle of NHF estimated from observations with the NHF from Regional Climate Model ALADIN, some differences may be noticed in summer

and fall/winter, certainly due to an overestimation of the latent heat flux and the short-wave radiation in the model. The spatial and temporal variability of the HSR in the Mediterranean Sea and its link with dynamic structures like oceanic gyres are also discussed.

3.1 Introduction

The Mediterranean Sea is a semi-enclosed basin connected with the Atlantic (the Gibraltar Strait, ˜300m depth) and with the Black Sea (the Dardanelles Strait, ˜100m depth). It is composed of two main basins, the Western and the Eastern Mediterranean (WMED and EMED) separated by the strait of Sicily (˜ 400m depth), and eight sub-basins. The Alboran Sea, the Algerian Basin , the Northwestern Mediterranean (delimited to the South by the Balearic Islands and the Sardinia) and the Tyrrhenian Sea compose the WMED, while the Ionian Sea , the Adriatic Sea , the Aegean Sea and the Levantine Basin compose the EMED (figure 3.1).

In particular the Mediterranean Sea has different deep convection zones (in the West and in the East) and a well-defined overturning circulation (Wüst [1961]; Robinson et al. [2001] with distinct intermediate and deep water masses. The total Mediterranean heat and freshwater surface budgets over a long multi-year period are negative. These deficits of freshwater and heat are compensated by exchanges through the Strait of Gibraltar (positive net water and heat transports), where the inflow is composed by a relatively warm and fresh (15.4°C, 36.2 psu) upper water, and the outflow to the Atlantic is relatively cooler and saltier (13°C, 38.4 psu) (Bryden et al. [1994]; Tsimplis and Bryden [2000]; Soto-Navarro et al. [2010]; Criado-Aldeanueva et al. [2012]).

Recently new estimates of the Net Heat Flux (NHF) due to surface air-sea exchanges were proposed: -3 ± 8 W.m^{-2} using in-situ and satellite-derived datasets (see HB3 in table 5 in

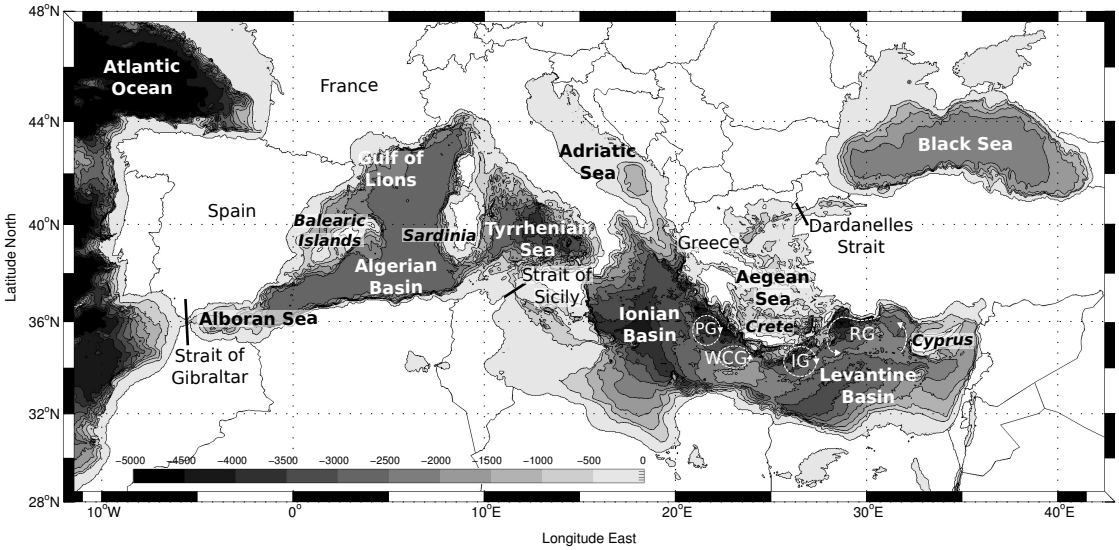

Figure 3.1: Bathymetry of the Med Sea with the main sub-basins. Positions of the Pelops Gyre (PG), the Western Cretan Gyre (WCG), the Ierapetra Gyre (IG) and the Rhodes Gyres (RG) according to Poulain et al. [2012], are also shown.

Sanchez-Gomez et al. [2011]), -7 W.m^{-2} using empirical corrections of the ERA40 atmospheric parameters plus bulk formula (Pettenuzzo et al. [2010]) and a range of [-6.4 ; -1.7] W.m^{-2} using the historical runs of 5 fully-coupled Atmosphere-Ocean Regional Climate Models (AORCMs) in Dubois et al. [2011]. These recent studies show that NHF estimates are in agreement with the Gibraltar transport measurements, between 3 and 10 W.m^{-2} (Bethoux [1979]; Bunker et al. [1982]; Macdonald et al. [1994]. It is worth to note however that atmosphere-only Regional Climate Models (RCMs) evaluated in Sanchez-Gomez et al. [2011] show a wide spread range of values for the Mediterranean NHF (from -40 to +21 W.m^{-2} with an ensemble mean equal to -9 W.m^{-2}) using 12 state-of-the-art 25km RCMs driven by the ERA40 reanalysis showing the key role of atmosphere model physics and air-sea coupling in simulating the Mediterranean NHF. Those studies also highlight the need for better knowledge of the heat fluxes between ocean and atmosphere and the usefulness of independent approaches to estimate the NHF, to improve model accuracy and to better understand air-sea interactions. In the current study, we propose an indirect and independent estimate of the NHF based on ocean heat rate study.

Several past studies analyzed the climatological structure of the salinity and temperature fields of the Mediterranean Sea from observations, based on a variational inverse model (Brankart and Brasseur [1998]), or on inverse methods (Tziperman and Malanotte-Rizzoli [1991]), and even fewer studies estimated the heat content changes in the Mediterranean (Krahmann et al. [2000]; Matsoukas et al. [2005]). In this work we estimate the heat content changes only in the upper layer of the Mediterranean, because the number of observational data is very large compared to deeper layers. We define the upper-ocean layer as a combination of an upper mixed layer, where temperature is almost vertically uniform, and a seasonal thermocline. The depth of the seasonal thermocline is determined as the depth of the temperature minimum on temperature profiles, except in cases of no distinguishable seasonal thermocline (in winter) where we use the mixed layer depth. The temperature minimum associated to the seasonal thermocline can be viewed as the mixed layer temperature during deep winter ventilation of the water column. We choose to calculate heat storage rates down to the seasonal thermocline in order to not miss heat stored below the mixed layer depth.

For the first time, climatologies of the seasonal thermocline depth and averaged temperature, together with climatology of the upper-ocean heat storage rate, are provided for the Mediterranean Sea. In addition, 8 supplementary years of data (corresponding to more than 60 000 profiles, thanks to massive Argo profiling floats and gliders deployments) are available since the computation of the last MLD climatology for the Mediterranean by D'Ortenzio et al. [2005], thus this work provides also an updated version of the seasonal cycle of the mixed layer depth and temperature for the 1969-2012 period. As in D'Ortenzio et al. [2005], we choose to use simple averaging method to stay close to the raw dataset, in order to compare to previous studies and to identify basics statistics. It represents an intermediate step between the raw dataset of individual profiles and a final analysis using advanced statistics methods, like objective analysis or variational analysis (Troupin et al. [2010]).

The paper is organized as follows. First we describe the data sets and the method in section 3.2. Then we present our results in the section 3.3, such as climatologies of the mixed layer depth and temperature, together with climatologies of the seasonal thermocline depth and

averaged temperature, on the whole Mediterranean on a monthly climatological basis. We also propose a new independent estimate of the seasonal cycle of the mean Net surface Heat Flux (NHF), calculated on average over the Mediterranean Sea for the 1969-2012 period, based only on in-situ observations. Finally we discuss the spatial and temporal variability of the HSR in the Mediterranean Sea. Conclusions and perspectives are given in section 3.4.

3.2 Data sets and methods

3.2.1 Profile Database

The first source of data for this study is the *Medar-MEDATLAS*project (MEDAR Group [2002]). We also use data from the World Ocean Database (Conkright et al. [2002]), from additional Italian (D'Ortenzio et al. [2005], http://www.mediterranean-marinedata.eu/moong/home.htm) and Spanish cruises (Puig et al. [2012]), from the CORIOLIS data center (see Coriolis, http://www.coriolis.eu.org) and from deployments of gliders, which are relatively new oceanographic platforms (Testor et al. [2010]) carried out in the framework of several European and national projects (see EGO, http://www.ego-network.org). Gliders profiles are considered as vertical and are checked with the same quality control than Argo data.

After removal of duplicates and application of quality control procedures (elimination of profiles without data above 10m below the surface, with constant temperature values, or with excessive temperature gradients; see details in De Boyer Montégut et al. [2004]), 140 083 profiles from 1969 to 2012 were kept out of the 190 000 initial ones. This database is composed by 45.8% of mechanical bathythermograph (MBT) and expandable bathythermograph (XBT/X-CTD), 25.8% of conductivity-temperature-depth data (CTD from Research vessels cruises), 4.8% of ARGO profiling floats data and 23.6% of EGO gliders data. This database is also composed of 74 934 salinity profiles (0.5% of XCTD, 47.2% of CTD, 8.9% of ARGO profiling floats data and 43.4% of EGO gliders data). This represents more than 50 000 additional salinity profiles compared to the mixed layer climatology made by D'Ortenzio et al. [2005]. This is mainly due to the increasing number of glider deployments (43 since 2006). However the spatial distribution of these salinity profiles (often distributed along repeat-sections) is still not yet sufficient to have a horizontal description of a pycnocline climatology. The 110 000 supplementary temperature profiles, compared to the salinity profiles, is one of the main reason why we chose to work on the thermocline base, rather than on the pycnocline base.

Because XBT and MBT data compose almost 50% of our database and are known to be biased in temperature, we pay a special attention in the correction of these data. The manufacturer's technical sheet specify a depth accuracy of >1% of sample depth and a temperature accuracy of 0.1°C for MBT, and a depth accuracy of 5m (0-250m) or 2% below 250m and a temperature accuracy of 0.2°C for XBT. The MBT are characterized by smaller and less time-variable biases compared to the XBT. Recently Gouretski and Koltermann [2007] discovered the existence of a globally time-dependent and systemic warm bias in XBT profiles, caused by depth error calculation and thermistor error. Since that time, several authors have deduced a time-variable bias, modeling the bias as a depth error only (Wijffels et al. [2008];

Ishii and Kimoto [2009]), a temperature bias Levitus et al. [2009], or a combination (Gouretski and Reseghetti [2010]; Cheng et al. [2011]; Hamon et al. [2012]; Cowley et al. [2013]).

In this work we correct the depth calculation and temperature biases in Bathythermograph data. The mechanical bathythermograph (MBT) data are corrected using the updated correction from Gouretski and Koltermann [2007] (http://www.nodc.noaa.gov/OC5/mbt-bias/gouretski_new.html), while the expendable bathythermograph (XBT) data are corrected using Cowley et al. [2013]. The large database of over 4100 side-by-side deployments of XBTs and CTD data used in Cowley et al. [2013] allowed them to separate out the pure temperature bias from depth error in a way that was not previously possible. The correction steps apply on our XBT data can be summarized by: 1) an identification of the appropriate correction depending of the probe type. If there is no information about XBT types (74500 of the 86000 profiles), the terminal depth is used to determine the probe type for data carried out before 1996. XBT data from 1996 to the present with no depth equation information (2000 profiles) are not included in the climatology calculation, since we do not know which depth equation was used (manufacturer or Hanawa fall rates equation, Hanawa et al. [1995]); 2) Convert to Hanawa fall rates if required; 3) Apply Cowley thermal gradient corrections. A more detailed description of the correction steps can be read on http://www.nodc.noaa.gov/OC5/XBT_BIAS/cowley.html.

3.2.2 Mediterranean Heat Budget Calculation

Following, the formalism of Moisan and Niiler [1998], which derived the heat storage rate equation based on the conservation of mass equation and the conservation of heat equation (without thermal conductivity term). We can express the heat conservation equation integrated from the surface down to a chosen time- and space-dependent depth h= *f(x,y,t)* as follows:

$$h\frac{\partial T_a}{\partial t} = -\, h\mathbf{v}_a\cdot\nabla T_a \,-\, \nabla\cdot\left(\int_{-h}^{0}\hat{\mathbf{v}}\hat{T}\,dz\right) - (T_a - T_{-h})\times\left(\frac{\partial h}{\partial t} + \mathbf{v}_{-h}\cdot\nabla h + w_{-h}\right) + \frac{NHF - q_{-h}}{\rho c_p} \qquad \text{(Eq. 3–1)}$$

Here h is the depth level above which the depth-averaged temperature T_a and the depth-averaged horizontal velocity $\mathbf{v}_a$ are calculated, ∇ is the horizontal gradient operator, $\nabla\cdot$ is the horizontal divergence operator, $\hat{\mathbf{v}}$ is the deviation from the vertically averaged horizontal velocity ($\mathbf{v} = \mathbf{v}_a + \hat{\mathbf{v}}$), $\widehat{T}$ is the deviation from the vertically averaged temperature ($T = T_a + \widehat{T}$), T_{-h} and w_{-h} are the temperature and the vertical speed at the depth level h, NHF is the net heat flux across the ocean surface, q_{-h} is the flux of heat at h, and ρ and c_p are the mean density and specific heat of seawater.

The Heat Storage Rate (HSR, left term in Eq. 3–1 can be expressed in terms of horizontal heat advection, vertical temperature/velocity covariance, entrainment processes at the depth h (deepening or shoaling of the h interface, horizontal advection through the sloping h interface, and vertical velocity at the base of the h interface), net surface heat flux adjusted for the

amount of short wave radiation that penetrate the depth h.

In their study, Moisan and Niiler [1998] defined the integration depth h as the depth of the isotherm whose temperature is one degree less than the annual coldest surface temperature in each region. This cannot be applied in the Mediterranean because most of the time, temperature can be colder in winter, at the surface than at any other depth. We chose an integration depth h corresponding to the bottom of the seasonal thermocline, therefore the flux of heat through the bottom q_{-h} can be considered as negligible and vertical gradients are much weaker.

Monthly values of HSR are calculated using monthly median value of h and T_a for the Mediterranean Sea at a spatial resolution of 1°x1° and a time period spanning 1969 to 2012. The monthly climatology of HSR is used to propose a new independent estimate of the monthly mean NHF over the Mediterranean Sea. Equation Eq. 3–2 represents the mean heat budget of the Mediterranean integrated from the surface to the bottom of the seasonal thermocline:

$$HSR = Q_{medin} + NHF + EHF \qquad \text{(Eq. 3–2)}$$

Here Q_{medin} is the inflow of heat from the Atlantic Ocean to the Mediterranean Sea passing through the Strait of Gibraltar, and EHF is the term corresponding to the heat flux due to entrainment processes at the base of the seasonal thermocline. The advected heat flux through the Black Sea is less than 1 W.m^{-2} each (Garrett et al. [1993]) and is considered negligible. The basin-mean value of HSR can be calculated by summing spatially the monthly gridded climatology. By using the mean heat budget integrated from the seasonal thermocline to the bottom of the Mediterranean (Eq. 3–3), one can express NHF as the sum of an upper-ocean heat storage rate term (HSR), a heat storage rate term for the deep ocean (DHSR) and the net inflow of heat from the Atlantic Ocean to the Mediterranean (Eq. 3–4).

$$DHSR = -Q_{medout} - EHF \qquad \text{(Eq. 3–3)}$$

$$NHF = HSR + DHSR - (Q_{medin} - Q_{medout}) \qquad \text{(Eq. 3–4)}$$

where Q_{medout} is the outflow of heat from the Mediterranean to the Atlantic Ocean.

3.2.3 Determination of the integration depth and the mixed layer depth

In order to calculate HSR down to the base of the thermocline, we need to define first the thermocline in our profiles. We choose the integration depth as the depth where there is a local temperature minimum in the first 200 meters. This temperature minimum can be viewed as the mixed layer temperature during deep winter ventilation of the water column. In winter, the strong surface buoyancy losses increase the mixed layer depth (MLD) and

the seasonal thermocline cannot be distinguishable on temperature profiles (figure 3.2 a). The Atlantic Water (AW) locally cooled during cold wind events becomes denser, and will be overlaid by warmer and less dense AW coming from the surroundings. The cooled AW would be prevented from any interactions with the atmosphere. Such a temperature minimum can be encountered in several other places in the Western Mediterranean and is recognized as the Western Mediterranean Intermediate Water (WIW, previously named as Winter Intermediate Water). The coldest WIW is found in the Northwestern Mediterranean, and it is expected to follow mainly the path of AW (Millot [1999]). The transformation processes of AW into WIW are roughly similar to those occurring in the Eastern Mediterranean Sea, where a saltier AW is transformed into Levantine Intermediate Water (LIW) in the Levantine Basin (Lascaratos et al. [1993]).

A double criterion is chosen to calculate the integration depth h. For each individual profile, we calculate the MLD (using a ΔT=0.1°C criterion and a reference level at 10m depth) and the seasonal thermocline base (corresponding to the depth where a temperature minimum occurred in the upper 200m). If the MLD is deeper than the seasonal thermocline base (determined using a temperature minimum criterion), the integration depth is chosen to be the base of the MLD, and otherwise the integration depth h is chosen to be the depth of the seasonal thermocline.

Unlike D'Ortenzio et al. [2005] who used a ΔT=0.2°C criterion, we choose a ΔT=0.1°C

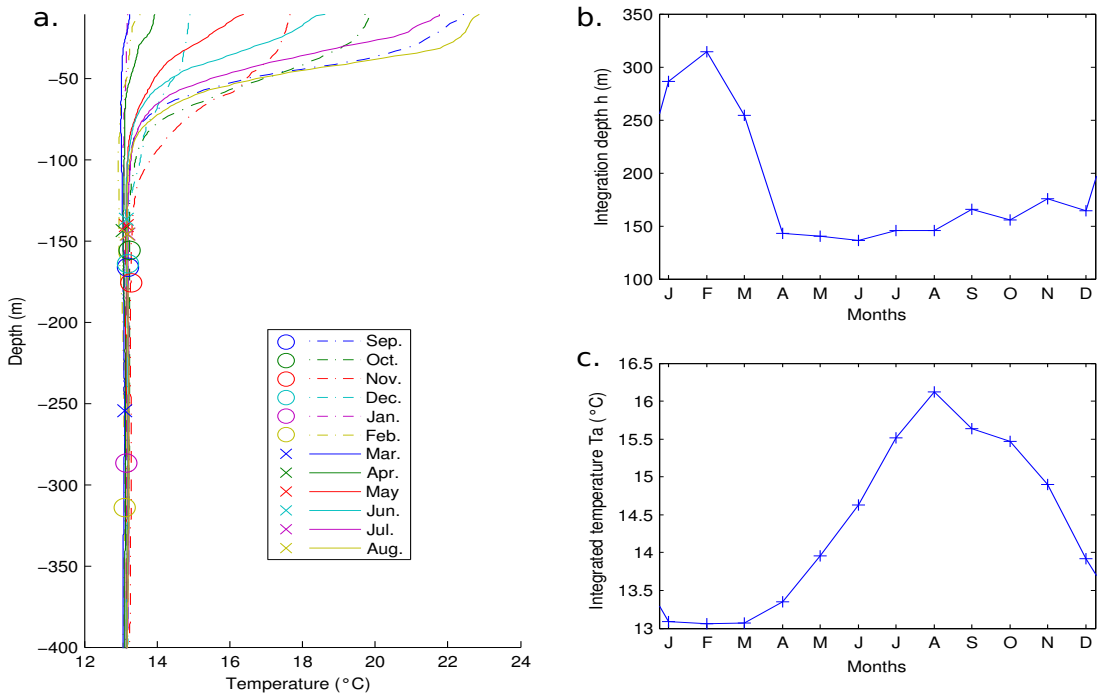

Figure 3.2: (a) The mean monthly temperature profiles from the 41°-42°N, 4.5°-5.5°E bin, the integration depth h is indicated for each month by a circle or a cross. The time series of (b) h and (c) T_a are shown for this bin.

criterion to define the MLD on our profiles, because a finest temperature criterion reduces the difference between a MLD calculated with a temperature criterion and a MLD calculated on temperature-salinity profiles with a density criterion. Maps of the monthly mean differences between MLD calculate with a temperature criterion and MLD calculated with a density criterion are shown on figure 3.3. We use all available temperature-salinity profiles and we calculated for two ΔT criterion (0.2°C and 0.1°), the MLD based on a temperature criterion and a density criterion. The density criterion is determined, following De Boyer Montégut et al. [2004], as a threshold value $\Delta\sigma_T = \sigma_T\ (T_{10} + \Delta T, S_{10}, P_0)$ - $\sigma_T\ (T_{10}, S_{10}, P_0)$, where T_{10}, S_{10} are the temperature and salinity values at the reference depth Z=10m, and P_0 the pressure at the ocean surface to compute the surface potential density.

Results from December to April are shown on figure 3.3 for ΔT=0.2°C (on the left) and for ΔT=0.1°C (on the right). One can see that the differences are smaller for a ΔT=0.1°C criterion than a ΔT=0.2°C criterion, indicating that in the Mediterranean Sea a ΔT=0.1°C should be used preferably to a ΔT=0.2°C criterion if one does not want to overestimated the MLD. However even with a ΔT=0.1°C there are still differences between a temperature based estimations and a density based criteria particularly in the dense water formation areas (in the Gulf of Lions in March or in Rhodes Gyre in January).

In the Mediterranean, mixing occurs along the pathway of surface water, caused by the strong air-sea interactions or by straits constraint. The differences in the MLD estimates may be explained by the decoupling of the temperature and salinity fields due to mixing processes. In the WMED, surface waters are strongly vertically thermally homogeneous, the temperature-based MLD estimations often result in deeper estimations than the density based criteria. The higher differences are found in the Gulf of Lions, in March (figure 3.3). These differences might be explained by the restratification process that occurs at the end of the deep ocean convection, when the surface net heat flux starts to become positive (Houpert et al. [2014]), and saltier waters (LIW) are advected in the open-ocean deep convection area. At that time, these waters might have a temperature relatively close to the one of the upper-layer but they are saltier. This can explain the decoupling between the temperature and the salinity fields, and the important variations between the temperature-based MLD estimation and the density based criterion.

There are also cases of shallower temperature based MLD estimations, particularly in the Gulf of Lions and in the Rhodes Gyres in January. That time corresponds to the period of deepening of the mixed layer, and the difference in the temperature and density based estimations are related to an isothermal layer shallower than the isopycnal one. Vertical compensation occurs between salinity and temperature, creating a compensated layer beneath the well-mixed layer (De Boyer Montégut et al. [2004]). In January in the Gulf of Lions, the surface layer is colder and fresher than the intermediate layer composed by the warmer and saltier LIW, so the isothermal layer is decoupled from the isopycnal layer explaining the overestimation of the MLD with a density criterion (figure 3.3). The same process explains the difference observed in January in the Rhodes Gyre, but in this case the surface layer is warmer and saltier than the intermediate layer (Lascaratos et al. [1993]).

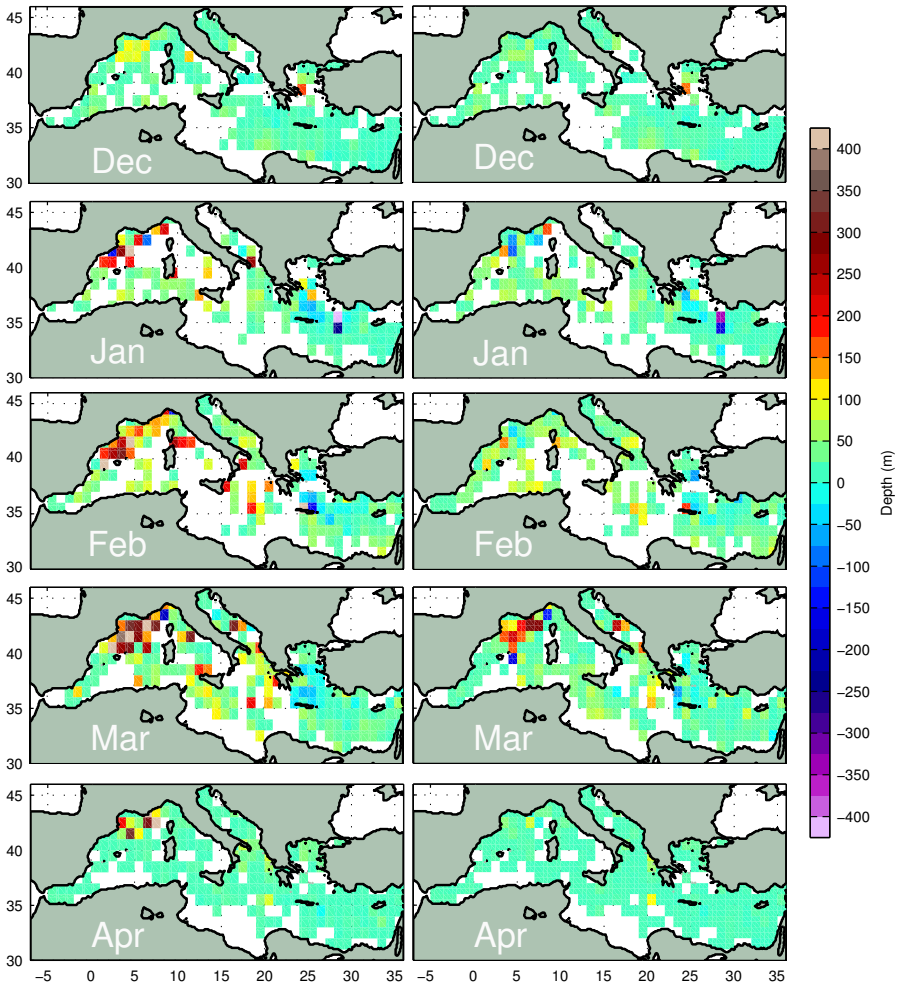

Figure 3.3: On the left (resp. right), monthly maps of the MLD difference between a ΔT=0.2°C (resp. 0.1°C) criterion and a variable $\Delta\sigma_T$ corresponding to a fixed ΔT decrease of 0.2°C (resp. 0.1°C).

3.2.4 Climatologies of h and T_a

h and T_a were calculated from each single profile for the period 1969-2012 and are binned into a 1° latitude by 1° longitude grid. Median are calculated for each box and for each month of each year. In the following we will refer to the median estimates as $h^{b,y,m}$ and $T_a^{b,y,m}$, where b correspond to the box index over the horizontal grid, y indicates the year between 1969 and 2012 and m loop over the month (from 1 to 12).

We smooth out short spatial fluctuations in our estimations of $h^{b,y,m}$ and $T_a^{b,y,m}$, by taking slightly displaced binned data and then taking the average value on the 0.5°x0.5° overlapping grid. So with 4 different 1°x1° grids we reconstruct estimation of $h^{b,y,m}$ and $T_a^{b,y,m}$, and the standard deviation $\sigma(h^{b,y,m})$ and $\sigma(T_a^{b,y,m})$ on a 0.5°x0.5° grid.

Finally, mean seasonal cycles are obtained in all b boxes by calculating the mean $\overline{h^{b,m}}$, $\overline{T_a^{b,m}}$, and the standard deviation $\sigma(h^{b,m})$, $\sigma(T_a^{b,m})$, of $h^{b,y,m}$ and $T_a^{b,y,m}$ over the years. Calculations are done only in boxes that contain at least 3 values for each climatological month m. In

our climatology definition, we chose to give the same weights for all years to avoid effects of oversampling during some specific years and to obtain a climatology less biased by the non-uniform sampling density in time. For example due to massive glider deployments like in 2007 and 2008 in the Northwestern Mediterranean, or due to the fact that glider data, largely deployed only since 2004 in the Mediterranean, may represent 80% of the available profiles in some boxes.

The processing steps are summarized on a flowchart, figure 3.4.

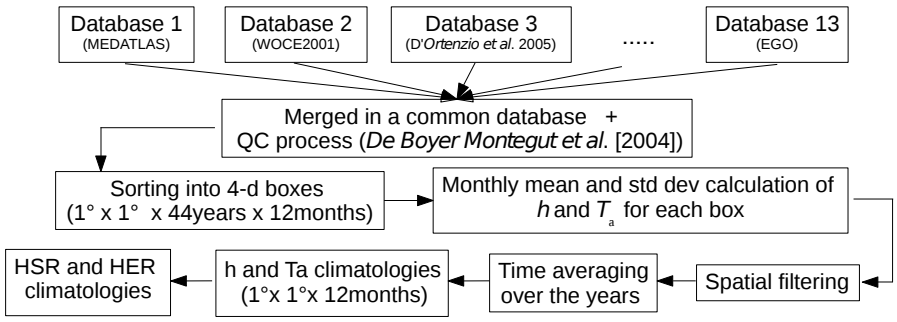

Figure 3.4: Flowchart describing the computational steps for the climatology calculation

Errors in the estimation of the seasonal cycle of the mixed layer depth and temperature may be due to different sources. First, the spatial averaging in the griding procedure, for each month of each year, can introduce a significant amount of error, particularly when observations are sparse. To reduce theses errors, for each month of each year, individual values of temperature are compared to the mean and standard deviation calculated from all temperature profiles made in the same box for the same month (defined by a monthly mean value of temperature $\overline{T_a^{0\ b,m}}$ and a standard deviation $\left(T_a^{0\ b,m}\right)$). Individual values are rejected in the calculation of $T_a^{b,y,m}$ if their deviation from $\overline{T_a^{0\ b,m}}$ is 3 times superior to $\sigma(T_a^{0\ b,m})$.

Another source of error is the effect of potential instrumental bias, but assuming this error is random for each year due to changes in the instruments and in the platform tracks (which ensure on average a relatively homogeneous spatio-temporal coverage), it should be restricted to individual monthly data set and should not affect the seasonal climatology. In addition, since the 70s (date chosen for the beginning of our climatologies), the temperature sensors do not show strong bias (maximum value of 0.1-0.2 °C), compared with conductivity sensors that are more prone to drift over time.

MBT and XBT represent 45% of the database and their corrections do not affect the basin-mean seasonal cycle of h, T_a and HSR, since they are two order lower than the amplitude of their seasonal variations. The basin-mean differences between climatologies with XBT/MBT corrections and climatologies calculated without corrections are comprised between: 1) 0.1m and 2.3m for h, and 2) -0.04°C and -0.02°C for T_a and 3) -2.1 W.m^{-2} and 2.0 W.m^{-2} for HSR.

3.2.5 Climatology of HSR

The calculation of HSR is done only in boxes that contain a full 12-month time series of the $\overline{h^{b,m}}$ and $\overline{T_a^{b,m}}$ with at least 3 values for each month. The heat storage rate $\overline{HSR^{b,m}}$ is calculated using centered derivative for each month m and each grid point b:

$$\overline{HSR^{b,m}} = \rho c_p \frac{\overline{T_a^{b,m+1}} - \overline{T_a^{b,m-1}}}{\Delta t} \overline{h^{b,m}} \qquad \text{(Eq. 3–5)}$$

$\overline{T_a^{b,m}}$ is the temperature averaged from the surface to the depth h for each month m and each box b, Δt is the number of seconds between the center of the month $m+1$ and the center of the month $m-1$. For m equal to the first month (resp. the last month) of the year, $m-1$ (resp. $m+1$) corresponds to the last month (resp. the first month) of the year.

To estimate the uncertainties on HSR, we compute a Monte Carlo test (Krahmann et al. [2000]) at each grid point b and for each month m. A Kolmogorov-Smirnov test (Gille [2004]) is performed for each box b and for each month m to compare the inter-annual values of the monthly averaged $T_a^{b,m,y}$(resp. $h^{b,m,y}$) to a normal distribution with mean $\overline{T_a^{b,m}}$(respectively $\overline{h^{b,m}}$) and standard deviation $\sigma(T_a^{b,m})$ (respectively $\sigma(h^{b,m})$). The null hypothesis is that $T_a^{b,m,y}$ (resp. $h^{b,m,y}$) came from a normal distribution. We obtain as results that in the two cases, we can not reject this hypothesis at a 5% significant level. This test justifies why we choose random numbers from normal distributions in the Monte Carlo tests.

Ten thousand estimations $HSR_i^{b,m}$ are calculated, wherein each estimation X_i (respectively Y_i and Z_i) come from random number chosen from normal distribution with mean $\overline{T_a^{b,m+1}}$ (respectively $\overline{T_a^{b,m-1}}$ and $\overline{h^{b,m}}$) and standard deviation $\sigma(T_a^{b,m+1})$ (respectively $\sigma(T_a^{b,m-1})$ and $\sigma(h^{b,m})$). The mean heat storage rate $< HSR^{b,m} >$ for these 10 000 realizations is calculated by the formula:

$$< HSR^{b,m} > = \frac{1}{N} \sum_{i=1}^{N} HSR_i^{b,m} = \frac{1}{N} \sum_{i=1}^{N} \rho c_p \frac{X_i - Y_i}{2\Delta t} Z_i \qquad \text{(Eq. 3–6)}$$

where N is the number of realizations. The standard deviation is calculated as:

$$\sigma(HSR^{b,m}) = \sqrt{\frac{1}{N-1} \sum_{i=1}^{N} \left(HSR_i^{b,m} - < HSR^{b,m} > \right)^2} \qquad \text{(Eq. 3–7)}$$

This Monte Carlo approach, compared to a classical calculation of error propagation, specifies our estimation of the standard deviation of HSR, $\sigma(HSR^{b,m})$. On average, the results from the Monte Carlo test reduce the standard deviation on $HSR^{b,m}$ by 100W.m^{-2} compared to the error propagation method. In some places, like in the Ierapetra Gyre (South East of Crete), the standard deviation on $HSR_i^{b,m}$ is reduced by 500W.m^{-2} using the Monte Carlo method.

This may be explained by the important standard deviation value for T_a that increases the value of the standard deviation obtained by the error propagation method, particularly in the temperature derivative calculation.

Even if the estimates of $< HSR^{b,m} >$ are close to the estimates of $\overline{HSR^{b,m}}$ (the basin-average difference is less than 0.1W.m^{-2}), there are some discrepancies, up to 10W.m^{-2} in January in the Gulf of Lions. They may be explained by the non-linearity of the HSR term. This area is a well-known place where deep ocean convection and dense shelf water cascading occurs (CIESM [2009]; Durrieu de Madron et al. [2013]). So, the high inter-annual variability associated with these DWF process is reflected in the high standard deviation of h, which is superior to 200m from December to March. A maximum value of 670m for the standard deviation is found in January in the Gulf of Lions with 13 years of data available in January (figure 3.5). Boxes with differences between $< HSR^{b,m} >$ and $\overline{HSR^{b,m}}$ also correspond to boxes were the standard deviation of $HSR^{b,m}$ was significantly reduced when using the Monte Carlo method. In the following, HSR will be used to refer to $< HSR^{b,m} >$.

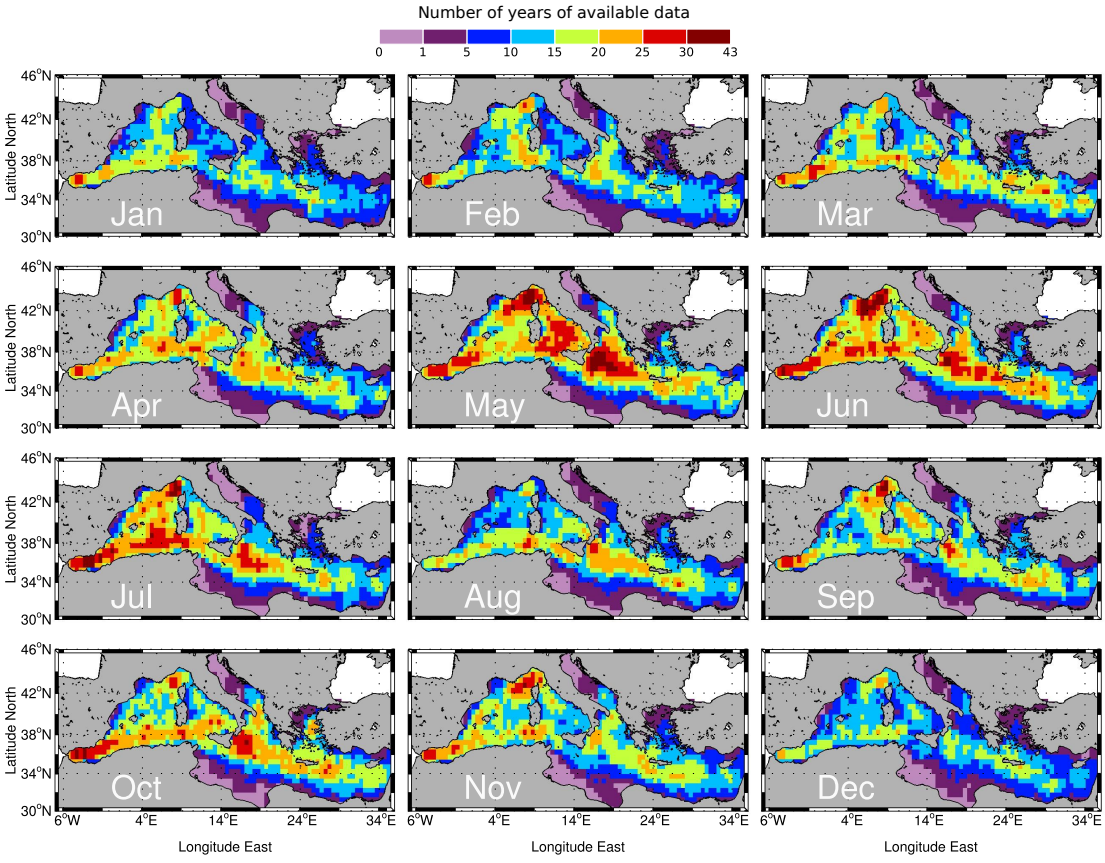

Figure 3.5: Number of years in which measurements were available for the climatology

3.2.6 Complementary data sets

3.2.6.1 Atmospheric net heat flux

In order to complete the Mediterranean heat budget, we also need a gridded estimate of the surface NHF. For the purpose of the current study, we need a long-term, temporally homogeneous, unbiased and high-resolution data set. Operational weather forecast models are not homogeneous over a long period of time, reanalysis have also shown their limitations for the representation of the Mediterranean heat budget and wind field (lack of resolution, Herrmann et al. [2008, 2011], strong biases, e.g. Sanchez-Gomez et al. [2011]; Dubois et al. [2010]). Even if RCMs have also shown some limits (Sanchez-Gomez et al. [2011]), we prefer here to rely on a recent homogeneous, long-term (1979-2011), very- high resolution (12-km) dynamical downscaling of the ERA-Interim reanalysis performed with the RCM ALADIN-Climate developed at Météo-France/CNRM and specifically adapted to the study of the Mediterranean climate and sea (Herrmann et al. [2011]).

A description of ALADIN-Climate, version 5 (dynamics and physics) can be found in Colin et al. [2010] and Herrmann et al. [2011]. The version 5 is used in the framework of the international CORDEX exercise over various domains (Mediterranean, Africa, North America) and is close to the ARPEGE-Climate version used in the CMIP5 exercise. Different configurations of this model can be used. They are obtained by varying the spatial resolution, the size and position of the domain, and the dataset used for the large scale forcing. More complex and unusual options are also available as the use of spectral nudging and interactive air-sea coupling techniques (see Herrmann et al. [2011]). Those options are not used in the current study. We use here a configuration with a Lambert conformal projection for pan-Mediterranean domain at horizontal resolutions of 12 km centered at 14°E, 43°N with 432 grid points in x and 288 grid points in y including the bi-periodization (11) and the relaxation zone (2 x 8). The model version has 31 vertical levels. The time step used is 600s. This geographical set- up allows to fully include the Med-CORDEX official domain in the model central zone.

A description of ALADIN-Climate, version 5 (dynamics and physics) can be found in Colin et al. [2010] and Herrmann et al. [2011]. The version 5 is used in the framework of the international CORDEX exercise over various domains (Mediterranean, Africa, North America) and is close to the ARPEGE-Climate version used in the CMIP5 exercise. We use here a configuration with a Lambert conformal projection for pan-Mediterranean domain at horizontal resolutions of 12 km centered at 14°E, 43°N with 432 grid points in x and 288 grid points in y including the bi-periodization (11) and the relaxation zone (2 x 8). The model version has 31 vertical levels. The time step used is 600s. This geographical set-up allows to fully include the Med-CORDEX official domain in the model central zone.

After a 2-year spin-up, ALADIN-Climate is driven by the ERA-Interim reanalysis (80-km at its full resolution) at its lateral boundary conditions. If we rely on the ALADIN model physics, this downscaling exercise may give the best model assessment of the Mediterranean regional climate and is sometimes called “poor-man” regional reanalysis. Indeed, the large-scale pattern are driven by our best knowledge of the 4D dynamics of the atmosphere (a global

reanalysis) and the associated small-scale are free to develop inside the 12-km RCM. To our knowledge, this 12-km dynamical downscaling of ERA-Interim is the higher-resolution simulations ever produced to study the past Mediterranean climate variability over a multi-decadal period (data are available through the Med-CORDEX database, http://www.medcordex.eu). With respect to the ERA40-driven 25km-resolution RCMs (1958-2001) evaluated in (Sanchez-Gomez et al. [2011]), the ERA-Interim-driven 12km-resolution ALADIN simulation (1979-2011) is as good as the 2 best models among 12 in terms of NHF (UCLM: -5 W.m^{-2}, KNMI: - 10 W.m^{-2}). We are however aware that the choice of the driving reanalysis (ERA- Interim) and the choice of the RCM (ALADIN-Climate) may introduce uncertainty in the results.

From this simulation, we extracted the daily fields of the air-sea fluxes (downward and upward short-wave radiation, downward and upward long-wave radiation, latent heat flux and sensible heat flux) in order to compute the monthly mean time series of the neat heat flux (NHF) for each mesh, for each month of each year for the whole available period (1979 to 2011). Then the mean and the variance were calculated on the 33 year long time series for each climatological month and for each mesh.

3.2.6.2 Gibraltar heat fluxes estimates

To close the heat budget on the Mediterranean, we have to take into account the heat flux through the Gibraltar Strait. Recent studies estimated seasonal cycle of the inflow and the outflow in the Gibraltar Strait from in situ measurements. Using the climatological monthly averaged value (from 2004 to 2009)

To estimate the basin-mean seasonal cycle of the surface Net Heat Flux from in-situ observations over the Mediterranean, we take into account the heat flux through the Gibraltar Strait. Recent studies estimated seasonal cycle of the inflow and the outflow in the Gibraltar Strait from *in situ* measurements. Using the climatological monthly averaged value (from 2004 to 2009) of the inflow (Soto-Navarro et al. [2010]) and outflow (Sánchez-Román et al. [2009]) and their associated temperature Criado-Aldeanueva et al. [2012]), the heat flux from the Atlantic Ocean to the Mediterranean can be estimated. These data sets are used in the section 3.3.3, where we will show our results averaged over the Mediterranean.

3.3 Results and Discussion

3.3.1 Seasonal cycle of the mixed layer, the integration depth h and the depth-averaged temperature T_a

3.3.1.1 Mixed layer depth and integration depth

After the processing stages described in the section 3.2.4, we get the seasonal climatologies of h and T_a. The depth of the seasonal thermocline (figure 3.6) shows mainly two seasons: the vertically mixed season (no seasonal thermocline) and the presence of a T minimum in the May to November seasons to be associated to the Atlantic Water layer deepening during

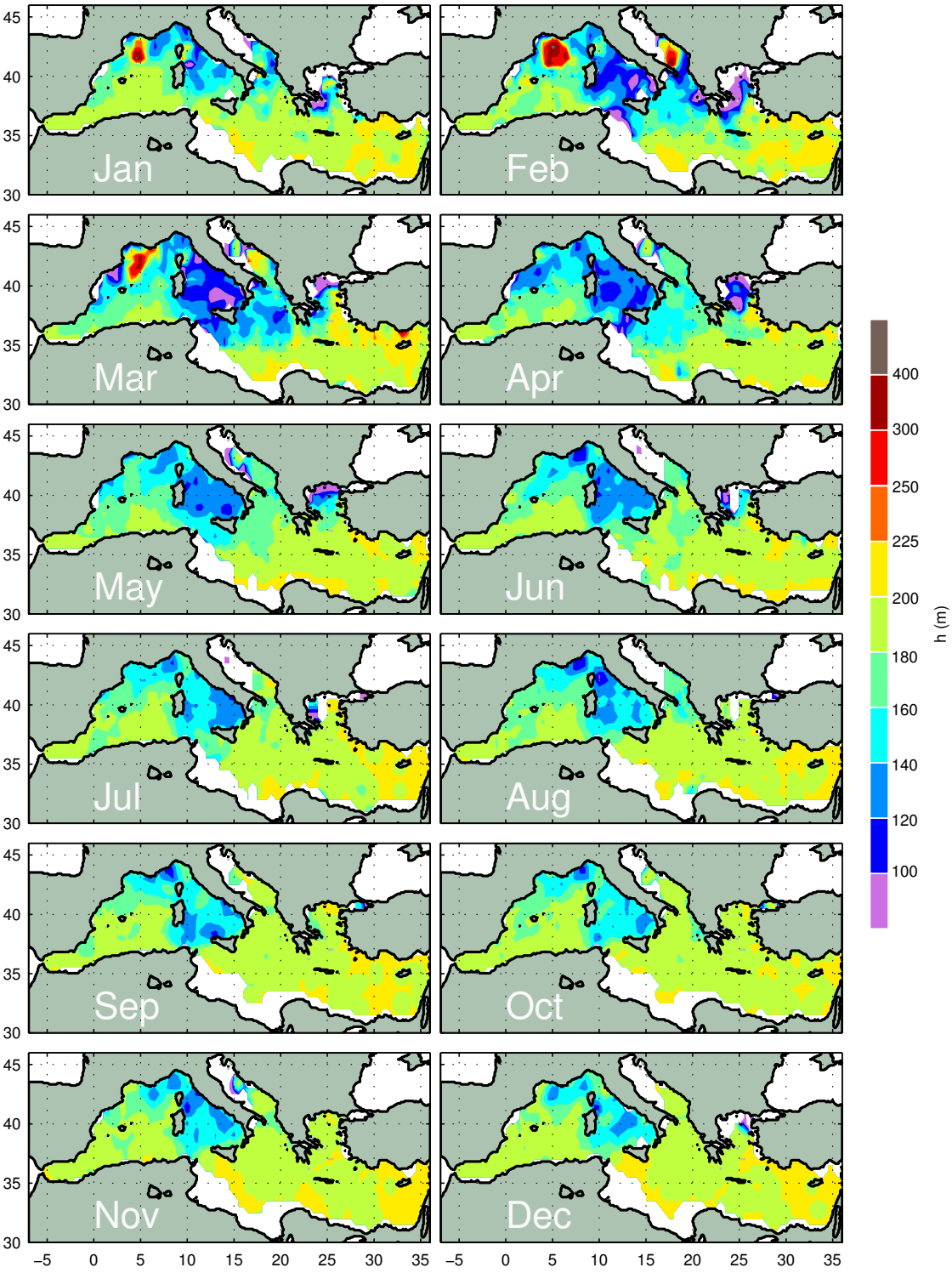

Figure 3.6: Mediterranean climatology of the upper-ocean layer h, determined by the depth of the seasonal thermocline, except in cases of no distinguishable seasonal thermocline (in winter) where the mixed layer depth was used.

the winter ventilation of the water column. From January to March, h shows higher values due to the winter deepening of the mixed layer (figure 3.7), like in the previous median-MLD climatology of D'Ortenzio et al. [2005]. Maxima are found in wintertime in known places of DWF regions (Lascaratos et al. [1999]) like the Gulf of Lions (≈ 42°N 5°E, MEDOC Group [1970]), the Southern Adriatic Sea (≈ 42°N 18°E, Pollak [1951]), the Rhodes Gyre (≈ 36°N 29°E, Ovchinnikov [1984]) and the Aegean Sea (≈ 37°N 25°E, Pollak [1951]). In February, maximal monthly mean values of 425m depth and 300m depth are found respectively in the Gulf of Lions and in the Southern Adriatic Sea. There are others regions that present a local maximum of mixed layer depth (figure 3.7) and these regions are associated to anticyclonic circulation: the Southwest of Greece (≈ 36°N 22°E in February/March, Malanotte-Rizzoli et al. [1997]) and the region in the South of Cyprus (≈ 34°N 33°E from January to March, Zodiatis et al. [2005]). Although the region south-east from Crete (≈ 34°N 27°E) does not show a clear maximum in the monthly MLD climatology (figure 3.7), it is associated with higher standard deviation values (figure 3.8) certainly related to the presence of the anticyclonic Ierapetra Gyre (Menna et al. [2012]). The presence of anticyclonic or cyclonic gyres is more evident on the climatology of the depth-averaged temperature, discussed later in this section. One can also distinguish a local MLD maximum in the North Ionian Sea, in a place where the upper-ocean circulation shows a decadal variability, known as the Bimodal Oscillating System (BiOS, Gačić et al. [2010]).

Our monthly MLD climatology presents similarities with the one made by D'Ortenzio et al. [2005], we find the same kind of seasonal variations for the whole basin and we also find zones of deep winter ventilation. The difference of the MLT (Mixed Layer Temperature) between the 2 climatologies is on average less than 0.1°C, but in some very specific locations (coastal areas), the difference reach 0.8°C. Concerning the MLD, the main differences are found in winter (≈ 20m), except in the Gulf of Lions where the difference between the two MLD climatologies can be up to 250m, particularly the maximum deepening of the mixed layer is not reached the same month (in February in our climatology). There are several sources of explanation for these differences:

1. the ΔT=0.1°C criterion used in this work compared to the ΔT=0.2°C of D'Ortenzio et al. [2005], that gives us shallower estimations of the MLD, particularly in March, which is more in agreement with an isopycnal definition of the MLD,

2. the grid and the estimator chosen for the climatology calculation (in this work we chose to maximizing the number of profiles in each box by making monthly-average over the year in 1°x1° boxes, while D'Ortenzio et al. [2005] preferred to use median values on 0.5°x0.5°boxes),

3. the 8 additional years of measurements (from 2004 to 2012) used in our climatology, since 2004 the number of measurements increased in the whole Mediterranean, especially thanks to the numerous Argo and glider deployments made in addition to the "classical" XBT/CTD monitoring. Another difference from previous climatologies is the event of DWF in 2005-2006, which changed the stratification of the water column, and thus the mixed layer structure of the Gulf of Lions in the years to follow (Smith et al. [2008]; Schroeder et al. [2008]; Herrmann et al. [2010]).

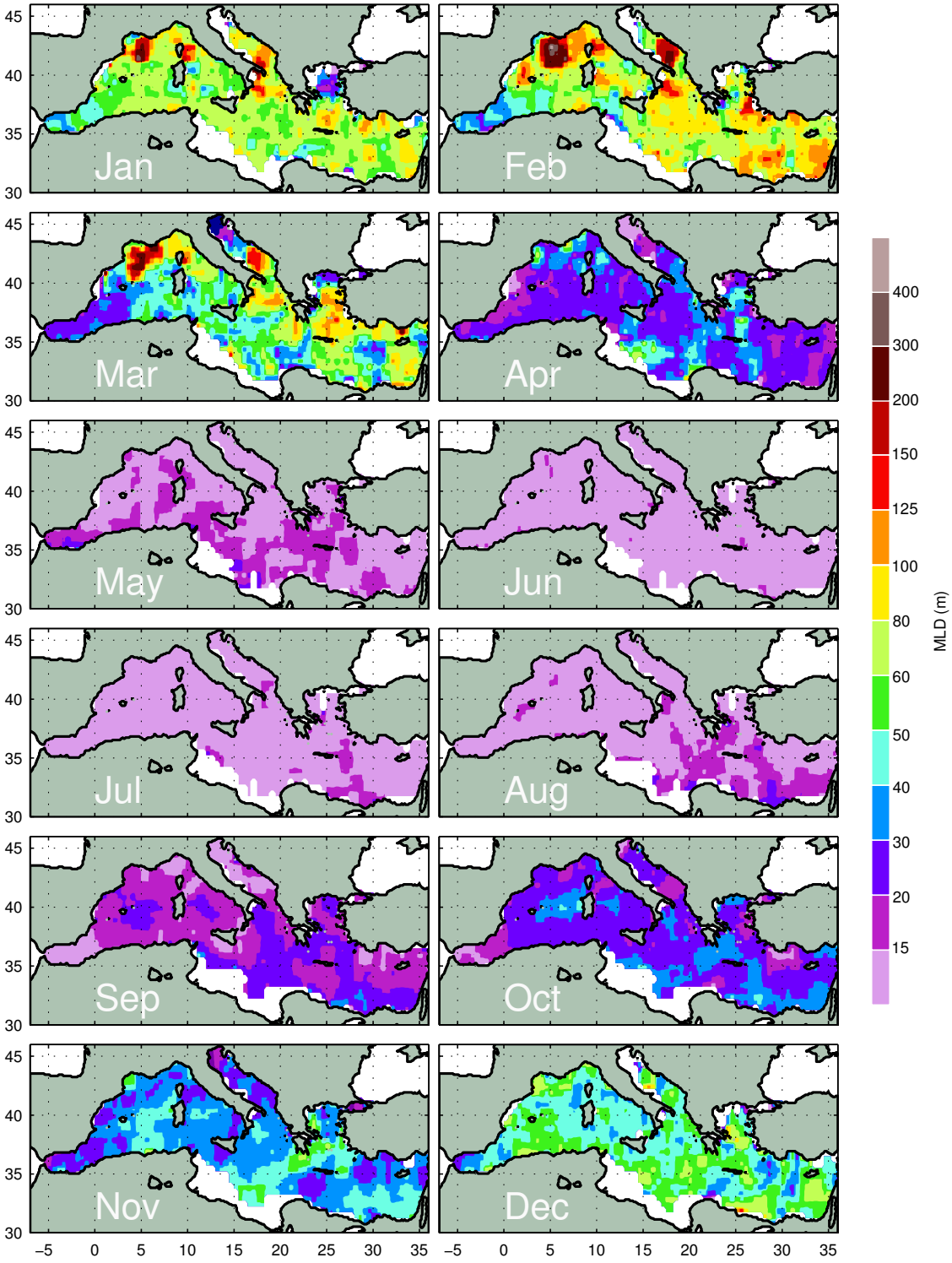

Figure 3.7: Mediterranean climatology of the MLD, based on a temperature difference criterion of ΔT=0.1°C applied to individual profiles.

Standard deviations values of the mixed layer depth are generally below 30m for most of the basin from September to December (figure 3.8). In winter and in April, the standard deviation values increase strongly throughout the whole basin, reaching the maximum values in the Gulf of Lions area (550m). The irregular intensity and occurrence of the DWF processes (Mertens and Schott [1998]) are mainly responsible for these important standard deviation values. As an example, in the Gulf of Lions, deep convection can reach the bottom some years like in 2009, 2010, 2011 and 2012, while other years the winter mixing do no reach greater depths than 200m like in 2007 or 1000m like in 2008. Moreover, recent measurements show that from one year to another the deepening of the mixed layer did not start exactly at the same time and the time lag, for the mixed layer to pass the Levantine Intermediate Water (LIW) located at 200-400m depth, can be up to 1 month and a half (Houpert et al. [2014]).

The standard deviation of h ($\sigma(h^{b,m})$) can be seen on figure 3.9. $\sigma(h^{b,m})$ is inferior to 10 m from May to December in the east of the EMED, comprised between 10 and 50m in the east Alboran Sea, Algerian Basin and Ionian Sea, and higher values comprised between 30 and 50m are found in the Tyrrhenian Sea and in the Northwestern Med. From January to April, the standard deviation is important in the regions of DWF and, as for the MLD, is due to the irregular intensity and occurrence of the DWF processes. For most of the Mediterranean, areas of high standard deviation values are the results of variable h intra box estimations due to the mesoscale activity associated with fronts, or DWF processes.

3.3.1.2 Mixed layer temperature and the upper-ocean depth averaged temperature

The depth averaged temperature T_a is presented on figure 3.10. On average over the whole Mediterranean, the depth averaged temperature in the upper-ocean is going from 14.6°C to 16.8°C in September). One can clearly notice the contrast between the Western and the Eastern Mediterranean, with a colder basin-mean depth averaged temperature in the WMED (from 13.7°C in March to 15.9°C in September) than in the EMED (from 15.3°C in March to 17.5°C in September). Another striking fact is the strong temperature anomalies along the Cretan Arc (at the junction of the Aegean Sea with the Ionian and Levantine basins, figure 3.1), from July to January, corresponding to known anticyclonic (warm anomaly) and cyclonic (cold anomaly) gyres (from West to East: the anticyclonic Pelops Gyre (PG), the cyclonic West Cretan Gyre (WCG), the anticyclonic Ierapetra Gyre (IG), the cyclonic Rhodes Gyre (RG)). The seasonal cycle of T_a in the center of RG is comprised between 15.2°C in March to 16.2°C in September, while in the WCG the same seasonal extrema are reached one month later respectively in April and October. The seasonal cycle of the upper-ocean temperature in the anticyclonic IG is more pronounced, with a minimal value of 15.8°C reached in March and a maximal value of 18.8 reached in October.

The standard deviation of T_a is comprised between 0.46°C and 0.75°C on average on the whole Mediterranean. Maximum values (up to 2°C) can be found in the east of the IG in October (figure A.1). These higher standard deviations may be explained by the inter-annual variability of the position and the dimension of the gyres, already pointed out by Marullo et al. [1999].

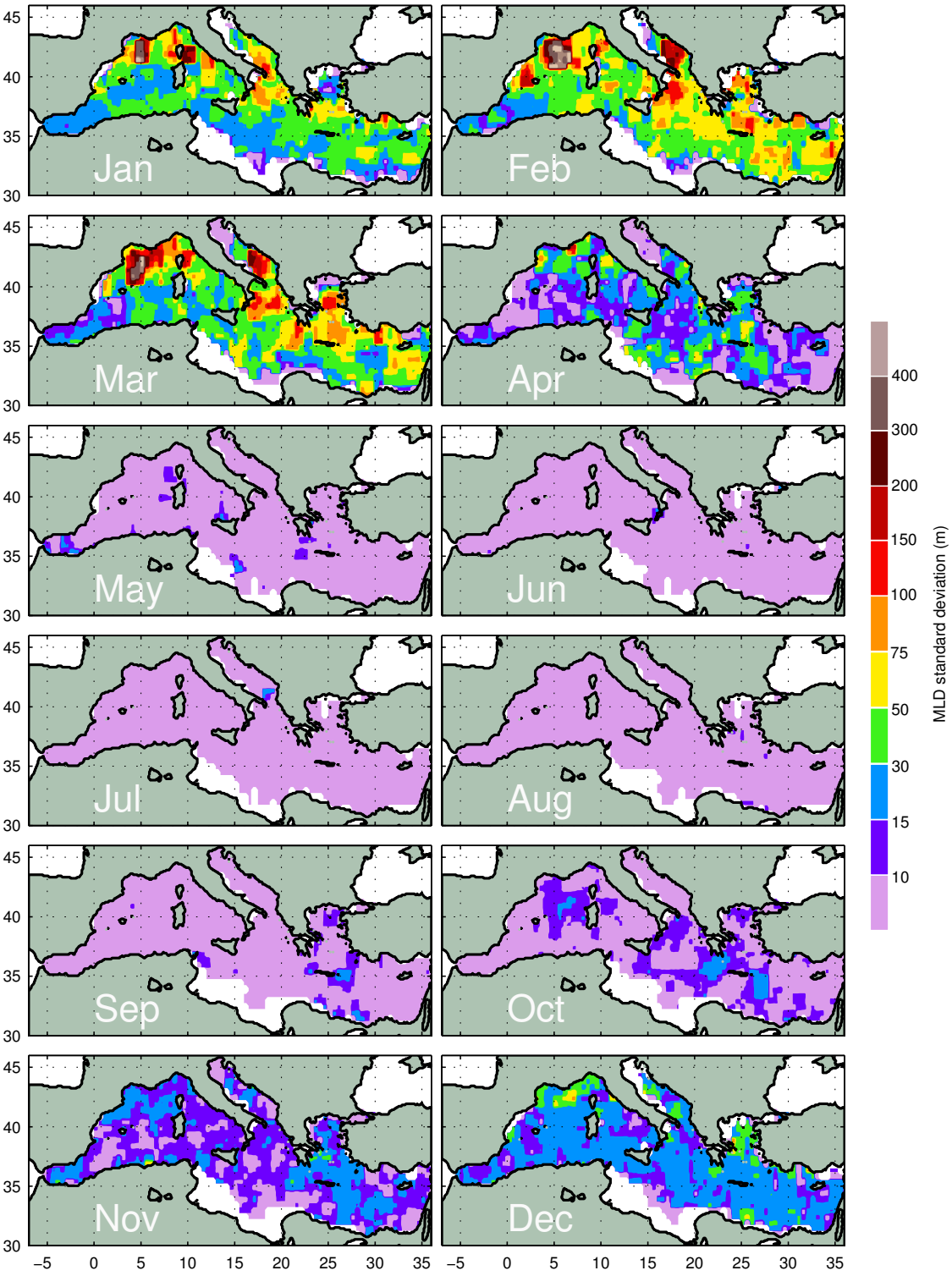

Figure 3.8: Maps of the standard deviation associated to the mesh box averages of the MLD shown on figure 3.7.

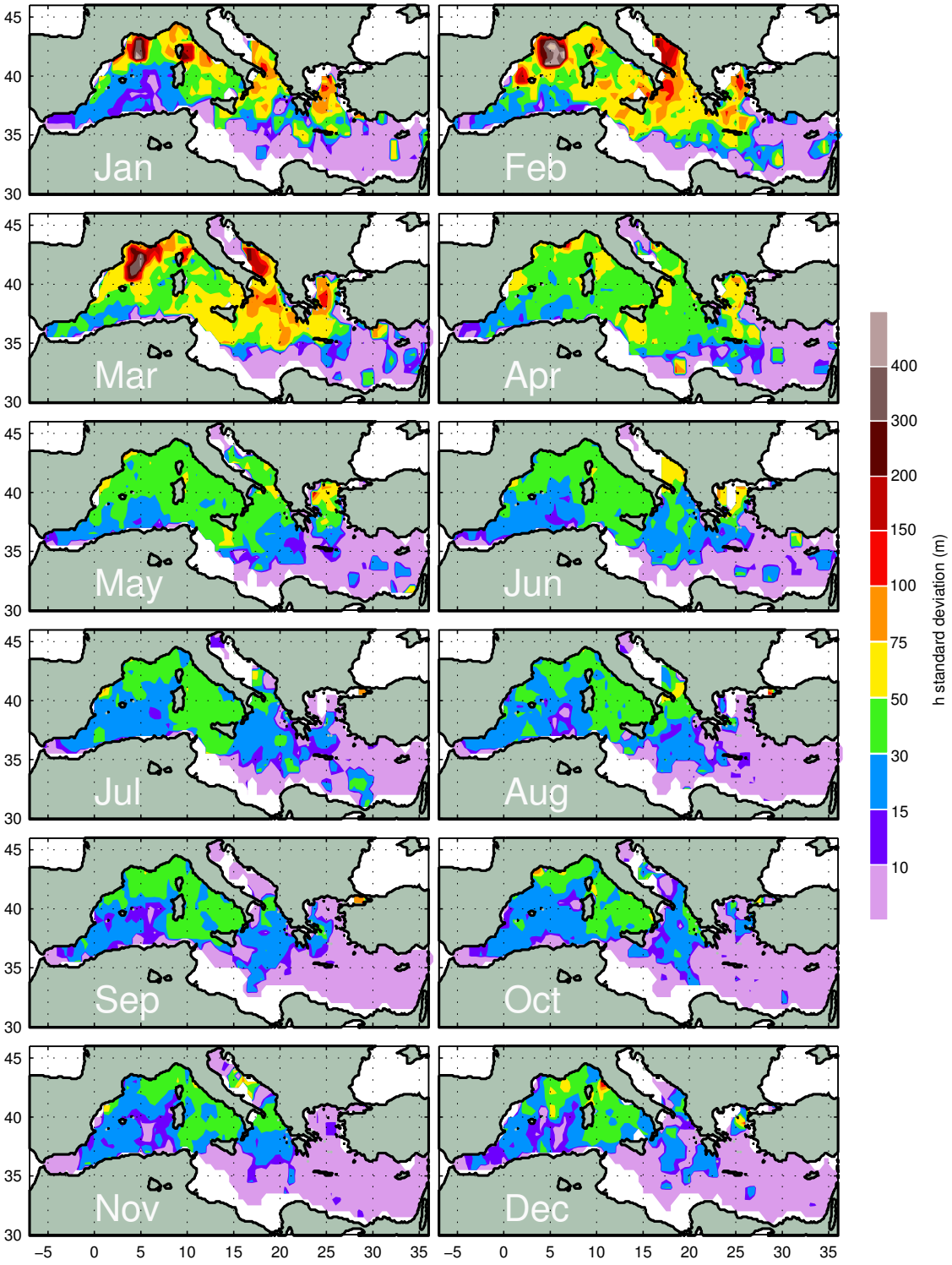

Figure 3.9: Maps of standard deviation associated to the mesh box averages of the upper-ocean layer shown on figure 3.6.

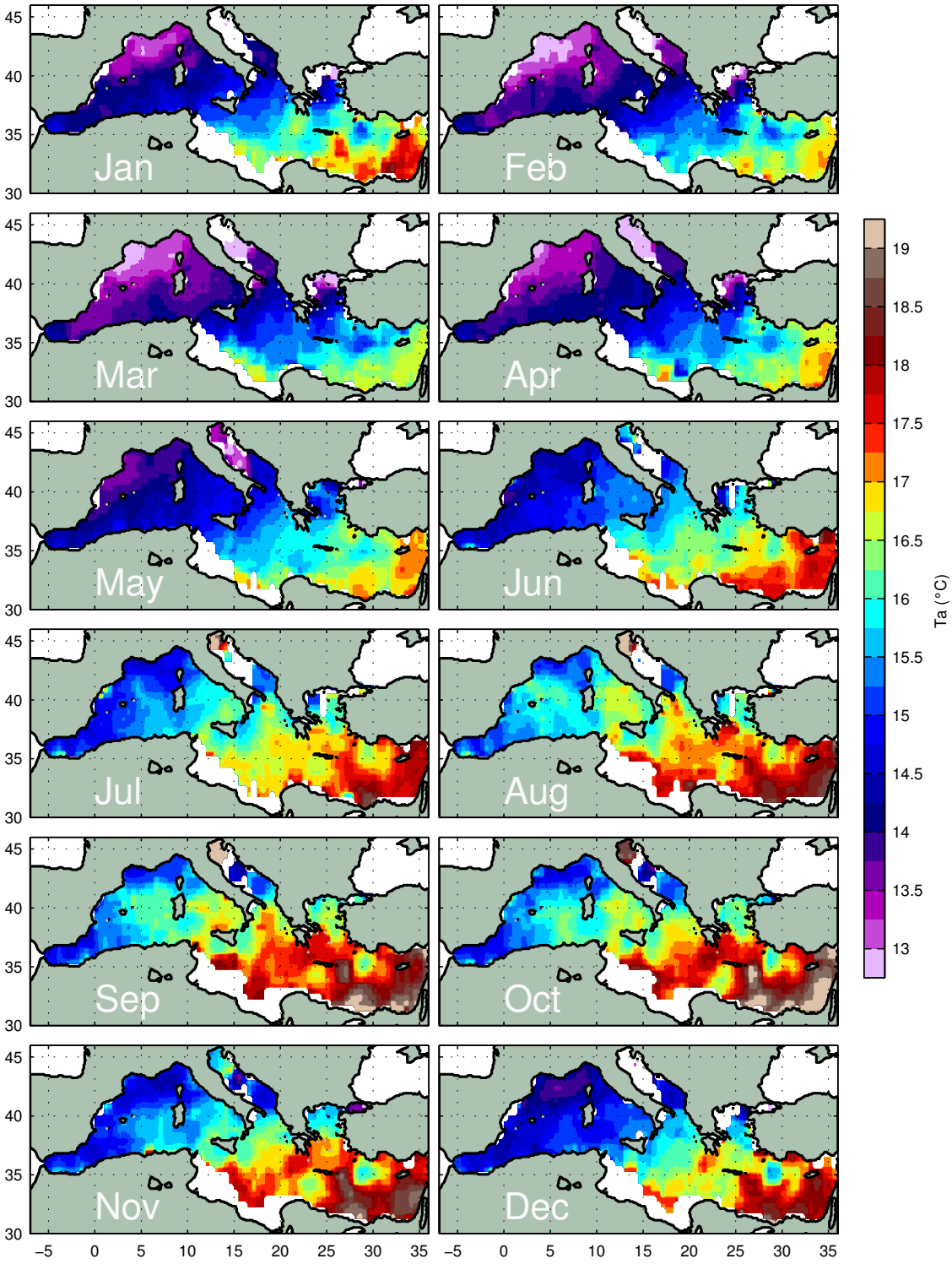

Figure 3.10: Mediterranean climatology of the upper-ocean temperature T_a, determined by the depth averaged temperature from the surface to the depth h.

Unlike the depth-averaged temperature T_a, the mixed layer temperature presents a more pronounced seasonal cycle (figure 3.11), with minimal values below 13°C found in February in the Adriatic Sea and in the Gulf of Lions, and maximal values reaching 28.0°C are found in August in the east of the Levantine Basin. The basin-mean of the mixed layer temperature is going from 14.8°C in February to 24.9°C in August for the Mediterranean Sea, from 14.0°C in Feb. to 24.2°C in Aug. for the WMED, and from 15.4°C in Mar. to 25.5°C in Aug. for the EMED. The seasonal variability of the surface layer, strongly impacted by the solar heat flux, masks the upper-ocean temperature anomaly associated with the presence of the anticyclonic and cyclonic gyres in the EMED. They are more easily distinguishable by their depth average temperature T_a (figure 3.10). The standard deviation of the mixed layer temperature (figure A.2) presents more variability than the standard deviation of the depth integrated temperature T_a, particularly in summer when the mixed layer is shallow and thus is more sensitive to the temporal and spatial variability of air-sea exchanges.

3.3.2 Seasonal cycle of the thermocline

Once the climatology of the depth of the seasonal thermocline base is done, one can easily produce a climatology of the seasonal thermocline slope. We define the seasonal thermocline slope as $\frac{T_{-h}-MLT}{h-MLD}$, where T_{-h} is the temperature at the base of the thermocline, MLT is the temperature at the base of the mixed layer, h is the depth of the thermocline and MLD is the mixed layer depth.

The monthly variability of the seasonal thermocline slope (figure 3.12) is characterized by a global decrease of the slope from September to February and an increase from April to August. This seasonal cycle is in good agreement with the seasonal cycle of the mixed layer (figure 3.7). Maxima are found in August, essentially in the Tyrrhenian Sea (0.08-0.1°C.m^{-1}) and around the Balearic Islands (0.07-0.08°C.m^{-1}). One can also notice that some regions like the DWF zones in the Northwestern Mediterranean, in the Adriatic Sea, in the Aegean Sea or the Rhodes Gyre, present a less pronounced seasonal thermocline than the other parts of the basin. Some regions like the DWF zones in the Northwestern Mediterranean, in the Adriatic Sea, in the Aegean Sea or the Rhodes Gyre, present a less pronounced seasonal thermocline than the other parts of the basin. These results are expected as t hose areas are known as the main zones of intermediate and deep water formation in the Mediterranean Sea (Schroeder et al. [2012]). As the water column is well mixed almost every year in those areas, the local stratification and consequently the thermocline is weaker locally as illustrated for example in Herrmann et al. [2010].

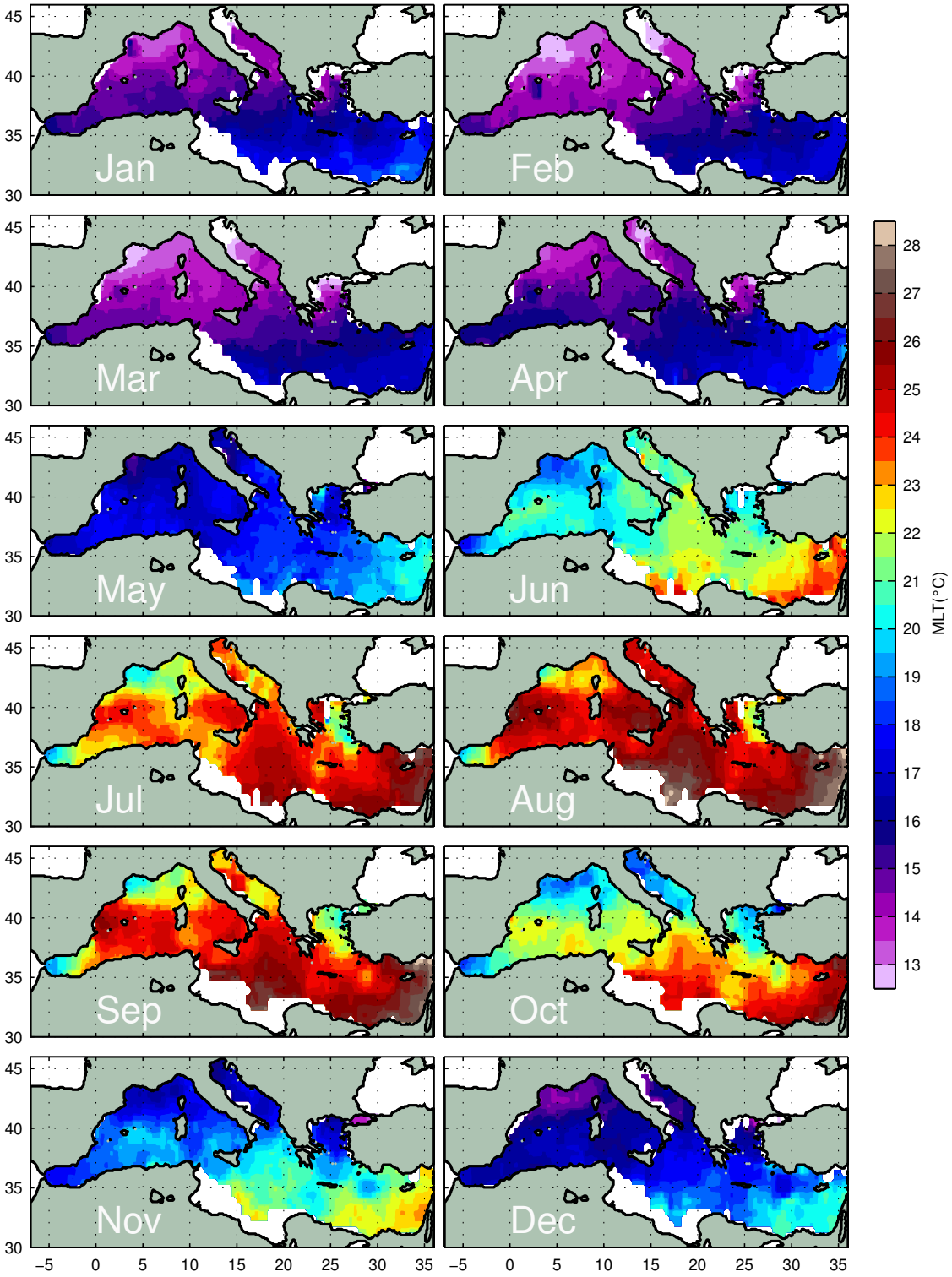

Figure 3.11: Mediterranean climatology of the mixed layer temperature.

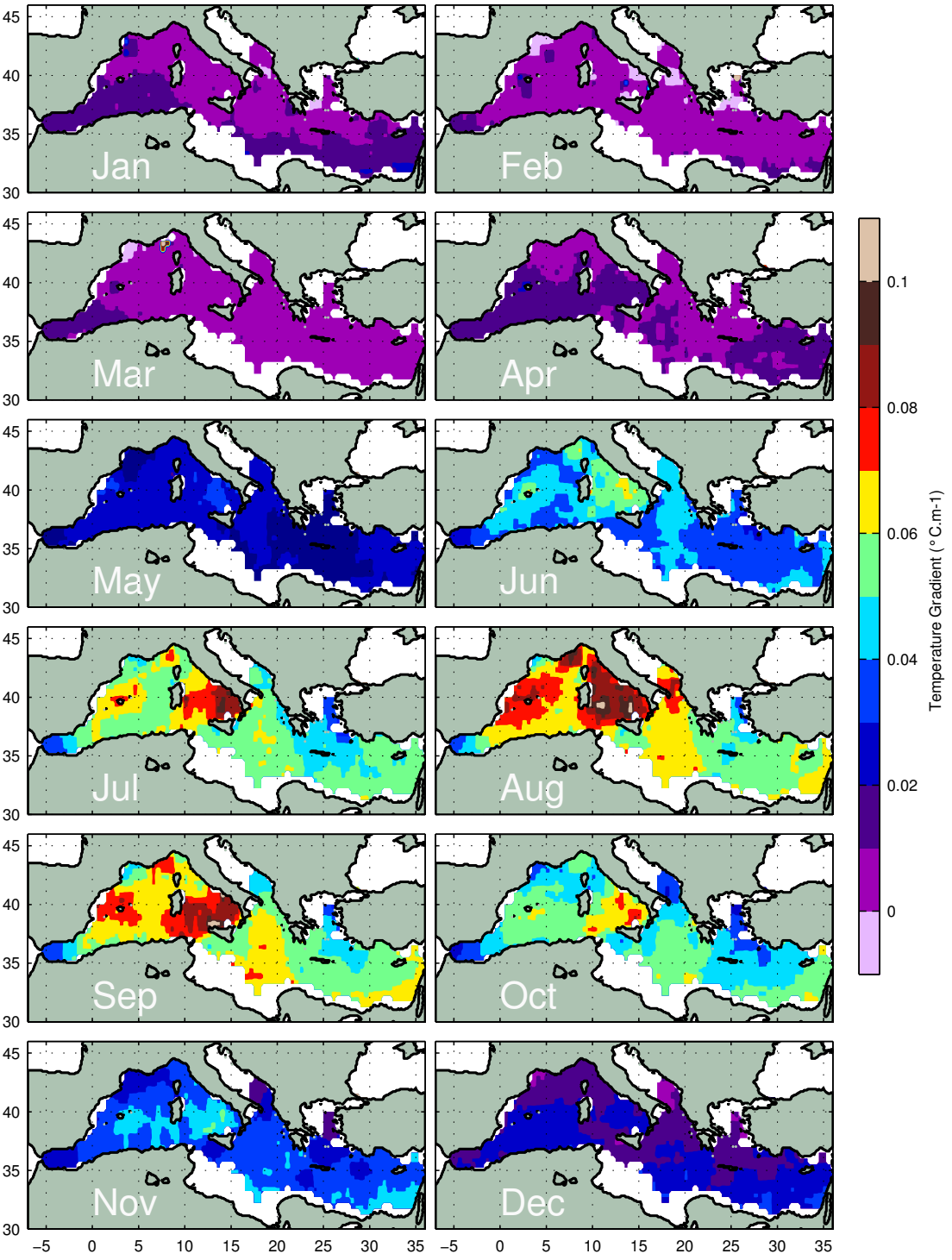

Figure 3.12: Mediterranean climatology of the thermocline slope

3.3.3 Estimation of the seasonal cycle of the surface Net Heat Flux from in-situ observations on average over the Mediterranean

3.3.3.1 Annual value of the basin-mean of NHF

For the whole Mediterranean, the annual value of the basin-mean of HSR is estimated at -1.9±4.0 W.m^{-2} for the 1969-2012 period. This does not establish a clear warming trend in the upper-ocean in contrast to Rixen et al. [2005] who showed a warming of the surface layer since the 1980s, but is not in contradiction with their results due to our uncertainties on HSR. Rixen et al. [2005] found also a warming of the 150m-bottom layer equal to [10-20] x 10^{20} J for the 1980–2000 period, corresponding to a trend of [0.004-0.008] °C/year and to a heat storage rate DHSR=0.8-1.6 W.m^{-2}.

Using the climatological monthly averaged value of the Atlantic inflow (Soto-Navarro et al. [2010]) and outflow (Sánchez-Román et al. [2009]) and their associated temperature Criado-Aldeanueva et al. [2012]), the net heat flux through the Strait of Gibraltar can be estimated: Q_{medin} - Q_{medut} = Q_{mednet} = 4±1.7 W.m^{-2}.

The sum of the annual mean values of HSR, DHSR and Q_{mednet} conducts to an estimation of the annual value of NHF of -4.7±4.4 W.m^{-2} (Eq. 3–4). This value is close to recent estimates of NHF using *in situ* and satellite-derived data sets (-3 +/- 8 W.m^{-2}, Sanchez-Gomez et al. [2011]), using empirical corrections of the ERA40 atmospheric parameters plus bulk formula (-7 W.m^{-2}, Pettenuzzo et al. [2010]) and using the historical runs of 5 fully-coupled AORCMs ([-6.4 ; -1.7] W.m^{-2}, Dubois et al. [2011]). Results from ALADIN simulations gave us an annual NHF of -5.0±3.9 W.m^{-2} for our study area.

Uncertainties on the basin estimates of HSR are calculated using a Monte Carlo test, following the same method used in the section 3.2.4. The test produces 1000 estimates of the basin mean of HSR, then uncertainties are calculated as the standard deviation of these 1000 realizations. Each estimation of the basin mean is calculated as the sum of the climatology box estimates. For each box, HSR values are randomly chosen from a normal distribution characterized by the climatological mean and standard deviation calculated for this box. This approach covers mainly uncertainty due to inter-annual variability of T_a and h. For periods of strong deepening of the mixed layer, as it is frequent in winter particularly in the DWF zones, the uncertainties from others sources like sampling errors, are indistinguishable from the inter-annual variability and are thus included. As an example, for a specific month, our calculations may over- or under- estimated monthly mean values due to the high temporal variability of the mixed layer deepening in a month. However, we believe that our approach covers most of the uncertainty of our method. Concerning uncertainties on the net heat flux through Gibraltar Strait, we use the one given by Soto-Navarro et al. [2010] and Criado-Aldeanueva et al. [2012].

3.3.3.2 Monthly climatological cycle of the basin-mean of NHF

Figure 3.13 displays the basin-mean climatological annual cycle for NHF estimated (NHF_{obs}) from ocean observations (in blue), NHF from Aladin RCM (NHF_{mod}, in green) and the differ-

ence between the two (in magenta), over the Mediterranean. One can see that the climatological annual cycle for NHF_{obs} has a clear seasonal signal with minimal and maximal values being about -169.3±4.7W.m^{-2} in December, and +125.2±3.9W.m^{-2} in June. NHF_{mod} is varying from -178.3±5.5W.m^{-2} in December to +158.0±2.3W.m^{-2} in June. One can observe on figure 13 that even if there is a good agreement in the shapes of NHF_{obs} and NHF_{mod}, there are some discrepancies, particularly in summer and fall/winter. The same differences are found using the seasonal cycle of NHF_{obs} calculated over the same time period that ALADIN simulations (1979-2011).

A possible explanation for these differences is the overestimation of the latent heat flux and the short-wave radiation in the ALADIN model, which do not occur necessarily at the same period. These errors can offset each other on an annual basis and thus the average annual value of NHF remains in the range of acceptable values. One has to keep in mind that the seasonal cycle of the NHF is mostly imposed by short-wave seasonal cycle, but the spatial pattern and local extremes are mostly driven by the latent heat flux. According to the 5 fully-coupled Atmosphere-Ocean Regional Climate Models (AORCMs) and the different observations data sets used by Dubois et al. [2011], the maximum of the short-wave radiation is in June/July, while in 4 of the 5 AORCMs and in the observations, the latent heat flux maximum

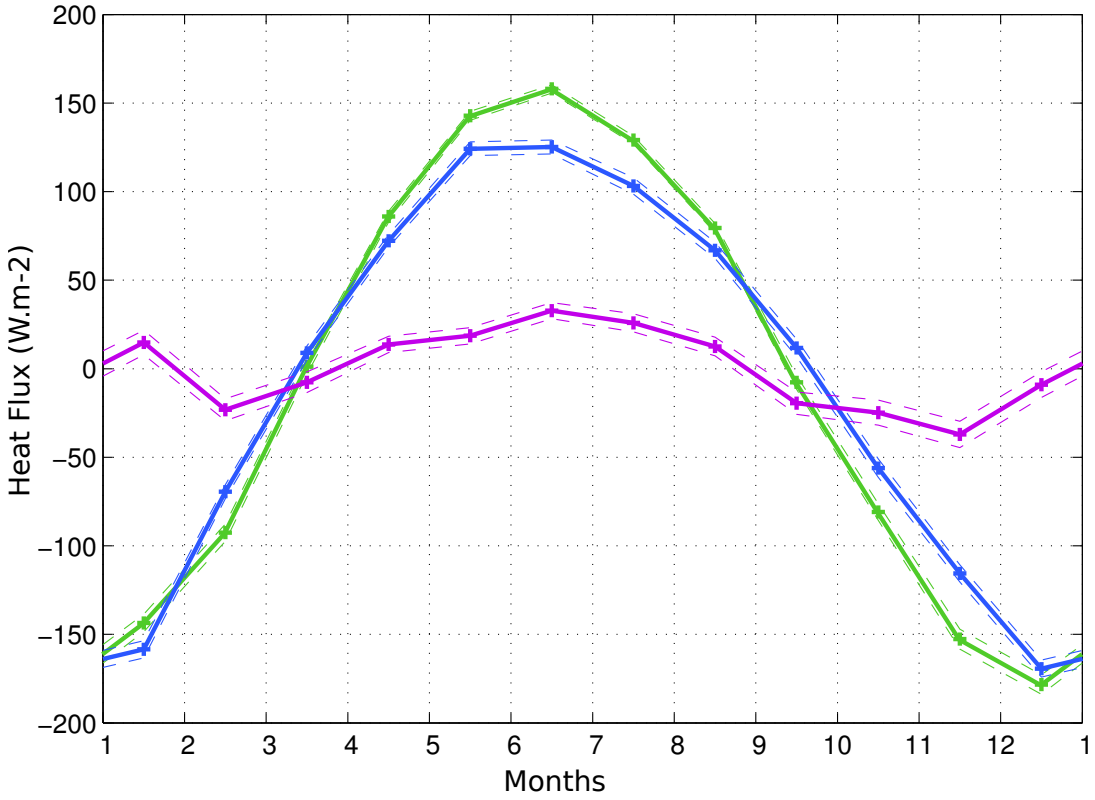

Figure 3.13: Seasonal cycle of the basin-mean Net Heat Flux for the Mediterranean Sea estimated from oceanic observations (blue) and from ALADIN RCM (green). Differences between the two estimates are indicated by the magenta line.

occurred in November/December.

Over the Mediterranean Sea for the 1979-2011 period, ALADIN simulates a NHF equal to -4 W.m^{-2} with 204 W.m^{-2} for the net shortwave radiation flux, -85 W.m^{-2} for the net long-wave radiation, -113 W.m^{-2} for the latent heat flux and -10 W.m^{-2} for the sensible heat flux. The net heat flux, the long-wave radiation flux and the sensible heat flux are in good agreement with Pettenuzzo et al. [2010] and Sanchez-Gomez et al. [2011] estimates whereas both the short-wave radiation flux and latent heat loss are overestimated by about 20 W.m^{-2}.

3.3.4 Discussion on Local Heat Storage Rates

The seasonal cycle of the HSR is presented in figure 3.14. The basin variability of the upper-ocean heat content changes is dominated by a seasonal cycle oscillating between minimal value found in December, and maximal value in June (figure 3.13 and section 3.3.3). Zero values are reached in February/March and in September/October, due to extrema in the seasonal cycle of the depth-averaged temperature. The standard deviation of HSR, shown on figure 3.15, is highly variable: from 25-50W.m^{-2} in March in the Tyrrhenian Sea to more than 300W.m^{-2} in January in the Gulf of Lions, in fall in Ierapetra Gyre. Location of high standard deviation values for HSR are related to high standard deviation of h (e.g. in winter in DWF zones, figure 3.9) and of T_a (e.g. in summer/fall, especially in the Ierapetra Gyre, figure A.1).

Figure 3.16 represents the seasonal cycle of the monthly HSR anomalies from the basin mean (HSR_{ano}). This figure shows region that are gaining or losing heat more or less quickly than the whole basin. HSR_{ano} presents significant local variations, some as high as 200W.m-2. A positive HSR_{ano} associated with a positive basin-mean (respectively a negative HSR_{ano} associated with a negative basin-mean) indicates regions gaining (resp. losing) heat more quickly than the whole basin. In contrast, a positive HSR_{ano} associated with a negative basin-mean (or the opposite) indicate region losing heat less quickly than the whole basin. These local modulations of HSR can be due to different forcings: 1) surface net heat flux, 2) horizontal heat advection, and 3) entrainment mixing at the interface depth, that cannot be calculated with our dataset. Local variations of HSR_{ano} seem to be related to specific dynamic structures, like oceanic gyres.

3.3.4.1 The Alboran Sea

Coherent patterns can be distinguished from the map of monthly HSR anomalies (figure 3.16). From October to January in the Alboran Sea, anomalies are between 75 and 100 W.m^{-2} higher than the basin mean which is negative (-53.0, -112.3, -166.7 and -155.5 W.m^{-2}), while in summer anomalies are between 50 and 100W.m^{-2} lower than the basin mean which is positive (from +126.6 W.m^{-2} in May to +15.3 W.m^{-2} in September). The proximity of this sub-basin to the Gibraltar Strait and thus to the inflow of heat coming from the Atlantic Ocean, may explain why seasonal variations of HSR are reduced compared to the rest of the Mediterranean Sea.

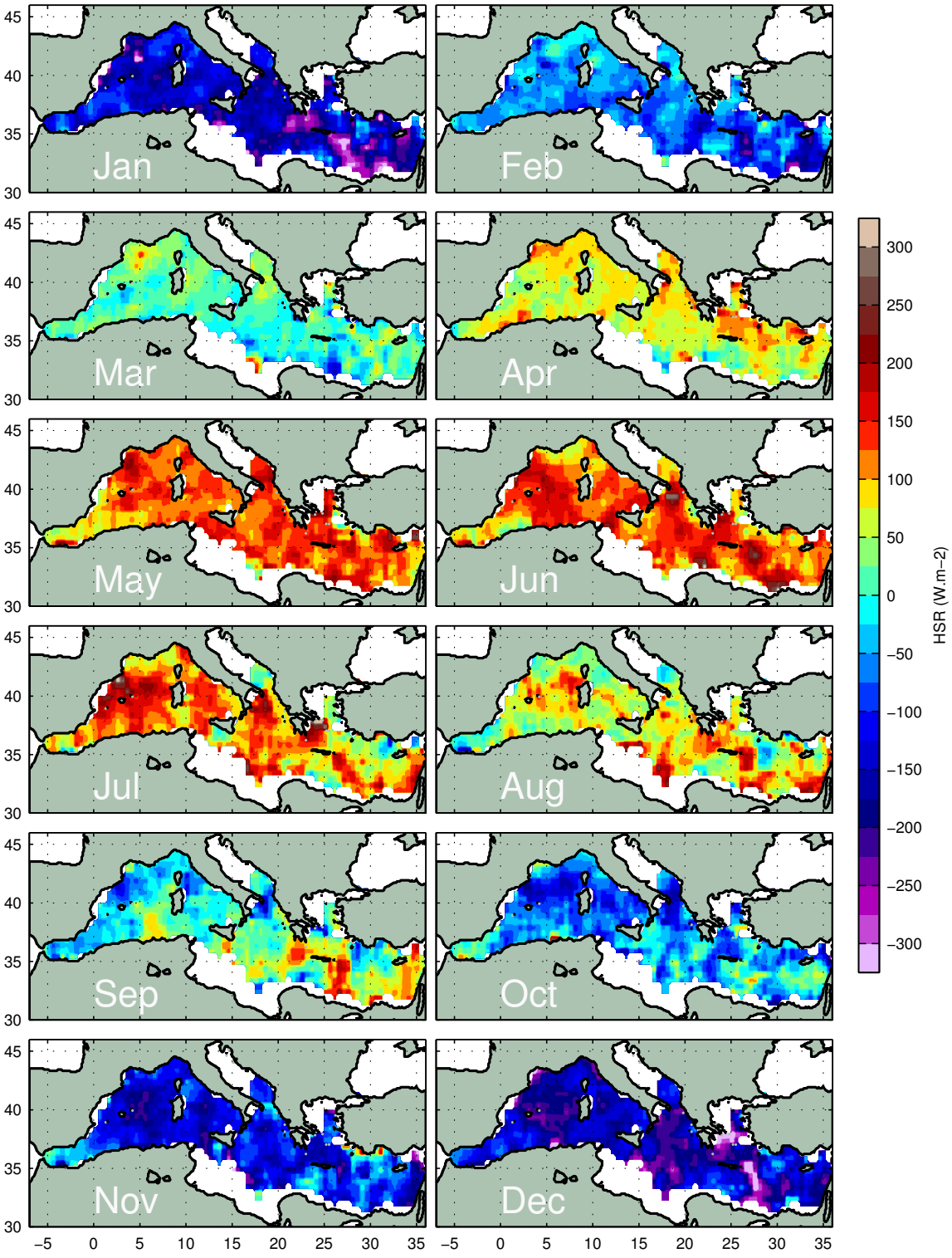

Figure 3.14: Mediterranean climatology of the Heat Storage Rate HSR

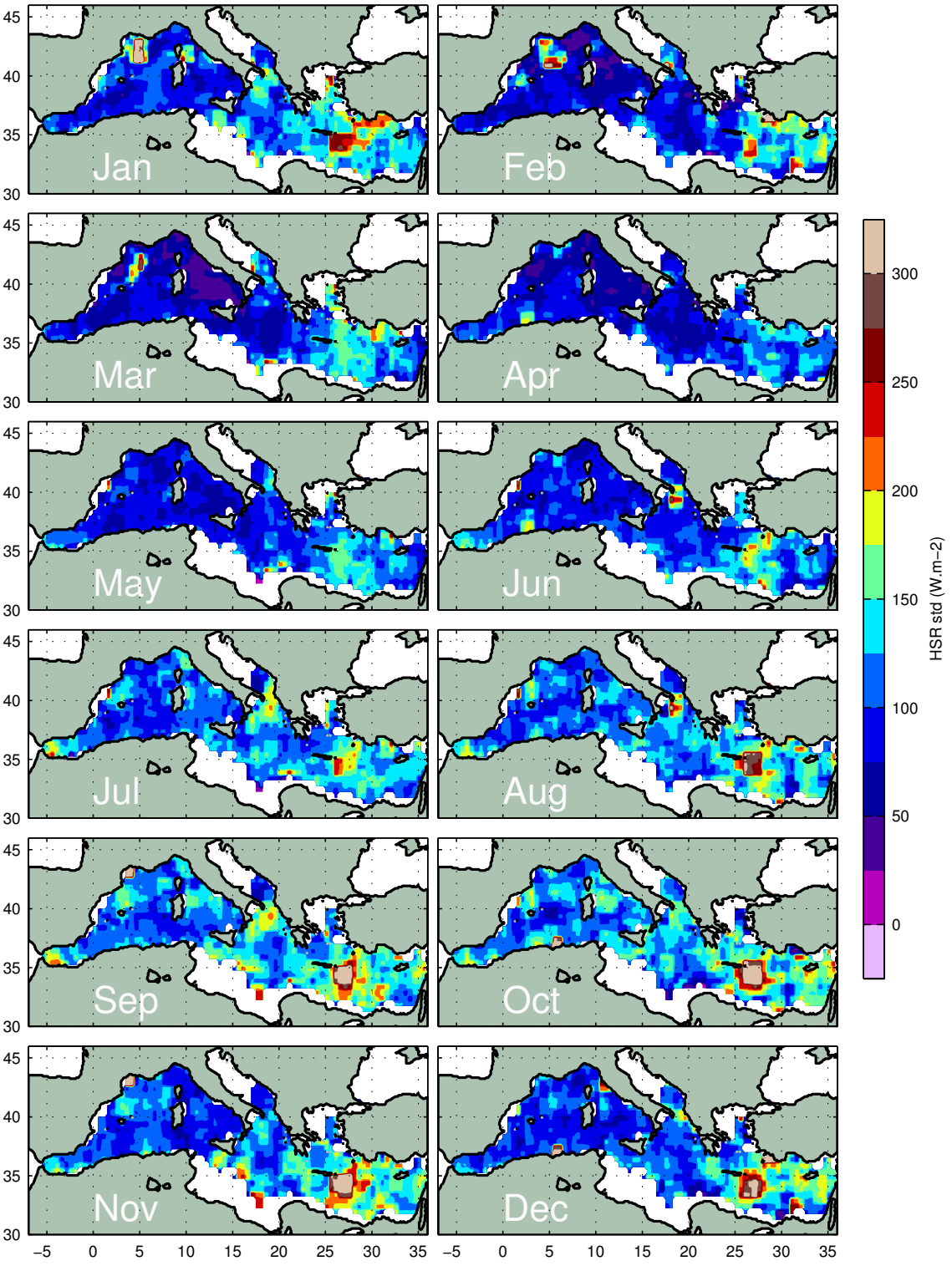

Figure 3.15: Maps of the standard deviation associated to the mesh box averages of HSR shown on figure 3.14

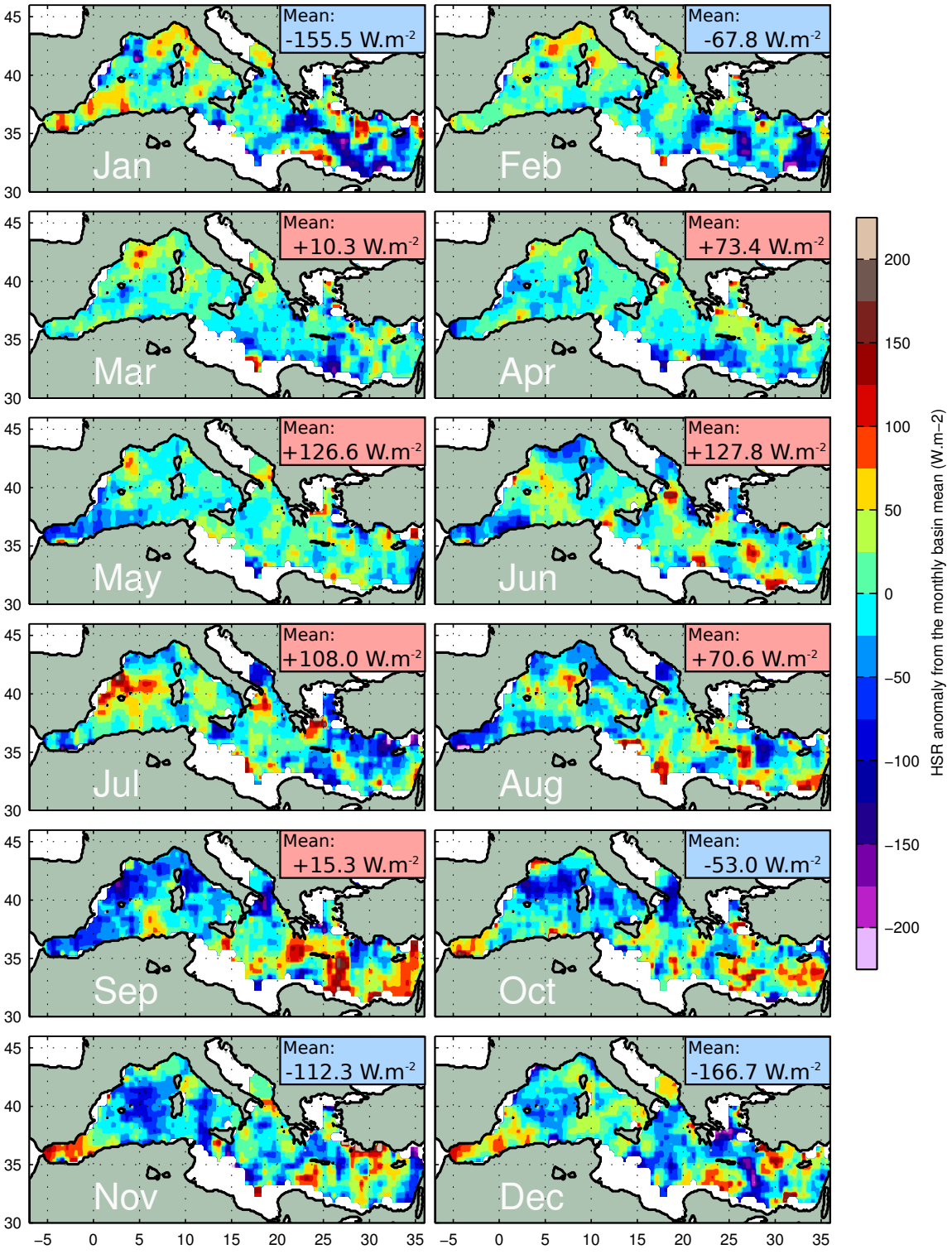

Figure 3.16: Mediterranean climatology of HSR anomalies related to the basin mean

3.3.4.2 The Balearic Islands

High HSR values can be seen along the 40° parallel in the WMED between the Spain mainland and Sardinia, and through the Balearic Islands, from June to August (figure 3.14), with larger HSR values (up to 260 W.m^{-2}) than in the rest of the WMED. These high values for HSR are also found by looking HSR_{ano} (figure 3.16) which presents positive values (between -50 and -100 W.m^{-2}). These positive anomalies indicate that this region is gaining heat quickly than the rest of the basin. At that time of the year, this might be due to a more pronounced heat convergence in the upper-ocean.

This region has the particularity to be a place where a strong thermal front in winter separates warm Atlantic surface water from the South to cold Mediterranean surface water from the North (Lacombe and Tchernia [1972]). The regional circulation around the Balearic Islands is linked to the Northern Current which carries down surface water from the Gulf of Lions along the continental slope of the Iberian Peninsula into the Balearic subbasin (Font et al. [1988]). In the South, the cyclonic recirculation of anticyclonic eddies in the Algerian Basin carries Atlantic Water from the Algerian boundary Current to the South of the Balearic Islands (Taupier-Letage and Millot [1988]; Puillat et al. [2002]).

Two hypotheses may explain the persistence of the positive HSR anomaly during the summer around the Balearic Islands. First this region is under the influence of the WIW, this mode water is formed in winter in the whole northwestern Mediterranean Sea and spreads southwards following the general circulation (Millot [1999]; Fuda et al. [2000]). The accumulation of these cold and fresh lenses of WIW in the Balearic Sea may explain why HSR are higher in that region, in particular because of the horizontal heat fluxes from relative warm surrounding water to these cold water.

The other hypothesis may have its source in the dramatic and frequent changes of the circulation around the Balearic Islands in summer (Monserrat et al. [2008]). The Northern Current may be blocked when reaching the Ibiza Channel by anticyclonic channel-size eddies and then recirculates with a cyclonic way in the Balearic Sea without significant transport of water through the Ibiza Channel (Castellón et al. [1990]). These channel-size eddies are composed of cold and relative fresh water (Pinot et al. [2002]), corresponding to WIW characteristics. In the North of the Balearic Islands, the recirculation of the Northern Current joins the eastward Balearic Current, while in the South, the flow due to recirculation of eddies into the Algerian Basin is westward (Testor et al. [2005]). So, this summer anticyclonic circulation around the Balearic Islands might keep isolated relative cold subsurface water (WIW) from the surrounding warm water and induced a horizontal heat transfer. These two hypothesis may explain why we have positive HSR anomalies in summer around the Balearic Islands.

3.3.4.3 The Cyclonic and Anticyclonic Gyres of the Cretan Arc

In the EMED, strong negative HSR anomalies from November to February and positive anomalies from June to September are located in places of known anticyclonic gyres (the PG and the IG, discussed section 3.3.1). Unlike anticyclonic gyres, cyclonic gyres (the WCG and the

RG, section 3.3.1) present positive HSR anomalies from December to February and negative anomalies in July and August.

The two anticyclonic gyres have a more permanent signature on the seasonal climatology of HSR (particularly the IG) than cyclonic gyres in winter and summer. This may be explained by the structure of gyres: in anticyclonic gyres the thermocline is pushed down, unlike cyclonic ones where the thermocline is pushed up. So, anticyclonic gyres tend to expand the layer that exchanges heat with the atmosphere. The "warm core" structure of anticyclonic gyres is responsible for temperature difference between the gyre core and the relative colder surrounding waters, which may induce a heat transport, particularly in winter when this horizontal temperature gradient is more pronounced.

3.4 Conclusions

We present here a new climatology of the mixed layer depth and temperature, and of the thermocline depth on a 1°x1° grid, based on recent data collected between 1969 and 2012 containing more than 190 000 profiles. The depth and the temperature of the mixed layer and the thermocline, together with the thermocline slope, revealed well known Mediterranean circulation features.

This work is the first quantification of heat storage rate in the upper-ocean for the whole Mediterranean based only on *in situ* oceanographic data, thereby providing a new benchmark in particular for the development of ocean models. In particular, we propose a new independent estimate of the seasonal cycle of the basin-mean surface Net Heat Flux, by combining our HSR climatology to existing climatology of the horizontal net heat flux from the Atlantic Ocean to the Mediterranean Sea at Gibraltar Strait. The annual mean value of NHF calculated from ocean observations is -4.7±4.4 $W.m^{-2}$. NHF presents a clear seasonal signal with minimal and maximal values being about -169.3±4.7$W.m^{-2}$ in December and +125.2±3.9$W.m^{-2}$ in June respectively. This is in agreement with the NHF from Regional Climate Model ALADIN, but some differences may be noticed in summer and fall/winter, certainly due to an overestimation of the latent heat flux and the short-wave radiation in the model. Future comparisons between this climatology of HSR and other heat fluxes climatologies may be useful to test heat fluxes parametrization and thus improve the accuracy of the models, particularly in the context of long term climate simulations that require, among others, a good modeling of the thermohaline circulation.

This work also highlights the implication of known Mediterranean circulation patterns (like the anticyclonic and cyclonic gyres in the Eastern Mediterranean, or the circulation around the Balearic Islands) in the spatial and temporal variability of the heat storage rate. Local modulations of HSR can be due to different forcings (surface net heat flux, horizontal heat advection, and entrainment mixing at the interface depth) that cannot be calculated with our dataset. So future works would also be to use complementary datasets, such as other climatologies deduced from surface geostrophic currents estimates (Rio et al. [2007]; Poulain et al. [2012]), or from surface flux datasets (OAFlux, HOAPS, NOC) to estimate other terms in the heat budget equation, like the horizontal heat advection term, or the NHF term.

Finally, the limitations of our studies (period covered, uncertainties) stress the need of sustained observing systems (like repeated cruises, Argo profiling floats, mooring lines and gliders), if we want to better estimate the seasonal cycle of heat fluxes in key regions like the Gibraltar Strait, the Alboran Sea, the Deep Water Formation areas, the anticyclonic and cyclonic gyres in the Ionian and Levantine Basin. This sustained effort of observation will also allow us to distinguish and/or confirm any long-term trend, as the reduction of the Mediterranean thermohaline circulation.

4 Recent Advances in the Understanding of Open-Ocean Deep Convection in the Gulf of Lions

Contents

Open-Ocean Deep Convection (OODC) is a key process that connects the surface ocean to the deep ocean. In addition to heat and salt, OODC may transfer also biogeochemical components to the deep water like oxygen and inorganic and organic matter, contributing to the ventilation and the "feeding" of the deep pelagic and benthic ecosystems. During this thesis, I had also the opportunity to collaborate on two studies related to the impacts of OODC on the deep pelagic and benthic ecosystems.

I worked on a study based on the impact of OODC on particle fluxes and sediment dynamics. The time period covered by this study runs from September 2007 to Avril 2009. This work points out the influence of OODC on bottom sediment resuspension, especially through results from sediment traps deployed at 1000 and 2300m depth. This significant remobilization of sediments, in the basin of the Gulf of Lions after a OODC event, has been likely to induce a subsequent alteration of the seabed and to impact the functioning of the deep-sea ecosystem.

My contribution to this study was done through data processing and analyzing of deep LION mooring line, the provision of ECMWF atmospheric heat fluxes, the detailed physical descriptions of OODC events and of changes in the structure of deep waters, the discussion on the variability of the open-ocean convection and its impacts on deep particle fluxes and benthic ecosystems. This paper is available in the appendix C, and is published in Biogeosciences under the reference :

Stabholz, M., X. Durrieu de Madron, M. Canals, A. Khripounoff, I. Taupier-Letage, P. Testor, S. Heussner, P. Kerhervé, N. Delsaut, L. Houpert, G. Lastras, and B. Dennielou. 2013. Impact of open-ocean convection on particle fluxes and sediment dynamics in the deep margin of the Gulf of Lions. Biogeosciences 10: 1097–1116., doi:10.5194/bg-10-1097-2013

I also collaborated in another study on enhancement of deep-sea biological activity by dense water formation. It is based on a 2.5-year long record of light emission by deep-sea pelagic organisms, measured from December 2007 to June 2010 at the ANTARES underwater neutrino telescope in the deep Northwestern Mediterranean Sea, together with synchronous hydrological records. This work highlights the importance of dense water formation events and newly-formed deep water in activating deep-sea pelagic ecosystem by fueling it through the supply of relative "fresh" organic matter, and thus stimulating bioluminescence activity.

During this work, I was responsible of the data processing and analyzing of the deep LION mooring line and I also contributed to the discussion on the variability of deep ocean convection and newly-formed deep water, and their link with bioluminescence blooms. This article is presented in appendix D, and is published in PLoS ONE under the reference :

Tamburini, C., M. Canals, X. Durrieu de Madron, L. Houpert, D. Lefèvre, et al. 2013. Deep-Sea Bioluminescence Blooms after Dense Water Formation at the Ocean Surface. PLoS ONE 8(7): e67523., doi:10.1371/journal.pone.0067523

In the following of this chapter, we present an article in preparation entitled "High Resolution Monitoring of Open-Ocean Deep Convection in the Gulf of Lions over the recent period (2007-2012)". 5 consecutive years of deep ocean convection, monitored by a deep mooring line in the Gulf of Lions have been investigated. We point out essentially the temporal scales of the different deep convection phases, the numerous eddy occurrences and the implication of deep convection in the evolution of deep water thermohaline characteristics.

Abstract

A mooring line was setup since 2007 in the Gulf of Lions (42°N-4.6°E) to monitor the deep convection process. This observation system is composed by 20 potential temperature sensors, 10 salinity sensors and 5 current meters between 150m depth and the bottom (2330m depth). Theses recent measurements reveal the temporal evolution of the physical processes interfering in the phases of deep convection (deepening of the mixed layer depth, violent vertical mixing and restratification).

Some remarkable features point out from the analysis of four deep convection events observed between 2009 and 2012. The time for the mixed layer deepening is comprised between 1 and 2 months. Due to the strong heat loss and evaporation, the mixed layer reached the bottom, and the violent vertical mixing of the whole homogeneous water column is in the range of 9-12 days.

Horizontal currents were strongly equivalent barotropic during each deployment between 150m and 2300m depth. The first EOF dominate the variability, containing 85% to 95% of the variance, while the second mode contains 5% to 10%. Strong currents were also recorded during the different events of deep ocean convection: high frequencies vertical velocities exceeded 15 $cm.s^{-1}$ during the violent vertical mixing phase and strong mesoscale horizontal currents reached $40cm.s^{-1}$ during the restratification phase. Using a eddy-detection method based on a kinematic model, 37 eddies crossing the mooring line were detected between November 2009 and July 2012, 19 cyclones and 18 anticyclones. The radii (velocities) ranging from 0.7 km to 20.0 km (0.9 $cm.s^{-1}$ to 25.1 $cm.s^{-1}$). The main mode of the distribution of eddies radii is centered at 4km for the cyclones and 5km for the anticyclones.

The apparition of newly-formed deep waters was detected in winter 2009, 2010, 2011 and 2012. In winter 2010, two newly-formed deep waters were detected after the deep convection event, both present a different potential temperature but a similar salinity, suggesting that both might be formed in the cyclonic gyre, but in different locations. In 2012, two new deep waters were detected at the mooring location, one was identified as a result of open-ocean deep convection, while the other seems to be the result of a dense shelf water cascading event that occurred in winter 2012.

Each of these deep water formation events modified the deep stratification by producing a new deep water. The thermohaline changes of the bottom water between 2007 and 2012 corresponds to a potential density (σ) increase of 0.015 $kg.m^{-3}$ in 4 years, linked to a salinity (S) increase of 0.03‰ and a potential temperature (θ) increase of 0.03°C. These stepwise increases

in bottom water characteristics are marked by positive jumps in θ , S and σ, and correspond to the mixed layer reaching the bottom in February. We interpret the 0.02°C decrease in potential temperature after each jump, as the primarily effect of the persistent net heat loss after that the MLD reached the bottom, since no significant salinity variation was recorded at the same time.

4.1 Introduction

Open-ocean deep convection is a key process that transfers the heat and salt contents from the surface to the deep ocean and takes place in a few regions of the world. In addition to polar regions as the Labrador (Lazier [1973]; Clarke and Gascard [1983]), the Greenland (Schott et al. [1993]), the Weddell and Ross Seas (Killworth [1983]), open-ocean deep convection takes place in more temperate regions as the East/Japan Sea (Kim et al. [2008]) and the Mediterranean (Gulf of Lions, Adriatic Sea, Aegean Sea, CIESM [2009]). High surface buoyancy loss associated to northern winds (Mistral, Tramontane) leads to deep mixing that forms the Western Mediterranean Deep Water (WMDW). The first experiment (MEDOC Group [1970]), took place in 1969 and identified the three phases of convection.

The preconditioning phase involves a weakening of the ocean stratification. This isopycnal doming is mainly caused by the global cyclonic circulation in the NW basin (MEDOC Group [1970]; Millot [1999]), but other topographic (Hogg [1973]; Madec et al. [1996]) or mesoscale (Killworth [1979]; Legg and Marshall [1998]; Lherminier et al. [1999]; Legg and McWilliams [2001]; Steffen and D'Asaro [2004]) features can also contribute to this preconditioning phase.

Vigorous buoyancy losses during the cooling and evaporation event, such as the strong wind outburst of continental air, initiates the deep convection of the very weakly stratified water in the core of the cyclonic gyre. The vertical mixing occurs in plumes of horizontal scale of O(1km), at vertical speeds up to 10cm.s^{-1}. These small scale features were first observed by Voorhis and Webb [1970] using isobaric floats, then by Schott and Leaman [1991] and Schott et al. [1996] using moored ADCPs. More recently, downward vertical velocities measurements up to 10cm.s^{-1} were observed using gliders (Merckelbach et al. [2010]). Theses plumes mix properties over the preconditioned site, forming a deep "mixed patch" ranging in scale from several tens of kilometers to >100 km in diameter. The characteristics of the newly formed water mass can be linked to the frequency and the intensity of the surface forcing (Artale et al. [2002]; Grignon [2009]) and to the heat and salt content of the "preconditioned" state (Schroeder et al. [2010]; Herrmann et al. [2010]).

The density contrast between the mixed patch and the surrounding would establish a rim current at the edge of the mixed patch which would be baroclinically unstable and shed eddies of scale O(5-10km) which could be considered as geostrophic given the low stratification of the area. The spreading of dense water is made through the action of these eddies (Testor and Gascard [2003, 2006]; Demirov and Pinardi [2007]; Herrmann et al. [2008]). Half of the newly-formed deep waters would be incorporated in the boundary circulation (Send et al. [1996]; Herrmann et al. [2008]) and the other half would propagate throughout the whole western Mediterranean Sea in the core of such eddies that can be long-lived features (1> year).

The 3 phases can overlap but restratification processes dominate as soon as the atmospheric forcing does not trigger active mixing anymore. After the end of the deep convection, the restratification of the upper ocean is mainly due to both the boundary current and the mesoscale structures that advect surface light water on top of the mixed patch Leaman and Schott [1991]; Schott et al. [1996]; Herrmann et al. [2008]).

The significant interannual variability of convection activity in the Gulf of Lions (Mertens and Schott [1998]; L'Hévéder et al. [2012]) leads also to an interannual variability in thermohaline characteristics of WMDW. The evolution of WMDW thermohaline characteristics through deep convection events might explain the long-term warming and salting trends observed in the deep layers of the WMED by several authors (Bethoux et al. [1990, 1998]; Rohling and Bryden [1992]; Leaman and Schott [1991]; Krahmann and Schott [1998]; Rixen et al. [2005]; Vargas-Yanez et al. [2010a,b]).

Abrupt changes in WMDW characteristics and stratification occurred during winter 2004-2005 and 2005-2006 (Lopez-Jurado et al. [2005]; Schroeder et al. [2006, 2008]; Font et al. [2007]; Smith et al. [2008]). Salat et al. [2006]; Puig et al. [2012] highlight the contribution of major cascading events (export through the canyons of dense water formed by convection on the shelf), especially in 2005, to changes in the WMDW stratification.

Three phenomena responsible for these intense deep convection events were identified. First, winter 2004-2005 was one of the coldest and driest winter of the last 40 years (Lopez-Jurado et al. [2005]). Second, Gasparini et al. [2005] showed that the Eastern Mediterranean Transient (EMT, Malanotte-Rizzoli et al. [1999]; Lascaratos et al. [1999]; Klein et al. [1999]) induced a remarkable injection of heat and salt in the eastern waters flowing westward through the Sicily channel to the deep Tyrrhenian subbasin. The propagation of this T-S increase from the Eastern Mediterranean basin could have induced a warming and salting of the intermediate layer of the NWMED (Schroeder et al. [2010]). Results from modeling studies (Herrmann et al. [2010]) assess the role of the EMT, by deepening the heat and salt maxima, in the high volume of WMDW formed in 2005, but also highlight the fact that a number of weak deep convection events before the winter 2005 could have induced a more pronounced Levantine Intermediate Water (LIW) layer as well as enhanced heat and salt contents at intermediate depths. Grignon et al. [2010] showed that even a normal winter would have led to deep convection in 2004/2005 due to low pre-winter stratification. Moreover the high interannual and decadal variability of the temperature and the salinity of Atlantic surface water in the Gulf of Lions (Vargas-Yanez et al. [2010b]) may also influence the intensity of deep convection (Rixen et al. [2005]).

There is a lot of efforts in modeling but very few observational evidences of open-ocean deep convection. It is the first time since the MEDOC experiment (MEDOC Group [1970]) that deep convection is monitored from year to year, in the framework of MOOSE (Mediterranean Ocean Observing System on Environment).

In this paper, we present recent measurements made in the deep convection area especially through results of the LION mooring line. In section 4.2 and 4.3, we describe the data and

methods used in our analysis. In section 4.4, we analyze 5 winters in order to precise the temporal scales associated to the different phases of the deep convection and the subsequent thermohaline changes of deep waters. Then, in section 4.3, we discuss the horizontal extent of the deep convection area using ocean color images. In section 4.6, we study the seasonal variations of the vertical structure of horizontal currents, while in section 4.7 we focus on the (sub) mesoscale dynamics that take place in the deep convection area, especially through a census of eddies using a wavelet-based detection method of isolated horizontal velocity anomalies. Finally, in section 4.8, we discuss the effects of surface buoyancy losses and the water column stratification on the interannual variability of the open-ocean deep convection.

4.2 Meteorological and Oceanographic Data

4.2.1 LION Mooring

The mooring site was chosen in the center of the convection zone described by MEDOC Group [1970], Leaman and Schott [1991] and The THETIS Group [1994] at 42°02.4'N, 4°41.0'E. There were six deployments (LION1 to LION6) during which the line was equipped with 8 to 26 instruments between September 2007 and July 2012. The evolution of the instrumented line over the years is presented in Table 4.2.

RBR (temperature recorders), SeaBird Microcat SBE37 (conductivity-temperature-pressure recorders) were used until June 2011. Since then, the 10 RBR were replaced by SeaBird Temperature Logger SBE56. Nortek Aquadopp were deployed since LION3 (September 2008) at 5 levels mesuring horizontal and vertical currents, while there were only 2 Aanderaa RCM 9 at 1000m and 2300m depth during LION1 (Sep. 2007 / Mar. 2008) and 1 Aanderaa RCM 9 at 1000m LION2 (Sep. 2008). During these two first deployments, we get only the horizontal currents. The vertical sampling was better since LION3 with 20 temperature records, 10 salinity records and 5 current records spanning depths from 150 m to the bottom (2300 m). Here we did not use the Aquadopp temperature data because of the low resolution and accuracy of the sensor (0.1°), and because for each current meter there was another much more accurate temperature sensor available nearby (a few meters).

The severe environmental conditions imposed us the use of a subsurface mooring, this prevent us from recording the upper 150m heat content. This lack of data could be filled by close glider profiles (<40km) and by temperature records of the French buoy Lion (<4.5km, detailed in the section 4.2.2). RBR were set up with a 15 seconds sampling, while Microcat and current meters had a sampling of respectively 6 minutes and 30 minutes. In order to have a consistent data set, we undersampled RBR and Microcat to get 30-minutes time-series.

In general all the mooring instruments returned good data, except for some periods. During LION3, the 500m depth Aquadopp seemed to have encountered writing problems. Due to a breaking at the base of the line during the recovery (April 2009), we lost the bottom Aquadopp and no current data were obtained at 2300m for the period from September 2008 to March 2009. During LION5, there were some battery issues on five Microcat (165m, 1100m, 1300m, 1780m and 200m) which stopped recording in February 2011. A delayed recovery of the

Table 4.1: Description of the LION mooring line

Deployment Name		LION1		LION2		LION3	LION4	LION5	LION6
Date		9 Sep 2007 27 Mar 2008		28 Mar 2008 21 Sep 2008		24 Sep 2008 5 Apr 2009	27 Oct 2009 23 Jun 2010	23 Jun 2010 12 Jun 2011	13 Jun 2011 26 Jul 2012
Temperature sensor	Type	RBR TR-1060		RBR TR-1050/60		RBR TR-1050/60	RBR TR-1050/60	RBR TR-1050/60	Seabird SBE56
	Nominal depth (m)	250-350-500-600		150-200-230-250-350-400-450-550-600-650		150-200-230-250-350-400-450-550-600-650	150-200-230-250-350-400-450-550-600-650	150-200-230-250-350-400-450-550-600-650	150-200-230-250-350-400-450-550-600-650
	Sampling	15 sec.		15 sec.		15 sec.	15 sec.	15 sec.	15 sec.
Conductivity-Temperature-Depth sensor	Type	Seabird SBE37SM		Seabird SBE37SM		Seabird SBE37SM	Seabird SBE37SM	Seabird SBE37SM	Seabird SBE37SM
	Nominal depth (m)	170-700-1500-2300		170-300-500-700-1500-2300		170-300-500-700-850-1100-1300-1500-1750-2000-2300	170-300-500-700-850-1100-1300-1500-1750-2000-2300	170-300-500-700-850-1100-1300-1500-1750-2000-2300	170-300-500-700-850-1100-1300-1500-1750-2000-2300
	Sampling	6 min.		6 min.		3 min. / 6 min.	3 min. / 6 min.	3 min. / 6 min.	3 min. / 6 min.
Current meter	Type	Aanderaa RCM9	RDI ADCP	Aanderraa RCM9	Nortek Aquadopp	Nortek Aquadopp	Nortek Aquadopp	Nortek Aquadopp	Nortek Aquadopp
	Nominal depth (m)	1000	2300	1000	2300	150-250-500-1000	150-250-500-1000-2300	50-250-500-1000-2300	150-250-500-1000-2300
	Sampling	30 min.	30 min.	30 min.	30 min.	30 min.	30 min.	30 min.	30 min.

Table 4.2: Desciption of the oceanic sensors of the MF-LION surface buoy

Date		13 Nov 2009 2 Mar 2010	2 Mar 2010 5 Nov 2010	5 Nov 2010 28 Sep 2011	28 Sep 2011 30 Jan 2013
NKE SP2T Temperature sensor	Nominal depth (m)	10-20-50-100-200	10-200	5-10-15-20-25-30-35-40-50-60-70-75-80-90-100-120-150-175-200-250	5-10-15-20-25-30-35-40-50-60-70-75-80-90-100-120-150-175-200-250
	Sampling	5 min.	5 min.	5 min.	5 min.
Seabird SBE37 CTD	Nominal depth (m)	n.a	n.a.	n.a.	2
	Sampling	n.a.	n.a.	n.a.	10 sec

mooring in July 2012 caused battery issues for most of the current meters: the 150m and the 2300m depth current meter have stopped from recording the 11 June 2012, while the 250m and the 500m depth have stopped the 14 July.

Since the recovery of LION4 (in June 2010), intercalibration of the moored instruments after and before each deployment are done. Niskin bottles are removed from the shipboard Rosette, then Microcat and RBR (or SBE56) are attached instead. We perform an hydrographical cast with a 20 minutes stop at 1000m depth, thus we can have a relative calibration of the moored instruments with the CTD probe SBE 19plus. Post- and/or pre- cruise calibrations, together with in-lab analysis of salinity bottles with a Salinometer (Guideline Autosal) calibrated using standard water at 38‰ give us an absolute accuracy, for all records used in this study, better than 0.005‰ for S, and 0.001°C for θ. From September 2007 to April 2009, no intercalibration was done. Comparisons with gliders and CTD stations was the only solution to detect some biases in the conductivity measurements. The conductivity corrections applied to the Microcat correspond to equivalent salinity corrections ranging from 0.000‰ to 0.005‰.

4.2.2 Météo-France Meteorological Buoy

A useful complementary dataset to the deep LION mooring is the instrumented Météo-France meteorological buoy MF-LION. This meteorological buoy is located at 42.0637°N 4.6482°E, 4-4.5 kilometers from the deep mooring location. In addition to the atmospheric sensors and to the sea surface temperature sensor, a 250m mooring line was fixed below the surface buoy since November 2009 (table 4.2). This line is currently equipped by 20 temperature sensors NKE SP2T which extend from 5 to 250 meters below the sea surface. An additional SeaBird Microcat SBE37 was installed at 2m depth in September 2011. Since that time, we also have surface salinity.

4.2.3 Profile Data

CTD

The CTD profiles were carried out from several oceanographic cruises (DOCONUG2007, DOCONUG2008, 42N5E, MOOSE-GE2010, CASCADE, MOOSE-GE2011 and MOOSE-GE2012) that took place in the NWMED. 230 CTD stations were carried out in the Gulf of Lions (between 41°N/44°N and 3°E/7°E) and more precisely 46 CTD stations are located at less than 30 km from the location of the LION mooring.

At all stations, pressure, temperature and conductivity were measured with a CTD Sea-Bird SBE 911+. Water samples were collected and analyzed on a Guideline Autosal salinometer to calibrate the conductivity sensor. The accuracy is estimated to be ± 0.004‰ for salinity and ± 0.001° for temperature.

Gliders

Another source of data came from gliders which are relatively new oceanographic platforms (Testor et al. [2010]) carried out in the framework of several European and national projects

(see Everyone's Gliding Observatories (EGO), http://www.ego-network.org, EU FP6 MERSEA, ANR LIVINGSTONE, NERC DOCONUG, SOERE MOOSE, HyMeX/MerMeX). Gliders profiles were considered as vertical and were checked with quality control procedures. Repeated surveys over the Northwestern Mediterranean were conducted between 2007 and 2012, with 77 deployments between January 2007 and August 2012 corresponding to 36513 profiles (2844 profiles corresponding to 28 deployments were made at less than 30km around the LION mooring).

4.2.4 Atmospheric reanalysis Era-Interim

The ERA-Interim reanalysis data set contains consistent atmosphere and surface analyses for the period from 1979 until real time, based on the ECMWF numerical weather prediction model.The reanalysis makes use of the ECMWF Integrated Forecast System at T255 spectral resolution (80 km horizontal resolution) with 91 vertical levels. We considered here the daily fields of the air-sea fluxes (downward and upward short-wave radiation, downward and upward long-wave radiation, latent heat flux, sensible heat flux, total precipitation and evaporation) in order to compute the daily net heat flux (Q_{net}) and the net freshwater flux out of the ocean.

4.2.5 Ocean Color

The 1-day Level 3 standard mapped images of MODIS Aqua surface chlorophyll at 9 km resolution were obtained from the NASA web site (http://oceancolor.gsfc.nasa.gov/) for the 2007-2012 period.

4.3 Methods

4.3.1 Mixed layer depth calculation

As the buoy oceanographic sensors and the deep mooring instruments are not the same, the resolution and the accuracy of the different sensors are also different. In this work we use a double criterion to estimate the mixed layer depth. After merging the deep mooring line with the buoy sensors, we make a linear interpolation on the potential temperature. Then we choose a first criterion ΔT_1 large enough to overcome the low accuracy of the buoy sensors. From November 2009 to July 2012 we chose $\Delta T_1 = 0.1$°C and a reference level at 10m. Since there was no instrument below the LION surface buoy before November 2009, we can use only the sea surface temperature sensor at 1m depth for the winter 2007-2008 and 2008-2009. Due to the low accuracy of this sensor, we fix $\Delta T_1 = 0.6$°C for calculations going from September 2007 to November 2009. A Mixed Layer Depth (MLD) is then calculated for the first 300m of the upper water column.

The second criterion is fixed to define a more precise MLD on our mooring data. We define $\Delta T_2 = 0.01$°C with a reference level at 310m. If the mixed layer calculated with the ΔT_1

criterion goes deeper than 300m depth then we use the second criterion ΔT_2 to define the MLD, otherwise we keep the MLD calculated with the ΔT_1 criterion. We chose to not use the head of the mooring line (170m) as the reference level, since strong horizontal barotropic currents during the restratification phase (up to 40 cm s^{-1}) caused the mooring to tow by more than 100m on numerous occasions (at the extreme by 700m).

4.3.2 Eddy-detection from mooring data

The significant current variability in this area of peculiar dynamic motivated us to apply an eddy-detection method on our horizontal current time series. Lilly and Rhines [2002] showed that the presence of an eddy event moving past a mooring produces a hodograph with peculiar shapes. D-shaped curves, closed circles, or straight lines, all result from a closed vortex's turning velocities.

As in Lilly et al. [2003], we used a wavelet analysis on our horizontal current time series. One of the advantage of this analysis compared to traditional Fourier analysis is that the analysis is performed on many temporal scales which enables us to separate eddy events from the background variability. Furthermore, the complex wavelet transform, applied on complex current time series $U + iV$, takes into account the two-dimensionality of the eddy currents that can not be done with the Fourier transform. Following the recommendations of Lilly and Olhede [2012], we choose a wavelet amongst the generalized Morse wavelets, characterized by two parameters γ and β, where γ determines the lowest-order departure of the wavelet from a Gaussian form, and β determines the Fourier-domain bandwidth. The most symmetric, most nearly Gaussian, and generally most time-frequency concentrated wavelet of this family occurs for $\gamma = 3$. The choice of the β parameter is made following Lilly et al. [2003]. Choosing $\beta = 3$ yields to wavelet of which the real (imaginary) part of the wavelet is roughly similar to the velocity component of an eddy-like event parallel (normal) to the advection flow. The centers and durations of eddy-like events are identified through the location of local maxima on the wavelet transform "topography" (detailed in section 4.7).

Even if the wavelet-based detector presented here is not fully objective, it allows a precise definition of what is not an eddy, permitting a final subjective decision to be based on a relatively small set of events. However the interpretation of currents from a single point is difficult, and a positive diagnosis of an advected eddy requires an assessment of it vertical θ-S and current structure. Events are examined in details and "apparent eddies" are labeled by examining the currents and water mass structures. To judge an event as an eddy, it must have a velocity hodograph that is qualitatively similar to those generated by simple models of isolated or mutually advecting eddies (details in Lilly and Rhines [2002]). Furthermore, a well-defined θ-S core is necessary in order to confidently label an event as an eddy.

However the form of actual physical eddies may be distorted during its recording by the mooring. An eddy will yield a recognizable velocity structure in a mooring time series only if the advecting flow varies relatively slowly over the eddy duration. So the analysis present here is expected to reject some "true eddies" (due to highly variable currents for example) but to

accept very few non-eddies.

Following Lilly and Rhines [2002], refined values for apparent eddy's center t_0 and half duration ΔT are calculated, maximizing the relation :

$$\tilde{V}_{n_0} = |\xi(t_0 - \Delta T) - \xi(t_0 + \Delta T)| \tag{Eq. 4–1}$$

where ξ is the complex velocity $U + iV$. For a constant background flow advecting an azimuthally symmetric eddy, $\tilde{V}_{n_0}$ corresponds to the velocity component perpendicular to the advecting flow. A more generalized measure of the eddy velocity can be carried out by substracting an estimate of the advecting flow:

$$\tilde{V}_{max} = \frac{1}{2}\left|\xi(t_0 - \Delta T) - \tilde{U}_a e^{i\tilde{\Theta}_a}\right| - \frac{1}{2}\left|\xi(t_0 + \Delta T) - \tilde{U}_a e^{i\tilde{\Theta}_a}\right| \tag{Eq. 4–2}$$

where the advection flow $\tilde{U}_a e^{i\tilde{\Theta}_a}$ is estimated by low-passing the velocity time series $\xi = U + iV$ at the eddy center t_0. The filter is a Hamming window whose width is four times the width of the eddy core. In equation Eq. 4–2, V_{max} corresponds to the mean of the 2 maxima of the eddy velocity when the eddy core R_{max} crosses the mooring (at $t_0 - \Delta T$ and $t_0 + \Delta T$).

Since the eddies will be generally sliced off-center, the apparent eddy size as observed from the mooring $X = U_a \Delta T$ will tend to be smaller than the actual radius R_{max}. As in Fan et al. [2013], we use a kinematic model to estimate the eddy radius R_{max} of eddies crossing the LION mooring line. This model, known as the Rankine vortex model, assumes the eddy is a vortex in solid body rotation within a core ($r < R$) and $1/r$ decay elsewhere. The azimuthal velocity $V(r)$ can be expressed as:

$$V(r) = \begin{cases} V_{max}\dfrac{r}{R_{max}}, & r < R_{max} \\ V_{max}\dfrac{R_{max}}{r}, & r > R_{max} \end{cases} \tag{Eq. 4–3}$$

Projecting this solid body model in a rotated frame, with x the direction of the advection and y the direction perpendicular to this, we obtain the following equations:

$$\begin{cases} u_{eddy} = V_{max}\dfrac{y_0}{R_{max}} + U_a \\ v_{eddy} = -V_{max}\dfrac{X}{R_{max}} \end{cases} \tag{Eq. 4–4}$$

where $X = U(t - t_0)$, t is the time and y_0 is the offset of the eddy-center in the y-direction. We can obtain V_{max}/R_{max} (respectively y_0) with a linear (resp. constant) fit on the plot of the observed velocities v_{eddy} (resp. $u_{eddy} - U_a$) depending on X (resp. t). In this work, we will

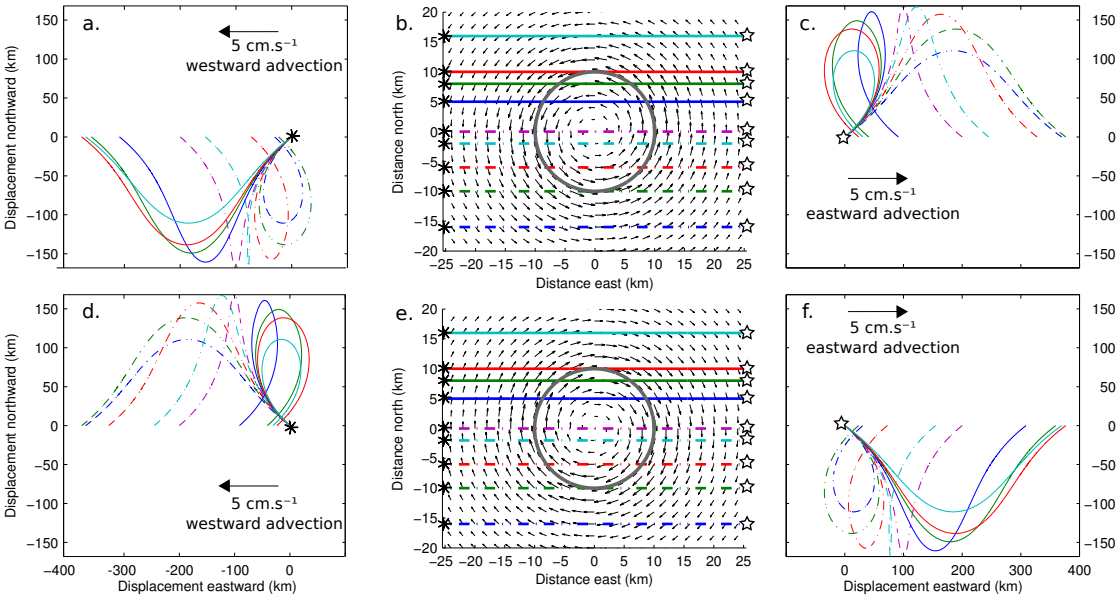

Figure 4.1: Examples of progressive vector diagrams obtained from a virtual mooring located at the west (black asterisk) or at the east (stars) of a cyclonic (b) or anticyclonic eddy (e). Four cases were considered: cyclonic eddy advected by a westward flow (a), cyclonic eddy advected by a eastward flow (c), anticyclonic eddy advected by a westward flow (d) and anticyclonic eddy advected by a eastward flow (f). In all case we considered a Rankine vortex (see eq Eq. 4–3) defined by a radius of 10km and a maximal azimuthal velocity of 15 cm s^{-1}, and the magnitude of the constant advective flow is fixed at 5 cm s^{-1}.

keep only events that have a perpendicular velocity component (v_{eddy}) matching the Rankine model, for at least one depth level ($R^2 > 0.90$).

Case studies of simple cyclonic and anticyclonic eddies crossing a mooring line

Thanks to the method of eddies census described in this section, the direction of rotation of an eddy can be determined using the advection direction of the mean flow. The magnitude and the direction of the mean flow advection can be estimated by low passing the complex velocity time serie. Once this is done, the eddy velocity can be obtained by projecting the horizontal current recorded by the mooring line onto the advection direction. The velocity component perpendicular to the advection gives us the eddy velocity.

Data from current meters installed on a mooring are Eulerian information. As the water flows past the instrument, the current is recorded at the instrument's location as a function of time. The Lagrangian method is based on observations of the trajectory of a water parcel, such as obtained from a drifting buoy or float. As the float moves with the flow, its position is recorded as a function of time. However, the Lagrangian way of following the movement of water parcels is often more illuminating than looking at records of current speed and direction, or at current components. So the progressive vector diagram was devised to simulate a La-

grangian display from Eulerian measurements. The progressive vector diagram is constructed by drawing the first current vector in a Cartesian co-ordinate grid. The second vector is than added to the first vector, its tail sitting on the head of the first vector, and so on.

On figure 4.1, 4 families of progressive vector diagrams are drawn according to the eddy rotation and the advection direction:

- a cyclonic eddy advected by a westward flow (fig. 4.1a),
- a cyclonic eddy advected by a eastward flow (fig. 4.1c),
- an anticyclonic eddy advected by a westward flow (fig. 4.1d),
- an anticyclonic eddy advected by a eastward flow (fig. 4.1f).

The progressive vector diagrams are computed from horizontal currents recorded by each "virtual" current meter (indicated by an asterisk or a star, figs. 4.1b,e). The color of the progressive vector diagrams depend of the position of the "virtual" mooring relative to the eddy center.

Whatever the direction of the advection (eastward or westward), the deviation of the progressive vector diagram perpendicular to the advection direction is always to the left for cyclonic eddies (figs. 4.1a,c) and to the right for anticyclonic eddies (figs. 4.1d,f), in the northern hemisphere. Here the figure 4.1 illustrates a "simple" case where the eddy can be easily distinguishable from the advecting flow. In reality it is more complicated, especially because advection is usually not constant in the mooring area. Thus in summer/fall, it is difficult to clearly observe an eddy because advection is very small and mostly is not constant in direction. If in summer/fall the diagram looks like a plate of spaghetti (fig: 4.2), where the direction of advection is difficult to determine, in winter/spring the progressive vector diagram is more stretched (fig: 4.2) because advection is stronger, and thus the eddies are easily distinguishable from the advection. However the higher the advection speed (compared to the eddy velocity) is, the more the progressive vector diagram will be flattened, approaching the progressive vector diagram of a constant flow.

4.4 Water Column Variability and Transients in the Deep Convection Area

The LION mooring is monitoring the water column since September 2007 and is still in place. We present in details the processes that occur during the Winter 2010 in section 4.4.1, then we extend our analysis to others winters in 4.4.2. In section 4.4.3 we analyze the evolution of the heat and salt contents of the water column. Finally, we discuss the evolution of the deep waters relative to the 5 consecutive open-ocean deep convection events that occurred between September 2007 and July 2012 in section 4.4.4 and 4.4.5.

4.4.1 The case study of the November 2009 – December 2010 period

Deep convection events can be seen as a succession of phases (MEDOC Group [1970]; Marshall and Schott [1999]) that may overlap. In winter 2010, deep convection occurred in the Gulf of Lions, this can be seen in the time series of potential temperature and salinity (figs. 4.3a and 4.3b), where the water column is completely homogenized (less than 0.01°C and 0.005‰ between all the sensors) during the month of February. At the same time, huge vertical currents were recorded (fig. 4.4c) with vertical speed exceeding 15cm.s^{-1}, comparable to measurements conducted in 1991 by Leaman and Schott [1991].

The deepening of the mixed layer

In September, the monthly mean value of Q_{net} is close to 0 W.m^{-2}. The strong heat losses begin in October and November (fig. 4.4d), corresponding to a monthly value between -150 and -200 W.m^{-2} for Q_{net}. They gradually cool the surface layers and lead to the formation of Winter Intermediate Water (WIW), characterized by a lower potential temperature and a lower salinity (S < 38.42‰). The upper sensor (at 170m) recorded potential temperature (salinity) close to 13.05°C (38.4‰) at the end of December / beginning of January (dark blue line on figs. 4.3a and 4.3b). This different water mass can be seen more clearly on a θ-S, where it has a very distinct signature (fig. 4.5b1) compared to the "classical" Atlantic Water (AW) that usually occupies this layer (fig. 4.5a1). Moreover the eddy-detection analysis (see section 4.3.2 for details) identified a large anticyclonic eddy passing through the mooring location at the same time, with a center detected the 29/12/2009, an eddy radius R_{max} = 19.1 km and a maximal

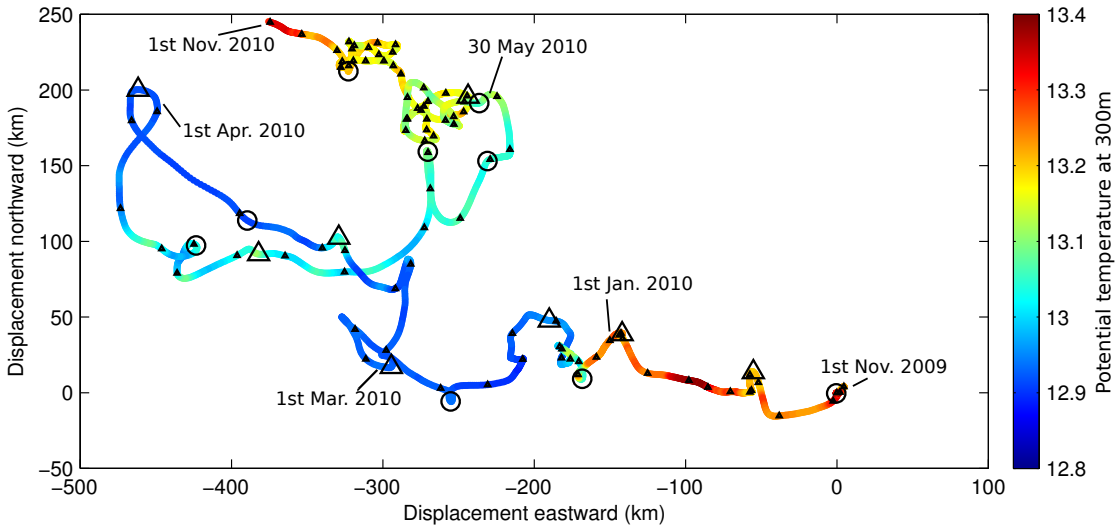

Figure 4.2: Progressive vector diagram at 1000m depth from the 1st November 2009 to the 1st November 2010, the colorbar shows the temperature measured at 300m depth, indicating the "presence" (high temperature) or "absence" (low temperature) of LIW. Small black filled triangles correspond to time markers scattered every 4 days. Big black circles (triangles) correspond to the center of cyclones (anticyclones) detected.

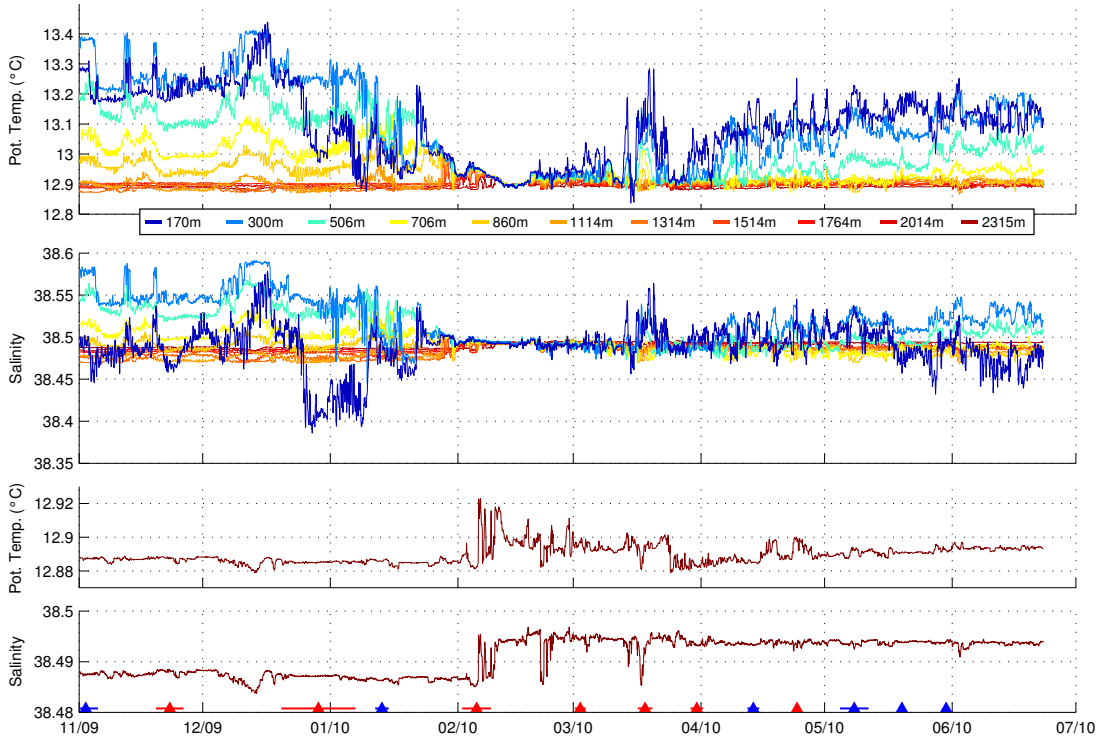

Figure 4.3: Temperature (a) and salinity (b) records at Seabird Microcat depth from 170m (dark blue) to 2330m (dark red) between November 2009 and July 2010. The near-bottom potential temperature (c) and salinity (d) are also presented with a separate vertical scale. Red and blue triangles correspond to the center of cyclones, respectively anticyclones, detected by the method presented in the part 4.3.2, the horizontal line indicating the estimated time period of the event.

azimuthal velocity $V_{max} = 4.6$ cm.s^{-1} (table 4.4).

After this period of strong cooling (the 170m depth Microcat recorded a drop of ≈0.3°C), the mixing goes deeper with vertical current detected at 250m (≈15 cm.s^{-1}) and 500m depth (≈5 cm.s^{-1}) from January 9 from January 12 (fig. 4.4c), associated to strong daily heat losses (>-800 W.m^{-2}, fig. 4.4d) . The warm and salty Levantine Intermediate Water (LIW) is therefore entrained by the vertical mixing. This results in a decrease in potential temperature and salinity at 300m and 500m depth (see blue and cyan lines on figs. 4.3a,b). At the same time, the heat and salt content of the LIW is vertically homogenized with the upper-ocean that induces a warming and an increase in salinity of the upper-ocean (dark blue line on figs. 4.3a,b). Another interesting point is the possible formation of a cyclonic eddy that could become a Submesoscale Coherent Vortice (SCV), forthwith after the end of the vertical mixing, January 13 (table 4.4). The eddy is characterized by a core centered at 500m depth, an eddy radius $R_{max} = 1.9$ km and maximal velocity $V_{max} = 7.0$ cm.s^{-1}.

From January 15 to January 23, the weakness of atmospheric forcing makes stop the vertical mixing and the increase of potential density in the upper-ocean layer (fig. 4.4a). Between January 23 and January 26, there is a sharp increase in potential temperature (0.2°C) and salinity (0.1‰) at 170m depth, indicating the entrainment of the LIW in the mixed layer. At

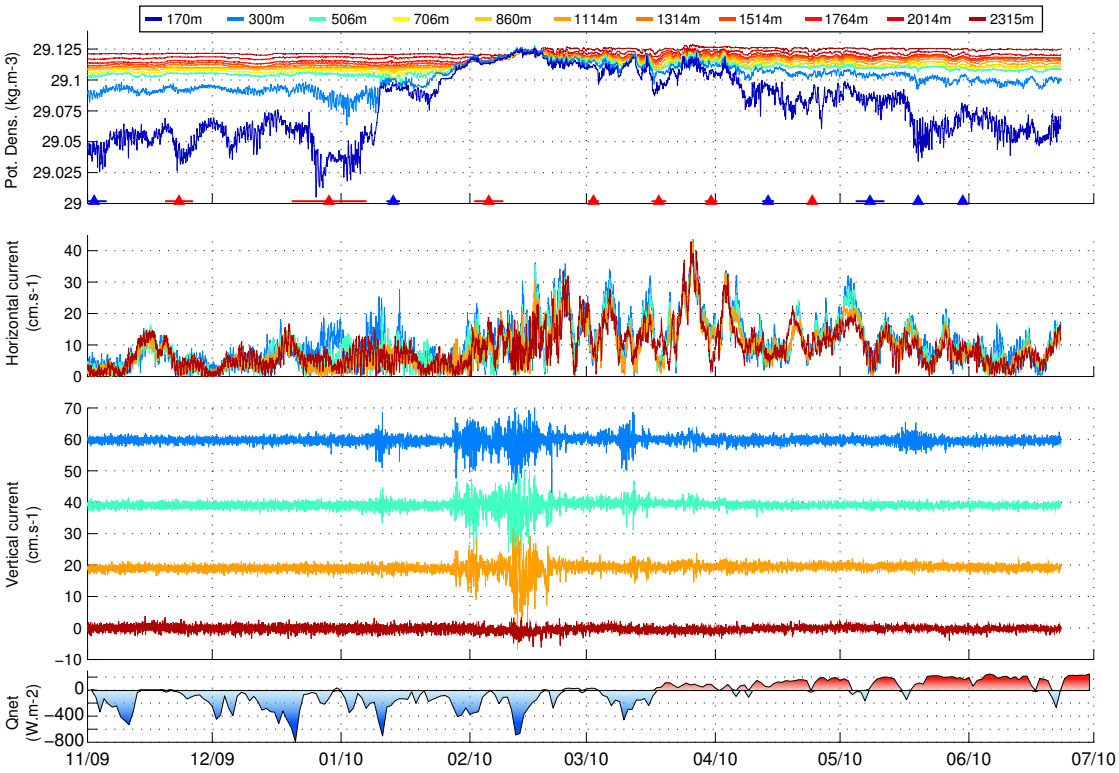

Figure 4.4: Potential density (a) records at Seabird Microcat depth from 170m (dark blue) to 2330m (dark red) between November 2009 and July 2010, with horizontal (b) and vertical (c) currents recorded by the 250m (blue), 500m (green), 1000m (orange) and 2330m (dark red) Aquadopp, and daily net heat flux Q_{net} (d) estimated by Era-Interim at the mooring location. Red and blue triangles on (a) correspond to the center of cyclones, respectively anticyclones, detected by the method presented in the part 4.3.2, the horizontal line indicating the estimated time period of the event.

that time the MLD reaches 800m (fig. 4.6). This increase in the MLD is not linked to an increase of atmospheric heat loss or to an increase in the vertical velocity. This would indicate to us that this homogeneous water column was advected into the area rather than formed by a vertical mixing.

From January 27 to January 29, the mixed layer deepens for more than 500m. This event is associated with an increase in surface heat losses and vertical velocities (more than 5 cm.s^{-1} at 250, 500 and 1000m depth). The vertical mixing increases until the MLD reaches 2000m the February 1 (fig. 4.6)). Vertical mixing stops in February 3, at the same time that atmospheric heat losses. However in February 5, the dramatic increase in potential temperature (0.04°) and salinity (0.01‰) recorded at 2300m depth (figs. 4.3c,d) is characteristic of the deep salty and warm mixed layer, indicating that deep convection seems to have already reached the bottom. When the mixed layer reaches the deep layer, the colder and fresher old deep water undergoes a heat and salt input. At that time the violent mixing did not seem to reach bottom as shown by the current meter at 1000m depth indicating a relative quiet period without particular signal on the vertical velocity record. Deep convection certainly reached the bottom first nearby and then the newly-formed deep waters are advected at the mooring location by the anticyclonic

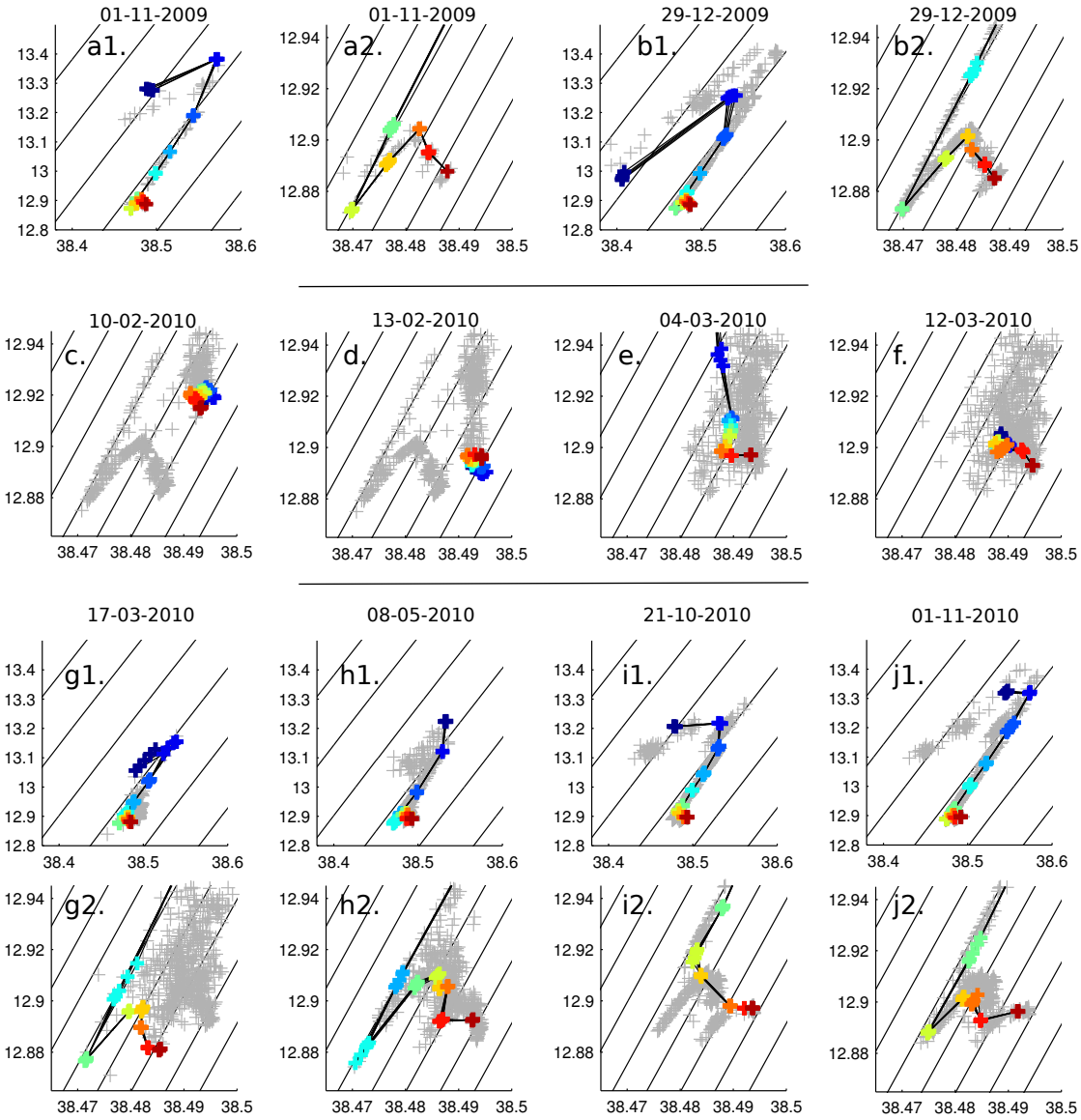

Figure 4.5: θ-S plots of particular stages in the evolution of the water column from December 2009 to November 2010. The top, middle and bottom panel correspond show periods corresponding to before, during and after the vertical mixing. In the top and bottom panel, two different zooms are considered. The nominal depth of the different Microcat is indicated by the color marks (from 170m to 2300m), while gray marks correspond to the data of the past month. The slanting black lines are σ_θ contours.

eddy detected (R_{max} = 5.7 km and V_{max} = 11.2 cm.s^{-1}).

Deep convection down to the bottom

The intensification of atmospheric forcing on February 10 led to very strong heat losses (daily values exceed -600W.m−2) and to the resuming of the vertical mixing, with the strongest vertical currents recorded during this winter at 250m, 500m and 1000m depth (figs. 4.4c,d).

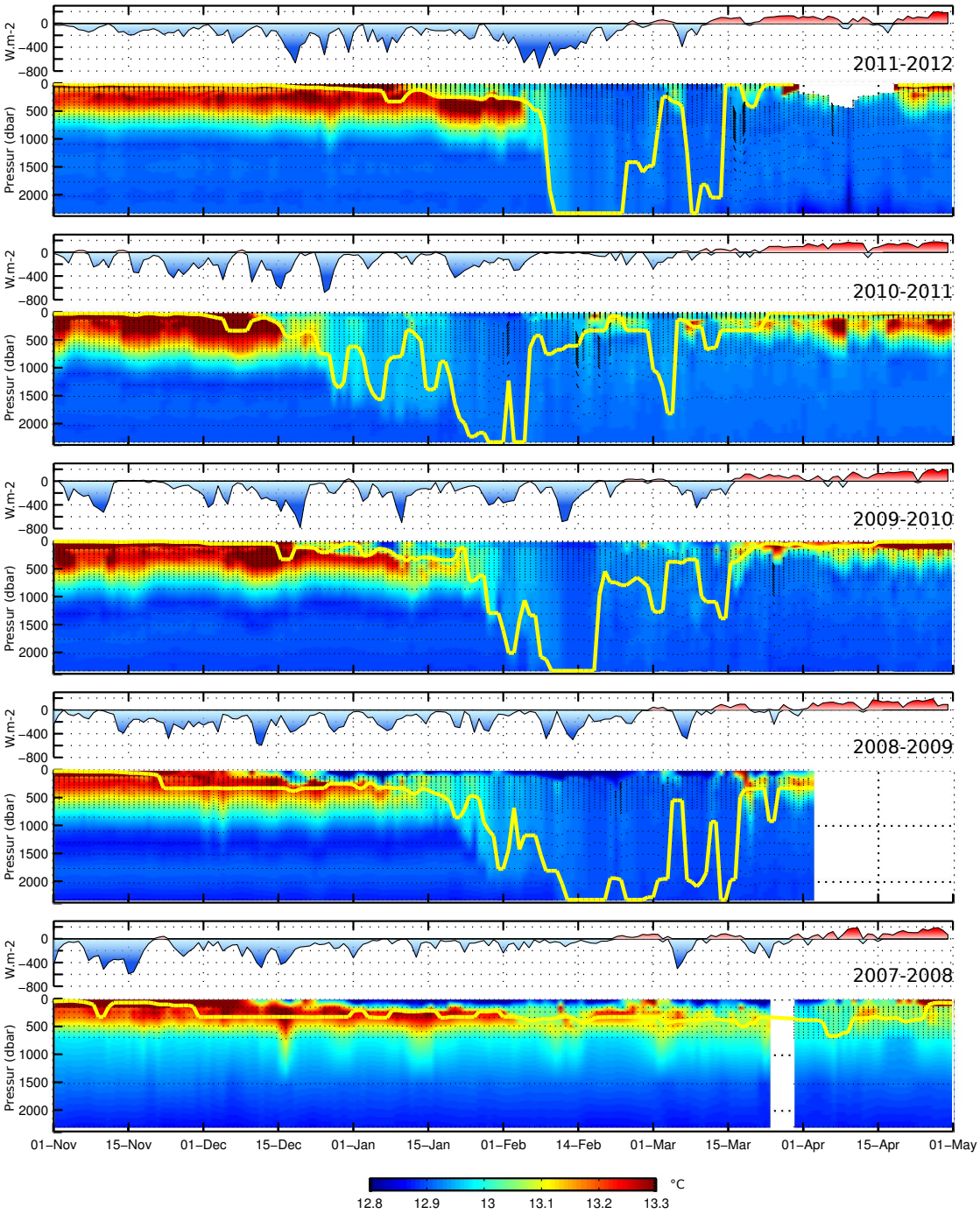

Figure 4.6: 5 years of net atmospheric heat flux from Era-Interim reanalysis and potential temperature with mixed layer depth, contoured over instruments of the deep LION mooring and the LION surface buoy, from December to May. Black dotted lines show the pressure at the instruments depth. Yellow thick line indicates the mixed layer depth estimated (see the text for a description of criterion chosen)

Vertical speed can sporadically exceed +10cm.s^{-1} and -15cm.s^{-1}.

From February 10 to February 13, potential temperature of the whole water column de-

creased of more than 0.02° (figs. 4.5c,d), related to the strong heat losses and the fact that the deepening of the mixed layer is limited by the bottom. At the same time, salinity did not present any detectable change. The winter buoyancy fluxes are largely dominated by the heat fluxes (Grignon et al. [2010]), so the salinity of the newly-formed deep water is mostly set by the salt content of the water column before convection, while its potential temperature results from a combination of the initial heat content and the surface heat fluxes.

The February 16, one day from the end of the violent vertical mixing phase, horizontal speed become stronger (30-38 cm.s^{-1} until 1000m, 20cm.s^{-1} at 2300m, see 4.4b). This current intensification caused a 150m deepening of the mooring's head. The deepening of the mooring's head occurred several times from February to April. Each time, it was associated to strong horizontal currents (more than 30cm.s^{-1} for the 250m, 500m and 1000m current meters).

Second event of deep vertical mixing

From February 18 to March 8, total atmospheric heat flux is close to zero, even positive, and vertical mixing stopped. High horizontal currents start to advect more stratified water in the mooring area (figs. 4.4a and 4.5e). The last strong winter cooling event occurred from March 9 to March 12, associated to an increase in vertical currents until 1000m depth. Based on θ-S diagram, the homogeneous water column reached 1750m depth,4.5f), also seen on daily MLD time series (fig. 4.6).

End of the deep convection, horizontal homogenization

After the last event of vertical mixing, the water column progressively restratified. The surface heat gain and the surface advection of light water (Leaman and Schott [1991]; Schott et al. [1996]; Herrmann et al. [2008]), increase the vertical gradient of potential temperature, salinity and density inside the water column. Using the eddy-detection methods, several eddies which are involved in the input of surrounding waters in the area of deep water formation, were identified the March 17, March 30, April 13, April 24 and May 8 (table 4.4). The vertical distribution of water masses for these cyclonic or anticyclonic eddies present similar characteristics.

First, they are characterized by a salty and warm water mass in subsurface (between 150m and 400/500m depth), which indicates the presence of LIW in that region. The less pronounced θ/S characteristics and low stratification of this sub-surface water mass (compared to the period before the deep convection, figs. 4.5g1,h1) might be related to the winter mixing that occurred in January. At that time the mixing homogenize the first 700m of the water column. Second, lower potential temperature and salinity are found in the 750/1200m layer (figs. 4.5g2,h2), corresponding to the "old" WMDW θ/S characteristics.

Then the last 1000m of the water column is mainly composed of newly-formed deep water, which are saltier and denser than the "old" deep water. As the potential temperature of the newly-formed deep water is strongly related to the intensity of the winter atmospheric forcing, the warming of the deep water can be reduced by strong heat losses occurring during the intense vertical mixing phase, once the mixed layer has reached the bottom. For example,

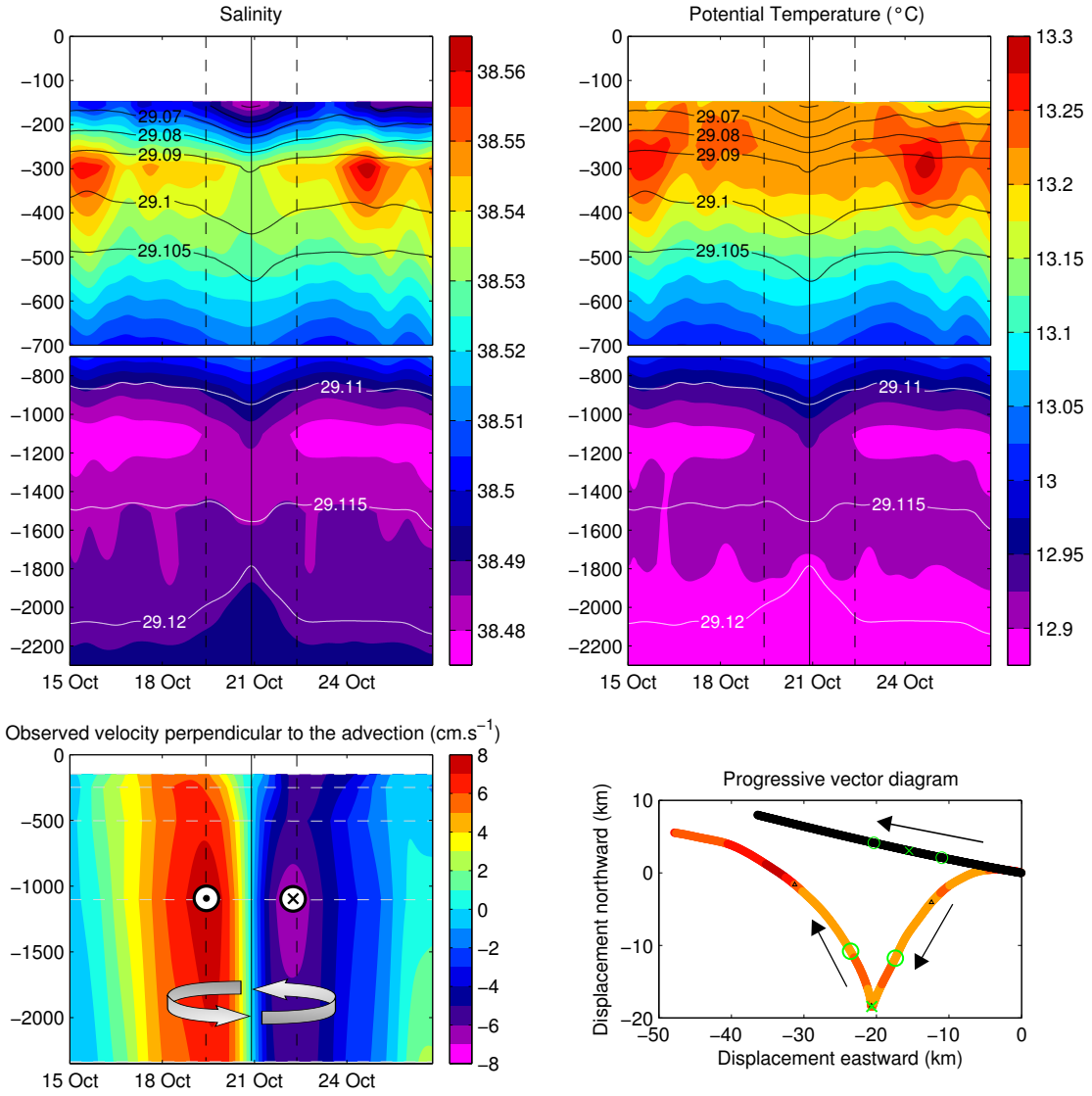

Figure 4.7: Salinity, potential temperature, eddy currents, and progressive vector diagram of the eddy crossing the mooring line the 21 October 2010. Black and white horizontal thin lines on salinity and potential temperature graphs, correspond to isopycnals. Vertical black lines correspond to the eddy center and black dotted vertical lines correspond to the eddy rim. On the progressive vector diagram, the color line corresponds to the horizontal current recorded by the 1000m current meter with a colormap corresponding to the potential temperature recorded by the 300m microcat instrument, while the black line corresponds to the estimated advection. Green cross and circles indicate respectively the center and the rim of the eddy. The projection of the horizontal velocity recorded by the current meter onto the advection direction gives us the observed velocity perpendicular to the advection, corresponding to the eddy velocity (bottom left panel).

during winter 2010 the potential temperature at 2300m depth increased by 0.03°C once the mixed layer has reached the bottom but the consecutive ten days of strong heat loss have made decrease the mixed layer potential temperature by 0.02°C. While at the same time the salinity

has varied only slightly compared to the potential temperature, indicating that evaporation does not play a significant role in setting the salinity on the new deep water, at least during the 9-12 days period of intense vertical mixing corresponding to the period when the deep convection has reached the bottom.

Concerning the 5 eddy-events bringing relatively salty and warm intermediate water, 4 of these events are associated with newly-formed deep water (higher salinity than before the OODC [fig. 4.3d] and changes in the deep stratification [fig. 4.5h2] that will stay until next winter [fig. 4.5j2]), while the March 18 eddy presents a potential temperature and salinity at 2300m depth (figs. 4.3c,d) and a deep stratification (figs. 4.5a2,g2) corresponding to the ones before the OODC.

Occasionally, cyclonic eddies with a deep core can also cross the mooring line several months after the deep convection, like the one on October 21, 2010 (fig. 4.7). This eddy is characterized by a current strengthening detected at 1000m depth, an eddy radius R_{max} = 4.8 km and a maximal azimuthal velocity of V_{max} = 5.5 cm.s^{-1}. The first 1000m of the water column is characterized by a sinking of the isopycnals, like surface anticyclonic eddy. The big difference is in the deeper part of the water column, between 1600 and 2300m, where there is a doming of the isopycnals. The flat isopycnals at 1700m indicate the location of the eddy core, what we can not see using the data from current meters, because there are no measurements at this depth (the current meters are only at 1000m and 2300m depths).

The absence of the usual deep stratification (fig. 4.5i2) and the θ/S characteristics at 1750m, 2000m and 2300m depth, makes us infer that this eddy might have been formed during the past deep convection event. The lifetime for this cyclonic eddy is at least estimated at 5 months. These deep θ/S characteristics are very close to the one recorded the 4 March 2010 (fig. 4.5e), just before the second vertical mixing event and the huge horizontal currents (> 40cm.s^{-1}) appearing to homogenize the mixed patch with the surrounding water masses. Instabilities of the rim current (bordering the DWF zone) may be the cause of the generation of this kind of eddy.

The stratification of the water column will continue to increase until the surface buoyancy flux become negative (usually in September), then the buoyancy losses will “erode” progressively the surface stratification. If the forcing is intense enough and if the water column is not too stratified, the vertical mixing can go deep (below the LIW). This scenario occurred every winter since the winter 2007-2008. If the vertical mixing seems to stop at 700m depth in winter 2007-2008, in winters 2008-2009, 2009-2010, 2010-2011 and 2011-2012 it reached the bottom (fig. 4.6).

4.4.2 Similarities and Differences between five Deep Convection Events

Characteristics of the different winters of OODC are summarized in the table 4.3. The chronology of the different events is not exactly the same, mainly due to the interannual variability of the heat losses and the stability of the water column (discussed in section 4.8.2). For example

	2008	2009	2010	2011	2012
Mixed layer deepens below 150m	17/12/07	15/12/08	17/12/09	15/12/10	08/01/12
WIW detected (S<38.42)	21/12/07	30/12/08	09/01/10	16/12/10	03/02/12
LIW mixed	02/04/08	08/01/09	23/01/10	19/12/10	07/02/12
Bottom reached	no (700m)	12/02/09	10/02/10	27/01/11	10/02/12
Bottom pot. temperature increase	x	0.040°	0.030°	0.022°	0.042°
Bottom salinity increase	x	0.009	0.007	0.006	0.012
End vertical mixing (until 1000m)	x	26/02/09	20/02/10	05/02/11	23/02/12
Temperature decrease of the MLD at the end of the vertical mixing	x	0.024°	0.019°	0.012°	0.032°
Bottom potential density increase at the end of the mixing ($kg.m^{-3}$)	x	0.0044	0.0062	0.0030	0.0090
Number of events of deepening of mooring's head > 100m	0	5	9	10	10
Max. deepening of mooring head	0	450m	700m	550m	600m
Second vertical mixing event					
Time period	x	6/03/09-08/03/09	9/03/10-12/03/10	01/03/11-04/03/11	07/03/12-11/03/12
Max. depth on W	x	>1000m	>1000m	>500m <1000m	>1000m
Max. depth on MLD	x	2000m	1500m	1700m	2300m
End of the vertical mixing / Onset of restratification	04/04/08	09/03/09	13/03/10	05/03/11	11/03/12
Area of low surface chlorophyll (<0.12$mg.m^{-3}$) in km^2	113	9446	10276	14020	13092
Area of low surface chlorophyll (<0.20$mg.m^{-3}$) in km^2	2649	21752	25331	23523	27624

Table 4.3: Characteristics of deep convection events from LION data

in 2011 the vertical mixing penetrated below the LIW, one month earlier than in 2009, 2010 or 2012. The December 26, 2010, the MLD reaches 1200m (fig. 4.6), homogenizing the water column (decrease in potential temperature and salinity on figs. 4.8a,b and increase in potential density on fig. 4.9a on the 170m-, 300m- and 700m-Microcat), while significant vertical velocity superior at $15cm.s^{-1}$ were recorded at 150, 250 and 500m depth, fig. 4.9c.

During winter 2011-2012, the mixed layer quickly reaches the bottom, it takes approximatively 1 month from the mixing to go from 150m depth to the bottom (table 4.3, fig. 4.6), while it takes between 1.5 or 2 months for the 2009, 2010 or 2011 winter. For these winters it takes between 2.5 weeks and 1 month for the mixed layer to go from the LIW to the bottom, while in 2012 it takes only 5 days. According to Visbeck et al. [1996], the maximum depth of the convection is reached when lateral buoyancy flux offsets the buoyancy loss at the surface. The strong heat (buoyancy) losses that occurred during 4 months in 2012, might partly explain the fast deepening of the MLD.

Some common features point out from the analysis of the four last events of deep convection observed between 2009 and 2012. The time for the mixed layer deepening is comprised between 1 and 2 months. Once the mixed layer has reached the bottom, the violent vertical mixing phase of the whole water column is in the range of 9-12 days, leading to a potential

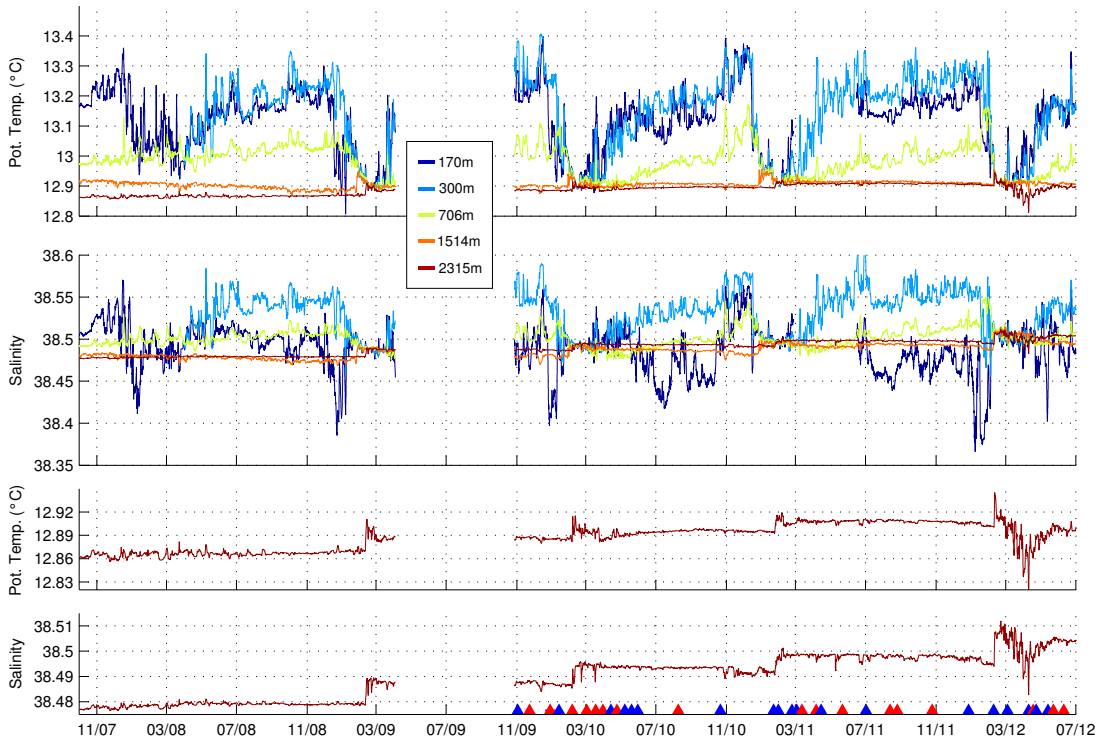

Figure 4.8: Daily potential temperature (a) and salinity (b) records at Seabird Microcat depth from 170m (dark blue) to 2330m (dark red) between October 2007 and July 2012. The daily near-bottom potential temperature (c) and salinity (d) are also presented with a separate vertical scale. Red and blue triangles correspond to the center of cyclones, respectively anticyclones, detected by the method presented in the part 4.3.2.

temperature decrease of the whole water column between 0.015° and 0.03°. Since there are no significant changes in salinity at that time, we suggest that evaporation during this 10-days period, did not play a role in setting the salinity of the newly-formed deep water, unlike the influence of heat losses on potential temperature.

Winters from 2009 to 2012 present all a second vertical mixing period that generally occurs in March after the main event of deep ocean convection. This short event (2-4 days) happens when the restratification begins. The water column is weakly stratified at that time and a 3-6 days period of heat losses (like winter storm) can easily destabilize the water column, leading to vertical mixing.

4.4.3 Evolution of Heat and Salt Contents of Water Column

One of the interest of the LION mooring line is heat or salt budget calculation for specific water masses. To take into account the upper ocean layer (0-150m), we merged the MF-LION surface buoy to the deep LION mooring line, this give us 5 to 17 additional potential temperature levels in the first 150m since 2009 and 1 additional salinity level at 2m depth since 2011.

Even if the vertical resolution of the mooring line has a good coverage of the water column,

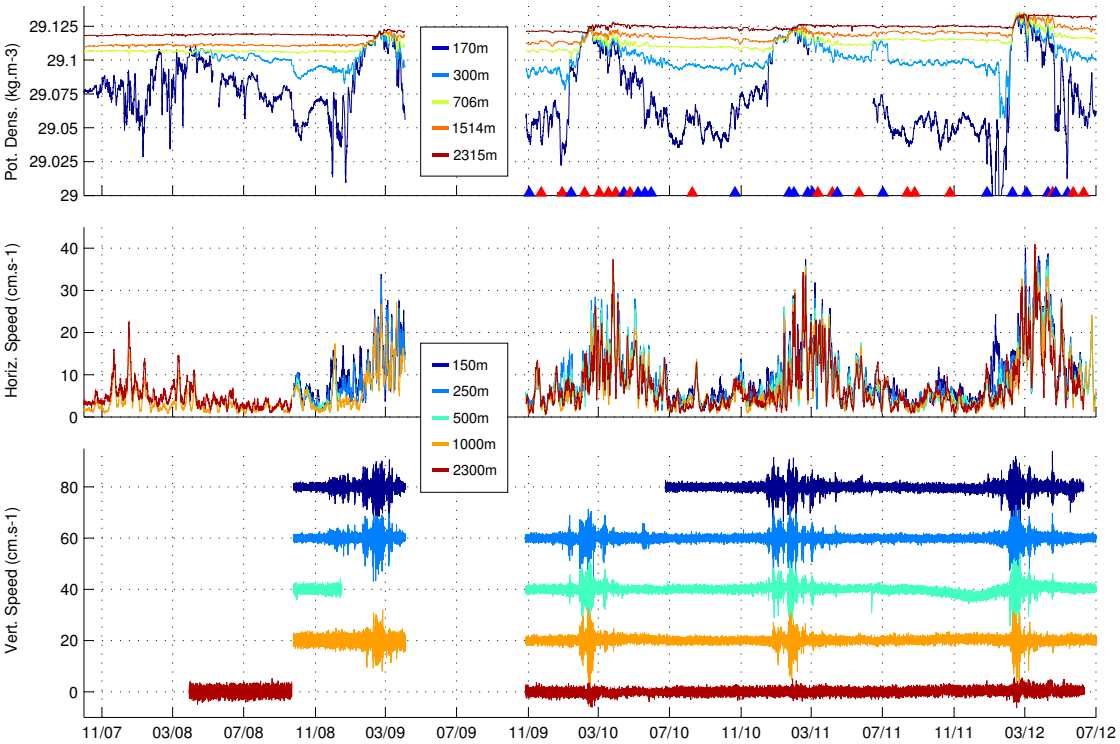

Figure 4.9: Daily potential density (a) records at Seabird Microcat depth from 170m (dark blue) to 2330m (dark red) between October 2007 and July 2012, with daily horizontal (b) and bi-hourly vertical (c) currents recorded by the 250m, 500m, 1000m and 2330m Aquadopp. Red and blue triangles on (a) correspond to the center of cyclones, respectively anticyclones, detected by the method presented in the part 4.3.2.

especially since 2009 with 20 potential temperature levels and 10 salinity levels, there is still sometimes large gaps between the instruments. To make budget calculation, we make a linear interpolation of potential temperature and salinity over the depth, and we obtain 1m resolution profiles from 2m to 2300m every 30 minutes.

In order to quantify the error in heat or salt budget in specific layer due to this linear interpolation, we used the 1m-binned CTD and glider profiles made close to the mooring (in a 30km radius circle). We choose a distance of 30km, following (Houpert [2010]), where the spatial covariance function was modeled using numerous temperature and salinity profiles carried out close to the mooring location. Although the covariance decreases quickly with the distance (77% of the variance at 4km, 40% at 10km), at 30 km the covariance is still equal to 30 % of the variance. This indicates that profiles made 30km from the mooring location are not completely uncorrelated with measurements from the mooring line.

We estimate the error due to the vertical interpolation for each different mooring and buoy configurations. By taking into account problems faced by the different instruments (unexpected shutdown due to low battery, air bubbles in the near-surface sensors), we get 31 different configurations of the merged mooring-buoy line between September 2007 and July 2012 for the daily data and 160 different configurations when we look for the bi-hourly data. The greater number of configurations for 30 minutes data is explained by the fact that

the buoy surface temperature sensor can be out of the water several times a day when the sea is too rough. The error is estimated for each layer, using the CTD and gliders profiles. We calculate it as the difference between the mean (potential temperature, salinity or density) of the 1m-binned original profile and the mean calculated with the same profile undersampled and linearly interpolated.

Figures 4.10, 4.11 and 4.12 show the mean potential temperature, salinity and potential density for the main water masses of the WMED: the modified Atlantic Water (0-200m), the Levantine Intermediate Water (200-600m) and the deep water (600-2300m). A distinction is made for the deep waters comprised between 600 and 1500m and between 1500 and 2300m, as θ-S diagrams show since 2005 different deep waters for these levels (Lopez-Jurado et al. [2005]; Salat et al. [2006]; Schroeder et al. [2006], figure 4.13).

The daily mean of the mooring line data are represented by the dark line, while data from profiles (CTD stations, gliders) are indicated by the red dots. We also compute errors due to the discrete vertical levels of the mooring instruments (cyan lines). As explain this section, we use hydrological profiles to calculate errors due to the linear interpolation from the discrete levels of the mooring line and surface buoy LION. For each new configuration of the mooring line and surface buoy, we select the available profiles comprised in a 2-months period around the new configuration date at which the error is estimated. For each profile, we calculate the error, associated to the vertical discretization, in the estimation of the mean potential temperature, salinity or potential density for each layer. Then we estimate the error on the time series as the mean of the errors calculated on all these hydrological profiles plus or minus three standard deviations.

We can clearly distinguish a seasonal cycle in the mean potential temperature of the surface layer (0-200m) varying from 13±0.2 °C in winter to 17 ±2 °C in summer. The higher error during summertime is mainly due to the undersampling of the strong surface gradient in potential temperature associated to the summer thermocline, while in winter the surface layer is homogeneous in potential temperature and salinity so there are smaller errors associated to the linear interpolation at that time.

Since conductivity sensor was installed on the surface buoy LION in September 2011, no salinity and density data are available for the September 2007 - September 2011 period. In addition, the low level of sampling (2 levels in the first 200m) since September leads to a significant error in the estimation of the mean salinity and density for the surface water.

If we can clearly distinguish a seasonal cycle in the surface water with a potential temperature maximum in summer, the variability of the heat and salt content of the intermediate layer (200-600m) at the location of the LION mooring line is mainly driven by the deep convection events, with a ≈0.3°C decrease in potential temperature (fig. 4.10) and ≈0.05‰ decrease in salinity (4.11) when deep convection reaches the bottom. Again the low number of conductivity sensors (see table 4.2) can explain why the error on the mean salinity is such important compared to the error in the mean potential temperature estimate.

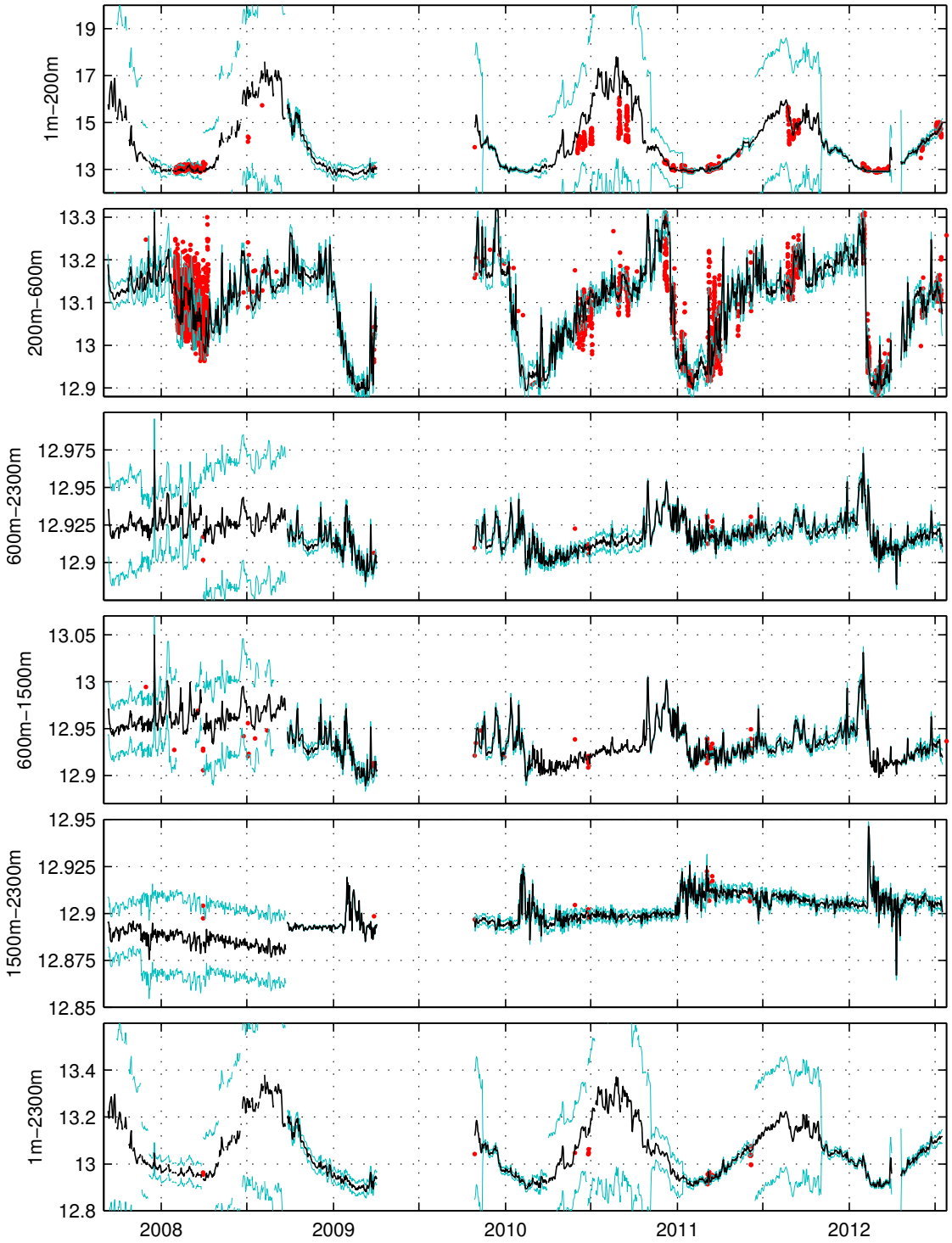

Figure 4.10: Temporal evolution of the mean potential temperature (°C) of the water column and specific layers at the LION mooring site. The associated error due to the vertical integration is represented by the blue line. The red dots correspond to mean potential temperature calculated on vertical profiles close to the mooring (<40km).

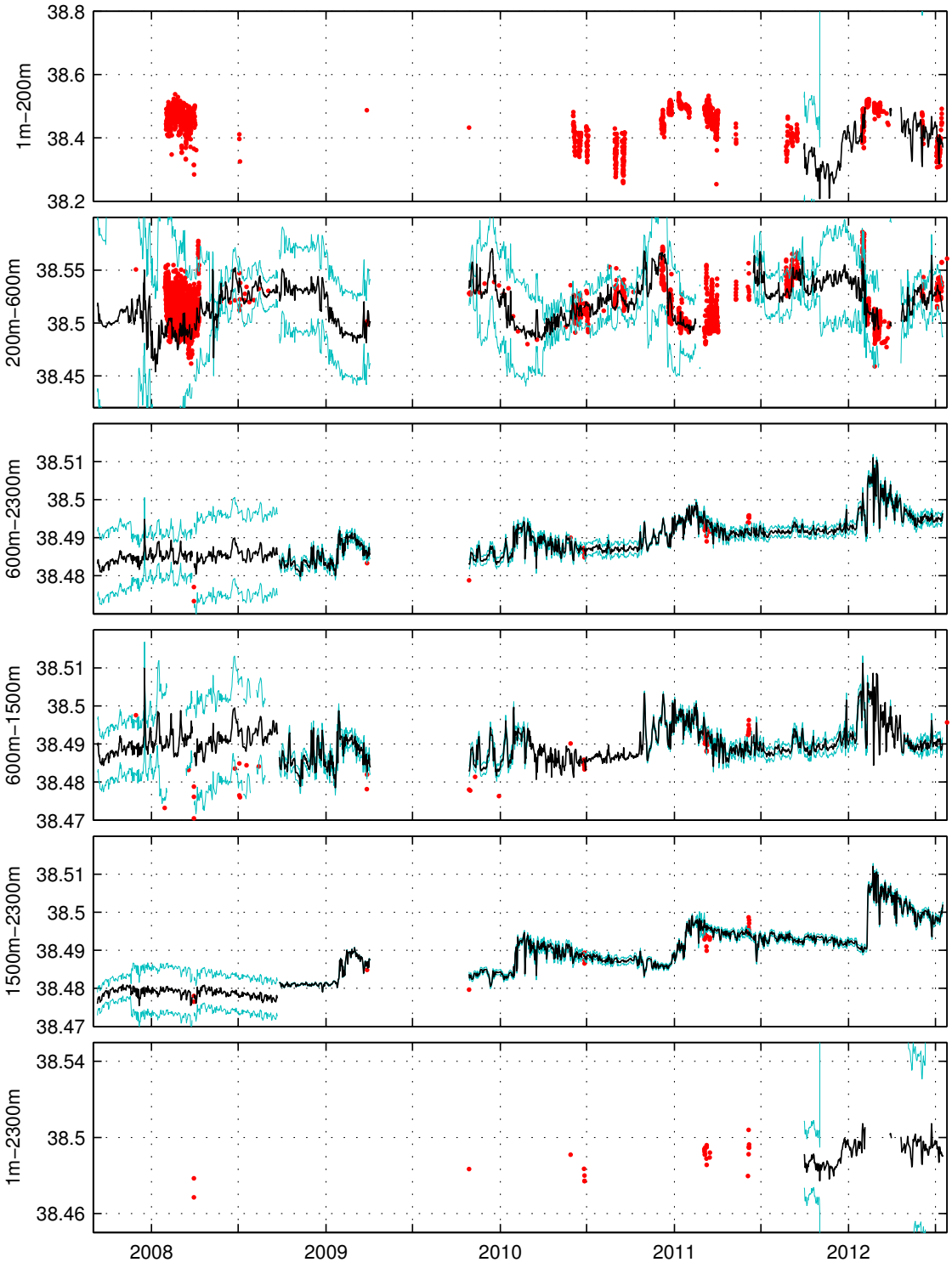

Figure 4.11: Same as figure 4.10 except for mean salinity.

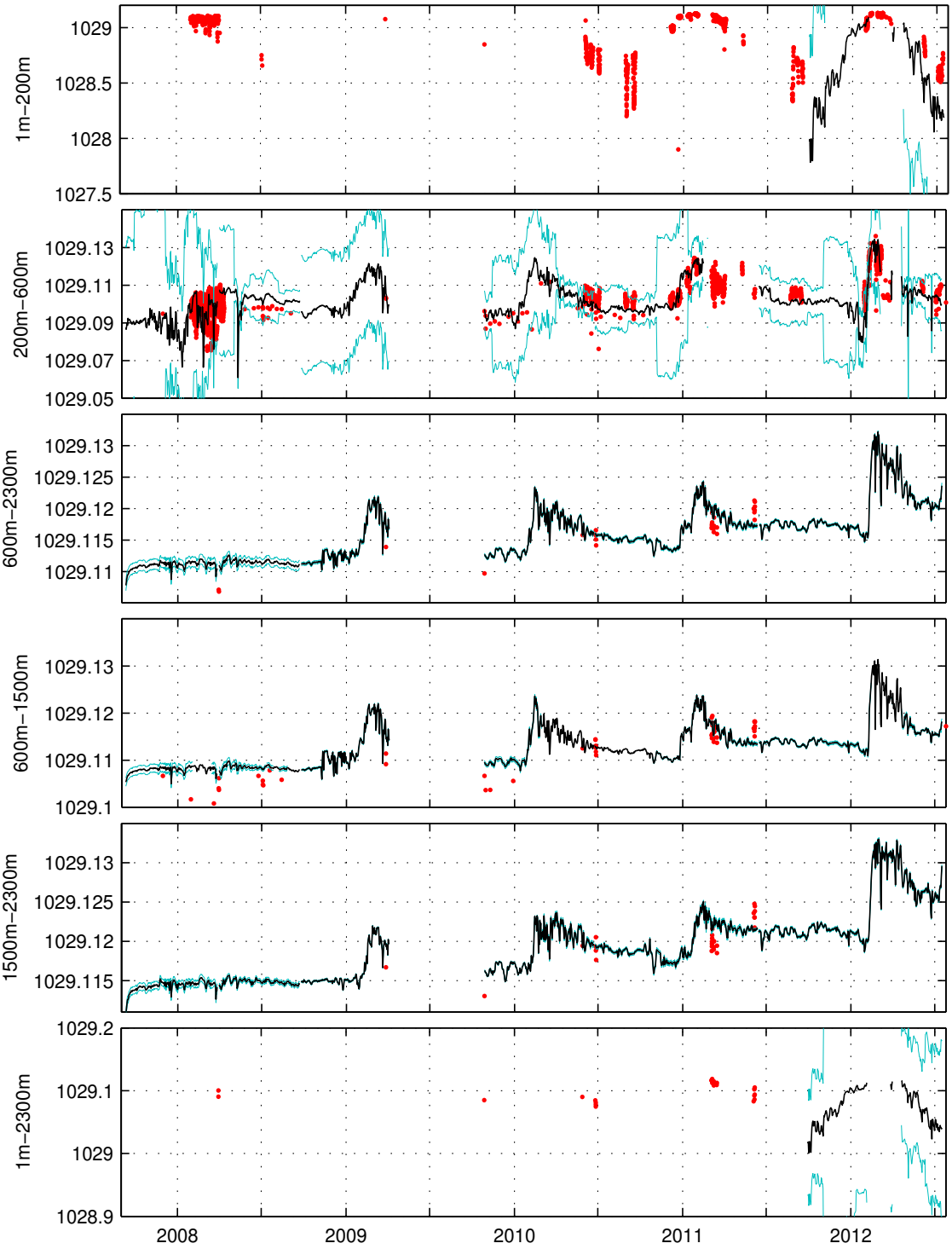

Figure 4.12: Same as figure 4.10 except for mean potential density (kg m^{-3}).

No clear signal of warming of the 200-600m layer appears for the 2007-2012 period, even if the potential temperature at the beginning of winter seems to be higher (+0.1°C) in 2009/2010, 2010/11, 2011/2012 than in 2007/08 and 2008/09. This might indicate a “slowdown“ of the accumulation of LIW in the mooring location and/or an increase of the temperature and salinity of the LIW for the 2009-2012 period.

Since error on potential density is not negligible, the restratification time of this layer after a deep convection event may be expressed as the time needed by this layer to recover 50% of its heat content lost during deep convection. Using the mean potential temperature for the 200-600m layer for year 2010, 2011 and 2012, we determine the time for this layer to compensate a half of the heat lost during the deep convection event, as being 2.5 months (in 2011 and 2012) and 4.3 months (in 2010). If the ”restratification time” inferred from potential temperature did not seem to be the same for all years, it did not seem to be related to the intensity of deep convection (see the end of the section 4.5 for discussion about the intensity of a deep convection event) because winter 2011 is the event that seems to have produced the “less” deep waters, and winter 2012, the event that seems to have produced the more, but they have both the same restratification time.

If the warming of the deep layer (600-2300m) is not obvious for the 2008-2012 period (fig. 4.10), it seems to become saltier (fig. 4.11), especially since October 2008 when the error linked to the vertical resolution was considerably reduced due to additional instruments. Salinity for the 600m-2300m layer increase by 0.015‰ for the October 2008 - July 2012 period (≈0.01‰ for the 600-1500m layer and ≈0.02‰ for the 1500-2300m layer).

The spreading of the newly-formed deep water may be seen on the figure 4.12. At the end of the intense vertical mixing, the potential density reaches a local maximum. Once the atmospheric forcing has stopped, the potential density begins to decrease, indicating the spreading of the newly-formed deep water.

Looking at the 600-2300m layer, it takes approximatively between 1.5 months (in 2011) and 3 months (in 2010) for the deep layer to dissipate 50% of the potential density increase due to the formation of new deep water. 75% of this potential density increase is dissipated after a period going from 3 (in 2011) to 6 (in 2010) months, indicating the spreading and the mixing of the newly-formed deep water with the ambient deep water.

The long restratification and spreading time that can be observed after each winter of deep convection indicate that the restratification/spreading phase did not seem finished when the deep convection event begins during the following winter. This highlights again the overlapping of the 3 “phases” of deep convection, and implies an essential role of the modeling of the eddies throughout the year if one wants correctly simulate the phenomenon of deep water formation.

4.4.4 Seasonal Variability and Transients in the Bottom Layer

The stepwise increases in bottom water characteristics occurring for four consecutive years (2009-2012) are marked by positive jumps in θ and S (figs. 4.8c,d, table 4.3). These changes in the characteristics of the bottom water are related to the deep convection which reached the bottom in February.

If salinity remains relatively constant after each jump, potential temperature may undergo a significant decrease (figs. 4.5c,d), ranging from 0.012° in 2011 to 0.032° in 2012 (table 4.3). These potential temperature decreases induce an increase in potential density between 0.003 kg m^{-3} to 0.009 kg m^{-3} for the 4 winters of deep convection studied here.

We interpret these decreases in potential temperature of the mixed layer, already seen by Schroeder et al. [2013], as the effect of the persistent net heat losses after that the MLD reached the bottom. The absence of increase in the salinity of the bottom water can be explained by the domination of the winter buoyancy fluxes by the heat fluxes (Grignon et al. [2010]). The salinity of the newly-formed deep water is mostly set by the salt content of the water column before convection, while its potential temperature results from a combination of the initial heat content and the surface heat fluxes.

The figure 4.4c shows an interesting feature after the end of the deep convection of winter 2010. By the end of March a sharp decrease in the bottom water potential temperature occurs (≈0.02°C) without any link with the atmospheric forcing (fig. 4.4d), then the potential temperature progressively increases until reaching an equilibrium state in August (fig. 4.8c). No similar signal was recorded by conductivity sensors. The range of salinity since the end February 2010 was never recorded before at that depth level. This may suggest that this different bottom water mass appearing at the end of March, should have been formed this year.

We suggest that this colder potential temperature (and higher potential density), appearing at the end of March, is related to formation of deep water at another location. The hypothesis of different deep water masses formations occurring in different locations inside the cyclonic gyre, was already suggested by Lacombe et al. [1985]. This place may be the location where gliders have recorded an homogeneous mixed layer until 1000 m in 2008, also the area with the lowest surface chlorophyll concentration detected by MODIS in 2008 (see section 4.5). Assuming that the buoyancy flux are the same in the two locations, a lower stratification in this area could induce a faster deepening of the mixed layer. A shallower bottom could also make the MLD to reach the bottom depth faster and so, the whole homogeneous water column would be exposed to longer heat loss, which would lead to a stronger potential temperature decrease and to the formation of colder deep water. However it seems that this formation mode is a minority. From the end of March 2010 to August 2010, the potential temperature of the bottom water will continue to rise, until it reaches a level close to the one reached just after the end of the deep convection (figs. 4.3c and 4.8c). This slow increase in the bottom potential temperature may be seen as the effect of the horizontal mixing of these two different water masses.

Another remarkable signal occurs between March 2012 and May 2012 characterized by a sharp and noisy diminution of the bottom potential temperature and salinity, while at the same time, potential density did not present high frequency fluctuations (fig. 4.9a). The origin of the bottom waters characterized by a lower potential temperature and salinity, was identified as a result of dense shelf water cascading (Durrieu de Madron et al. [2013]). The peculiar atmospheric conditions of winter 2012 triggered a massive formation of dense water over the continental shelf that overflowed the shelf edge and cascade down to the bottom (see chapter 5 for details).

The strongest θ and S signal occurs the 10 April 2012 when a cyclonic eddy crossed the mooring (see section 5.2 for more details), with a strong decrease in θ (-0.1°C) and S (-0.03‰) associated to the core of the eddy. Its core radius was estimated to be 12.0 km with a peak observed azimutal speed of 15.7 cm.s^{-1}.

4.4.5 Fate of the Deep Water Masses

Although deep ocean convection is the main mechanism for the renewal of the WMDW, the influence of dense shelf water cascading on WMDW has been first suggested by Bethoux et al. [2002]. Puig et al. [2012] highlight the persistence in the deep waters since winter 2005 of a θ-S anomaly link to dense shelf water water cascading. The coexistence of deep waters formed by deep convection and by dense shelf water cascading can be clearly seen on θ-S diagram, where it takes a V-shape structure. Several authors report this shift in deep water characteristics since 2005 (Lopez-Jurado et al. [2005]; Schroeder et al. [2006, 2008]; Canals et al. [2006]; Smith et al. [2008]; CIESM [2009]).

In 2007, CTD stations made in the Gulf of Lions clearly show 3 different deep water masses (fig. 4.13), indicated by the V-shape structure below the Levantine Intermediate Water (>600m). One can clearly see the stacking of three different water masses (indicated by a θ-S extremum), with the "old" WMDW (oWMDW, between 800 and 1400m), the "new" WMDW formed by deep convection in winters 2004/2005 and 2005/2006 ($nWMDW^{(2007)}_{2005/06-OC}$, between 1400 and 1900m) and the "new" WMDW formed in winter 2004/2005 by dense shelf water cascading ($nWMDW^{(2007)}_{2005-CS}$), between 2000m and the bottom). In the naming of the different deep water masses, we use the superscript in order to precise the year when the deep water was observed. The characteristics of these transient new deep waters may change from year to year due the permanent turbulent mixing, which tends to homogenize the deep layer. As an example, in 2005 the θ-S characteristics of the bottom water ($nWMDW_{2005-CS}$) recorded in the Gulf of Lions by Schroeder et al. [2006] was close to θ = 12.76 and S = 38.46‰, while two years later the observed θ-S characteristics of this water mass are less pronounced (θ = 12.87 and S = 38.48‰). The year to year evolution of a specific deep water mass can be tracked on θ-S diagrams, particularly during years withtout deep convection.

In 2008, CTDs stations revealed a mitigation of deep water characteristics, especially for the deep water mass between 1400m and 1900m. The temperature of the $nWMDW^{(2007)}_{2005/06-OC}$ has decreased by 0.02°C in one year, while for salinity the decrease is about 0.005‰. However one

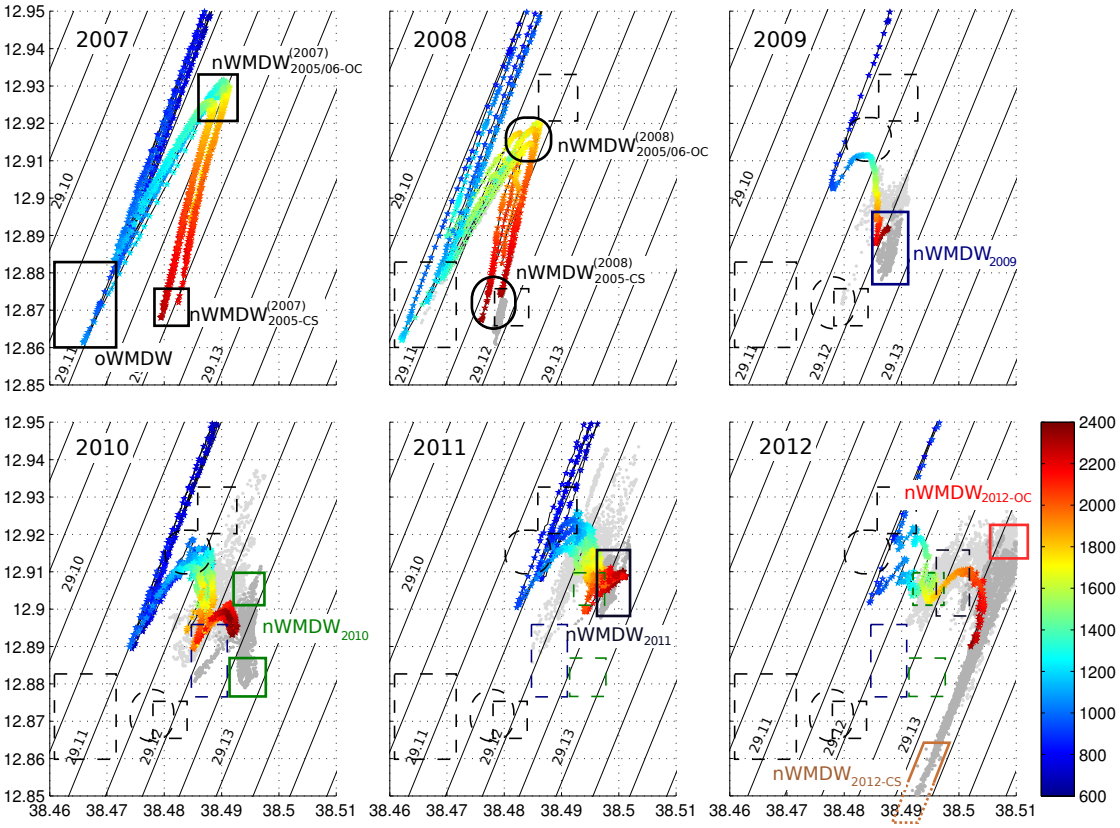

Figure 4.13: θ-S diagrams of WMDW from CTD stations close to the LION mooring (<40km) with pressure represented in color (2007: DOCONUG2007; 2008: DOCONUG2008; 2009: 42N5E; 2010: MOOSE_GE_2010; 2011: MOOSE_GE_2011; 2012: MOOSE_GE_2012). Dark gray dots indicate the θ-S properties recorded by the 2300m Microcat at the end of the vertical mixing phase, light gray dots correspond to the 1500m Microcat

has to interpret this salinity increase with caution because it is of the same order of magnitude than our confidence in the value of salinity measured during both cruises.

In July 2009, CTD stations reveal an homogenization of the deep waters, with a less pronounced V-shape structure. This year a new thermohaline anomaly appears on θ-S diagram. On the last 200m of the water column, a relative warmer and saltier water mass was detected (fig. 4.13). As presented earlier in this work, 2009 was a year of deep convection (figs. 4.9c and 4.6), where an increase in potential temperature and salinity of the bottom water was noticed after the deep convection event (figs. 4.8c,d).

The range of salinity and potential temperature recorded by the 2300m Microcat just at the end of the vertical mixing is showed by the dark blue rectangle on figure 4.13. These potential temperature and salinity correspond to the characteristics of the newly-formed deep water of 2009 ($nWMDW_{2009}$) exactly when it was formed, while CTD casts made in July have revealed an "attenuated" bottom water, which has already started to mix with "older" deep water. If the detection of a newly-formed deep water on a θ-S diagram is relatively straightforward in

the months following the deep convection period (apparition of a new extremum in the θ-S diagram), the identification of older deep water masses is more difficult in profiles carried out in a region which has undergone a significant vertical mixing. However, the local maximum between 1200 and 1500m depth that can be noticed on the θ-S diagram in 2009 and 2010 suggests the presence of a water mass with θ-S characteristics close to the $\text{nWMDW}^{(2008)}_{2005/06-OC}$.

In June 2010, CTD stations still show the V-shape structure between 800 and 1800m, but a new thermohaline structure appears below 1800m. This structure also presents a V-shape. One can relate this second V-shape with the characteristics of the newly-formed deep water of 2010 (nWMDW_{2010}). As we suggested it earlier, 2010 may be a year where two different deep water masses were formed, which could explain the small positive gradient of θ in the θ-S diagram tail. Salinity and potential temperature recorded by the 2300m instrument of the mooring line at the end of the vertical mixing period are represented on the θ-S diagram (dark gray dots, with the two extrema indicated by green rectangles on fig. 4.13). These 2 extrema detected in March 2010 are in good agreement with the deep stratification measured by the CTD stations in June 2010, even if the gradient of θ is smaller in June than in March. A possible explanation to this mitigation is again the permanent turbulent mixing, which tends to homogenize the deep waters.

Winter 2011 was also a winter of deep convection (figs. 4.9c and 4.6) where a new warmer and saltier deep water was produced (see nWMDW_{2011} on fig. 4.13). This new bottom water was also observed on CTD stations performed in June 2011.

2012 was the first winter of deep convection and dense shelf water cascading since 2006 (Durrieu de Madron et al. [2013]). In addition to the mooring data, where a significant drop of potential temperature and salinity has occured in April 2012, this can be clearly seen on CTD stations performed in July 2012 (fig. 4.13). A new V-shape structure has appeared on the θ-S diagram tail, below 1600m. This thermohaline anomaly extends over more than 600m on CTD stations made close to the mooring location. The shape of the anomaly can be related to the new deep water formed in winter 2012 by deep convection ($\text{nWMDW}_{2012-OC}$) and by dense shelf water ($\text{nWMDW}_{2012-CS}$) indicated in dark grey on figure 4.13. The extremum in θ and S of the dense shelf water monitored by the mooring line is θ=12.8°C and S=38.479‰.

Although the observations of the long-term persistence of several deep waters in the WMED could be partly related to the large number of observations collected during the last decade, this new insight on the deep water dynamics is a major element in our understanding of the thermohaline circulation in the Mediterranean. Traditionally it was commonly believed that there was only a major deep water in the WMED, which could be ventilated every year, undergoing minor changes in temperature and salinity, the distinction between new and old deep water disappearing quickly. The 6-year evolution of the θ-S diagrams made in the deep convection area clearly shows the apparition of new deep water masses after each deep water formation event that reached the bottom. After each event, the newly-formed deep water

spreads into the whole basin and progressively mixes with the former deep waters, explaining the “attenuated” characteristics of deep waters recorded during the summer CTD-surveys, comparing to winter extrema recorded by the deep mooring line. The long-term persistence of several deep waters in the WMED since 2005 might be related to a deep mixing less intense than previously thought, or to an increase in the volume of newly formed deep water these last years.

4.5 Horizontal Extent of the Deep Convection Area

Ocean color satellite can provide estimates of sea surface chlorophyll *a* (chl-*a*). In the Gulf of Lions, it is a useful tool to get a first idea of the maximum extension of the deep water formation. During wintertime, the Gulf of Lions is often characterized by a region of low surface chl-*a* (fig. 4.14). This low chl-*a* patch indicates that the phytoplankton has no time to grow in the euphotic layer, which can be explained by an active vertical mixing at that time. However we cannot know the depth of the vertical mixing, we can just consider that a low surface chl-*a* indicates a vertical mixing going deeper than the euphotic zone (100-200m).

Although there are many gaps during wintertime in the daily data, mainly due to the cloud coverage, there are some good daily images that can be used to estimate the extension the maximum extension of the deep water formation area. There is no real coincidence that some cloudless images are available during periods of vertical mixing (fig. 4.14 and table 4.3). When the Mistrals cold and dry wind blows over the convection area, the sky is usually clear.

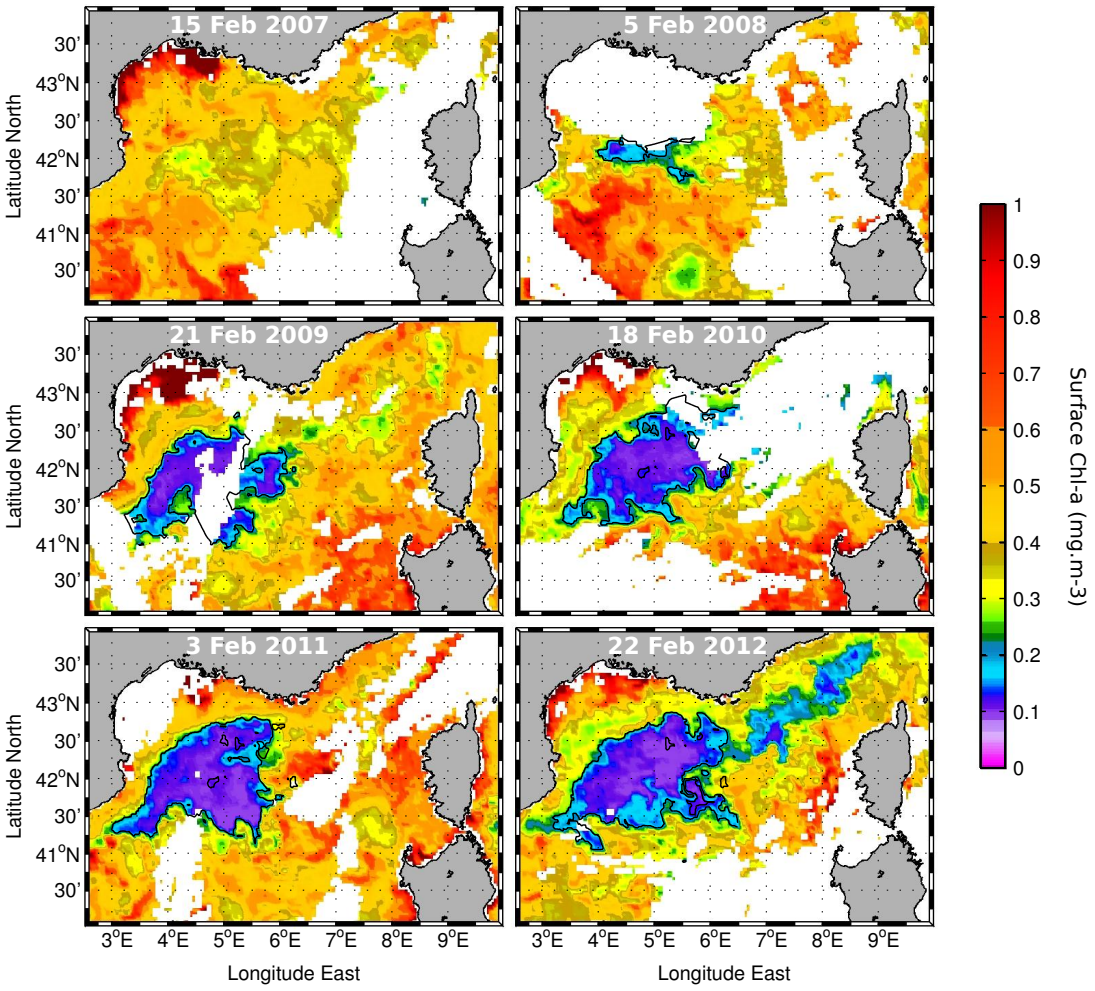

Figure 4.14: Daily surface chlorophyll images from MODIS for winter 2007 to 2012.

Since there are still gaps in selected images, we just performed a basic 2d-linear interpolation to have an idea of the area of low surface chlorophyll. We choose two different criteria (<0.12 mg.m^{-3} and <0.2 mg.m^{-3}) to calculate the area inside the Gulf of Lions (right boundary at 6.5°E). We decide to calculate this area only for the Gulf of Lions because the generalization of our results on the LION mooring line may be valid only in the Gulf of Lions, and this place is the major site of deep ocean convection in the NWMED (no deep convection was observed at DYFAMED in the Ligurian Sea for the 2008-2012 period, *Laurent Coppola pers. com.*). Results for the 2 criteria are indicated in table 4.3, while the black line on figure 4.14 indicated the 0.2 mg.m^{-3} contour. The choice of a too restrictive criterion, for calculating the maximum extension of the deep convection with only one image of the area, might be a contradiction, so the 0.2 mg.m^{-3} criterion was chosen instead of the 0.12 mg.m^{-3} to propose a superior limit of the extension of the deep convection area.

The occurrence and the relative intensity of deep convection can be seen on satellite images. In 2007, the area of deep convection estimated with a 0.2 mg.m^{-3} criterion is null (fig. 4.14. This absence of deep convection was confirmed also by glider data. 5 of the 8 gliders deployed during EGO2007 were in the Gulf of Lions from January 2007 to May 2007 and recorded a maximal mixed layer near 400m depth (Testor et al. [2007]).

In 2008, another big experiment took place in the Gulf of Lions (EGO2008), with 6 of the 9 gliders deployed sampling the water column from January to April. That year a MLD reaching 1000m depth was sporadically recorded mid-March by gliders 50 km westward of the LION mooring location (near 42.1°N 4.1°E), while the MLD was not superior to 700m depth at the mooring location. This seems in good agreement with the satellite image of the 5 February 2008, where the low chl-*a* patch extends westward of the mooring location. This might suggest that the most favorable site of deep open-ocean convection in the Gulf of Lions may be further west than the LION mooring and close to 42.1°N 4.1°E.

Strong deep convection occurs in the Gulf of Lions the other 4 years (table 4.3, fig. 4.9c). This can also be seen on satellite images, where the surface estimated of deep convection in the Gulf of Lions is comprised between 21 000 and 27 000 km^2, 9 or 10 times greater that the surface estimated in 2008 (fig. 4.14, table 4.3).

If we can clearly distinguish winters with or without deep convection on satellite images, it is more complicated to compare the intensity of the deep convection based only on its maximum extension determined on instantaneous satellite images.

Due to the very close estimations of area of the deep convection zone in estimations made from winter 2009 to winter 2012, one criteria can be used to distinguish the intensity of deep convection for these winters, as the increase in potential density recorded at the bottom due to arrival of newly-formed deep water (table 4.3), if we assume that the water column stratification did not change a lot between the different winters. According to this criterion, the deep convection produced more deep water in 2012, with a 0.009 kg.m^{-3} increase of near bottom potential density after the event. Then we estimate by decreasing intensity the winter 2010 (0.0062 kg.m^{-3} increase), 2009 (0.0044 kg.m^{-3} increase) and 2011 (0.0030 kg.m^{-3}

increase).

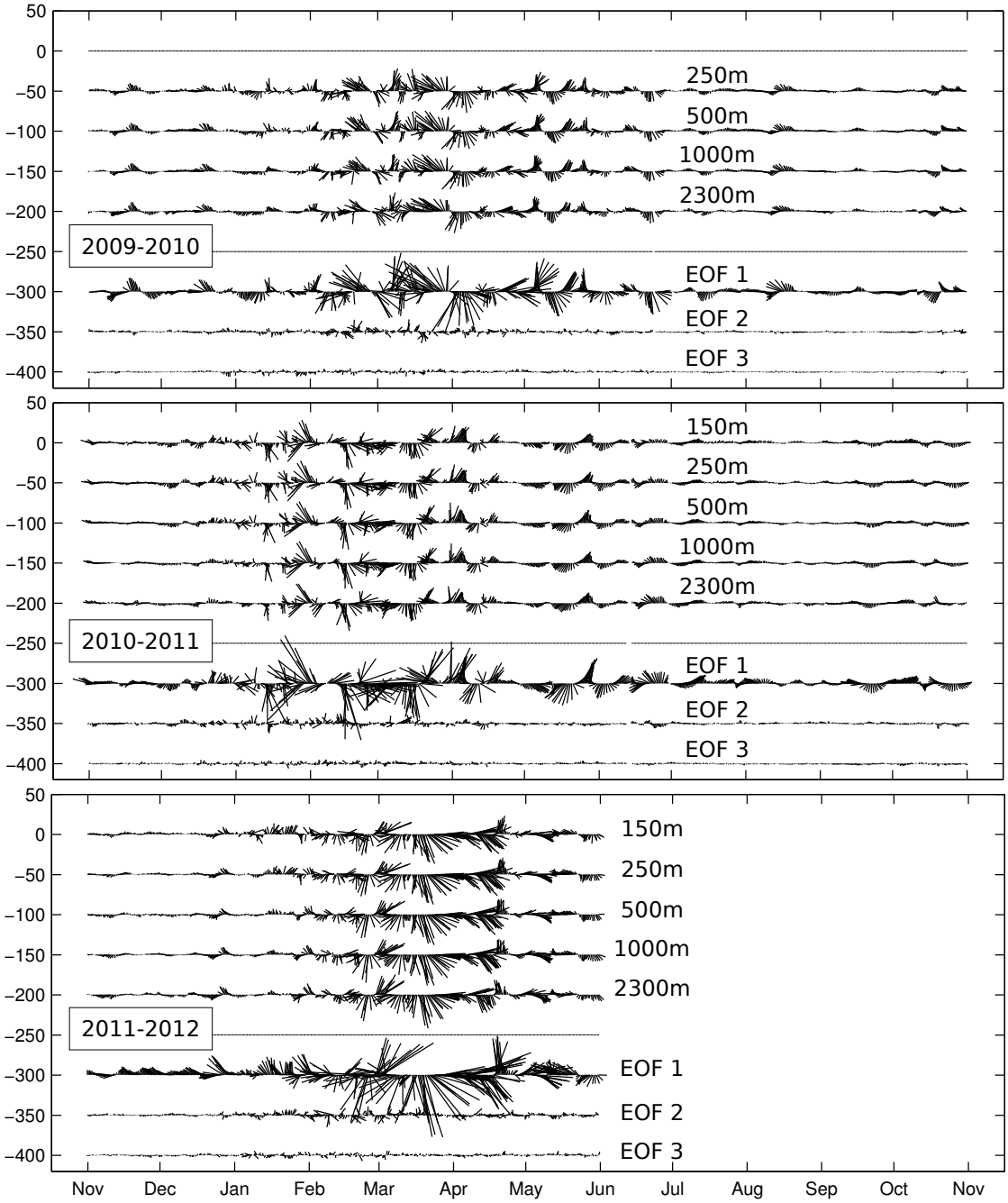

Figure 4.15: Stick diagram of currents at the 5 (4 for 2009-2010) depths measured by Aquadopp and the first three EOFs. The original time series are decimated to one point per twenty-four hours, and are offset by -50 cm s^{-1} for display purpose.

4.6 Seasonal Variations of the Vertical Structure of Horizontal Currents

Strong currents were also recorded during the different events of deep ocean convection: high frequency vertical velocities exceeded 15 cm.s^{-1} during the violent vertical mixing phase and strong mesoscale horizontal currents reached 40cm.s^{-1} during the restratification phase (figs. 4.9b,c).

The seasonal variation in the current magnitude and structure can be investigated using empirical orthogonal functions (EOFs). We used the bi-hourly complex time series ($u + iv$) filtered with a 48-h Hanning filter for each year (from the 1st November to the 31 October) and for each month. For this part of the study, we did not use data for winter 2007-2008 or 2008-2009, since the vertical resolution was not optimal.

The time series of the first EOF from the current meters are presented on figure 4.15 for each year. For the 2009-2010 period (respectively 2010-2011 and 2011-2012), EOF 1 accounts for 94.3% (resp. 94.7% and 96.1%) of the variance, while EOF 2 contains 4.1% (resp. 3.6% and 2.7%). The third mode contains a few percent of the variance. Calculations for the 2011-2012 period were carried out only on the 7 months of available data (2 current meters have stopped in June and the mooring line was recovered in July), this may explain why the EOF 1 is higher for this time period.

The structures of the modes is generally similar in all cases. The first EOF is globally in phase at all depths, while the second EOF is nearly linear over the whole water column and bottom intensified (fig. 4.16). This suggests an interpretation of these two EOFs as the equivalent barotropic mode (since we have not the surface current) and the first baroclinic mode. By studying the monthly variation, we clearly see that the first EOFs dominated the variability, containing 75% to 98% of the variance, while the second mode contains 1% to 18%. Horizontal currents are mainly barotropic between 150 and 2300m depth, as the stick vector diagrams clearly show us (fig. 4.15).

The ‘less equivalent barotropic“ states coincide with the deep convection period (from November to February). The vertical structure of the first EOF (solid line, fig. 4.16), presents a seasonal cycle in the surface intensification, with a strengthening of the projection at the beginning of the deepening of convection (cyan star at 150m and 250m depth for winter 2010 and winter 2012, and dark blue square for winter 2011). This period of ”baroclinization“ of the first EOFs correspond also to the deepening of deep convection (fig. 4.6), which would show a decoupling between the currents in the mixed layer and below..

In December 2010, the vertical structures of the first EOF are different from the one of January 2010 or January 2012. In December 2010, the first-mode projection is nearly uniform for the 2 subsurface current meters (150m and 250m depth), then it presents a jump between 250m and 1000m and a uniform projection for the 1000m and 2300m instruments. This jump may be linked to the presence of the deep pycnocline, as we can see it on fig. 4.6, considering that the mixed layer is similar to the pycnocline during the deepening of the deep convection.

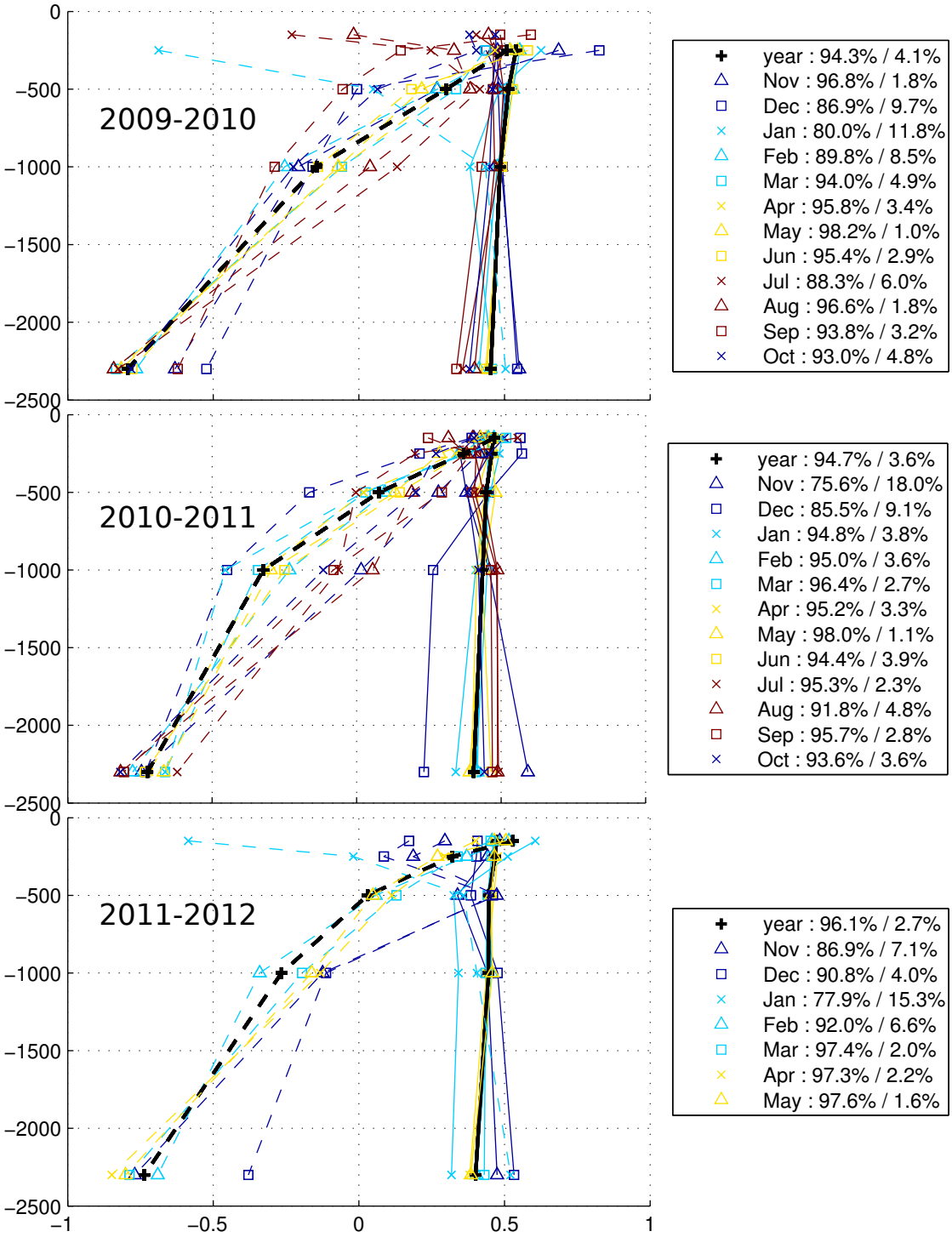

Figure 4.16: Magnitude of the projection of EOF1 (solid line) and EOF2 (dotted line) onto the five instruments (4 from November 2009 to July 2010) for the years (thick black line) and for each month (see legend for the symbol description). The percent of explained variance by EOF1 and EOF2 are given in the legend

In January 2012, the mixed layer did not reach the 250m current meter, that may explain the absence of a uniform projection of the first EOF onto the 150m and 250m instruments, as in December 2010. On the other side, it is nearly linear between 150m and 500m depth, reflecting a more "baroclinic state" of the first EOF than in December 2010. It is more or less the same situation for January 2010 (at that time the 150m instrument did not work), but the mixed layer reaches 1500m at the end of January. This abrupt deepening at the end of January may explain why we do not have the same uniform situation between 500m depth and 2300m depth than in January 2012.

In January 2010 and January 2012, the shape of the second EOF is very different from the "usual" linear trend over the whole water column and bottom intensified. They are the only months where the 2nd EOF is surface intensified, with a linear increase from 1000m depth in 2010 (500m depth 2012) and a nearly uniform projection from 1000m depth (500m depth in 2012) to the bottom. This change in the vertical structure of the 2nd EOF for this two months is synchronous with the changes in the vertical structure of the 1st EOF. This "baroclinic state" of the water column seems to be in good agreement with the deepening of the mixed layer or pycnocline). Although the structure for spring (AMJ) and summer(JAS) seem similar, currents during these time periods differ dramatically in magnitude, with JAS currents being about an half of AMJ currents (fig. 4.9b).The kinetic energy is then higher in spring but lower in summer.

As in Lilly et al. [1999], the energy cycle combined with the EOF variations can be used to characterize the seasonal variations of currents.

In our case, we can distinguish four dynamical periods for layer comprised between 150 and 2300m depth:

- a baroclinic and quiet period (ND),
- a baroclinic and energetic period (JF),
- a equivalent barotropic and energetic period (MAMJ),
- a equivalent barotropic and quiet period (JASO)

In the late fall baroclinic flows are excited, and intensified during the wintertime, then they evolve into barotropic flows in spring. The currents decay during late summer / early fall but retain their barotropic character. This annual cycle is close to the one describe by Lilly et al. [1999]from mooring observations in the Labrador sea, and we support the same cause of wintertime current excitation: the thermodynamic forcing of the region by surface buoyancy flux. Mesoscale currents become stronger with the deep convection activity and the transfer of the potential energy of the "mixed patch" into kinetic energy, increasing the "baroclinization" of the water column. When the atmospheric forcing stops, the baroclinic flow field will tend to evolve into a barotropic one, as a result of the geostrophic turbulence cascade to large scales (Rhines [1979]; Venaille et al. [2012]).

4.7 Census of Eddies in the Deep Convection Area from Nov. 2009 to Jul. 2012

The wavelet transform of the complex time series of horizontal currents ($U + iV$) maps out rich details of the horizontal currents across the time-frequency plane (fig. 4.17a). First, the inertial wave band shows up as a horizontal stripe of enhanced transform amplitude for a period comprised between 0.5 and 1 day. The actual inertial period for a point located at 42° North is close to 17.9h.

Eddy-like events were identified (white squares on fig. 4.17c) as local maxima of the wavelet transform topography. Maxima of the wavelet transform topography indicate a localized organization of the currents at a given scale. As in the Labrador Sea (Lilly et al. [2003]), there is a clear seasonal variability, with an increase in the transform amplitude at small scales (especially smaller than 3 days) that tend to occur during February and March. At that time, vertical mixing is very intense at 1000m depth (fig. 4.17b) and isolated eddies seem to blend into a background of high frequencies activity.

The small amplitude of the wavelet transform for February/ March 2008 at 1000m depth clearly distinguishes this year from the other winters of very intense deep convection.

The wavelet transform of the horizontal currents at 1000m gives us a representation of eddy-rich time series and reveals localized structures with their temporal variations. Once a first guess of eddy-like events was obtained, we improve the definition of the center and the duration of the eddy, then we used a kinematic model to estimate eddy characteristics, as explained in section 4.3.2.

From the 95 eddy-like events detected on the wavelet topography between October 2009 and July 2012, 37 have a perpendicular velocity component matching the Rankine model, for at least one depth level ($R^2 > 0.90$). Characteristics of eddies detected for this period are summarized in table 4.4. The 18 anticyclones detected have a radius ranging from 0.7 km to 19.1 km, while the 19 cyclones have a radius comprised between 1.8 km and 20.0 km and (fig. 4.18c). The maximal azimuthal speed for anticyclones ranges from 0.9 cm s^{-1} to 16.4 cm s^{-1}, (fig. 4.18b), while for cyclones, V_{max} ranges from 2.5 cm s^{-1} to 25.1 cm s^{-1}. The radii and the speed of the detected eddies do not seem to follow a normal distribution. However one can distinguish two modes on the distribution of the cyclones radii (fig. 4.18a), the center of the first mode seems to be at 4 km, while the second mode seems to be centered 12km. This first analysis of the eddies radii distribution might suggest that there is two different families of cyclones which could be related to different sites/processes of formation. The distribution of anticyclones radii present a mode centered at 5km, but we cannot observe a second mode in our data. One has to keep in mind that we can detect only part of the eddies that crossed the mooring, so the event detected here are certainly not exhaustive. We may have missed a significant number of eddies in summer / early fall, when the advection in the mooring area seems relatively weak in magnitude and highly variable in direction (see the end of the section 4.3.2).

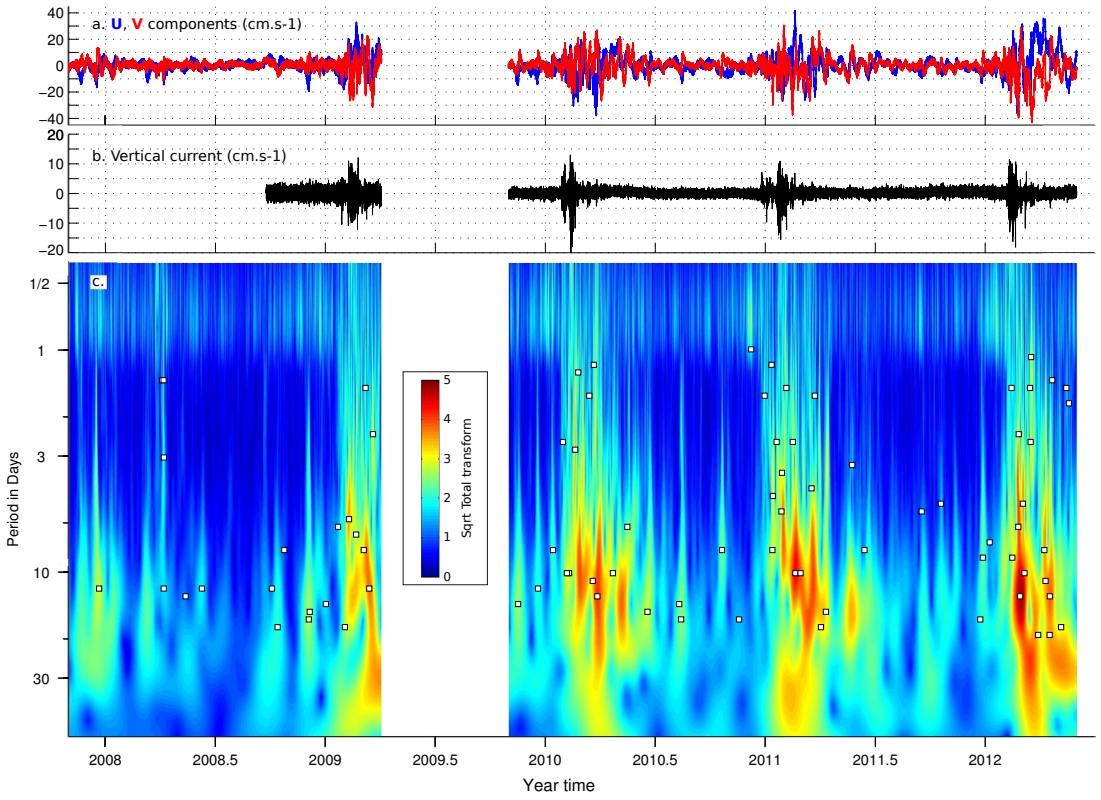

Figure 4.17: Horizontal (top) and vertical currents (mid) observed during the 5 years of measurements at the LION mooring location at 1000m depth and square root of the total wavelet transform (bot.) made on complex time series of horizontal currents at 1000m depth. Small squares mark the location of events identified by the the method described in Lilly et al. [2003], see section 4.3.2 for more details

The eddy current strength V_{max} and its radius R_{max} can be used to form a Rossby number:

$$R_o = \frac{2|V_{max}|}{R_{max} f}$$

Rossby numbers of the mooring cyclones ranged from 0.1 to 0.76 (table 4.4), while R_o for anticyclones ranged from 0.05 to 0.56. These Rossby numbers suggest that the two kinds of eddies are not completely dominated by the geostrophy, especially the cyclones which present higher maximal and minima in their R_o distribution.

Due to the low number of eddy occurrences and the relatively small period of available observations (only 2 summers and 3 winters), we did not try to describe these seasonal variations on a monthly basis, therefore we choose to bin the eddy-events into three periods of time. We define each period as being related to one of the "dynamical phases" of deep convection. (the preconditioning, the violent mixing and the spreading/restratification phase, MEDOC Group [1970]; Marshall and Schott [1999]). Although these phases overlap, we use them to describe the "main dynamic regime" of the region during the detection of different

eddies.
Each eddy detected was binned into one of the three following time-periods:

- We first define the vertical mixing phase as the phase during which significant vertical velocities (>5 cm s^{-1}) were recorded by the current meters.
- Then, the second phase corresponds to the spreading/restratification of the deep convection area. It begins at the end of the vertical mixing and stops when horizontal kinetic energy strongly decreases (late spring / early summer).
- The last phase, described as the preconditioning phase, corresponds to a quiet energetic period in which the ocean gradually restratifies. It extends from early summer to the beginning of the next deep convection event.

On the 13 eddies detected during the vertical mixing phase, 70 % are cyclones. During the spreading/restratification 16 eddies were detected, with more or less as many cyclones (56 %) than anticyclones (44 %). Less eddies were detected during the preconditioning phase (8), but anticyclones seem to dominate the flow (88 %).

The relative absence of cyclones during the preconditioning phase (1 occurrence, 10% of the total of eddies, fig. 4.18c), compared to the vertical mixing phase (9 occurrences, 70% of the

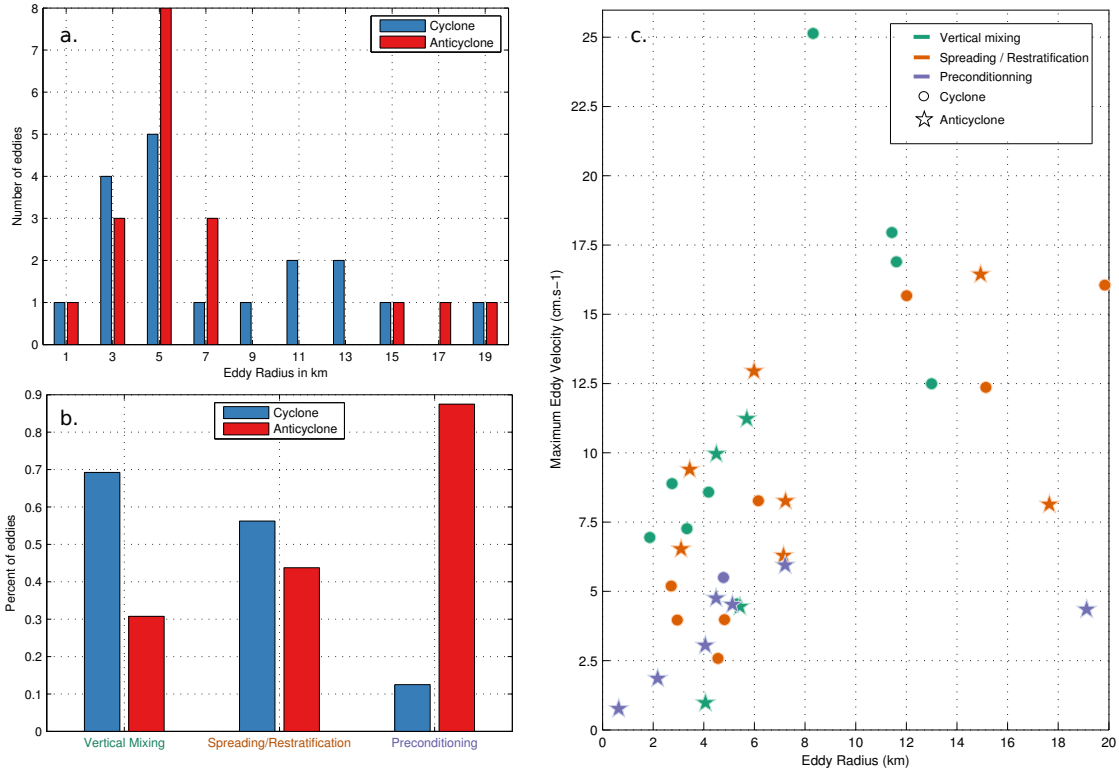

Figure 4.18: Results from eddy-detection at the LION mooring. (a.) Number of cyclones and anticyclones found at a given radius scale (R_{max} in km). (b.) Number of cyclones and anticyclones for each "dynamical phase" (see text for more details). (c.) Maximum azimuthal velocities (cm s^{-1}) encountered for each cyclone and anticyclone, plotted against radius. for each "dynamical phase" (see text for more details)

total of eddies) might indicate that this latter time period is more favorable to the formation of cyclones than anticyclones. This hypothesis is supported by results from laboratory basin experiments of Rhines [1998] and numerical experiments Akitomo [2010], where convection into an initially unstratified water column tends to favor cyclones.

During the restratification/spreading phase, 16 eddies were detected with almost as many cyclones (9) than anticyclones (7). The increasing number of anticyclonic eddies compared to the vertical mixing phase (almost twice more), might be partly explained by the baroclinic instability of the rim current that grows once the surface forcing abates.

Finally, the preconditioning period (defined as the period before significant vertical mixing were detected at 150m depth) is the longest period (from early/mid July to the end of December) and the quietest in terms of horizontal kinetic energy (see figs. 4.9b and 4.18d).

As explain earlier, this quiet period is also the most complicated to detect eddies with our method, since the flow seems relatively weak in magnitude and without a constant direction (see the end of the section 4.3.2). In addition, only 2 "full preconditioning periods" were used in this work (2010 and 2011), since the deployment of the mooring line took place at the end of October 2009, and the last recovery was at the end of July 2012. By making the assumption that the ratio of the eddies detected (12% of cyclones and 88% of anticyclones) is representative of this time period, one might see the decay of cyclones (relative to anticyclones), as being a consequence of their age.

As we saw it earlier, cyclones seem to be mainly formed during the deepening of the mixed layer and the intense vertical mixing phase. The ”age“ of cyclones might explain why they are less numerous than anticyclones during the preconditioning phase. This phase takes place 5 to 10 months after the estimated formation date of cyclones, while anticyclones are mainly detected during the restratification/spreading phase.

These results are only a first non-exhaustive analysis of the eddies crossing the LION mooring. Many aspects need to be further improved like :

- our estimation of the advecting flow. Other estimates of the advection velocity may be determined, by finding the depth-independent offset that makes the observed shear and observed total currents parallel to each other, or by using the momentum equation and assuming a cyclogeostrophic balance between the velocity observations and the density observations (Lilly et al. [2003])
- check, and adapt if necessary, the eddy-center calculation in order to not reject self-advecting dipoles (or ”hetons“), due to a bad estimation of the advecting flow
- the distinction of the eddies through their origins and the θ-S characteristics of their cores (eddy of newly-formed deep water or LIW).

4.8 Water Column Stratification and Deep Convection Intensity

4.8.1 Atmospheric Forcing

Mertens and Schott [1998] already showed the significant interannual variability of deep convection and the impact of the local heat flux in driving deep convection. The heat fluxes composition for the winter 2008 to winter 2012 are presented on fig. 4.19. Mean heat fluxes are

Table 4.4: Eddy events detected at the LION mooring

Date	Time	Period (days)	Typ.	R_{max} (km)	V_{max} (cm/s)	R_o	Advection Vel. (cm/s)	Advection Dir. (°)	y_0 (km)
23-11-2009	00:30	3,35	A	7,22	-5,94	0,17	2,83	173,51	1,88
29-12-2009	02:30	9	A	19,12	-4,35	0,05	2,48	168,62	3,17
13-01-2010	14:30	1,25	C	1,87	6,95	0,76	2,31	172,55	0,13
28-01-2010	13:15	0,45	A	4,07	-0,97	0,05	1,19	37,88	3,34
05-02-2010	12:00	3,5	A	5,7	-11,22	0,4	2,49	177,01	1,03
13-02-2010	19:30	0,81	A	5,43	-4,45	0,17	4,62	-175,23	4,48
19-02-2010	13:00	0,58	C	3,33	7,26	0,45	9,3	163,8	2,07
02-03-2010	16:30	1,31	A	4,5	-9,96	0,45	4,77	44,89	1,34
18-03-2010	10:00	1,77	A	7,23	-8,26	0,23	4,92	147,12	0,4
13-04-2010	16:45	1,45	C	6,15	8,27	0,28	5,61	-35,15	5,72
08-05-2010	04:45	3,45	C	19,84	16,06	0,17	6,66	25,8	7,52
19-05-2010	19:00	0,56	C	4,56	2,58	0,12	8,75	49,18	1,13
09-08-2010	02:00	6,06	A	4,49	-4,75	0,22	1,16	133,66	1,51
21-10-2010	07:00	1,48	C	4,78	5,5	0,24	3,97	166,85	0,2
21-01-2011	20:30	1,02	C	2,74	8,89	0,66	3,79	-150,92	0,41
25-01-2011	05:00	0,83	C	5,32	4,55	0,18	6,88	177,49	4,82
30-01-2011	09:00	1,46	C	11,43	17,95	0,32	10,72	163,36	4,83
22-02-2011	19:15	1,84	C	13	12,5	0,2	9,26	-34,98	10,14
03-03-2011	05:14	2,47	C	11,61	16,9	0,3	5,58	-64,91	0,11
12-03-2011	08:59	1,48	A	3,45	-9,4	0,56	2,28	-82,12	3,29
27-03-2011	00:00	3	C	15,14	12,36	0,17	5,14	91,85	1,28
06-04-2011	00:00	3,5	A	17,65	-8,14	0,09	5,01	84,35	5,77
14-04-2011	16:00	0,6	C	2,71	5,19	0,39	4,23	53,9	1,15
21-05-2011	18:30	3,63	A	5,99	-12,95	0,44	1,23	-54,76	1,22
01-07-2011	18:30	2,56	C	4,82	3,98	0,17	2,39	38,05	1,13
27-07-2011	00:00	4,5	A	4,06	-3,05	0,15	1,03	73,03	0,1
12-08-2011	17:00	3,77	A	2,18	-1,85	0,17	0,73	151,16	1,52
25-08-2011	05:45	1,43	A	0,64	0,76	0,24	0,21	-132,63	0,09
25-10-2011	00:00	5	A	5,13	-4,52	0,18	0,87	-92,78	1
08-02-2012	21:36	1,2	C	4,19	8,58	0,42	5,04	-145,79	0,39
04-03-2012	07:00	1,67	C	8,32	25,14	0,62	6,23	-82,97	4,9
10-04-2012	01:30	0,9	C	12,01	15,67	0,27	19,96	-19,48	5,83
17-04-2012	14:30	1,77	A	14,94	-16,44	0,23	12,33	-9,73	0,32
22-05-2012	19:00	2,02	A	7,15	-6,29	0,18	5,22	-161,14	0,9
10-06-2012	03:30	2,62	A	3,1	-6,53	0,43	1,32	-16,03	1,59
09-07-2012	08:45	1,41	C	2,96	3,97	0,28	2,99	177,42	0,97

calculated from the 1st November to the end of February. The more intense winter in terms of heat and integrated buoyancy losses is Winter 2012 (196 W.m^{-2}, 1.35 m^2.s^{-3}) , while the less is winter 2008 (135 W.m^{-2}, 0.94 m^2.s^{-3}). The net heat flux during wintertime is mainly dominated by the latent heat flux, between 75% (2010) and 86% (2008) of the net heat flux, while the sensible heat flux represents 17% (2008) to 24% (2010) of the total heat flux. The radiative heat flux is close to zero (between 1% and 3%).

On figure 4.20, we can clearly see that the surface buoyancy flux is strongly related to the surface heat flux, as it was showed by Grignon et al. [2010]. One could try to explain the intensity of deep convection by the strength of the winter heat (or buoyancy) losses. The winter 2012 was the 5th coldest winter of the 1980-2012 period according to Era-Interim Reanalysis (fig. 4.20); 2009, 2010 and 2012 were three of the nine coldest winter of the 1980-2012 period. However that might not be the only reason, as example, the winter 2004 present a heat loss superior to 2011, but deep convection or newly-formed water masses were not detected on CTDs stations (Lopez-Jurado et al. [2005]). The 4-months mean of surface heat or buoyancy losses might not be sufficient to explain the occurrence of deep convection, strong wind bursts of a few days duration might play also a role (Leaman and Schott [1991]). But another crucial parameter is the hydrographic preconditioning of the water column, that can be as important as the winter buoyancy fluxes (Grignon et al. [2010]).

4.8.2 Surface Buoyancy Flux and Buoyancy Content of the Water Column

Following Marshall and Schott [1999], we can express the surface buoyancy flux, which depends on the heat and freshwater fluxes at the sea surface, as:

$$B = \frac{g}{\rho_0}\left(\frac{\alpha_\theta}{c_w}Q_{net} + \rho_0\beta_S S(E-P)\right) \qquad \text{(Eq. 4–5)}$$

where g= 9.81 m s^{-2} is the acceleration due to gravity, ρ_0=1000 kg m^{-3} is the density reference, α_θ = 2x10^{-4} K^{-1} and β_S = 7.6x10^{-4} are the thermal expansion and haline contraction coefficients, c_w = 4000 J Kg^{-1} K^{-1} is the heat capacity of water, Q_{net} is the surface heat loss, S is the sea surface salinity and $E-P$ represents the net freshwater flux.

The influence of the stratification of the water column on the deep convection occurrence can be studied using a 1D approach, where only the surface buoyancy flux is being used to deepen the mixed layer. This approach was also used in Grignon et al. [2010] and L'Hévéder et al. [2012].

The buoyancy content BC of the water column is defined as:

$$BC(t) = \frac{g}{\rho_0}\int \rho(z,t)\,\mathrm{d}z \qquad \text{(Eq. 4–6)}$$

and the conservation of buoyancy content BC, undergoing a buoyancy flux B between t and

$t + dt$:

$$BC(t+dt) - BC(t) = \int B\,\mathrm{d}t \qquad \text{(Eq. 4–7)}$$

Following Turner's formalism (Turner [1973]) and hypothesis (the mixed layer h is non penetrative: the density of the mixed layer is the same one than the one observed at the mixed layer depth before the deepening), we obtain the equation:

$$\frac{h\partial h}{\partial t} = \frac{B(t)}{N^2(h)} \qquad \text{(Eq. 4–8)}$$

where N is the buoyancy frequency in s^{-1} $\left(N^2 = -\frac{g}{\rho_0}\frac{\partial \rho}{\partial z}\right)$, and B the surface buoyancy flux defined in section 4.8.2 (Eq. 4–5).

Integrating Eq. 4–8 gives:

$$IS(Z) = \int_0^Z N^2(h)h\,\mathrm{d}h = \int_{t_0}^{t} B(t)\,\mathrm{d}t \qquad \text{(Eq. 4–9)}$$

where $IS(Z)$ represents an index of stratification of the water column (Herrmann et al. [2010]). In this approach the lateral flux of buoyancy is neglected. We will define Z as equal to 1000m, t_0 as the 1st November and t the end of February.

We calculated $IS(Z)$ using our mooring data. As describe in section 4.4.3, first we interpolated the mooring and buoy data from the surface to 2300m depth. Since there was no conductivity sensor at the sea surface before November 2011, we did not know the stratification due to the salinity in the first 200m. We chose to calculate anyway a stratification for the first 200m of the water column using a fixed salinity (the salinity at 170m depth) and we compute the error due to this calculation. To do that, we used our profile database. We compute IS for each available profile, then we compute $IS_{S_{fix}}$ in which salinity was fixed. The difference give us a good estimation on the error made in IS calculation with a fixed salinity. In this calculation, we also take into account the error due to the low vertical resolution. We compute $IS_{S_{fix}}$ without using the full potential temperature profile, but we used a "undersampled" potential temperature profile. As in section 4.4.3, we used only the depth levels corresponding at each mooring instruments depth, then we interpolated linearly the potential temperature every meter. We used this interpolated profile in the calculation of $IS_{S_{fix}}$. For depth greater than the first conductivity sensor, we did not have to fix the salinity but still we calculated the error due to the low vertical resolution of the mooring.

Another kind of error can occur in the derivative calculation of N^2, this error is linked to the intercalibration of the different instruments. As we estimated the accuracy on the potential density at 0.005 kg m^{-3}, we propagated this error in the calculation of IS. For an integration to 1000m depth (IS_{1000}), the error due to the accuracy of the conductivity sensor, represents between 13% and 34% of the profile total error (fixed salinity + vertical discretization + intercalibration), while for an integration down to 2300m (IS_{2300}) the error due to the intercalibration is comprised between 76% to 92%. This profile total error is indicated by the red vertical lines

on figs. 4.19 and 4.20.

Finally, the last kind of error considered here, is the error related to the time-representativity of the mooring profile used for the calculation of IS. To illustrate this, we calculated the mean and the standard deviation of the distribution of IS, comprising the different IS calculated for each hourly profile on a 6 days window centered on the 1st November. Then we define this time-representativity error as three standard deviations. The profile total error is indicated by a red line on figures 4.19 and 4.20, while the green line corresponded to the sum of the profile total error with the time-representativity error.

Calculation of $IS(1000)$ from 2008 to 2012 is showed on fig. 4.20 (red circle), with the profile total error represented by the vertical red lines. The higher is $IS(1000)$, the greater the integrated buoyancy losses have to be to enable the deep convection to reach 1000m depth. If

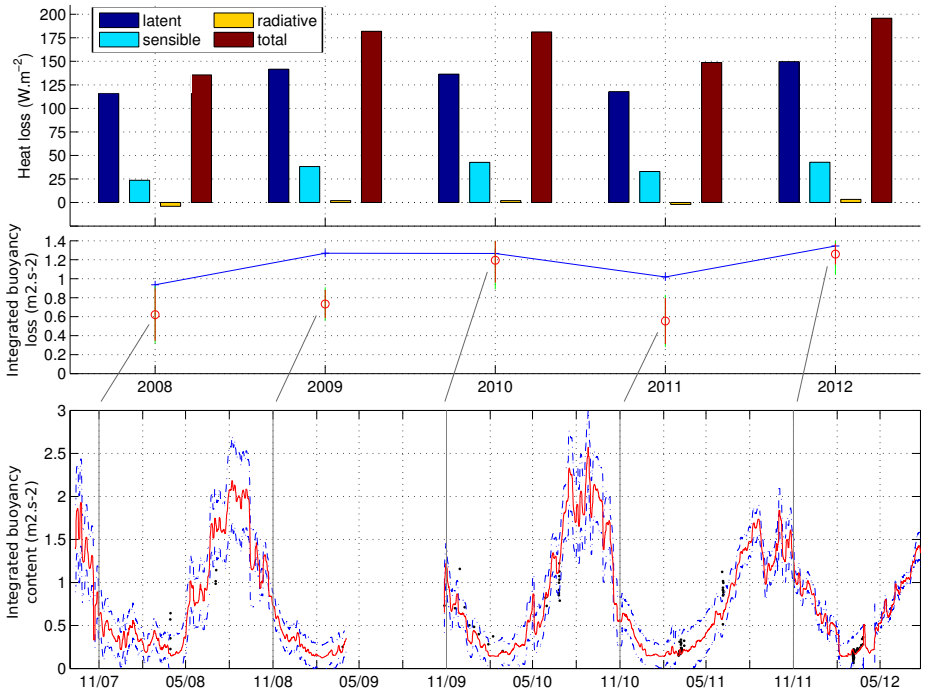

Figure 4.19: Era-Interim surface heat fluxes composition (top) and integrated surface buoyancy loss (mid) for winter 2007-2008 to winter 2011-2012 from Era-Interim. Red circle indicated (mid) the integrated buoyancy content of the first 1000m of the water column estimated the 1st November of each year, using the deep mooring line and the LION surface buoy. The red and green vertical lines indicate the associated error (see the text for more details).
The bottom panel represent the temporal series of the integrated buoyancy content of the first 1000m ($IS(1000)$ in red), with the associated error (dotted blue line). The black dots correspond to $IS(1000)$ calculated on vertical profiles close to the mooring (<40km)

.

in November, $IS(1000) > \int_{Nov.}^{Feb.} B(t)\,\mathrm{d}t$, the deep convection will no reach 1000m depth. For all winter, $IS(1000)$ is below the integrated surface buoyancy losses from the 1st November to the end of February, indicating that the deep convection could deepen up to 1000m. Another point is that 2011 seems to be the winter during which the water column was the less stratified in November. This may explain why 2011 was a "deep-convective" year, while heat losses were comparable to 2004 (a year without deep convection).

4.9 Conclusion

We have presented here new results from a temporal high resolution survey in the center of open-ocean deep convection zone, in the Northwestern Mediterranean. Through these 5 year long timeseries, 5 consecutive winters of deep convection were presented, especially 1 winter where deep convection has reached 1000m depth (2008) and 4 winters where deep convection has reached the bottom (2300m depth). In winter 2012, dense shelf water cascading was also observed on the deep LION mooring.

The time for the mixed layer deepening is comprised between 1 and 2 months. Once the mixed layer has reached the bottom (usually at the end of January / beginning of February), there is a violent vertical mixing phase of the whole water column (with a duration of 9-12 days). Winters from 2009 to 2012 present all a second vertical mixing period that generally

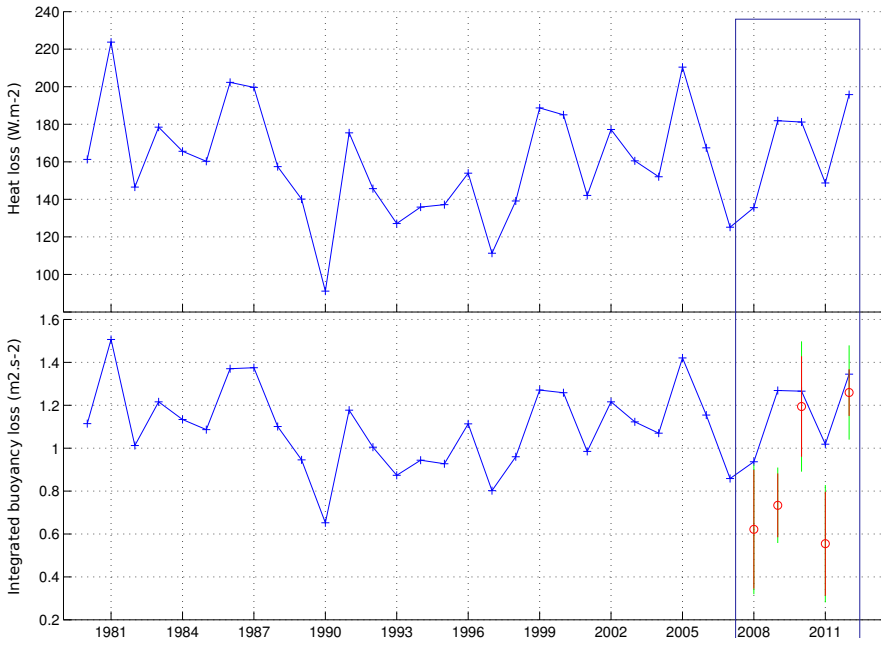

Figure 4.20: Era-Interim mean surface net heat flux (up) and mean surface integrated buoyancy loss (down) calculated on the 1980-2012 period, from the 1st November to the end of February. Red circle indicated the integrated buoyancy content of the first 1000m of the water column estimated the 1st November of each year, using the deep mooring line and the LION surface buoy. The red and green vertical lines indicate the associated error (see the text for more details).

occurs in March after the main event of deep ocean convection. This short event (2-4 days) happens just after the restratification of the area has begun. The water column is not much stratified at that time and a 3-6 days period of buoyancy loss (due to Mistral/Tramontane events that are intense and frequent in winter) can easily destabilize the water column, leading to vertical mixing. We define a "restratification time" of the intermediate layer (200-600m) as the time needed by this layer to recover 50% of its heat content lost during deep convection. Using the mean potential temperature for the 200-600m layer for year 2010, 2011 and 2012, we determine the time for this layer to compensate a half of the heat lost during the deep convection event, as being comprised between 2.5 and 4.5 months. Finally, we calculate a "spreading time" of the newly-formed deep water, as the time needed to the water column to dissipate 50% (respectively 75%) of the potential density increase in the 600-2300m layer, at the end of the strong vertical mixing phase. The dissipation of 50% (75%) of the potential density increase in the deep layers due to OODC, takes approximatively 1.5 to 3 months (3 to 6 months), reflecting the spreading and the mixing of the newly-formed deep water with the ambient deep water.

The long restratification and spreading times that can be observed after each winter of deep convection show that the restratification/spreading phase is still active at the beginning of the next deep convection event, indicating a "memory effect" of the water column and a overlapping of the 3 "phases" of deep convection. This also highlights the crucial need of a correct modeling of eddies throughout the year if one wants correctly simulate the phenomenon of deep water formation.

For the first time in the Gulf of Lions, we were able to highlight the seasonal variations of the vertical structure of horizontal currents between 150m and 2300m depth. 85% to 95% of the variance of the horizontal currents (between 150m and 2300m depth) can be explained by the 1st EOF (interpreted as the equivalent barotropic mode, since we did not know the surface/sub-surface currents), while the second mode (interpreted as the 1st baroclinic mode) contains 5% to 10% of the variance. Theses new results indicated that the vertical structure of horizontal currents from 150m to 2300m is mainly barotropic, and seasonal variations in currents seem to be running as a 4-phase cycle:

- a baroclinic and quiet period in late fall,
- a baroclinic and energetic period in winter,
- a equivalent barotropic and energetic period in spring / early summer,
- a equivalent barotropic and quiet period in late summer / early fall

This wintertime excitation of currents may have been generated by the thermodynamic forcing of the region by surface buoyancy flux. Mesoscale currents become stronger with the deep convection activity due to the transfer of the potential energy of the "mixed patch" into kinetic energy, and this seems to lead to the "baroclinization" of the water column. The evolution of the baroclinic flow field into a barotropic one might be the result of the geostrophic turbulence cascade to large scales (Rhines [1979]; Venaille et al. [2012]).

37 eddies were detected between October 2009 and July 2012 (18 anticyclones and 19 cyclones), with radii (velocities) ranging from 0.7 km to 20.0 km (0.9 cm.s^{-1} to 25.1 cm.s^{-1}). The main mode of the distribution of eddies radii is centered at 4km for the cyclones and 5km for the anticyclones. Cyclones might have been mainly formed during the intense vertical mixing phase, when the very weak stratification leads to a small Rossby radius of deformation, while anticyclones are detected mainly from the spreading / restratification phase.

The deep LION mooring line is also a useful tool to monitor the formation and the characteristics of new deep water. The newly-formed deep water undergoes, first, a significant increase of potential temperature (between 0.02 and 0.04°C), due to the deepening of the mixed layer down to the bottom. Then the intense vertical mixing and strong buoyancy loss period (9-12 days) produce a decrease of the potential temperature of the mixed layer, and hence the potential temperature of the newly-formed deep water, ranging from 0.01 to 0.03°C. Unlike the potential temperature, the salinity of the newly-formed deep water does not shown significant variations after the deepening of the mixed layer down to the bottom. The salinity of the new deep water seems to be fixed by the salinity of the mixed layer once it reaches the bottom, corresponding to an increase between 0.006‰ and 0.012‰, for the 2007-2012 period.

The apparition of newly-formed deep waters was detected after every winter of deep convection from 2009 to 2012. In winter 2010, two newly-formed deep waters were detected after the deep convection event. They present a different potential temperature but a similar salinity, suggesting that both might be formed in the cyclonic gyre, but in different locations. In 2012, two new deep waters were detected at the mooring location, one was identified as a result of open-ocean deep convection, while the other seems to be the result of a dense shelf water cascading event that occurred in winter 2012.

If the long-term increase in salinity of the deep layer seems to be strongly related to the formation of new salty deep waters, the long-term warming trend of WMDW might be reduced during very strong event of deep convection, since the strong buoyancy loss during the intense vertical mixing of the whole water column may decrease the potential temperature of the mixed layer by several hundredths of degrees and therefore the potential temperature of the newly-formed deep water.

If the skies are fairly merciful, ocean color images can be a very useful qualitative tool to assess whether a deep convection event occurred or not. However, alone, they do not enable us to analyze several events of deep convection quantitatively.

Finally, a comparison between the buoyancy content of the water column before wintertime and the surface buoyancy losses integrated on the November-February period was done. Although the factors responsible of these 5 consecutive deep convection events were highlighted, this comparison also points out the needs of additional conductivity sensors in the first 200m of the water column for accurate calculations. In order to minimize the error on the calculation of the buoyancy content of the water column before the deep convection (an

indication of the “preconditioning state” of the ocean), it would be best to have full profiles created with a single instrument (like a profiler or a CTD cast) at the end of October / beginning of November. The repeated surveys that are carried out by gliders in the framework of MOOSE in the Gulf of Lions may be useful to get 1000m-depth profiles close to the LION mooring.

Further works have to be done to better understand the origin and the fate of the different eddies detected in this study. Numerical experiments might be a good tool to study the eddy generation and decay, but numerical grids are certainly too large to describe precisely these small scale eddies. Thus the combined use of a real-time mooring and gliders would be a useful tool to easily trigger sampling cruises and followed the evolution of these kind of eddies. Moreover the recent development of biogeochemical sensors can also be useful to have additional informations on the "biogeochemical signature" of these eddies and their potential impacts on triggering phytoplankton blooms in the Northwestern Mediterranean, since they can carry in their cores complete ecosystems, relatively isolated from the outside.

Another outlook will be to track the spreading of the newly-formed deep water outside the NWMED (with deep mooring deployed at key locations, together with basin-scale surveys using gliders and ships, for example), to quantify transports of heat and salt, and the diffusion linked to the mixing of these new deep waters with the surrounding waters. This heat and salt diffusion is throughout the spreading of the new deep waters in the Western Basin and in the Strait of Gibraltar, where some of them are part of the outflow, and therefore part of the Mediterranean Waters which spread at 1000m depth into the North Atlantic and thus join the global circulation.

5 Dense Shelf Water Formation in the Gulf of Lions

Contents

The Gulf of Lions (GoL) is a micro-tidal, river-dominated continental margin, subject to an energetic meteorological regime, mainly during Winter (Millot [1990]). The GoL is dominated by a westward circulation, that promotes a convergence of water and entrained particles at the southwestern end of the GoL. This trend is greatly enhanced under marine storms (East-SouthEast), which intensify the cyclonic circulation on the GoL shelf and produce a sea level rise next to the coast, promoting downwelling conditions that facilitated export of shelf water (Ulses et al. [2008a]).

The second major mechanism controlling shelf-slope exchanges is Dense Shelf Water Cascading (DSWC). In winter cold and dry winds (Mistral and Tramontane) may induce strong buoyancy losses of surface shelf waters through cooling and evaporation. During some years, this shelf convection may lead to a downslope sinking of surfaces waters into the continental

shelf canyons, known as DSWC (Durrieu de Madron et al. [2005]). During my PhD thesis I had the opportunity to collaborate in two studies based on these phenomena, mainly through my participation to the CASCADE (CAscading, Storm, Convection, Advection and Downwelling Events) oceanographic cruise in the GoL in March 2011.

The first one was devoted to the study of an episode of sediment transport along the southern flank of the Cap de Creus Canyon during several moderate eastern storms (in mid-March 2011). My contribution to this work was mainly done through my participation to the CASCADE cruise, the acquisition, the data processing and the interpretation of hydrological data (CTD stations, Shipboard-ADCP). I also contributed to the discussion on the setting up of the event (its temporal and spatial variability). Results, available in the appendix E, were published in Biogeosciences under the reference:

Martín, J., X. Durrieu de Madron, P. Puig, F. Bourrin, A. Palanques, L. Houpert, M. Higueras, A. Sanchez-Vidal, a. M. Calafat, M. Canals, S. Heussner, N. Delsaut, and C. Sotin. 2013. Sediment transport along the Cap de Creus Canyon flank during a mild, wet winter. Biogeosciences 10: 3221–3239, doi:10.5194/bg-10-3221-2013

I also have the opportunity to collaborate on a paper dedicated to the influence of deep dense shelf water cascading on the generation of thick bottom nepheloid layers (BNL). This study is mainly based on oceanographic surveys that took place in the NWMED from 1998 to 2011. It point out the formation of a thick BNL after deep DSWC events off the Gulf of Lions and Catalan margins, and the link between the thickness, the spreading and the persistence of the BNL with the volume of newly-formed deep waters after DWSC and OODC events.

My implication in this work was mainly done in the data processing and interpretation of several oceanographic cruises (DEEP, 42N5E, and CASCADE in which I also participated to the data acquisition). I also participate to the discussion on the variability and the persistence of the BNL, especially through the implications OODC events and newly-formed deep water. The article is available in the appendix F, and was published in Progress in Oceanography under the reference:

Puig, P., X. D. De Madron, J. Salat, K. Schroeder, J. Martín, A. P. Karageorgis, A. Palanques, F. Roullier, J. L. Lopez-Jurado, M. Emelianov, T. Moutin, and L. Houpert. 2012. Thick bottom nepheloid layers in the western Mediterranean generated by deep dense shelf water cascading. Progress in Oceanography 111: 1–23, doi:10.1016/j.pocean.2012.10.003

In the following of this chapter we present recent results from simultaneous deep DSWC and OODC events during the Winter 2012. Some results from the mooring line were already introduced in the previous chapter (chapter 4), but in the following we will stress on a "basin view" of the events. The first section of this chapter corresponds to a recent work published in Geophysical Research Letters, in which I participated in the deployment of the different instruments (CTD, mooring lines), I was responsible for the calibration and the analyze of the

data and I wrote a part of the paper. The second section of this chapter presents complementary analysis on the role of eddies on the propagation of newly-formed deep waters. The work presented in the first section of this chapter is available in the appendix G and was published in Geophysical Research Letters in April 2013, under the reference:

Durrieu de Madron, X., L. Houpert, P Puig, A. Sanchez-Vidal, P. Testor, A. Bosse, C. Estournel, S. Somot, F. Bourrin, M. N. Bouin, M. Beauverger, L. Beguery, A. Calafat, M. Canals, C. Cassou, L. Coppola, D. Dausse, F. D'Ortenzio, J. Font, S. Heussner, S. Kunesch, D. Lefevre, H. Le Goff, J. Martín, L. Mortier, A. Palanques, and P. Raimbault, 2013. Interaction of dense shelf water cascading and open-sea convection in the northwestern Mediterranean during winter 2012. Geophysical Research Letters, 40(7):1379–1385. doi: 10.1002/grl.50331.

5.1 Interaction of Dense Shelf Water Cascading and Open-Ocean Convection in the Northwestern Mediterranean during Winter 2012

Abstract

The winter of 2012 experienced peculiar atmospheric conditions that triggered a massive formation of dense water on the continental shelf and in the deep basin of the Gulf of Lions. Multi-platforms observations enabled a synoptic view of dense water formation and spreading at basin scale. Five months after its formation, the dense water of coastal origin created a distinct bottom layer up to a few hundreds of meters thick over the central part of the NW Mediterranean basin, which was overlaid by a layer of newly formed deep water produced by open-sea convection. These new observations highlight the role of intense episodes of both dense shelf water cascading and open-sea convection to the progressive modification of the NW Mediterranean deep waters.

5.1.1 Introduction

Dense shelf water cascading and open-sea convection coexist in a few regions around the world such as the Mediterranean (Gulf of Lions, Adriatic Sea, Aegean Sea, CIESM [2009]), the East/Japan Sea (Kim et al. [2008]), and Greenland Sea (Quadfasel et al. [1988]). However, interplay between both types of processes on the deep water mass characteristics is still poorly documented.

In the Gulf of Lions (GoL), dense water formation shows a high interannual variability. It is mostly produced by surface cooling and evaporation due to cold and dry northern winds, and preconditioning of the water column. Dense shelf water overflowing the shelf edge occasionally cascades down to more than 2000 m, resulting in the apparition of fresher and colder bottom water in the basin (Canals et al. [2006]; Font et al. [2007]). Open-sea convection involves a progressive deepening of the upper ocean mixed layer, which first reaches the

warmer and saltier underlying Levantine Intermediate Water and eventually extends all the way down to the bottom, should the atmospheric forcing be intense enough (L'Hévéder et al. [2012]).

Although open-sea convection is the main mechanism for the renewal of the WMDW, the influence of dense shelf water cascading has been suggested by several studies. Analysis of historical temperature-salinity profiles from the late 1960s suggested mixing of deep cascading and convection dense waters, with a subdecadal recurrence (Bethoux et al. [2002]), the winters 2005 and 2006 being the last major events (Puig et al. [2012]).

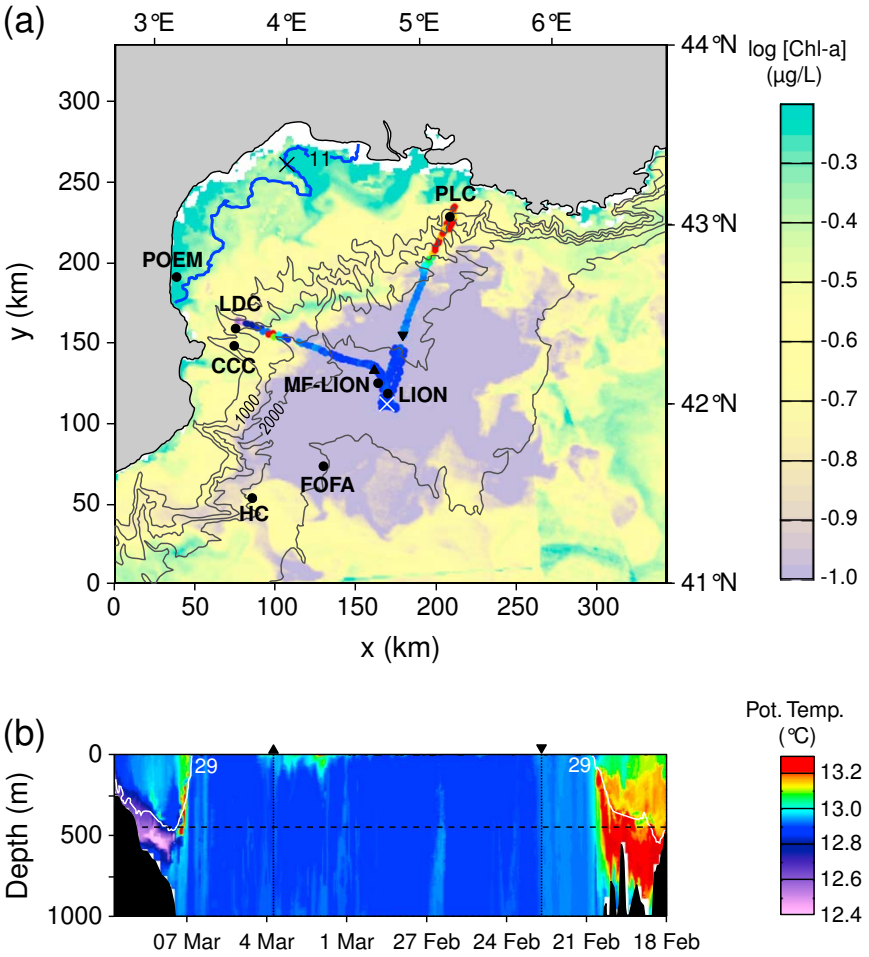

Figure 5.1: (a) Position of the moorings in the Planier (PLC), Lacaze-Duthiers (LDC), Cap de Creus (CCC) canyons, on the Catalan continental slope (HC, FOFA), and in the basin (LION), and of the surface buoys (POEM, MF-LION). Pale color patterns represent the surface Chlorophyll-*a* concentrations on 22 February 2012 derived from MODIS satellite image. The solid blue line on the shelf shows the offshore extension of the coldest surface water (<11° C) extracted from satellite-derived sea surface temperature on 22 February 2012. The V-shaped track represents the glider section performed between 19 February and 9 March 2012, and colors correspond to the potential temperature at 450 m depth. (b) Section of potential temperature (color) between the surface and 1000 m depth (or the bottom) along the glider section. The 29 kg m^{-3} isopycnal (white line) is superimposed. The horizontal dashed line indicates 450 m depth. Black triangles correspond to the reference points along the section.

Here we present a comprehensive set of hydrological and hydrodynamical observations collected during the winter and summer 2012 that provide new insights on the propagation and mixing of both type of the dense shelf waters, and their influence on the modification of the WMDW, as a new step in the Western Mediterranean Transition that started in 2005 CIESM [2009].

5.1.2 Data and Methods

Six mooring lines and two surface buoys constituted the observational design (Figure 5.1a). Three moorings were located at 1000 m depth in canyons at the NE (Planier, PLC) and SW ends (Lacaze-Duthiers, LDC; Cap de Creus, CCC) of the GoL margin, and three others between 1900–2500 m depth on the Catalan continental slope (HC, FOFA) and GoL basin (LION). Two meteorological buoys were located on the GoL inner shelf of the (POEM), and in the basin (MF-LION).

All the lines were equipped with current meters between 20 and 45 m above bottom, and the deepest ones also had a conductivity-temperature-depth (CTD) sensor. The line on the GoL basin, which extended from the seafloor to 150 m below sea surface, included 5 current meters, 11 CTD sensors regularly spaced along the line, and 10 supplemental temperature sensors above 650 m depth. Both buoys had a CTD sensor just below the surface, and the offshore buoy had also a thermistor string with 20 sensors between 2 and 200 m depth. The recording period lasted from December 2011 to June 2012.

Winter CTD data were collected between the surface and 1000 m deep with a Sea Glider deployed along a repeat-section in the GoL (Figure 5.1). A cruise (MOOSE 2012) was conducted in late July 2012 to perform an extensive CTD survey of the NW Mediterranean basin.

ERA-Interim reanalysis of atmospheric heat fluxes were collected from the European Centre for Medium-Range Weather Forecasts. We considered the modeled net heat fluxes from one grid point on the shelf and the closest grid point to the offshore buoy (see X marks in Figure 5.1a).

Merged product of Moderate Resolution Imaging Spectroradiometer (MODIS) and Operational Sea surface Temperature and sea-Ice Analysis (OSTIA) sea surface temperature was provided by ACRI-ST (http://www.acri-st.fr). MODIS ocean color observations of the surface chlorophyll-*a* (OC5 Chl-*a* products) were provided by the MyOcean project (http://www.myocean.eu/).

5.1.3 Results and Discussion

5.1.3.1 Atmospheric Conditions

The winds measured at the offshore buoy from mid- December 2011 to mid-March 2012 showed frequent NNW wind storms with speed ≥ 20 m.s^{-1} (Figure 5.2a). Several episodes of strong net heat loss both on the shelf and in the basin occurred in late December 2011 to early January 2012, and during the first two weeks of February 2012 (Figure 5.2b).

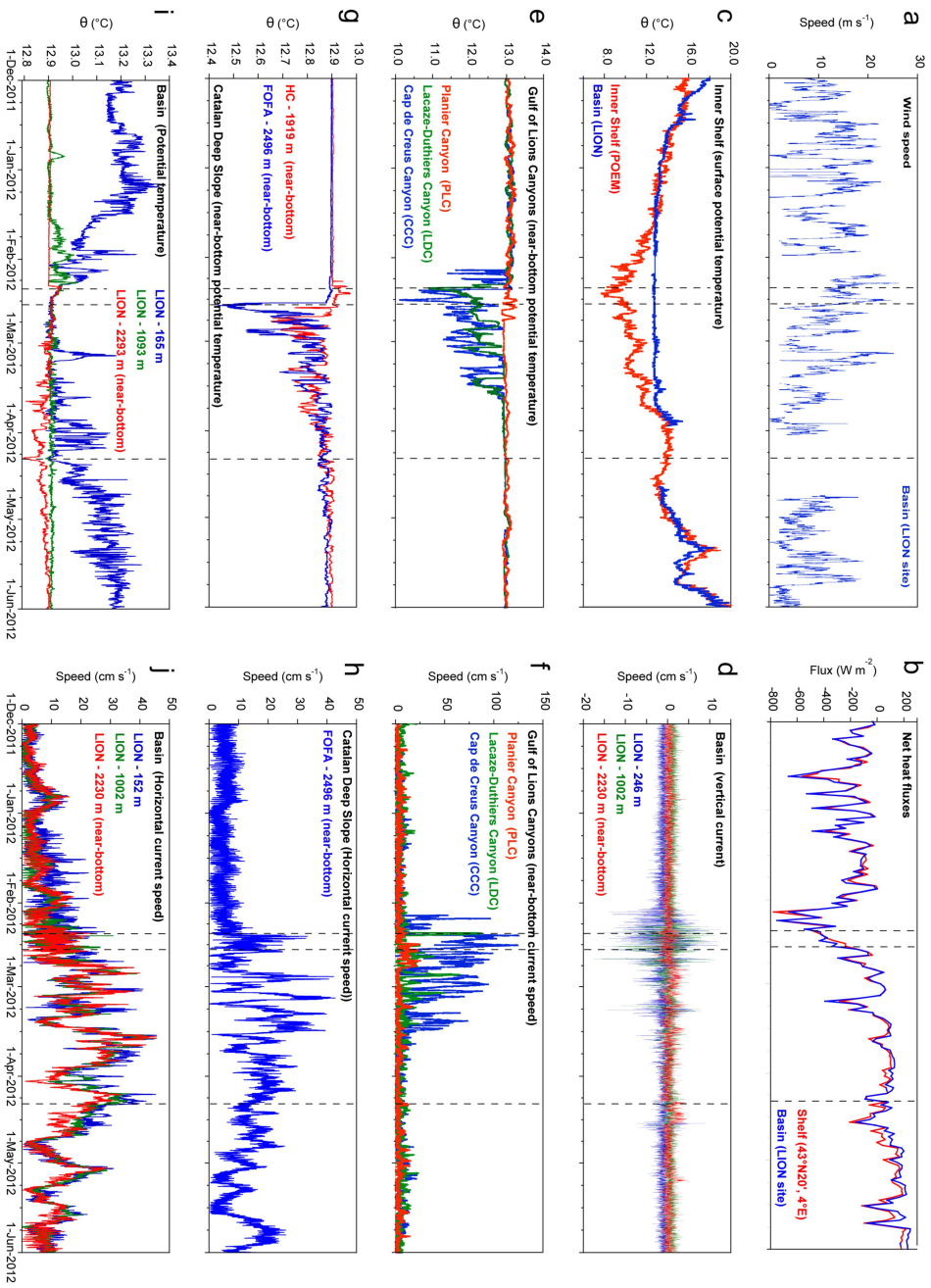

Figure 5.2: Time series of wind speed, net heat fluxes, potential temperature, and currents between 1 December 2011 and 1 June 2012. (a) Wind speed in the basin, (b) net heat fluxes on the shelf and in the basin, (c) near-surface temperature on the shelf and in the basin, (d) near-bottom temperature at 1000 m depth in the canyons of the GoL, (e) near-bottom horizontal current speed at 1000 m depth in the canyons of the GoL, (f) near-bottom temperature on the deep slope, (g) near-bottom horizontal current speed in the basin, (h) temperature at different depths in the basin, (i) vertical current speeds at different depths in the basin, and (j) horizontal current speed at different depths in the basin. Grey bands show the periods of AR weather regime.

Winter 2012 (*i.e.*, December 2011 to February 2012) can be considered as exceptional over the North Atlantic and Europe region. Following Cassou et al. [2010], the daily atmospheric synoptic circulation for this region can be described by four main weather regimes (fig. 5.3) : the negative (NAO–) and positive (NAO+) phases of the North Atlantic Oscillation, the Blockage (BL), and the Atlantic Ridge (AR). During a normal winter (DJF), the duration for each weather regime is respectively 20, 26, 23, and 22 days. However, during winter 2012, no day of NAO– was observed, whereas 44 days (+100%) of AR occurred. NAO+ and BL were closer to normal statistics. The AR regime is characterized by an anticyclonic anomaly in the North Atlantic and a cyclonic anomaly over the Baltic Sea, which is particularly favorable to strong, cold, and dry northerly winds over the GoL enhancing air-sea heat fluxes. During winter 2012, six periods could be identified with at least four consecutive days of AR conditions: 17–20 December, 4–14 January, 19–26 January, 2–5 February, 10–20 February, and 23–26 February. These episodes match well with the strong wind and intense heat loss events over the GoL (Figures 5.2a and 5.2b). It is worth to note that the AR pattern (based on daily weather regimes obtained by k-means objective classification) looks very similar to the negative phase of the East Atlantic

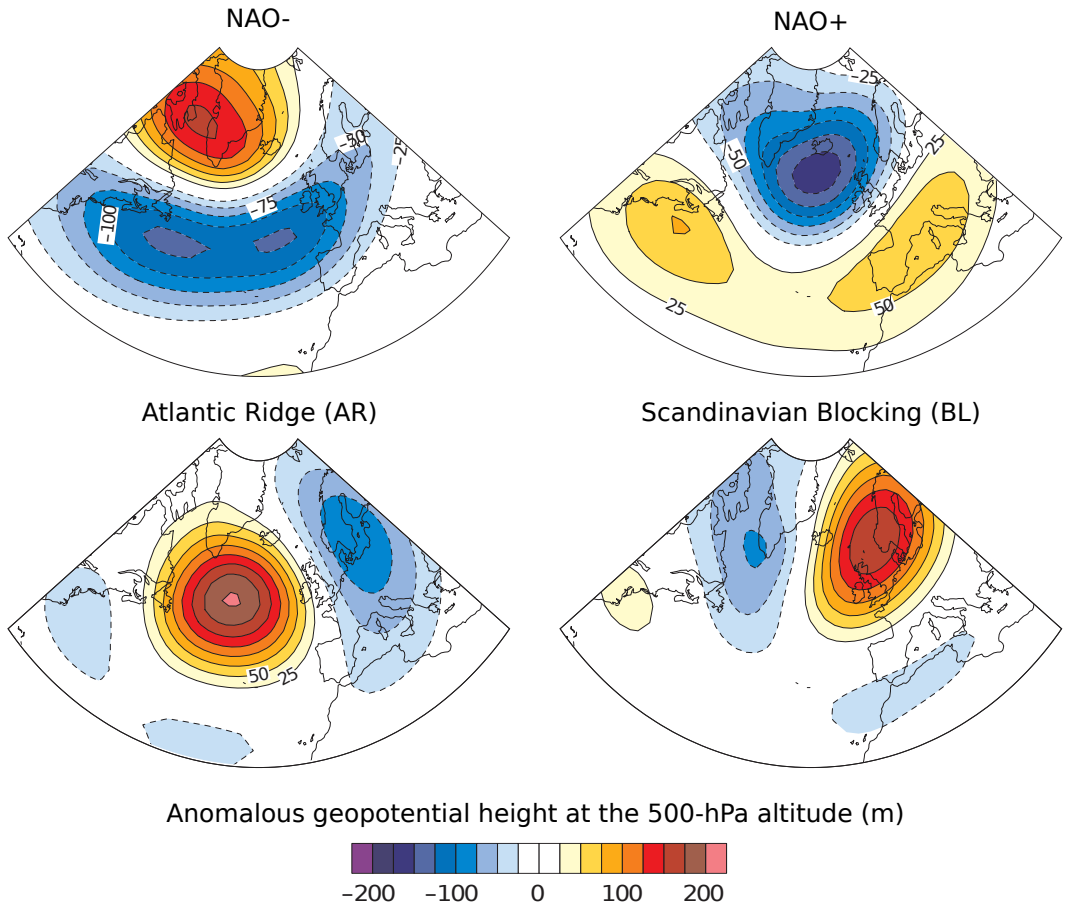

Figure 5.3: Centroids of the four weather regimes obtained from daily anomalous geopotential height at the 500-hPa altitude from the National Center for Environmental Prediction/National Center for Atmospheric Research (NCEP/NCAR) Reanalysis, adapted from Cassou [2008]

pattern identified by Josey et al. [2011] (based on monthly-mean climate pattern obtained by EOF techniques). Since 1958, the winters (DJF) with large positive anomalies of the number of AR days (at least +25%) and large negative anomalies of the number of NAO– days (at least -25%) were: 1966–1967, 1972–1973, 1975–1976, 1980–1981, 1998–1999, 1999–2000, 2004– 2005, and 2011–2012. Most of these winters correspond to years when thermo-haline anomalies indicative of intense shelf and open-sea convections were observed in the basin Bethoux et al. [2002]; Puig et al. [2012].

5.1.3.2 Formation of Dense Water on the Shelf and Cascading Along the Continental Slope

The winter heat loss induced a significant cooling of surface water (Figure 5.2c), especially on the inner and mid-shelf (Figure 5.1a). Temperature on the inner shelf was below 10°C during most of February, and fell to a minimum of 8°C on 13 February 2012 (Figure 5.2c). With this temperature and a salinity of 38.10, the potential density anomaly of the dense shelf water reached 29.710 kg m^{-3}, which exceeded the maximum density of the deep basin prior to the winter 2012 (29.126 kg m^{-3}).

The signature of dense water cascading in the GoL canyons was clearly visible through the temperature drop associated with strong downcanyon currents. While the eastern PLC did not exhibit significant changes, the southwestern LDC and CCC showed from 5 February 2012 to mid-March 2012 several episodes of dense shelf water cascading beyond 1000 m deep with a sharp temperature drop of 1 to 3°C (Figure 5.2d) and currents up to 125 cm.s^{-1} (Figure 5.2e). The cascading started earlier and was stronger in the CCC. The main cascading episode on 11 February 2012 was concomitant with the appearance of the coldest and densest water on the shelf (Figure 5.2c). A bottom plume of cold dense water about 200 m thick was visible in early March on the western end of the glider section along the LDC (Figure 5.1b).

The first anomaly reached the deep slope about 5 days after the main episode of dense water cascading off the GoL shelf. At 1900 m depth on the Catalan slope, a brief temperature drop of 0.15°C, indicating the passage of dense coastal waters was observed on 18 February 2012, while at ≈2500 m depth, the appearance of dense coastal waters was stronger (drop of 0.45°C) and earlier (16 February 2012) (Figure 5.2f). For both sites the temperature drops lasted until the beginning of April 2012.

Farther northeast in the basin, the signal of dense shelf water reached (≈2350 m depth) on 28 February 2012 (Figure 5.2h), and was delineated by potential temperature ≤ 12.905°C and density anomaly ≥ 29.13 kg m^{-3} corresponding to the horizontal cusp on the Theta-S curves (Figure 5.4). The temperature drops (up to 0.1°C) were primarily perceived near the bottom (last few hundred meters above the seabed). However, on some occasions, the negative thermal anomaly reached shallower levels of the water column, indicating the passage of plumes of dense shelf water of variable thickness. On 2–3 March 2012, and on 9–10 April 2012, remarkable anomalies were visible between the bottom and 1000 m depth (Figure 5.4). The maximum density of the new bottom water at the basin site reached 29.135 kg m^{-3}.

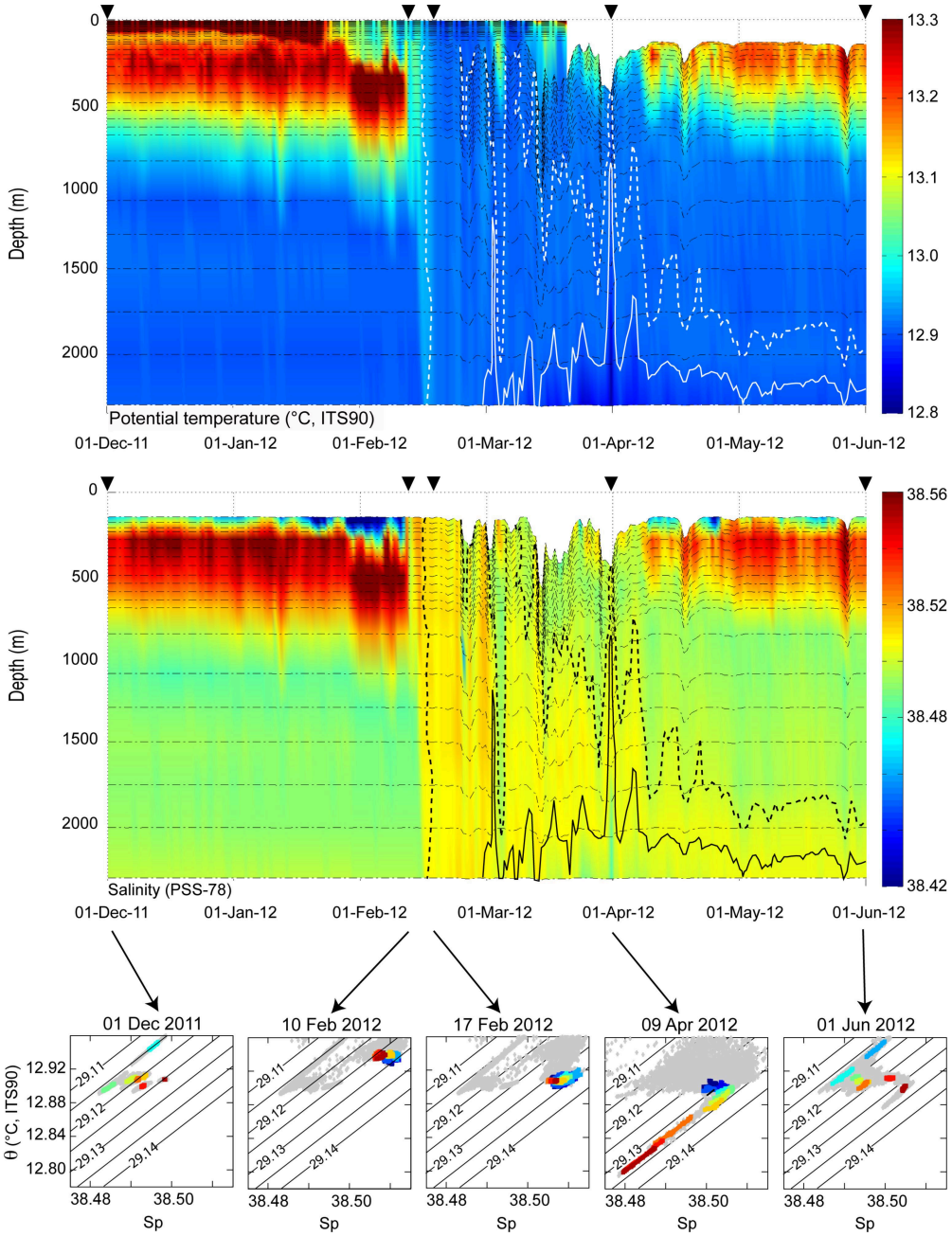

Figure 5.4: (a) Surface plot of temperature and salinity in the basin site (LION) between 1 December 2011 and 1 June 2012. The horizontal dashed-dotted lines indicated the depth of the sensors. The thick dashed line depicts the upper limit of water denser than 29.126 kg m^{-3}, and the thick solid the upper limit of bottom water denser than 29.13 kg m^{-3} and colder than 12.905°C. Theta-S plots (b) prior to the deep water formation, (c) at the time of arrival of the mixing layer at the bottom, (d) at the end of the strong mixing period, (e) during the apparition of colder and fresher bottom water, (f) during the spreading period. The colors correspond to the CTD measurements during a 12 h interval at the different levels (from the shallowest one in blue to the deepest one in dark red). The grey patterns represent the measurements during the month preceding the date of each diagram.

5.1.3.3 Formation of Dense Water in the Open Sea

The winter heat losses in the basin cooled the surface layer down to 12.6°C (Figure 5.2c). At the basin site, strong vertical mixing was evidenced by high frequency vertical velocities of about ±10 cm.s^{-1} (Figure 5.2i). The thickening of the mixed layer started in December 2011, reaching the Levantine Intermediate Water layer (characterized by a relative maximum temperature and salinity between 200 and 700 m depth, Figure 5.4) around mid-January 2012 and deepened rapidly to reach the seabed at 2350 m on 10 February 2012, provoking an increase of the near-bottom temperature and salinity (Figures 5.2h and 5.4). Between 10 and 17 February 2012, the sustained surface heat loss produced a supplementary cooling of the mixed water column of 0.04°C with no significant change of salinity. Hence, with a potential temperature of 12.905°C and a salinity of 38.508, the maximum density of the new deep water formed by open-sea convection at the basin site reached 29.134 kg m^{-3} (Figure 5.4). It eventually formed a deep layer, whose upper limit was identified with the isopycnal 29.126 kg m^{-3} (maximum bottom density encountered at the three deep sites prior to the convection period), overlying the bottom water layer (Figure 5.4).

The surface signature of the convection zone was recognized by a minimum surface chlorophyll concentration (< 0.1 μg L^{-1}, Figure 5.1a). The temperature and density distribution along the glider section across the northern half of the GoL basin confirmed the extension of the convection area down to 1000 m deep (Figure 5.1b). These observations suggest that the region of intense vertical mixing extended over a large (≈70 km radius) area, with the basin site being in the central part, and the deep slope sites being on the periphery. The open-ocean convection signal was sensed at the 1900 m site as a slight increase of near-bottom temperature preceding the arrival of cold dense shelf water, but it barely reached the 2500 m site. (Figure 5.2f).

5.1.3.4 Propagation of Newly Formed Deep and Bottom Water in the Deep Basin

Horizontal currents at the basin site were mostly barotropic and isotropic. Current speeds increased at the onset of newly deep waters advent, reaching maximum of 30 to 40 cm.s^{-1} during March and April, and decreasing afterward (Figure 5.2j). At the deep slope site, the period of strongest current speed was shorter (from mid-February to mid- March) and coincided with the cascading period (Figure 5.2g). At both sites, the currents presented large fluctuations around 2–15 days due to strong eddies contributing to the spreading of the newly-formed deep water, as shown by Testor and Gascard [2006].

The progressive spreading of the newly formed water by open-sea convection during the restratification period generated a ≈300 m thick layer, overlying bottom dense waters of coastal origin, ≈150 m thick (Figure 5.4). The extent and thickness of the newly formed deep and bottom waters remaining in the GoL and Ligurian basins in summer showed that the combination of the two layers formed a dome-shaped lens, with a maximum total thickness of 520 m (average 206 m) embracing the winter convection region (Figure 5.5a). The new deep water layer's thickness averaged 110 m, whereas the layer of new bottom water was thinner

and averaged 96 m. However, the summer survey evidenced the presence of two isolated stations on the western part of the lens with anomalous bottom water extending 1100 m above the seafloor (points d and e in Figure 5.5), likely indicative of eddies.

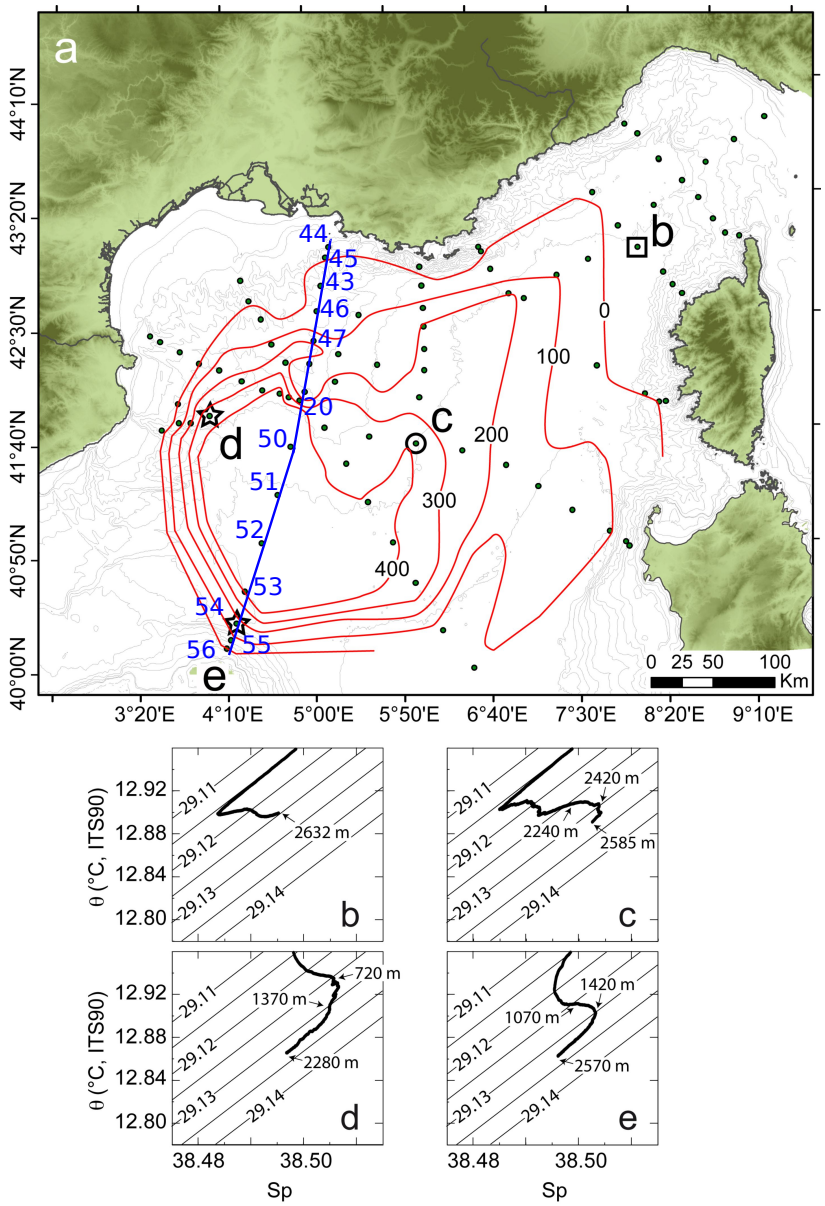

Figure 5.5: CTD stations performed during the summer cruise MOOSE (24 July to 8 August 2012), and cumulative thickness of the deep and bottom layers denser than 29.126 kg m^{-3}. The blue line indicates the hydrological section and the blue number indicated the CTD station discussed in the section 5.2 (a). Theta-S diagrams showing pre-2012 deep waters (square, b) and newly-formed ones (circle, c). Theta-S diagrams of the two peculiar stations (stars, d and e) showing a bottom anomaly extending about 1100 m above the seabed (not used in the mapping of thickness of the deep and bottom layers). The numbers indicate depths of the upper limit of the deep and bottom layers, and of the seabed.

5.1.3.5 Volume Estimates

The estimated volume of dense (≥ 29.126 kg m^{-3}) water formed by open-sea convection during the winter 2012, considering thickness of the mixed patch ≈2.2 km and a surface of ≈15,500 km^2 (horizontal extent with chl-*a* concentration ≤0.1 μg L^{-1}, Figure 5.1a), amounted to about 34,100 km^3, which corresponds to an annual mean flux of ≈1.1×10^6 m^3 s^{-1}. This flux is close to the mean production rate for the two winters 2005 and 2006 (≈2.4×10^6 m^3 s^{-1}) estimated by Schroeder et al. [2008]. The flux of dense shelf water cascading down the CCC, which concentrates about half the total volume of dense shelf water exported beyond 1000 m depth according to Ulses et al. [2008a], was approximated using the observed current speed associated with water colder that ambient water (*i.e.*, $\theta \leq 12.92$°C), and a plume cross-section of 200 m thick (inferred from Figure 5.1b) and 4 km wide (local canyon width). The cascading period accounted 43 days with a mean downcanyon speed of 36.6 cm s^{-1}, and the volume of dense shelf water exported beyond 1000 m depth in the CCC amounted to ≈1,100 km^3, which was comparable to the volume estimated by Ulses et al. [2008a] for the winter 2005. Assuming that the CCC exports half the total volume of dense shelf water, the mean flux to the basin corresponds to 0.07×10^6 m^3 s^{-1}, which is one order of magnitude less than the production of dense water by open-sea convection.

The volumes of newly formed deep ($\sigma_\theta \geq 29.126$ kg m^{-3}) and bottom ($\sigma_\theta \geq 29.13$ kg m^{-3} and $\theta \leq 12.905$°C) waters that have not yet been advected or diffused out of the central part of the NW Mediterranean in summer 2012 (Figure 5.5a) were estimated at 14,000 and 7,600 km^3, respectively. Albeit these values underestimated the actual volumes because the cruise did not cover the entire deep basin, the large in- crease of the volume of bottom water, with respect to that of the dense water exported from the shelf, implied a large entrain- ment of ambient waters during its propagation down the slope and in the basin, including newly-formed deep water. Finally, these volumes were large enough to markedly alter the thermo-haline characteristics of the deep basin even more, hence contributing to amplify the Western Mediterranean Transition CIESM [2009].

5.1.4 Concluding Remarks

Coastal and open-ocean deep convections are phenomena that ventilate the deep waters of the NW Mediterranean, and are potentially key processes for the climate variability. These observations allow to definitively conclude on the origin of the thermohaline anomalies that were repeatedly observed over the last 40 years in the GoL. Although the preconditioning is certainly a key factor, we showed that the combined formation of deep water of coastal and open-sea origin is likely related to peculiar large-scale atmospheric circulation patterns. This study provides a first quantitative benchmark and, in particular, useful estimates of spatial and temporal scales associated with these ventilation mechanisms. This reference case can contribute to improve the capacity of the numerical ocean models that do not yet well reproduce deep convections for thorough analyses of their impact on the long-term variability of the WMDW.

5.2 Complementary Results on Newly-Formed Deep Water Spreading in 2012

5.2.1 Eddy of newly-formed deep water flowed off Minorca

Additional results from the MOOSE-GE 2012 oceanographic cruise are presented on figure 5.6. In addition to the potential temperature and salinity section, we presented also the voltage signal of the Underwater Vision Profiler (UVP). This optical instrument, coupled to the CTD-Rosette package (Picheral et al. [2010]), acquires focus images in a virtual volume of water delimited by a light sheet issued from red light-emitting diodes (LEDs) of 625 nm wavelength at a frequency up to 6 Hz. The smaller size limit is fixed by optical resolution, whereas the larger size limit is determined by the volume of water illuminated per image. Recorded images can be automatically digitized, classified and analyzed, and the results can be expressed as abundance and/or size distributions. It enables to quantify the vertical distribution of macroscopic particles and zooplankton between 60 μm and 26 mm in size.

One can clearly see a strong dooming of the deep isopycnal at the station 54 (fig. 5.6, also corresponding to the cast "e" in the 5.5). The 750m elevation of the 29.128 kg.m^{-3} isopycnal at the station 54, together with the salinity anomaly from 200m to 2000m (fig. 5.6) may indicate the presence of a cyclonic eddy with a deep core composed from newly-formed deep water (S >38.5). Below this salty core, salinity and temperature decrease, and the potential density anomaly exceeds 29.132 kg.m^{-3}. The density of the bottom water is denser that the one observed during previous winters (chapter 4, figure 4.9) and this water mass is colder and fresher compared to the rest of the cross-basin hydrological section (fig. 5.6), indicating that this bottom water mass may have its origin in the 2012-DSWC event (see previous section).

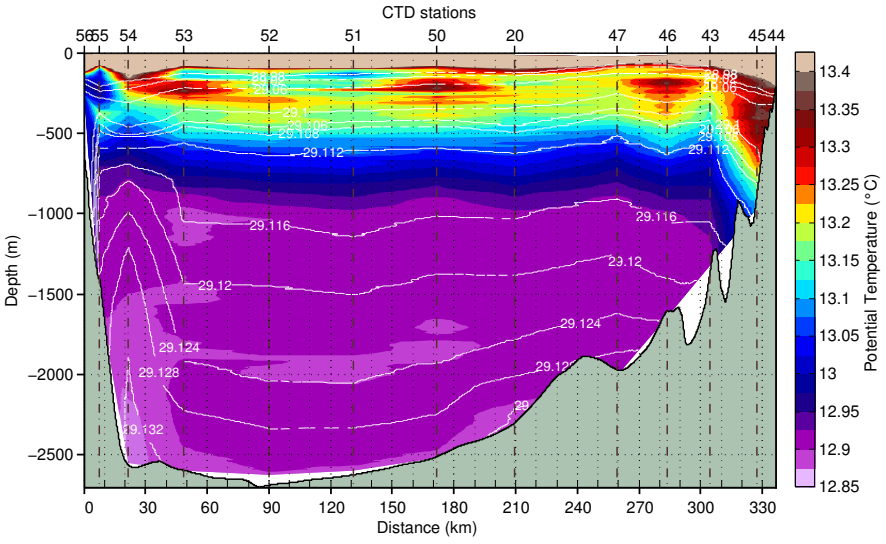

Figure 5.6: (Continued on the following page.)

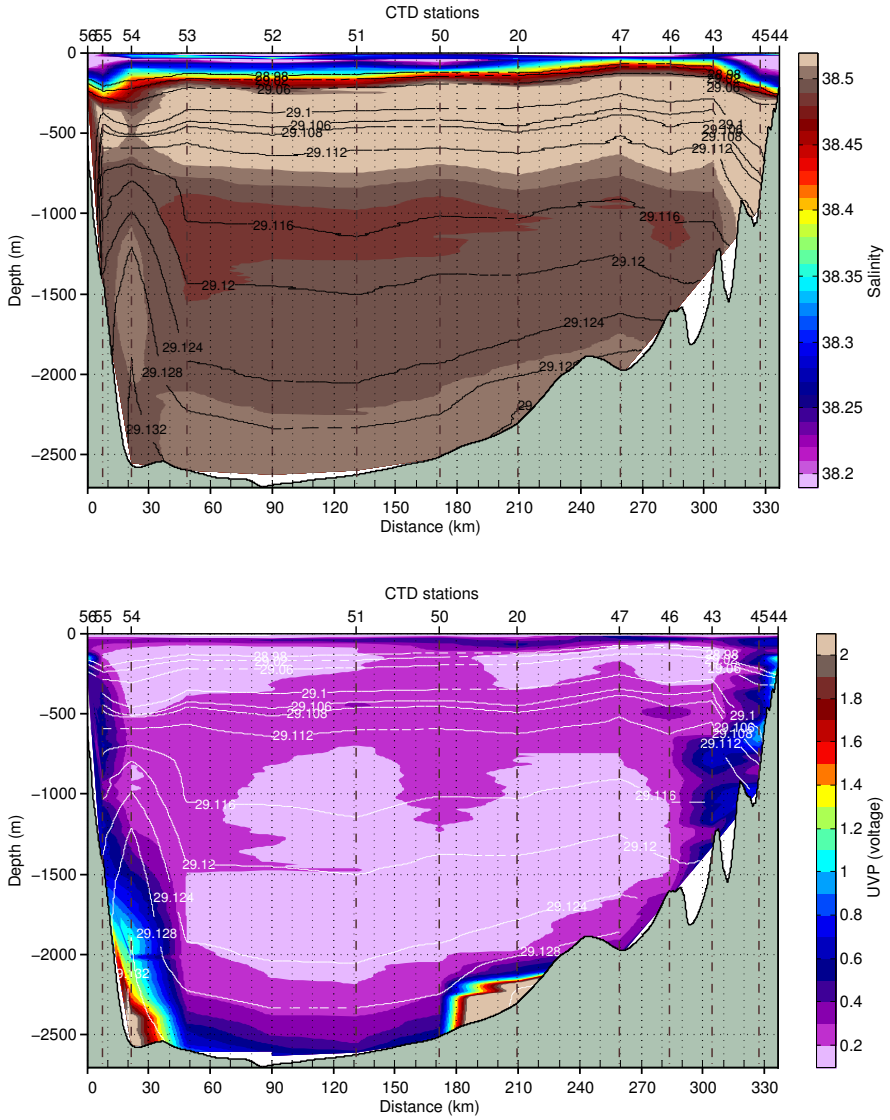

Figure 5.6: Potential temperature, salinity and a proxy of the particulate suspended matter (bottom) measured during the MOOSE-GE 2012 campaign. White and black contour line represent the potential density anomaly (kg m^{-3}). Locations of CTD stations are indicated on figure 5.5. The colormap is saturated in light brown for temperature above 13.4, salinity above 38.51 and signal of UVP exceeding 2. The same applies to salinity lower than 38.2 with a colormap saturated in light pink.

The relative cold and fresh θ/S anomalies of the bottom water mass observed during the CTD-station 54, is 500m thick, and is also related to a 500m elevation of the 29.132 kg.m^{-3} isopycnal. Moreover a clear signal on the UVP voltage channel was recorded when the CTD-Rosette has penetrated the bottom water mass (fig. 5.6). Another bottom turbidity anomaly was detected in the middle of the basin, near 42°N, 5°E at the CTD station 20 (see figure 5.5 for a more accurate location). Even if this turbidity anomaly is twice thinner than the one observed during the CTD cast 54, it is still 400m thick. In this case as well, the increased turbidity is also

related to an increase of the bottom potential anomaly density. These observations support results of the study made by Puig et al. [2012], where the formation, the spreading and the persistence of thick bottom nepheloid layer in the Gulf of Lions were related to dense water formation events (by DSWC and OODC).

Finally this eddy was detected off Minorca, in a region of strong f/h gradients. As the displacement of water masses is highly constrained by the f/h contours. This region might be view as a channel for the exportation of newly-formed water masses. This idea supports results from Send et al. [1996], who have estimated that 50% of the newly-formed water could be incorporated into the boundary current and thus into the general circulation.

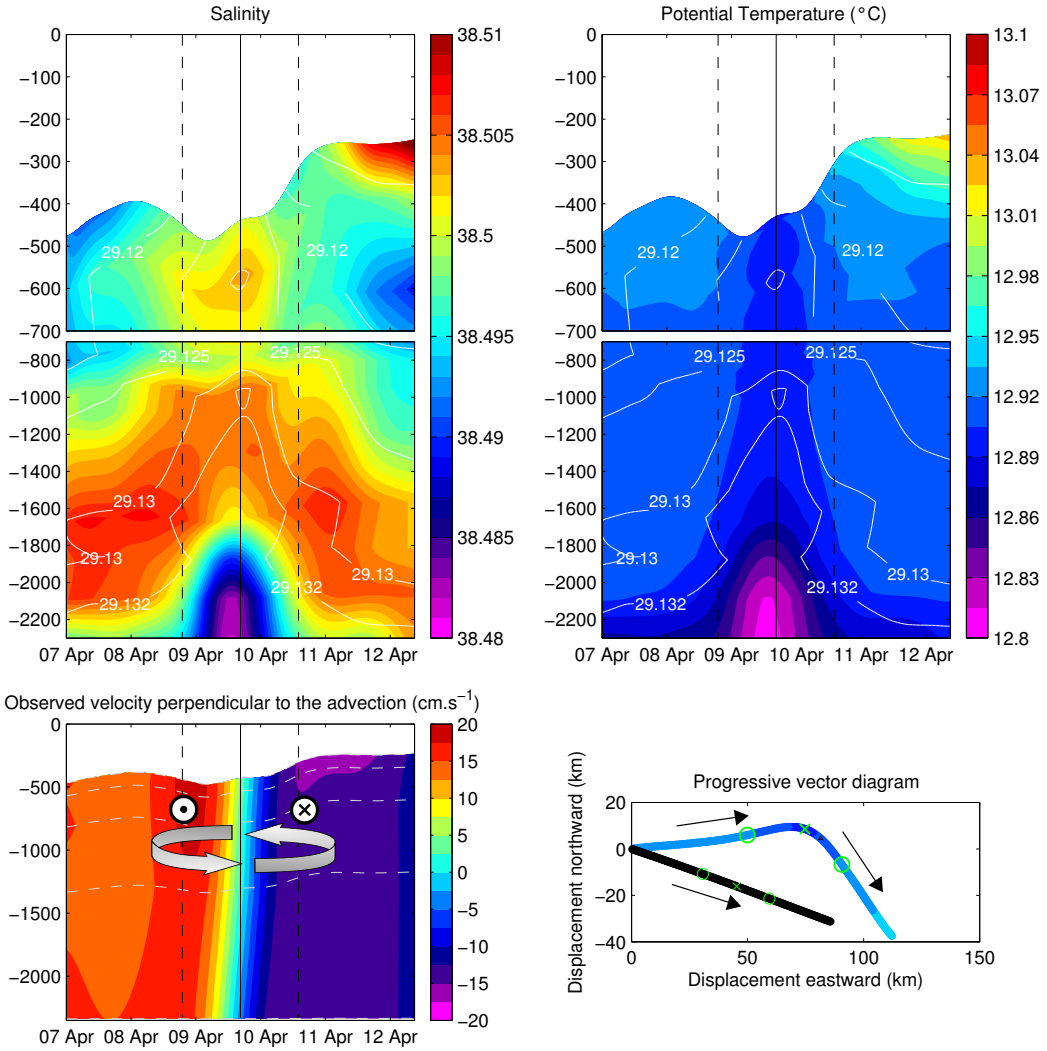

Figure 5.7: (Continued on the following page.)

Figure 5.7: Salinity, temperature, eddy current, and progressive vector diagram of the eddy crossing the mooring line the 10 April 2012. White horizontal thin lines on salinity and temperature graph, correspond to isopycnals. Vertical black lines correspond to the eddy center and black dotted vertical lines correspond to the eddy rim. On the progressive vector diagram, the color line corresponds to total velocity recorded by the 1000m current meter with a colormap corresponding to the temperature recorded by the 300m microcat instrument, while the black line corresponds to the estimated advection. Green cross and circles indicate respectively the center and the rim of the eddy. The projection of the horizontal velocity recorded by the current meter onto the advection direction gives us the observed velocity perpendicular to the advection, corresponding to the eddy velocity (bottom left panel).

5.2.2 Eddy of DSWC observed at the deep mooring line LION

As presented in the chapter 4, figure 4.9 and in this chapter, figure 5.4, a remarkable signal occurred the 10 April 2012 after that the MLD has reached the bottom, corresponding to a strong decrease in θ (-0.1°C) and S (-0.03) that indicates the arrival of dense shelf water to the mooring location. Using the eddy detection method (see section 4.3.2), this strong signal was identified as a cyclonic eddy crossing the mooring (figure 5.7). Its core radius was estimated to be 12.0 km with a peak observed azimutal speed of 15.7 cm.s^{-1}.

Even if the mooring line has sunk of 300m due to intense horizontal velocity >35 cm.s^{-1} (maximal value of 15.7 cm.s^{-1} for the eddy velocity plus an advection estimated at 20.0 cm.s^{-1}, table 4.4), one can cleary see on the figure 5.7, the 1000m elevation of the 29.132 kg.m^{-3} isopycnal corresponding to the eddy center detection. The maximal elevation of the 29.132 kg.m^{-3} was also associated to a 400m-thick bottom thermohaline anomaly with low values for θ and S that supports the hypothesis of a “coastal” origin for this deep water mass. The cyclonic direction of rotation for this eddy can also be found through the progressive vector diagram of the figure 5.7, and using the simple case studies presented in the chapter 4, section 4.3.2. As the progressive vector diagram of the observed current is deviating to the left compared to the perpendicular to the direction of the advection, this eddy has to be a cyclonic eddy.

Conclusions

Seasonality of the Upper Layer Stratification in the Mediterranean

A new climatology of the thermocline slope was produced for the Mediterranean, on a 0.5° latitude x 0.5° longitude x 12 months grid based on more than 140 000 profiles collected between 1969 and 2012. The distribution of the depth of the thermocline, together with the thermocline slope and the upper-ocean temperature revealed well known features of the Mediterranean circulation like the deep water formation zones or the anticyclonic and cyclonic gyres of the Cretan Arc. By pushing forward the analysis we were able to build the first climatology of the upper-ocean heat rate in the Mediterranean, based only on in-situ oceanographic data. This constitutes a new benchmark in particular for the development of ocean and/or coupled models. We highlight the implication of known Mediterranean circulation patterns in the heat storage and horizontal redistribution at a sub-basin scale. The seasonal cycle of the basin-mean upper ocean heat storage rate is estimated as varying from -162.5 $\pm$ 5.2 W m^{-2} in December to +129.8 $\pm$ 3.4 W m^{-2} in June, and its annual value is estimated at -2.6 $\pm$ 4.1 W m^{-2}. On an annual basis, the decrease of the upper ocean heat storage rate is partly compensated by an increase in the upper ocean heat entrainment rate estimated as +2.2 $\pm$ 2.0 W m^{-2}. Since the uncertainties on our results are superiors to the total upper ocean heat rate (the sum of storage and entrainment terms: - 0.4 $\pm$ 4.6 W m^{-2}), we cannot establish a significant long-term trend in the warming or cooling of the upper Mediterranean layer. The limitations of our studies (period covered, uncertainties) stress the need of sustained synoptic and long-term observing systems (repeated cruises, Argo profiling floats, network of gliders).

In addition to the important role that the oceanic mixed layer may play in the physical climate, particularly in the heat storage, this layer has also a major influence on chemical and biological processes (including the phytoplankton which is the first element of the marine trophic chain). The mixed layer depth control on the phenology of phytoplankton in the Mediterranean was also investigated through a collaboration with biogeochemists. If the MLD and the surface chlorophyll peaks are concomitant in the “no bloom” regime, MLD peak precedes surface chlorophyll peak by about 30 days in the ’bloom“ regime. Moreover for the “No Bloom” regime, observations indicate that phytoplankton would never be limited by light, whatever the MLD, and would even grow during the winter period thanks to small nutrient

inputs. For the “Bloom” regime, the important supplies of nutrients in surface waters by deep mixing and the low uptake rate by phytoplankton (episodically limited by a deficit of light), lead to the hypothesis that the nutrients accumulate in surface waters during winter, which could explain the 30 days time-lag between MLD and surface chlorophyll peak, characteristic of the “Bloom” regime.

Interannual Variability of Dense Water Formations in the Northwestern Mediterranean

Open-Ocean Deep Convection and Dense Shelf Water Cascading in the Gulf of Lions

The LION mooring line, together with CTD stations and glider deployments carried out in the Gulf of Lions since 2007, compose one of the major dataset used in this thesis. The deep LION mooring was set up in the Gulf of Lions in 2007 and is still maintained in the framework of the observing system MOOSE. The line was equipped with 8 to 26 instruments with currently 20 temperature sensors, 10 conductivity sensors and 5 current meters spanning between 150m and 2300m depth. Through these 5 year long timeseries, 5 consecutive winters of deep convection were monitored, especially 4 winters where deep convection has reached the bottom (2300m depth).

Several temporal scales associated to the deep convection process have been precised for the first time:

- The time for the mixed layer deepening is comprised between 1 and 2 months
- If the mixed layer has reached the bottom (usually at the end of January / beginning of February), there is a violent vertical mixing phase of the whole water column (with a duration of 9-12 days)
- The 4 severe winters (from 2009 to 2012) present a second vertical mixing period that generally occurs in March after the main event of deep ocean convection. This short event (2-4 days) happens when the water column is not fully stratified and a 3-6 days period of buoyancy loss (like winter storm) can easily destabilize the water column, leading to vertical mixing
- We define a ”restratification time“ of the intermediate layer (200-600m) as the time needed by this layer to recover 50% of its heat content lost during deep convection. For the years 2010, 2011 and 2012, the ”restratification time” is ranging between 2.5 and 4.5 months.
- A “spreading time” of the newly-formed deep water was defined as the time needed to the water column to dissipate 50% (respectively 75%) of the potential density increase in the 600-2300m layer that occurred at the end of the strong vertical mixing phase. It takes approximatively 1.5 to 3 months (resp. 3 to 6 months), reflecting the spreading and mixing of the newly-formed deep water with the ambient deep water.

The long restratification and spreading time that can be observed after each winter of deep convection show that the restratification/spreading phase is still active at the beginning of the next deep convection event, indicating a “memory effect” of the water column and a overlapping of the 3 “phases” of deep convection. This also highlights the crucial need of a correct modelization of eddies throughout the year if one wants correctly simulate the phenomenon of deep water formation.

For the first time in the Gulf of Lions, we were able to highlight the seasonal variations of the vertical structure of horizontal currents between 150m and 2300m depth. 85% to 95% of the variance of the horizontal currents (between 150m and 2300m depth) can be explained by the 1st EOF (interpreted as the equivalent barotropic mode, since we did not know the surface/sub-surface currents), while the second mode (interpreted as the 1st baroclinic mode) contains 5% to 10% of the variance. Theses new results indicated that the vertical structure of horizontal currents from 150m to 2300m is mainly barotropic, and seasonal variations in currents seem to be running as a 4-phase cycle:

- a baroclinic and quiet period in late fall,
- a baroclinic and energetic period in winter,
- a equivalent barotropic and energetic period in spring / early summer,
- a equivalent barotropic and quiet period in late summer / early fall

This wintertime excitation of currents may have been generated by the thermodynamic forcing of the region by surface buoyancy flux. Mesoscale currents become stronger with the deep convection activity and the transfer of the potential energy of the ”mixed patch“ into kinetic energy, increasing the ”baroclinization“ of the water column. The evolution of the baroclinic flow field into a barotropic one might be the result of the geostrophic turbulence cascade to large scales Rhines [1979]; Venaille et al. [2012].

Using a wavelet-based detection method of isolated horizontal velocity anomalies, 37 eddies were detected between October 2009 and July 2012 (18 anticyclones and 19 cyclones). The radii (velocities) ranging from 0.7 km to 20.0 km (0.9 cm.s^{-1} to 25.1 cm.s^{-1}). The main mode of the distribution of eddies radii is centered at 4 km for the cyclones and 5 km for the anticyclones. Cyclones might have been mainly formed during the intense vertical mixing phase, when the very weak stratification leads to a small Rossby radius of deformation, while anticyclones are detected mainly from the spreading / restratification phase.

The high temporal resolution of the mooring line enable a fine survey of the formation of new deep water and the evolution of their potential temperature and salinity characteristics. For the winters with an open-ocean convection that has reached the bottom, there is first a significant increase of potential temperature (between 0.02 and 0.04°C) in the bottom layer, due to the deepening of the mixed layer down to the bottom. Then the intense vertical mixing and strong buoyancy loss period (9-12 days) produce a decrease in the potential temperature

of the mixed layer, and hence the potential temperature of the newly-formed deep water, ranging from 0.01 to 0.03°C. Unlike the potential temperature, the salinity of the newly-formed deep water does not shown significant variations after the deepening of the mixed layer down to the bottom. The salinity of the newly-formed deep water seems to be fixed by the salinity of the mixed layer once it reaches the bottom, corresponding to an increase between 0.006‰ and 0.012‰, for the 2007-2012 period.

The apparition of newly-formed deep waters was detected in winter 2009, 2010, 2011 and 2012. In winter 2010, two newly-formed deep waters were detected after the deep convection event, both present a different potential temperature but a similar salinity, suggesting that both might be formed in the cyclonic gyre, but in different locations. In 2012, two new deep waters were detected at the mooring location, one was identified as a result of open-ocean deep convection, while the other seems to be the result of a dense shelf water cascading event that occurred in winter 2012.

For all winters we found that the integrated surface buoyancy losses from the 1st November to the end of February, based on Era-Interim reanalysis, are higher than the buoyancy content of the water column before each event of deep convection. This indicates that the water column is not enough stratified at the beginning of November to prevent the deepening of the convection, assuming than the horizontal advection of buoyancy content is relatively low at that time. On the 5 winters studied, 2011 seems to be the winter during which the water column was the less stratified in early November. This may explain why 2011 was a "deep-convective" year, while heat losses were comparable to 2004 (a year without deep convection).

For the winter 2011/2012, five additional mooring lines were used to monitor the formation and the propagation of an intense event of dense shelf water cascading that spread into the deep basin. The arrival of dense shelf water to the location of the LION mooring line has caused a strong decrease in θ (-0.1°C) and S (-0.03). This strong signal was identified as associated to a cyclonic eddy with a core radius estimated to be 12.0 km and a peak observed azimutal speed of 15.7 cm.s^{-1}. The detected eddy center was also related to a 1000m-elevation of the 29.132 kg.m^{-3} isopycnal and to a 400m-thick bottom thermohaline anomaly with low values for θ and S that supports the hypothesis of a "coastal" origin for this deep water mass.

Impacts on Particle Fluxes and Deep Ecosystems Activity

Open-Ocean Deep Convection and Dense Shelf Water Cascading are key processes that connect the surface ocean to the deep ocean. In addition to heat and salt, dense water formations may transfer also biogeochemical components to the deep water, like oxygen and inorganic and organic matter, contributing to the ventilation and the "feeding" of the deep pelagic and benthic ecosystems.

Trough collaborations with biogeochemists and sedimentologists, the influence of dense water formations on bottom sediment resuspension, and therefore on the thickness, the

spreading and the persistence of the bottom nepheloid layer were investigated. The significant remobilization of sediments, in the basin of the Gulf of Lions after dense water formation events, has been also likely to induce a subsequent alteration of the seabed and to impact the functioning of the deep-sea ecosystem. Dense water formation events and the spreading of newly-formed deep water were also revealed as an important factor in the activity of deep-sea pelagic ecosystem by fueling it through the supply of relative “fresh” organic matter, and thus by stimulating bioluminescence activity.

Research Perspectives

Future comparisons between the Mediterranean climatology of the upper ocean heat rate and other heat fluxes climatologies may be useful to test heat fluxes parameterization and thus improve the accuracy of Atmosphere-Ocean Global Circulation Models, particularly in the context of long term climate simulations that require, among others, a good modeling of the thermohaline circulation. Future works would also be to compare our estimated monthly climatology of horizontal advection of heat in the upper ocean to other estimates, like oceanic simulations and/or other climatologies deduced from surface geostrophic currents estimates.

In this study, a comparison between the buoyancy content of the water column before wintertime and the surface buoyancy losses integrated on the November-February period was done. Although the factors responsible of these 5 consecutive deep convection events were highlighted, this comparison also points out the needs of additional conductivity sensors in the first 200m of the water column for accurate calculations. In order to minimize the error on the calculation of the buoyancy content of the water column before the deep convection (an indication of the “preconditioning state” of the ocean), full profiles created with a single platform of measurements at the end of October / beginning of November might be useful. Thus, the repeated surveys that are carried out by gliders in the framework of the observing system MOOSE in the Gulf of Lions are valuable to get 1000m-depth profiles close to the LION mooring.

Further works have to be done to better understand the origin and the fate of the different sort of eddies detected in this study. Numerical experiments might be a good tool to study the eddy generation and decay, but numerical grids might be to large to describe precisely these small scale eddies (more than 50% of cyclones and anticyclones detected have a radius inferior to 6 km). Thus the combined use of a real-time mooring and gliders would be a useful tool to easily trigger sampling cruises and follow the evolution of these kinds of eddies. Moreover the recent development of biogeochemical sensors can also be useful to get additional informations on the "biogeochemical signature" of these eddies and to study their potential impacts on triggering phytoplankton blooms in the Northwestern Mediterranean, since they can carry in their cores complete ecosystems, relatively isolated from the outside.

Another perspective will be to track the spreading of the newly-formed deep water outside the NWMED (with a network of deep moorings deployed off Minorca and between Minorca

and Sardinia, for example), to quantify transports of heat and salt. The heat and salt diffusion is made throughout the spreading of the new deep waters in the Western Basin and in the Strait of Gibraltar, where some of them are part of the outflow, and therefore part of the Mediterranean Waters which spread at 1000m depth into the North Atlantic and thus join the global circulation. Different subbasin-scale surveys using gliders and ships could be very valuable to monitor the mixing of the newly-formed deep waters with the surrounding waters in different subbasin (Alboran Sea, Algerian Basin, Tyrrhenian Sea).

Conclusions

Cycle saisonnier de la stratification de la couche de surface en Méditerranée.

Une nouvelle climatologie de la pente de la thermocline a été produite pour la Méditerranée, sur une grille de 0.5° de latitude x 0.5° de longitude x 12 mois, construite à partir de plus de 140 000 profils recueillis entre 1969 et 2012. La distribution de la profondeur de la thermocline, ainsi que la pente thermocline et la température supérieure de l'océan révèlent des traits bien connus de la circulation océanique en Méditerranée, comme les zones de formation d'eaux profondes, ou les tourbillons cycloniques et anticycloniques qui bordent la Grèce. En développant notre analyse, nous avons pu construire la première climatologie du taux de chaleur dans la couche de surface de la Méditerranée, basée uniquement sur des données océanographiques *in situ*. Cela constitue une nouvelle référence, en particulier pour le développement des modèles océaniques et/ou couplés. Nous soulignons dans ce travail l'implication de composantes, connues dans la circulation méditerranéenne, dans le stockage de la chaleur et sa redistribution horizontale à l'échelle des sous-bassins. En moyenne sur l'ensemble de la Méditerranée, le cycle saisonnier du taux de stockage de chaleur dans l'océan de surface varie de -162,5±5,2 W m $^{-2}$ en Décembre à 129,8±3,4 W m $^{-2}$ en Juin. Sa valeur annuelle est estimée à -2,6±4,1 W m $^{-2}$ en moyenne. Sur une base annuelle, la baisse du taux de stockage chaleur dans la partie supérieure de l'océan, est en partie compensée par une augmentation du taux de chaleur lié à l'entrainement des couches inférieures et estimé à +2,2±2,0 W m $^{-2}$. Étant donné que les incertitudes sur nos résultats sont supérieures à la valeur moyenne du taux de chaleur (la somme des termes de stockage et d'entraînement est de -0,4±4,6 W m $^{-2}$), nous ne pouvons pas établir clairement de tendance significative à long terme dans le réchauffement ou le refroidissement de la couche supérieure de la Méditerranée. Les limitations de cette étude (période couverte, incertitudes dans nos calculs) soulignent l'importance de maintenir sur le long-terme des systèmes d'observation synoptiques (répéter des campagnes océanographiques à l'échelle du bassin et des sous-bassins, maintenir et développer les flotteurs profileurs Argo ainsi que des réseaux de gliders), afin d'améliorer notre compréhension des processus mais aussi de réduire les incertitudes sur nos calculs.

En plus de jouer un rôle important dans la physique du climat (transport de chaleur), la couche de mélange a une influence majeure sur les processus chimiques et biologiques de surface (notamment sur le phytoplancton, premier maillon de la chaîne alimentaire marine). Le contrôle de la couche de mélange océanique sur la phénologie du phytoplancton en Méditerranée a également été étudié à travers une collaboration avec des biogéochimistes. Si la couche de mélange et les pics de chlorophylle en surface sont concomitants dans le régime "Non-Bloom", le pic de couche de mélange précède le pic de chlorophylle de surface d'environ 30 jours dans le régime "Bloom". Par ailleurs, pour le régime "Non-Bloom", les observations indiquent que le phytoplancton ne serait jamais limité par la lumière, quelque soit la couche de mélange, et qu'il pourrait même croître au cours de la période hivernale grâce à de faibles apports de nutriments. Pour le régime "Bloom", les apports importants de nutriments dans les eaux de surface par le mélange profond et le faible taux d'absorption par le phytoplancton (épisodiquement limité par un déficit de la lumière), conduit à l'hypothèse que les nutriments s'accumulent dans les eaux de surface pendant l'hiver, ce qui pourrait expliquer le décalage de 30 jours entre la couche de mélange et le pic de chlorophylle de surface, caractéristique du régime "Bloom".

Variabilité interannuelle des formations d'eaux denses en Méditerranée Nord Occidentale

La convection profonde en haute mer et les plongées d'eau dense côtière dans le Golfe du Lion.

La ligne de mouillage LION, ainsi que les stations CTDs et les déploiements de gliders, réalisés dans le Golfe du Lion depuis 2007, constituent la majeure partie du jeu de données utilisé pendant cette thèse. Le mouillage profond LION a été mis en place dans le Golfe du Lion en septembre 2007 et reste maintenu dans le cadre du service d'observation MOOSE. La ligne a été équipée progressivement de 8 à 26 instruments. Actuellement elle compte 20 capteurs de température, 10 capteurs de conductivité et 5 courantomètres, s'étalant de 150m à 2300m de profondeur. Au cours de ces cinq années de suivi, cinq hivers consécutifs de convection profonde ont été enregistrés, dont les quatre derniers où la convection est allée jusqu'au fond (2300 m).

Différentes échelles temporelles associées au processus de convection profonde ont pu être précisées pour la première fois :

- La durée que met la couche de mélange pour s'approfondir est comprise entre 1 et 2 mois.
- Si la couche de mélange a atteint le fond (généralement à la fin de Janvier / début Février), il y a toujours ensuite une phase de mélange vertical violente de toute la colonne d'eau (entre 9 à 12 jours)
- Les 4 hivers rigoureux (2009-2012) présentent une seconde période de mélange verti-

cal qui se produit généralement en Mars après l'événement principal de convection profonde. Cet événement de courte durée (2-4jours) se produit lorsque la colonne d'eau est très peu stratifiée. Une période de 3 à 6 jours de pertes de flottabilité peut facilement déstabiliser la colonne d'eau, ce qui conduit à un nouvel épisode de mélange vertical.

- Nous définissons le temps de restratification de la couche intermédiaire (200-600m) comme le temps requis par cette couche pour récupérer 50 % de sa teneur en chaleur perdue lors de la convection profonde. En utilisant la température potentielle moyenne de la couche 200-600m pour l'année 2010, 2011 et 2012, nous déterminons le temps nécessaire à cette masse d'eau pour compenser la moitié de ses pertes de chaleur dues à l'événement de convection profonde, comme étant compris entre 2,5 et 4,5 mois.
- Le temps de propagation des eaux profondes nouvellement formées a été défini comme le temps nécessaire à la colonne d'eau pour dissiper 50 % (respectivement 75%) de l'augmentation de densité potentielle dans la couche 600-2300m, qui s'est produit à la fin de la phase de fort mélange vertical. Il faut approximativement 1,5 à 3 mois (resp. 3 à 6 mois), ce qui reflète bien le temps nécessaire à la dispersion et au mélange de l'eau profonde nouvellement formée avec les eaux environnantes.

La longue période de restratification et de dispersion des nouvelles eaux, qui peut être observée après chaque hiver de convection profonde, indique que la phase de restratification/-dispersion est toujours en cours au début de l'hiver suivant, lors du début de l'évènement de convection profonde. Ceci illustre bien le chevauchement des trois "phases" de la convection profonde, ainsi que le possible "effet mémoire" de la colonne d'eau lors du déclenchement d'évènements de convection profonde consécutifs. Il est donc crucial de modéliser correctement les tourbillons tout au long de l'année, si l'on veut pouvoir simuler correctement le phénomène de convection profonde.

Cette étude met en lumière, pour la première fois dans le Golfe du Lion, la forte saisonnalité de la structure verticale des courants horizontaux entre 150m et 2300m de profondeur. 85% à 95% de leur variance peut être expliqué par le 1er EOF (interprété comme le mode barotrope équivalent, car nous ne connaissons pas les courants de surface), alors que le second mode (interprété comme le premier mode de barocline) contient 5 % à 10 % de la variance. Ces nouveaux résultats semblent indiquer que la structure verticale des courants horizontaux de 150m à 2300m est principalement barotropique, et présente des variations saisonnières proche d'un cycle comportant 4 phases :

- une période barocline et calme en fin d'automne,
- une période barocline et énergétique en hiver,
- une période barotrope équivalente et énergétique au printemps / début de l'été,
- une période barotrope équivalente et calme en été / début de l'automne.

L'excitation des courants en hiver peut être générée par le forçage thermodynamique de la région lié à d'importants flux de flottabilité de surface. Les courants horizontaux deviennent

de plus en plus forts au cours de la période de convection profonde, notamment en raison de la conversion de l'énergie potentielle de la zone (liée à la formation d'eaux plus denses) en énergie cinétique, ce qui semble conduire à une "baroclinisation" de la colonne d'eau. L'évolution du champ d'écoulement barocline en un champ barotropique pourrait être le résultat de la cascade d'énergie de la turbulence géostrophique à grandes échelles (Rhines [1979]; Venaille et al. [2012]).

.

En utilisant une méthode basée sur l'analyse en ondelettes pour isoler les anomalies de vitesses horizontales sur les données du mouillage, 37 tourbillons ont été détectés entre Octobre 2009 et Juillet 2012 (18 anticyclones et 19 cyclones). Les rayons de ces tourbillons sont compris entre 0.7 km et 20.0 km, et leurs vitesses de rotation varient entre 0.9 $cm.s^{-1}$ et 25.1 $cm.s^{-1}$. Le principal mode de la distribution des rayons des cyclones est de 4 km, alors qu'il est de 5 km pour les anticyclones. Les cyclones sembleraient principalement formés pendant la phase de mélange vertical intense, lorsque la très faible stratification conduit à un petit rayon de déformation de Rossby, alors que les anticyclones sont détectés principalement à partir de la phase de restratification/dispersion.

La haute résolution temporelle des mesures acquises par les instruments de la ligne de mouillage permet une étude fine de l'évolution de la température potentielle et de la salinité des eaux profondes. Pour les hivers avec une convection en haute mer qui a atteint le fond, on observe d'abord une augmentation significative de la température potentielle (entre 0,02 et 0,04 °C) dans la couche de fond, en raison de l'approfondissement de la couche de mélange jusqu'au fond. Ensuite, la période d'intense mélange vertical et de fortes pertes de flottabilité (9-12 jours) fait baisser la température potentielle de la couche de mélange, et donc la température potentielle de l'eau profonde nouvellement formée (entre 0,01 et 0,03 °C). Contrairement à la température potentielle, la salinité de l'eau profonde nouvellement formée n'a pas montré de variations importantes après que l'approfondissement de la couche de mélange ait atteint le fond. La salinité de l'eau profonde nouvellement formée est fixée principalement par la salinité de la couche de mélange une fois que celle-ci atteint le fond, ce qui correspond à une augmentation entre 0,006‰ et 0,012‰, pour la période 2007-2012. L'apparition d'eaux profondes nouvellement formées a été détectée au cours des hivers 2009, 2010, 2011 et 2012. Au cours de l'hiver 2010, deux différentes nouvelles eaux profondes ont été détectées après l'épisode de convection profonde. Elles présentent une température potentielle différente mais une salinité similaire, ce qui suggère que ces deux nouvelles eaux profondes auraient pu être formées dans la zone de convection mais en des endroits différents. En 2012, deux différentes nouvelles eaux profondes ont aussi été détectées au niveau du mouillage LION. Par contre, cette année-ci, les eaux profondes nouvellement formées semblent avoir des origines différentes (convection profonde au large et plongées d'eau dense côtière).

Pour tous les hivers, nous avons constaté que les pertes intégrées de flottabilité à la surface, entre le 1er Novembre et la fin de Février, à partir des réanalyses ERA-Interim, sont plus élevées que le contenu en flottabilité de la colonne d'eau avant chaque événement de convection.

Cela indique que la colonne d'eau n'est pas assez stratifiée au début du mois de Novembre pour empêcher l'approfondissement de la convection, en supposant toutefois que l'advection horizontale de flottabilité reste négligeable. Sur les cinq hivers étudiés, 2011 semble être l'hiver au cours duquel la colonne d'eau était la moins stratifiée au début du mois de Novembre, ce qui pourrait expliquer pourquoi 2011 a été une année de convection profonde, alors que les pertes de flottabilité sont comparables à 2004 (une année sans convection profonde observée).

Pour l'hiver 2011/2012 , cinq lignes de mouillage supplémentaires ont été utilisées pour surveiller la formation et la propagation d'un événement intense de plongée d'eau dense côtière vers le bassin profond. L'arrivée d'eau dense, formée sur le plateau, à l'emplacement du mouillage LION correspond à une forte diminution de θ (-0,1 °C) et S (-0.03). Ce fort signal a été identifié comme étant associé à un tourbillon cyclonique dont le rayon du cœur est estimé à 12.0 km, avec un maximum de vitesse azimutale de 15.7 cm.s^{-1}. Le centre du tourbillon détecté est également lié à une élévation de 1000m de l'isopycnal 29,132 kg.m^{-3}, et à une anomalie thermohaline de fond s'étendant sur 400m d'épaisseur et présentant de faibles valeurs pour θ et S qui supportent l'hypothèse d'une origine côtière pour cette masse d'eau profonde.

Impacts sur les flux de particules et sur l'activité des écosystèmes profonds

La convection profonde en haute mer et les plongées d'eau dense côtière sont des processus clés qui relient l'océan de surface à l'océan profond. En plus de la chaleur et du sel, les formations d'eaux denses peuvent transférer aussi des composants biogéochimiques à l'océan profond, comme l'oxygène et la matière organique/inorganique, contribuant ainsi à la ventilation et l'alimentation des écosystèmes pélagiques et benthiques profonds.

À travers des collaborations avec des biogéochimistes et des sédimentologues, nous avons pu étudier l'influence des formations d'eau dense sur la remise en suspension de sédiments profonds, et donc sur l'épaisseur, la propagation et la persistance de la couche néphéloïde de fond. L'importante remobilisation de sédiments dans le bassin du Golfe du Lion, après les événements de formation d'eaux denses, sont également susceptibles d'induire une altération subséquente des fonds marins et d'influencer le fonctionnement des écosystèmes sous-marins. Les événements de formations d'eaux denses et la diffusion des eaux profondes nouvellement formées se sont révélées également comme étant un facteur important dans l'activité des écosystèmes pélagiques profonds en les alimentant par des apports de matière organique "fraîche", et ainsi en stimulant l'activité bioluminescente.

Perpsectives

Des comparaisons futures entre la climatologie du taux de chaleur dans la couche de surface de la Méditerranée, avec d'autres climatologies de flux de chaleur pourraient être utiles, pour tester la paramétrisation des flux de chaleur à l'interface air-mer, et ainsi améliorer la pré-

cision des modèles climatiques couplés océan-atmosphère, en particulier dans le cadre de simulations climatiques à long terme qui exigent, entre autres, une bonne modélisation de la circulation thermohaline. D'autres possibles travaux à venir seraient de comparer notre climatologie mensuelle de l'advection horizontale de chaleur estimée dans la couche de surface, à d'autres estimations, obtenues par des simulations océaniques et/ou d'autres climatologies déduites des estimations des courants géostrophiques de surface.

Dans cette étude, nous avons aussi réalisé une comparaison entre le contenu en flottabilité de la colonne d'eau avant l'hiver et les pertes de surface en flottabilité intégrées sur la période Novembre-Février. Bien que les facteurs responsables de ces cinq événements de convection profonde consécutifs ont été mis en évidence, cette comparaison souligne également les besoins de capteurs de conductivité supplémentaires dans les premiers 200m de la colonne d'eau afin de préciser les calculs. Dans le but de minimiser l'erreur sur le calcul du contenu en flottabilité de la colonne d'eau avant la convection profonde (une indication de l'état de "préconditonnement" de l'océan), des profils complets créés avec un instrument unique (comme un profileur ou à partir d'une station CTD) à la fin Octobre / début Novembre serait très utiles. Ainsi les déploiements répétés de gliders dans le cadre du service d'observation MOOSE, passant à proximité du mouillage LION, sont une précieuse source de données.

D'autres travaux doivent être effectués afin de mieux comprendre l'origine et le destin des différentes sortes de tourbillons détectées dans cette étude. Des expériences numériques pourrait être un bon outil pour étudier la genèse et la fin de vie de ces tourbillons, mais la résolution des mailles numériques peut être trop grande pour décrire précisément ces petits tourbillons (plus 50% des cyclones et anticyclones détectés ont un rayon inférieur à 6 km). Une des solutions pourrait venir de l'utilisation combinée d'un mouillage temps-réel et de gliders. Ce serait un outil utile pour déclencher facilement des campagnes de mesures et suivre ainsi l'évolution de ces tourbillons. De plus, le développement récent de capteurs biogéochimiques peut également être utile pour obtenir des informations supplémentaires sur la signature biogéochimique" de ces tourbillons et leurs impacts potentiels sur le déclenchement des blooms de phytoplancton dans la Méditerranée nord-occidentale, car ils peuvent transporter dans leurs cœurs des écosystèmes complets, relativement isolés du reste de l'océan.

Une autre perspective serait de suivre la propagation de l'eau profonde nouvellement formée en dehors de la Méditerranée nord-occidentale (avec des mouillages profonds déployés au large de Minorque, et entre Minorque et la Sardaigne, par exemple), afin notamment de quantifier les transports de chaleur et de sel liés à la propagation des eaux profondes. Tout au long de leur propagation dans le bassin occidental, les eaux profondes nouvellement formées vont se mélanger avec les eaux environnantes. Une partie d'entre elles quittent la Méditerranée par le Détroit de Gibraltar, où elles forment une "langue d'eau salée" méditerranéenne qui se propage dans tout l'Atlantique Nord et rejoint la circulation globale. L'utilisation conjointe de gliders et de campagnes océanographiques dans les différents sous-bassins de la Méditerranée Occidentale (Mer d'Alboran, Bassin Algérien, Mer Tyrrhénienne) permettrait notamment de

mieux quantifier le transport et la diffusion de chaleur et de sel liés à la propagation de ces nouvelles masses d'eau.

Bibliography

Akitomo, K., 2010. Baroclinic instability and submesoscale eddy formation in weakly stratified oceans under cooling. *Journal of Geophysical Research*, 115(C11):C11027. doi: 10.1029/2010JC006125.

Allen, J. T., S. C. Painter, and M. Rixen, 2008. Eddy transport of Western Mediterranean Intermediate Water to the Alboran Sea. *Journal of Geophysical Research*, 113(C4):C04024. doi: 10.1029/2007JC004649.

Artale, V., D. Iudicone, R. Santoleri, V. Rupolo, S. Marullo, and F. D'Ortenzio, 2002. Role of surface fluxes in ocean general circulation models using satellite sea surface temperature: Validation of and sensitivity to the forcing frequency of the Mediterranean thermohaline circulation. *Journal of Geophysical Research*, 107(C8):3120. doi: 10.1029/2000JC000452.

Benzohra, M. and C. Millot, 1995. Characteristics and circulation of the surface and intermediate water masses off Algeria. *Deep Sea Research Part I: Oceanographic Research Papers*, 42(10):1803–1830. doi: 10.1016/0967-0637(95)00043-6.

Bethoux, J., 1979. Budgets of the Mediterranean Sea- Their dependance on the local climate and on the characteristics of the Atlantic waters. *Oceanologica Acta*, 2:157–163.

Bethoux, J., X. Durieu de Madron, F. Nyffeler, and D. Tailliez, 2002. Deep water in the western Mediterranean: peculiar 1999 and 2000 characteristics, shelf formation hypothesis, variability since 1970 and geochemical inferences. *Journal of Marine Systems*, 33-34:117–131. doi: 10.1016/S0924-7963(02)00055-6.

Bethoux, J. P., B. Gentili, J. Raunet, and D. Tailliez, 1990. Warming trend in the western Mediterranean deep water. *Nature*, 347(6294):660–662. doi: 10.1038/347660a0.

Bethoux, J.-P., B. Gentili, D. Tailliez, and J. Bethoux, 1998. Warming and freshwater budget change in the Mediterranean since the 1940 s, their possible relation to the greenhouse effect. *Geophysical Research Letters*, 25(7):1023–1026. doi: 10.1029/98GL00724.

Brankart, J. and P. Brasseur, 1998. The general circulation in the Mediterranean Sea: a climatological approach. *Journal of Marine Systems*, 18(1-3):41–70. doi: 10.1016/S0924-7963(98)00005-0.

Bryden, H. L., J. Candela, and T. H. Kinder, 1994. Exchange through the Strait of Gibraltar. *Progress in Oceanography*, 33(3):201–248. doi: 10.1016/0079-6611(94)90028-0.

Bunker, A., H. Charnock, and R. Goldsmith, 1982. A note on the heat balance of the Mediterranean and Red Seas. *J. Mar. Res*, 40:73–84.

Canals, M., P. Puig, X. D. de Madron, S. Heussner, A. Palanques, and J. Fabres, 2006. Flushing submarine canyons. *Nature*, 444(7117):354–7. doi: 10.1038/nature05271.

Candela, J., 2001. Mediterranean water and global circulation. In J. C. Gerold Siedler and J. Gould, editors, *Ocean Circulation and Climate Observing and Modelling the Global Ocean*, volume 77 of *International Geophysics*, pages 419 – 429. Academic Press. doi: 10.1016/S0074-6142(01)80132-7.

Cassou, C., 2008. Intraseasonal interaction between the Madden-Julian Oscillation and the North Atlantic Oscillation. *Nature*, 455(7212):523–7. doi: 10.1038/nature07286.

Cassou, C., M. Minvielle, L. Terray, and C. Périgaud, 2010. A statistical–dynamical scheme for reconstructing ocean forcing in the Atlantic. Part I: weather regimes as predictors for ocean surface variables. *Climate Dynamics*, 36(1-2):19–39. doi: 10.1007/s00382-010-0781-7.

Castellón, A., J. Font, and E. García, 1990. The Liguro-Provençal-Catalan current (NW Mediterranean) observed by Doppler profiling in the Balearic Sea. *Scientia Marina*, 54(3):269–276.

Chelton, D. B., R. A. DeSzoeke, M. G. Schlax, K. El Naggar, and N. Siwertz, 1998. Geographical Variability of the First Baroclinic Rossby Radius of Deformation. *Journal of Physical Oceanography*, 28(3):433–460. doi: 10.1175/1520-0485(1998)028<0433:GVOTFB>2.0.CO;2.

Cheng, L., J. Zhu, F. Reseghetti, and Q. Liu, 2011. A New Method to Estimate the Systematical Biases of Expendable Bathythermograph. *Journal of Atmospheric and Oceanic Technology*, 28(2):244–265. doi: 10.1175/2010JTECHO759.1.

CIESM, 2005. Strategies for understanding mesoscale processes. *CIESM Workshop Monographs*, 27(May):132.

CIESM, 2009. Dynamics of Mediterranean deep waters. *CIESM Workshop Monographs*, 38:132.

Clarke, R. A. and J.-C. Gascard, 1983. The Formation of Labrador Sea Water. Part I: Large-Scale Processes. *Journal of Physical Oceanography*, 13(10):1764–1778. doi: 10.1175/1520-0485(1983)013<1764:TFOLSW>2.0.CO;2.

Colin, J., M. Déqué, R. Radu, and S. Somot, 2010. Sensitivity study of heavy precipitation in Limited Area Model climate simulations: influence of the size of the domain and the use of the spectral nudging technique. *Tellus A*, pages no–no. doi: 10.1111/j.1600-0870.2010.00467.x.

Conkright, M. E., J. I. Antonov, O. Baranova, T. P. Boyer, H. E. Garcia, R. Gelfeld, D. Johnson, R. A. Locarnini, P. P. Murphy, T. D. O'Brien, I. Smolvar, and C. Stephens, 2002. NOAA Atlas NESDIS 42, WORLD OCEAN DATABASE 2001 Volume1: Introduction. *U.S. Gov. Printing Office, Wash.,D.C.*, page 160pp.

Cowley, R., S. Wijffels, L. Cheng, T. Boyer, and S. Kizu, 2013. Biases in Expendable Bathythermograph Data: A New View Based on Historical Side-by-Side Comparisons. *Journal of Atmospheric and Oceanic Technology*, 30(6):1195–1225. doi: 10.1175/JTECH-D-12-00127.1.

Crepon, M., L. Wald, and J. M. Monget, 1982. Low-frequency waves in the Ligurian Sea during December 1977. *Journal of Geophysical Research*, 87(C1):595. doi: 10.1029/JC087iC01p00595.

Criado-Aldeanueva, F., F. J. Soto-Navarro, and J. García-Lafuente, 2012. Seasonal and interannual variability of surface heat and freshwater fluxes in the Mediterranean Sea: budgets and exchange through the Strait of Gibraltar. *International Journal of Climatology*, 32(2):286–302. doi: 10.1002/joc.2268.

De Boyer Montégut, C., G. Madec, A. S. Fischer, A. Lazar, and D. Iudicone, 2004. Mixed layer depth over the global ocean: An examination of profile data and a profile-based climatology. *Journal of Geophysical Research*, 109(C12):1–20. doi: 10.1029/2004JC002378.

Demirov, E. K. and N. Pinardi, 2007. On the relationship between the water mass pathways and eddy variability in the Western Mediterranean Sea. *Journal of Geophysical Research*, 112(C2):C02024. doi: 10.1029/2005JC003174.

Domingues, C. M., J. a. Church, N. J. White, P. J. Gleckler, S. E. Wijffels, P. M. Barker, and J. R. Dunn, 2008. Improved estimates of upper-ocean warming and multi-decadal sea-level rise. *Nature*, 453(7198):1090–3. doi: 10.1038/nature07080.

D'Ortenzio, F., D. Iudicone, C. De Boyer Montegut, P. Testor, D. Antoine, S. Marullo, R. Santoleri, and G. Madec, 2005. Seasonal variability of the mixed layer depth in the Mediterranean Sea as derived from in situ profiles. *Geophysical Research Letters*, 32(12):2–5. doi: 10.1029/2005GL022463.

D'Ortenzio, F. and L. Prieur, 2012. The upper mixed layer. In N. Stambler, editor, *Life in the Mediterranean Sea: A look at habitat changes*, pages 127–156. Nova Science Publisher.

Dubois, C., E. Sanchez-Gomez, A. Braun, and S. Somot, 2010. A gathering of observed air- sea surface fluxes over the Mediterranean Sea. *Note de centre n°113. Groupe de Météorologie de Grande Echelle et Climat. CNRM. August 2010 (available at clotilde.dubois@meteo.fr)*.

Dubois, C., S. Somot, S. Calmanti, a. Carillo, M. Déqué, a. Dell'Aquilla, a. Elizalde, S. Gualdi, D. Jacob, B. L'Hévéder, L. Li, P. Oddo, G. Sannino, E. Scoccimarro, and F. Sevault, 2011. Future projections of the surface heat and water budgets of the Mediterranean Sea in an ensemble of coupled atmosphere–ocean regional climate models. *Climate Dynamics*, 39(7-8):1859–1884. doi: 10.1007/s00382-011-1261-4.

Durrieu de Madron, X., L. Houpert, P. Puig, A. Sanchez-Vidal, P. Testor, A. Bosse, C. Estournel, S. Somot, F. Bourrin, M. N. Bouin, M. Beauverger, L. Beguery, A. Calafat, M. Canals, C. Cassou, L. Coppola, D. Dausse, F. D'Ortenzio, J. Font, S. Heussner, S. Kunesch, D. Lefevre, H. Le Goff,

J. Martín, L. Mortier, A. Palanques, and P. Raimbault, 2013. Interaction of dense shelf water cascading and open-sea convection in the northwestern Mediterranean during winter 2012. *Geophysical Research Letters*, 40(7):1379–1385. doi: 10.1002/grl.50331.

Durrieu de Madron, X., V. Zervakis, a. Theocharis, and D. Georgopoulos, 2005. Comments on "Cascades of dense water around the world ocean". *Progress In Oceanography*, 64(1):83–90. doi: 10.1016/j.pocean.2004.08.004.

Escudier, R., J. Bouffard, A. Pascual, P.-M. Poulain, and M.-I. Pujol, 2013. Improvement of coastal and mesoscale observation from space: Application to the northwestern Mediterranean Sea. *Geophysical Research Letters*, 40(10):2148–2153. doi: 10.1002/grl.50324.

Fan, X., U. Send, P. Testor, J. Karstensen, and P. Lherminier, 2013. Observations of Irminger Sea Anticyclonic Eddies. *Journal of Physical Oceanography*, 43(4):805–823. doi: 10.1175/JPO-D-11-0155.1.

Firing, E. and J. M. Hummon, 2010. Shipboard ADCP measurements. *The go-ship repeat hydrography manual: a collection of expert reports and guidelines. IOCCP report*, (14):1–11.

Firing, E., J. Ranada, and C. Patrick, 1995. Processing ADCP data with the CODAS software system version 3.1. Technical report, Joint Institute for Marine and Atmospheric Research, University of Hawaii & National Oceanographic Data Center.

Flexas, M. M., G. J. F. van Heijst, and R. R. Trieling, 2005. The Behavior of Jet Currents over a Continental Slope Topography with a Possible Application to the Northern Current. *Journal of Physical Oceanography*, 35(5):790–810. doi: 10.1175/JPO2705.1.

Font, J., P. Puig, J. Salat, A. Palanques, and M. Emelianov, 2007. Sequence of hydrographic changes in NW Mediterranean deep water due to the exceptional winter of 2005. *Scientia Marina*, 71(2):339–346. doi: 10.3989/scimar.2007.71n2339.

Font, J., J. Salat, and J. Tintoré, 1988. Permanent features of the circulation in the Catalan Sea. *Oceanol. Acta*, 9:51–57.

Fuda, J., C. Millot, I. Taupier-Letage, U. Send, and J. Bocognano, 2000. XBT monitoring of a meridian section across the western Mediterranean Sea. *Deep Sea Research Part I: Oceanographic Research Papers*, 47(11):2191–2218. doi: 10.1016/S0967-0637(00)00018-2.

Fuda, J.-L., G. Etiope, C. Millot, P. Favali, M. Calcara, G. Smriglio, and E. Boschi, 2002. Warming, salting and origin of the Tyrrhenian Deep Water. *Geophysical . . .*, 29(19):1898. doi: 10.1029/2001GL014072.

Gaillard, F., J.-C. Gascard, and P. Klein, 2000. A Methodology for Assessing the Postconvection Mesoscale Dynamics in the Gulf of Lion from Composite Datasets. *Journal of Physical Oceanography*, 30(12):3113–3133. doi: 10.1175/1520-0485(2000)030<3113:AMFATP>2.0.CO;2.

Garau, B., S. Ruiz, W. G. Zhang, A. Pascual, E. Heslop, J. Kerfoot, and J. Tintoré, 2011. Thermal Lag Correction on Slocum CTD Glider Data. *Journal of Atmospheric and Oceanic Technology*, 28(9):1065–1071. doi: 10.1175/JTECH-D-10-05030.1.

Garrett, C., R. Outerbridge, and K. Thompson, 1993. Interannual Variability in Meterrancan Heat and Buoyancy Fluxes. *Journal of Climate*, 6(5):900–910. doi: 10.1175/1520-0442(1993)006<0900:IVIMHA>2.0.CO;2.

Gascard, J. C. and C. Richez, 1985. Water masses and circulation in the Western Alboran sea and in the Straits of Gibraltar. *Progress in Oceanography*, 15(3):157–216. doi: 10.1016/0079-6611(85)90031-X.

Gasparini, G., a. Ortona, G. Budillon, M. Astraldi, and E. Sansone, 2005. The effect of the Eastern Mediterranean Transient on the hydrographic characteristics in the Strait of Sicily and in the Tyrrhenian Sea. *Deep Sea Research Part I: Oceanographic Research Papers*, 52(6):915–935. doi: 10.1016/j.dsr.2005.01.001.

Gasparini, G., G. Zodiatis, M. Astraldi, C. Galli, and S. Sparnocchia, 1999. Winter intermediate water lenses in the Ligurian Sea. *Journal of Marine Systems*, 20(1-4):319–332. doi: 10.1016/S0924-7963(98)00089-X.

Gaudin, M., S. Berné, J.-M. Jouanneau, A. Palanques, P. Puig, T. Mulder, P. Cirac, M. Rabineau, and P. Imbert, 2006. Massive sand beds attributed to deposition by dense water cascades in the Bourcart canyon head, Gulf of Lions (northwestern Mediterranean Sea). *Marine Geology*, 234(1-4):111–128. doi: 10.1016/j.margeo.2006.09.020.

Gačić, M., G. L. E. Borzelli, G. Civitarese, V. Cardin, and S. Yari, 2010. Can internal processes sustain reversals of the ocean upper circulation? The Ionian Sea example. *Geophysical Research Letters*, 37(9):n/a–n/a. doi: 10.1029/2010GL043216.

Gertman, I., I. Ovchinnikov, and Y. Popv, 1994. Deep convection in the eastern basin of the Mediterranean Sea. *Oceanology*, 34(1):19–25.

Gille, S. T., 2004. Using Kolmogorov-Smirnov Statistics to Compare Geostrophic Velocities Measured by the Jason, TOPEX, and Poseidon Altimeters. *Marine Geodesy*, 27(1-2):47–57. doi: 10.1080/01490410490465346.

Giorgi, F., 2006. Climate change hot-spots. *Geophysical Research Letters*, 33(8):L08707. doi: 10.1029/2006GL025734.

Gouretski, V. and K. P. Koltermann, 2007. How much is the ocean really warming? *Geophysical Research Letters*, 34(1):L01610. doi: 10.1029/2006GL027834.

Gouretski, V. and F. Reseghetti, 2010. On depth and temperature biases in bathythermograph data: Development of a new correction scheme based on analysis of a global ocean database. *Deep Sea Research Part I: Oceanographic Research Papers*, 57(6):812–833. doi: 10.1016/j.dsr.2010.03.011.

Grignon, L., 2009. *Causes of the Interannual Variability of Deep Convection*. Ph.D. thesis, University of Southampton.

Grignon, L., D. A. Smeed, H. L. Bryden, and K. Schroeder, 2010. Importance of the variability of hydrographic preconditioning for deep convection in the Gulf of Lion, NW Mediterranean. *Ocean Science*, 6(2):573–586. doi: 10.5194/os-6-573-2010.

Hamon, M., G. Reverdin, and P.-Y. Le Traon, 2012. Empirical Correction of XBT Data. *Journal of Atmospheric and Oceanic Technology*, 29(7):960–973. doi: 10.1175/JTECH-D-11-00129.1.

Hanawa, K., P. Rual, R. Bailey, A. Sy, and M. Szabados, 1995. A new depth-time equation for Sippican or TSK T-7, T-6 and T-4 expendable bathythermographs (XBT). *Deep Sea Research Part I: Oceanographic Research Papers*, 42(8):1423–1451. doi: 10.1016/0967-0637(95)97154-Z.

Herrmann, M., F. Sevault, J. Beuvier, and S. Somot, 2010. What induced the exceptional 2005 convection event in the northwestern Mediterranean basin? Answers from a modeling study. *Journal of Geophysical Research*, 115(C12):1–19. doi: 10.1029/2010JC006162.

Herrmann, M., S. Somot, S. Calmanti, C. Dubois, and F. Sevault, 2011. Representation of spatial and temporal variability of daily wind speed and of intense wind events over the Mediterranean Sea using dynamical downscaling: impact of the regional climate model configuration. *Natural Hazards and Earth System Science*, 11(7):1983–2001. doi: 10.5194/nhess-11-1983-2011.

Herrmann, M., S. Somot, F. Sevault, C. Estournel, and M. Déqué, 2008. Modeling the deep convection in the northwestern Mediterranean Sea using an eddy-permitting and an eddy-resolving model: Case study of winter 1986–1987. *Journal of Geophysical Research*, 113(C4):1–25. doi: 10.1029/2006JC003991.

Heussner, S., X. Durrieu de Madron, A. Calafat, M. Canals, J. Carbonne, N. Delsaut, and G. Saragoni, 2006. Spatial and temporal variability of downward particle fluxes on a continental slope: Lessons from an 8-yr experiment in the Gulf of Lions (NW Mediterranean). *Marine Geology*, 234(1-4):63–92. doi: 10.1016/j.margeo.2006.09.003.

Hogg, N. G., 1973. The preconditioning phase of MEDOC 1969—II. Topographic effects. *Deep Sea Research and Oceanographic Abstracts*, 20(5):449–459. doi: 10.1016/0011-7471(73)90099-5.

Hopkins, T. S., 1988. Recent observations in the intermediate and deepwater circulation in the Southern Tyrrhenian Sea. *Oceanol. Acta*, 9:41–50.

Houpert, L., 2010. Étude du renouvellement des eaux profondes en Méditerranée nord occidentale pendant la période 2007/2010. *Université Pierre et Marie Curie, Paris*, (http://lhoupert.fr/site/files/publications/houpert_master2_thesis.pdf):63.

Houpert, L., P. Testor, X. Durrieu de Madron, A. Bosse, and L. Mortier, 2014. High resolution monitoring of deep water formations in the northwestern Mediterranean over the recent period 2007-2012. *2014 Ocean Sciences Meeting, 23-28 February 2014, Honolulu, USA (available at http://lhoupert.fr/files/posters/houpert_et_al_OS2014.png)*.

IPCC, 2013. Climate Change 2013: The Physical Science Basis, Contribution of Working Group I to the Fifth Assessment Report of the Intergovernmental Panel on Climate Change.

Ishii, M. and M. Kimoto, 2009. Reevaluation of historical ocean heat content variations with time-varying XBT and MBT depth bias corrections. *Journal of Oceanography*, 65(3):287–299. doi: 10.1007/s10872-009-0027-7.

Ivanov, V., G. Shapiro, J. Huthnance, D. Aleynik, and P. Golovin, 2004. Cascades of dense water around the world ocean. *Progress in Oceanography*, 60(1):47–98. doi: 10.1016/j.pocean.2003.12.002.

Johnson, R. G., 1997. Climate control required a dam at the Strait of Gibraltar. *Eos, Transactions American Geophysical Union*, 78(27):277. doi: 10.1029/97EO00180.

Josey, S. A., S. Somot, and M. Tsimplis, 2011. Impacts of atmospheric modes of variability on Mediterranean Sea surface heat exchange. *Journal of Geophysical Research*, 116(C2):C02032. doi: 10.1029/2010JC006685.

Killworth, P. D., 1979. On "Chimney" Formations in the Ocean. *Journal of Physical Oceanography*, 9(3):531–554. doi: 10.1175/1520-0485(1979)009<0531:OFITO>2.0.CO;2.

Killworth, P. D., 1983. Deep convection in the World Ocean. *Reviews of Geophysics*, 21(1):1. doi: 10.1029/RG021i001p00001.

Kim, K., K.-I. Chang, D.-J. Kang, Y. H. Kim, and J.-H. Lee, 2008. Review of recent findings on the water masses and circulation in the East Sea (Sea of Japan). *Journal of Oceanography*, 64(5):721–735. doi: 10.1007/s10872-008-0061-x.

Kinder, T. H. and G. Parrilla, 1987. Yes, some of the Mediterranean outflow does come from great depth. *Journal of Geophysical Research*, 92(C3):2901. doi: 10.1029/JC092iC03p02901.

Klein, B., W. Roether, B. B. Manca, D. Bregant, V. Beitzel, V. Kovacevic, and A. Luchetta, 1999. The large deep water transient in the Eastern Mediterranean. *Deep Sea Research Part I: Oceanographic Research Papers*, 46(3):371–414. doi: 10.1016/S0967-0637(98)00075-2.

Krahmann, G. and F. Schott, 1998. Longterm increases in western Mediterranean salinities and temperatures: Anthropogenic and climatic sources. *Geophysical Research Letters*, 25(22):4209. doi: 10.1029/1998GL900143.

Krahmann, G., F. Schott, and U. Send, 2000. Seasonal heat content changes in the western Mediterranean Sea as a means for evaluating surface heat flux formulations. *Journal of Geophysical Research*, 105(C7):16941. doi: 10.1029/2000JC900039.

La Violette, P., 1994. Overview of the major forcings and water masses of the Western Mediterranean Sea. In P. La Violette, editor, *Seasonal and Interannual Variability of the Western Mediterranean Sea*, volume 46, pages 1–11. Washington, D.C., american g edition. doi: 10.1029/CE046p0001.

Lacombe, H. and P. Tchernia, 1972. Caractères hydrologiques et circulation des eaux en Méditerranée. *The Mediterranean Sea*, pages 26–36.

Lacombe, H., P. Tchernia, and L. Gamberoni, 1985. Variable bottom water in the Western Mediterranean basin. *Progress in Oceanography*, 14(1971):319–338. doi: 10.1016/0079-6611(85)90015-1.

Lascaratos, A., 1993. Estimation of deep and intermediate water mass formation rates in the Mediterranean Sea. *Deep Sea Research Part II: Topical Studies in Oceanography*, 40(6):1327–1332. doi: 10.1016/0967-0645(93)90072-U.

Lascaratos, A., W. Roether, K. Nittis, and B. Klein, 1999. Recent changes in deep water formation and spreading in the eastern Mediterranean Sea: a review. *Progress in Oceanography*, 44(1-3):5–36. doi: 10.1016/S0079-6611(99)00019-1.

Lascaratos, A., R. G. Williams, and E. Tragou, 1993. A mixed-layer study of the formation of Levantine intermediate water. *Journal of Geophysical Research*, 98(C8):14739. doi: 10.1029/93JC00912.

Lazier, J. R. N., 1973. The renewal of Labrador sea water. *Deep Sea Research and Oceanographic Abstracts*, 20(4):341–353. doi: http://dx.doi.org/10.1016/0011-7471(73)90058-2.

Leaman, K. D. and F. A. Schott, 1991. Hydrographic Structure of the Convection Regime in the Gulf of Lions: Winter 1987. *Journal of Physical Oceanography*, 21(4):575–598. doi: 10.1175/1520-0485(1991)021<0575:HSOTCR>2.0.CO;2.

Legg, S. and J. Marshall, 1998. The influence of the ambient flow on the spreading of convected water masses. *Journal of Marine Research*, 56(1):107–139. doi: 10.1357/002224098321836136.

Legg, S. and J. C. McWilliams, 2001. Convective Modifications of a Geostrophic Eddy Field. *Journal of Physical Oceanography*, 31(4):874–891. doi: 10.1175/1520-0485(2001)031<0874:CMOAGE>2.0.CO;2.

Levitus, S., J. I. Antonov, T. P. Boyer, R. a. Locarnini, H. E. Garcia, and a. V. Mishonov, 2009. Global ocean heat content 1955–2008 in light of recently revealed instrumentation problems. *Geophysical Research Letters*, 36(7):L07608. doi: 10.1029/2008GL037155.

Lherminier, P., J.-C. Gascard, and D. Quadfasel, 1999. The Greenland Sea in Water 1993 and 1994: preconditioning for deep convection. *Deep Sea Research Part II: Topical Studies in Oceanography*, 46(6-7):1199–1235. doi: 10.1016/S0967-0645(99)00020-X.

Lilly, J. M. and S. C. Olhede, 2012. Generalized Morse Wavelets as a Superfamily of Analytic Wavelets. *IEEE Transactions on Signal Processing*, 60(11):6036–6041. doi: 10.1109/TSP.2012.2210890.

Lilly, J. M. and P. B. Rhines, 2002. Coherent Eddies in the Labrador Sea Observed from a Mooring. *Journal of Physical Oceanography*, 32(2):585–598. doi: 10.1175/1520-0485(2002)032<0585:CEITLS>2.0.CO;2.

Lilly, J. M., P. B. Rhines, F. Schott, K. Lavender, J. Lazier, U. Send, and E. D'Asaro, 2003. Observations of the Labrador Sea eddy field. *Progress in Oceanography*, 59(1):75–176. doi: 10.1016/j.pocean.2003.08.013.

Lilly, J. M., P. B. Rhines, M. Visbeck, R. Davis, J. R. N. Lazier, F. Schott, and D. Farmer, 1999. Observing Deep Convection in the Labrador Sea during Winter 1994/95. *Journal of Physical Oceanography*, 29(8):2065–2098. doi: 10.1175/1520-0485(1999)029<2065:ODCITL>2.0.CO;2.

Longhurst, A., 1995. Seasonal cycles of pelagic production and consumption. *Progress in Oceanography*, 36(2):77–167. doi: 10.1016/0079-6611(95)00015-1.

Lopez-Jurado, J.-L., C. Gonzalez-Pola, and P. Velez-Belchí, 2005. Observation of an abrupt disruption of the long-term warming trend at the Balearic Sea, western Mediterranean Sea, in summer 2005. *Geophysical Research Letters*, 32(24):L24606. doi: 10.1029/2005GL024430.

L'Hévéder, B., L. Li, F. Sevault, and S. Somot, 2012. Interannual variability of deep convection in the Northwestern Mediterranean simulated with a coupled AORCM. *Climate Dynamics*. doi: 10.1007/s00382-012-1527-5.

Macdonald, A. M., J. Candela, and H. L. Bryden, 1994. An estimate of the net heat transport through the Strait of Gibraltar. In P. La Viollette, editor, *Seasonal and Interannual Variability of the Western Mediterranean Sea, Coastal Estuarine Stud.*, pages 12–32. AGU, Washington, D. C. doi: 10.1029/CE046p0013.

Madec, G., P. Delecluse, M. Crépon, and F. Lott, 1996. Large-Scale Preconditioning of Deep-Water Formation in the Northwestern Mediterranean Sea. *Journal of Physical Oceanography*, 26(8):1393–1408. doi: 10.1175/1520-0485(1996)026<1393:LSPODW>2.0.CO;2.

Malanotte-Rizzoli, P., B. B. Manca, M. R. D'Alcalà, A. Theocharis, A. Bergamasco, D. Bregant, G. Budillon, G. Civitarese, D. Georgopoulos, A. Michelato, E. Sansone, P. Scarazzato, and E. Souvermezoglou, 1997. A synthesis of the Ionian Sea hydrography, circulation and water mass pathways during POEM-Phase I. *Progress in Oceanography*, 39(3):153–204. doi: 10.1016/S0079-6611(97)00013-X.

Malanotte-Rizzoli, P., B. B. Manca, M. R. D'Alcala, A. Theocharis, S. Brenner, G. Budillon, and E. Ozsoy, 1999. The Eastern Mediterranean in the 80s and in the 90s: the big transition in the intermediate and deep circulations. *Dynamics of Atmospheres and Oceans*, 29(2-4):365–395. doi: 10.1016/S0377-0265(99)00011-1.

Mann, K. and J. Lazier, 2005. *Dynamics of Marine Ecosystems*. Blackwell Publishing Ltd., Malden, MA USA. doi: 10.1002/9781118687901.

Marshall, J. and F. Schott, 1999. Open-ocean convection: Observations, theory, and models. *Reviews of Geophysics*, 37(1):1–64. doi: 10.1029/98RG02739.

Marullo, S., R. Santoleri, P. Malanotte-Rizzoli, and A. Bergamasco, 1999. The sea surface temperature field in the Eastern Mediterranean from advanced very high resolution radiometer (AVHRR) data Part I. Seasonal Variability. *Journal of Marine Systems*, 20(1-4):83–112. doi: 10.1016/S0924-7963(98)00071-2.

Matsoukas, C., A. C. Banks, N. Hatzianastassiou, K. G. Pavlakis, D. Hatzidimitriou, E. Drakakis, P. W. Stackhouse, and I. Vardavas, 2005. Seasonal heat budget of the Mediterranean Sea. *Journal of Geophysical Research*, 110(C12):C12008. doi: 10.1029/2004JC002566.

MEDAR Group, 2002. MEDATLAS/2002 database. Mediterranean and Black Sea database of temperature salinity and bio-chemical parameters. Climatological Atlas. IFREMER Edition (4 Cdroms).

MEDOC Group, 1970. Observation of Formation of Deep Water in the Mediterranean Sea, 1969. *Nature*, 227(5262):1037–1040. doi: 10.1038/2271037a0.

Menna, M., P.-M. Poulain, G. Zodiatis, and I. Gertman, 2012. On the surface circulation of the Levantine sub-basin derived from Lagrangian drifters and satellite altimetry data. *Deep Sea Research Part I: Oceanographic Research Papers*, 65:46–58. doi: 10.1016/j.dsr.2012.02.008.

Merckelbach, L., D. Smeed, and G. Griffiths, 2010. Vertical Water Velocities from Underwater Gliders. *Journal of Atmospheric and Oceanic Technology*, 27(3):547–563. doi: 10.1175/2009JTECHO710.1.

Mertens, C. and F. Schott, 1998. Interannual Variability of Deep-Water Formation in the Northwestern Mediterranean. *Journal of Physical Oceanography*, 28(7):1410–1424. doi: 10.1175/1520-0485(1998)028<1410:IVODWF>2.0.CO;2.

Millot, C., 1990. The Gulf of Lions' hydrodynamics. *Continental Shelf Research*, 10(9-11):885–894. doi: 10.1016/0278-4343(90)90065-T.

Millot, C., 1999. Circulation in the Western Mediterranean Sea. *Journal of Marine Systems*, 20(1-4):423–442. doi: 10.1016/S0924-7963(98)00078-5.

Millot, C., 2007. Interannual salinification of the Mediterranean inflow. *Geophysical Research Letters*, 34(21):L21609. doi: 10.1029/2007GL031179.

Millot, C., 2009. Another description of the Mediterranean Sea outflow. *Progress in Oceanography*, 82(2):101–124. doi: 10.1016/j.pocean.2009.04.016.

Millot, C., 2013. Levantine Intermediate Water characteristics: an astounding general misunderstanding! *Scientia Marina*, 77(2):217–232. doi: 10.3989/scimar.03518.13A.

Millot, C., J. Candela, J.-L. Fuda, and Y. Tber, 2006. Large warming and salinification of the Mediterranean outflow due to changes in its composition. *Deep Sea Research Part I: Oceanographic Research Papers*, 53(4):656–666. doi: 10.1016/j.dsr.2005.12.017.

Millot, C. and J. Garcia-Lafuente, 2011. About the seasonal and fortnightly variabilities of the Mediterranean outflow. *Ocean Science*, 7(1):1–26. doi: 10.5194/os-7-1-2011.

Millot, C. and I. Taupier-Letage, 2005. Circulation in the Mediterranean sea. *The Handbook of Environmental Chemistry*, K(May):29–66. doi: 10.1007/b107143.

Moisan, J. R. and P. P. Niiler, 1998. The Seasonal Heat Budget of the North Pacific: Net Heat Flux and Heat Storage Rates (1950–1990). *Journal of Physical Oceanography*, 28(3):401–421. doi: 10.1175/1520-0485(1998)028<0401:TSHBOT>2.0.CO;2.

Monserrat, S., J. López-Jurado, and M. Marcos, 2008. A mesoscale index to describe the regional circulation around the Balearic Islands. *Journal of Marine Systems*, 71(3-4):413–420. doi: 10.1016/j.jmarsys.2006.11.012.

Nielsen, J. N., 1910. *Hydrography of the Mediterranean and Adjacent Waters*, volume 1. Copenhagen.

Nittis, K. and A. Lascaratos, 1998. Diagnostic and prognostic numerical studies of LIW formation. *Journal of Marine Systems*, 18(1-3):179–195. doi: 10.1016/S0924-7963(98)00011-6.

Ovchinnikov, I. M., 1984. The formation of Intermediate Water in the Mediterranean. *Oceanology*, 24:168–173.

Ozsoy, E., A. Hecht, U. Unluata, S. Brenner, H. I. Sur, J. Bishop, M. A. Latif, Z. Rozentraub, and T. Oguz, 1993. A synthesis of the Levantine Basin circulation and hydrography, 1985–1990. *Deep Sea Research Part II: Topical Studies in Oceanography*, 40(6):1075–1119. doi: http://dx.doi.org/10.1016/0967-0645(93)90063-S.

Palanques, A., X. Durrieu de Madron, P. Puig, J. Fabres, J. Guillén, A. Calafat, M. Canals, S. Heussner, and J. Bonnin, 2006. Suspended sediment fluxes and transport processes in the Gulf of Lions submarine canyons. The role of storms and dense water cascading. *Marine Geology*, 234(1-4):43–61. doi: 10.1016/j.margeo.2006.09.002.

Palanques, A., P. Puig, X. Durrieu de Madron, A. Sanchez-Vidal, C. Pasqual, J. Martín, A. Calafat, S. Heussner, and M. Canals, 2012. Sediment transport to the deep canyons and open-slope of the western Gulf of Lions during the 2006 intense cascading and open-sea convection period. *Progress in Oceanography*, 106:1–15. doi: 10.1016/j.pocean.2012.05.002.

Perkins, H. and P. Pistek, 1990. Circulation in the Algerian Basin during June 1986. *Journal of Geophysical Research*, 95(C2):1577. doi: 10.1029/JC095iC02p01577.

Pettenuzzo, D., W. G. Large, and N. Pinardi, 2010. On the corrections of ERA-40 surface flux products consistent with the Mediterranean heat and water budgets and the connection between basin surface total heat flux and NAO. *Journal of Geophysical Research*, 115(C6):C06022. doi: 10.1029/2009JC005631.

Picheral, M., L. Guidi, L. Stemmann, D. Karl, G. Iddaoud, and G. Gorsky, 2010. The Underwater Vision Profiler 5: An advanced instrument for high spatial resolution studies of particle size spectra and zooplankton. *Limnology and Oceanography: Methods*, 8:462–473. doi: 10:4319/lom.2010.8.462.

Pinardi, N., M. Zavatarelli, E. Arneri, A. Crise, and M. Ravaioli, 2006. The physical, sedimentary and ecological structure and variability of shelf areas in the Mediterranean sea. In A. R. Robinson and K. H. Brink, editors, *The Sea, Volume 14B: The Global Coastal Ocean Interdisciplinary Regional Studies an Syntheses*, volume 14, pages 1245–1331. Harvard un edition.

Pinot, J., J. López-Jurado, and M. Riera, 2002. The CANALES experiment (1996-1998). Interannual, seasonal, and mesoscale variability of the circulation in the Balearic Channels. *Progress in Oceanography*, 55(3-4):335–370. doi: 10.1016/S0079-6611(02)00139-8.

Pollak, M. I., 1951. The sources of deep water of the Eastern Mediterranean Sea. *Journal of Marine Research*, 10:128–152.

Potter, R. a., 2004. On the warming and salinification of the Mediterranean outflow waters in the North Atlantic. *Geophysical Research Letters*, 31(1):L01202. doi: 10.1029/2003GL018161.

Poulain, P.-M., M. Menna, and E. Mauri, 2012. Surface Geostrophic Circulation of the Mediterranean Sea Derived from Drifter and Satellite Altimeter Data. *Journal of Physical Oceanography*, 42(6):973–990. doi: 10.1175/JPO-D-11-0159.1.

Puig, P., X. Durrieu De Madron, J. Salat, K. Schroeder, J. Martín, A. P. Karageorgis, A. Palanques, F. Roullier, J. L. Lopez-Jurado, M. Emelianov, T. Moutin, and L. Houpert, 2012. Thick bottom nepheloid layers in the western Mediterranean generated by deep dense shelf water cascading. *Progress in Oceanography*. doi: 10.1016/j.pocean.2012.10.003.

Puig, P., A. Palanques, and J. Martín, 2013. Contemporary Sediment-Transport Processes in Submarine Canyons. *Annual review of marine science*, (July 2013):1–25. doi: 10.1146/annurev-marine-010213-135037.

Puig, P., A. Palanques, D. Orange, G. Lastras, and M. Canals, 2008. Dense shelf water cascades and sedimentary furrow formation in the Cap de Creus Canyon, northwestern Mediterranean Sea. *Continental Shelf Research*, 28(15):2017–2030. doi: 10.1016/j.csr.2008.05.002.

Puillat, I., I. Taupier-Letage, and C. Millot, 2002. Algerian Eddies lifetime can near 3 years. *Journal of Marine Systems*, 31(4):245–259. doi: 10.1016/S0924-7963(01)00056-2.

Pusceddu, a., M. Mea, M. Canals, S. Heussner, X. Durrieu de Madron, A. Sanchez-Vidal, S. Bianchelli, C. Corinaldesi, A. Dell'Anno, L. Thomsen, and R. Danovaro, 2013. Major consequences of an intense dense shelf water cascading event on deep-sea benthic trophic conditions and meiofaunal biodiversity. *Biogeosciences*, 10(4):2659–2670. doi: 10.5194/bg-10-2659-2013.

Quadfasel, D., B. Rudels, and K. Kurz, 1988. Outflow of dense water from a Svalbard fjord into the Fram Strait. *Deep Sea Research Part A. Oceanographic Research Papers*, 35(7):1143–1150. doi: 10.1016/0198-0149(88)90006-4.

Rhein, M., U. Send, B. Klein, and G. Krahmann, 1999. Interbasin deep water exchange in the western Mediterranean. *Journal of Geophysical Research*, 104(C10):23495. doi: 10.1029/1999JC900162.

Rhines, P., 1998. Circulation, covection and mixing in rotating, stratified basins with sloping topography. *Physical processes in lakes and oceans*, 54:209–226. doi: 10.1029/CE054p0209.

Rhines, P. B., 1979. Geostrophic Turbulence. *Annual Review of Fluid Mechanics*, 11(1):401–441. doi: 10.1146/annurev.fl.11.010179.002153.

Rio, M.-H., P.-M. Poulain, A. Pascual, E. Mauri, G. Larnicol, and R. Santoleri, 2007. A Mean Dynamic Topography of the Mediterranean Sea computed from altimetric data, in-situ measurements and a general circulation model. *Journal of Marine Systems*, 65(1-4):484–508. doi: 10.1016/j.jmarsys.2005.02.006.

Rixen, M., J.-M. Beckers, S. Levitus, J. Antonov, T. Boyer, C. Maillard, M. Fichaut, E. Balopoulos, S. Iona, H. Dooley, M.-J. Garcia, B. Manca, A. Giorgetti, G. Manzella, N. Mikhailov, N. Pinardi, and M. Zavatarelli, 2005. The Western Mediterranean Deep Water: A proxy for climate change. *Geophysical Research Letters*, 32(12):L12608. doi: 10.1029/2005GL022702.

Robinson, A., P. Malanotte-Rizzoli, A. Hecht, A. Michelato, W. Roether, A. Theocharis, U. Unluata, N. Pinardi, A. Artegiani, A. Bergamasco, J. Bishop, S. Brenner, S. Christianidis, M. Gacic, D. Georgopoulos, M. Golnaraghi, M. Hausmann, H.-G. Junghaus, A. Lascaratos, M. Latif, W. Leslie, C. Lozano, T. Oguz, E. Ozsoy, E. Papageorgiou, E. Paschini, Z. Rozentroub, E. Sansone, P. Scarazzato, R. Schlitzer, G.-C. Spezie, E. Tziperman, G. Zodiatis, L. Athanassiadou, M. Gerges, M. Osman, and The POEM Group, 1992. General circulation of the Eastern Mediterranean. *Earth-Science Reviews*, 32(4):285–309. doi: 10.1016/0012-8252(92)90002-B.

Robinson, A. R., W. G. Leslie, A. Theocharis, and A. Lascaratos, 2001. Mediterranean Sea Circulation. In J. H. Steele, editor, *Encyclopedia of Ocean Sciences*, pages 1689–1705. Academic Press, Oxford. doi: http://dx.doi.org/10.1006/rwos.2001.0376.

Rohling, E. J. and H. L. Bryden, 1992. Man-Induced Salinity and Temperature Increases in Western Mediterranean Deep Water. *Journal of Geophysical Research*, 97(C7):11191–11198. doi: 10.1029/92JC00767.

Salat, J., M. Emelianov, and J. L. López-Jurado, 2006. Unusual extension of Western Mediterranean deep water formation during winter 2005. *In: Proceedings 5a Asamblea Hispano-Portuguesa de Geodesia y Geofísica, Universidad de Sevilla, Sevilla, Spain.*

Salat, J. and J. Font, 1987. Water mass structure near and offshore the Catalan coast during the winter of 1982 and 1983. *Ann. Geophys*, 5:49–54.

Sammari, C., C. Millot, and L. Prieur, 1995. Aspects of the seasonal and mesoscale variabilities of the Northern Current in the western Mediterranean Sea inferred from the PROLIG-2 and PROS-6 experiments. *Deep Sea Research Part I: Oceanographic Research Papers*, 42(6):893–917. doi: 10.1016/0967-0637(95)00031-Z.

Sammari, C., C. Millot, I. Taupier-Letage, A. Stefani, and M. Brahim, 1999. Hydrological characteristics in the Tunisia–Sardinia–Sicily area during spring 1995. *Deep Sea Research Part I: Oceanographic Research Papers*, 46(10):1671–1703. doi: 10.1016/S0967-0637(99)00026-6.

Sanchez-Gomez, E., S. Somot, S. A. Josey, C. Dubois, N. Elguindi, and M. Déqué, 2011. Evaluation of Mediterranean Sea water and heat budgets simulated by an ensemble of high resolution regional climate models. *Climate Dynamics*, 37(9-10):2067–2086. doi: 10.1007/s00382-011-1012-6.

Sánchez-Román, A., G. Sannino, J. García-Lafuente, A. Carillo, and F. Criado-Aldeanueva, 2009. Transport estimates at the western section of the Strait of Gibraltar: A combined experimental and numerical modeling study. *Journal of Geophysical Research*, 114(C6):C06002. doi: 10.1029/2008JC005023.

Sanchez-Vidal, a., C. Pasqual, P. Kerhervé, A. Calafat, S. Heussner, A. Palanques, X. Durrieu de Madron, M. Canals, and P. Puig, 2008. Impact of dense shelf water cascading on the transfer of organic matter to the deep western Mediterranean basin. *Geophysical Research Letters*, 35(5):L05605. doi: 10.1029/2007GL032825.

Schlitzer, R., W. Roether, H. Oster, H.-G. Junghans, M. Hausmann, H. Johannsen, and A. Michelato, 1991. Chlorofluoromethane and oxygen in the Eastern Mediterranean. *Deep Sea Research Part A. Oceanographic Research Papers*, 38(12):1531–1551. doi: 10.1016/0198-0149(91)90088-W.

Schott, F. and K. D. Leaman, 1991. Observations with Moored Acoustic Doppler Current Profilers in the Convection Regime in the Golfe du Lion. *Journal of Physical Oceanography*, 21(4):558–574. doi: 10.1175/1520-0485(1991)021<0558:OWMADC>2.0.CO;2.

Schott, F., M. Visbeck, and J. Fischer, 1993. Observations of vertical currents and convection in the central Greenland Sea during the winter of 1988–1989. *Journal of Geophysical Research*, 98(C8):14401. doi: 10.1029/93JC00658.

Schott, F., M. Visbeck, U. Send, J. Fischer, L. Stramma, and Y. Desaubies, 1996. Observations of Deep Convection in the Gulf of Lions, Northern Mediterranean, during the

Winter of 1991/92. *Journal of Physical Oceanography*, 26(4):505–524. doi: 10.1175/1520-0485(1996)026<0505:OODCIT>2.0.CO;2.

Schroeder, K., J. Garcìa-Lafuente, S. A. Josey, V. Artale, B. B. Nardelli, A. Carrillo, M. Gačić, G. P. Gasparini, M. Herrmann, P. Lionello, W. Ludwig, C. Millot, E. Özsoy, G. Pisacane, J. C. Sánchez-Garrido, G. Sannino, R. Santoleri, S. Somot, M. Struglia, E. Stanev, I. Taupier-Letage, M. N. Tsimplis, M. Vargas-Yáñez, V. Zervakis, and G. Zodiatis, 2012. Circulation of the Mediterranean Sea and its variability. In P. Lionello, editor, *The Climate of the Mediterranean Region: from the past to the future*, pages 187–256. Elsevier. doi: 10.1016/B978-0-12-416042-2.00003-3.

Schroeder, K., G. P. Gasparini, M. Tangherlini, and M. Astraldi, 2006. Deep and intermediate water in the western Mediterranean under the influence of the Eastern Mediterranean Transient. *Geophysical Research Letters*, 33(21):L21607. doi: 10.1029/2006GL027121.

Schroeder, K., S. A. Josey, M. Herrmann, L. Grignon, G. P. Gasparini, and H. L. Bryden, 2010. Abrupt warming and salting of the Western Mediterranean Deep Water after 2005: Atmospheric forcings and lateral advection. *Journal of Geophysical Research*, 115(C8):1–18. doi: 10.1029/2009JC005749.

Schroeder, K., C. Millot, L. Bengara, S. Ben Ismail, M. Bensi, M. Borghini, G. Budillon, V. Cardin, L. Coppola, C. Curtil, A. Drago, B. El Moumni, J. Font, J. L. Fuda, J. García-Lafuente, G. P. Gasparini, H. Kontoyiannis, D. Lefevre, P. Puig, P. Raimbault, G. Rougier, J. Salat, C. Sammari, J. C. Sánchez Garrido, A. Sanchez-Roman, S. Sparnocchia, C. Tamburini, I. Taupier-Letage, A. Theocharis, M. Vargas-Yáñez, and A. Vetrano, 2013. Long-term monitoring programme of the hydrological variability in the Mediterranean Sea: a first overview of the HYDROCHANGES network. *Ocean Science*, 9(2):301–324. doi: 10.5194/os-9-301-2013.

Schroeder, K., A. Ribotti, M. Borghini, R. Sorgente, A. Perilli, and G. P. Gasparini, 2008. An extensive western Mediterranean deep water renewal between 2004 and 2006. *Geophysical Research Letters*, 35(18):L18605. doi: 10.1029/2008GL035146.

Send, U., C. Mertens, and J. Font, 1996. Recent observation indicates convection' role in deep water circulation. *Eos, Transactions American Geophysical Union*, 77(7):61. doi: 10.1029/96EO00040.

Shapiro, G., J. Huthnance, and V. Ivanov, 2003. Dense water cascading off the continental shelf. *Journal of Geophysical Research*, 108(C12):3390. doi: 10.1029/2002JC001610.

Smith, R. O., H. L. Bryden, and K. Stansfield, 2008. Observations of new western Mediterranean deep water formation using Argo floats 2004–2006. *Ocean Science*, 4(2):133–149. doi: 10.5194/os-4-133-2008.

Somot, S., F. Sevault, and M. Déqué, 2006. Transient climate change scenario simulation of the Mediterranean Sea for the twenty-first century using a high-resolution ocean circulation model. *Climate Dynamics*, 27(7-8):851–879. doi: 10.1007/s00382-006-0167-z.

Soto-Navarro, J., F. Criado-Aldeanueva, J. García-Lafuente, and A. Sánchez-Román, 2010. Estimation of the Atlantic inflow through the Strait of Gibraltar from climatological and in situ data. *Journal of Geophysical Research*, 115(C10):C10023. doi: 10.1029/2010JC006302.

Sparnocchia, S., G. Gasparini, M. Astraldi, M. Borghini, and P. Pistek, 1999. Dynamics and mixing of the Eastern Mediterranean outflow in the Tyrrhenian basin. *Journal of Marine Systems*, 20(1-4):301–317. doi: 10.1016/S0924-7963(98)00088-8.

Sparnocchia, S., P. Picco, G. M. Manzella, A. Ribotti, S. Copello, and P. Brasey, 1995. Intermediate water formation in the Ligurian Sea. *Oceanologica Acta*, 18(2):151–162.

Sprintall, J. and M. F. Cronin, 2009. Upper ocean vertical structure. In J. Steele, S. Thorpe, and K. Turekian, editors, *Elements of Physical Oceanography: A derivative of the Encyclopedia of Ocean Sciences*, pages 229–236. London UK, academic p edition.

Steffen, E. L. and E. a. D'Asaro, 2004. Meso- and Submesoscale Structure of a Convecting Field. *Journal of Physical Oceanography*, 34(1):44–60. doi: 10.1175/1520-0485(2004)034<0044:MASSOA>2.0.CO;2.

Straneo, F. and M. Kawase, 1999. Comparisons of Localized Convection due to Localized Forcing and to Preconditioning. *Journal of Physical Oceanography*, 29(1):55–68. doi: 10.1175/1520-0485(1999)029<0055:COLCDT>2.0.CO;2.

Taupier-Letage, I. and C. Millot, 1988. Surface circulation in the Algerian Basin during 1984. *Oceanol. Acta*, 9:119–131.

Testor, P. and J.-C. Gascard, 2003. Large-Scale Spreading of Deep Waters in the Western Mediterranean Sea by Submesoscale Coherent Eddies. *Journal of Physical Oceanography*, 33(1):75–87. doi: 10.1175/1520-0485(2003)033<0075:LSSODW>2.0.CO;2.

Testor, P. and J.-C. Gascard, 2006. Post-convection spreading phase in the Northwestern Mediterranean Sea. *Deep Sea Research Part I: Oceanographic Research Papers*, 53(5):869–893. doi: 10.1016/j.dsr.2006.02.004.

Testor, P., G. Meyers, C. Pattiaratchi, R. Bachmayer, D. Hayes, S. Pouliquen, L. P. de la Villeon, T. Carval, A. Ganachaud, L. Gourdeau, L. Mortier, H. Claustre, V. Taillandier, P. Lherminier, T. Terre, M. Visbeck, J. Karstensen, G. Krahmann, A. Alvarez, M. Rixen, P. Poulain, S. Osterhus, J. Tintore, S. Ruiz, B. Garau, D. Smeed, G. Griffiths, L. Merckelbach, T. Sherwin, C. Schmid, J. Barth, O. Schofield, S. Glenn, J. Kohut, M. Perry, C. Eriksen, U. Send, R. Davis, D. Rudnick, J. Sherman, C. Jones, D. Webb, C. Lee, and B. Owens, 2010. Gliders as a Component of Future Observing Systems. In J. Hall, D. E. Harrison, and D. Stammer, editors, *Proceedings of the "OceanObs'09: Sustained Ocean Observations and Information for Society"*, volume 2 of *ESA Publication*. OceanObs'09, Venice, Italy.

Testor, P., L. Mortier, U. Send, R. Davis, D. Smeed, L. Merckelbach, A. Alvarez, J. Tintore, P. Lherminier, T. Terre, and Others, 2007. European Gliding Observatories (EGO). *Coriolis Newsletter*, 4:11–12.

Testor, P., U. Send, J.-C. Gascard, C. Millot, I. Taupier-Letage, and K. Béranger, 2005. The mean circulation of the southwestern Mediterranean Sea: Algerian Gyres. *Journal of Geophysical Research*, 110(C11):C11017. doi: 10.1029/2004JC002861.

The MerMex Group, 2011. Marine ecosystems' responses to climatic and anthropogenic forcings in the Mediterranean. *Progress in Oceanography*, 91(2):97–166. doi: 10.1016/j.pocean.2011.02.003.

The THETIS Group, 1994. Open-ocean deep convection explored in the Mediterranean. *Eos, Transactions American Geophysical Union*, 75(19):217. doi: 10.1029/94EO00893.

Theocharis, A., D. Georgopoulos, A. Lascaratos, and K. Nittis, 1993. Water masses and circulation in the central region of the Eastern Mediterranean: Eastern Ionian, South Aegean and Northwest Levantine, 1986–1987. *Deep Sea Research Part II: Topical Studies in Oceanography*, 40(6):1121–1142. doi: 10.1016/0967-0645(93)90064-T.

Troupin, C., F. Machín, M. Ouberdous, D. Sirjacobs, a. Barth, and J.-M. Beckers, 2010. High-resolution climatology of the northeast Atlantic using Data-Interpolating Variational Analysis (Diva). *Journal of Geophysical Research*, 115(C8):C08005. doi: 10.1029/2009JC005512.

Tsimplis, M. and H. Bryden, 2000. Estimation of the transports through the Strait of Gibraltar. *Deep Sea Research Part I: Oceanographic Research Papers*, 47(12):2219–2242. doi: 10.1016/S0967-0637(00)00024-8.

Turner, J., 1973. *Buoyancy effects in fluids*. New York, cambridge edition.

Tziperman, E. and P. Malanotte-Rizzoli, 1991. The climatological seasonal circulation of the Mediterranean Sea. *Journal of Marine Research*, 49(3):411–434. doi: 10.1357/002224091784995783.

Ulses, C., C. Estournel, J. Bonnin, X. Durrieu de Madron, and P. Marsaleix, 2008a. Impact of storms and dense water cascading on shelf-slope exchanges in the Gulf of Lion (NW Mediterranean). *Journal of Geophysical Research*, 113(C2):1–18. doi: 10.1029/2006JC003795.

Ulses, C., C. Estournel, P. Puig, X. Durrieu de Madron, and P. Marsaleix, 2008b. Dense shelf water cascading in the northwestern Mediterranean during the cold winter 2005: Quantification of the export through the Gulf of Lion and the Catalan margin. *Geophysical Research Letters*, 35(7):n/a–n/a. doi: 10.1029/2008GL033257.

Vargas-Yanez, M., F. Moya, M. García-Martínez, E. Tel, P. Zunino, F. Plaza, J. Salat, J. Pascual, J. Lopez-Jurado, and M. Serra, 2010a. Climate change in the Western Mediterranean Sea 1900–2008. *Journal of Marine Systems*, 82(3):171–176. doi: 10.1016/j.jmarsys.2010.04.013.

Vargas-Yanez, M., T. Ramirez, D. Cortes, M. Sebastian, and F. Plaza, 2002. Warming trends in the continental shelf of Málaga Bay (Alborán Sea). *Geophysical Research ...*, 29(22):2082. doi: 10.1029/2002GL015306.

Vargas-Yanez, M., P. Zunino, A. Benali, M. Delpy, F. Pastre, F. Moya, M. D. C. García-Martínez, and E. Tel, 2010b. How much is the western Mediterranean really warming and salting? *Journal of Geophysical Research*, 115(C4):C04001. doi: 10.1029/2009JC005816.

Venaille, A., G. K. Vallis, and S. M. Griffies, 2012. The catalytic role of the beta effect in barotropization processes. *Journal of Fluid Mechanics*, 709(2001):490–515. doi: 10.1017/jfm.2012.344.

Visbeck, M., J. Marshall, and H. Jones, 1996. Dynamics of Isolated Convective Regions in the Ocean. *Journal of Physical Oceanography*, 26(9):1721–1734. doi: 10.1175/1520-0485(1996)026<1721:DOICRI>2.0.CO;2.

Voorhis, A. D. and D. C. Webb, 1970. Large Vertical Currents Observed in a Winter Sinking Region of the Northwestern Mediterranean. *Cahiers Oceanographiques*, XXII(6):571–580.

Wijffels, S. E., J. Willis, C. M. Domingues, P. Barker, N. J. White, A. Gronell, K. Ridgway, and J. a. Church, 2008. Changing Expendable Bathythermograph Fall Rates and Their Impact on Estimates of Thermosteric Sea Level Rise. *Journal of Climate*, 21(21):5657–5672. doi: 10.1175/2008JCLI2290.1.

Williams, R. and M. Follows, 2003. Physical transport of nutrients and the maintenance of biological production. In M. J. R. Fasham, editor, *Ocean Biogeochemistry: The Role of the Ocean Carbon Cycle in Global Change*, pages 19–51. Springer Berlin Heidelberg, Berlin, Heidelberg. doi: 10.1007/978-3-642-55844-3.

Wunsch, C., 2002. Oceanography. What is the thermohaline circulation? *Science*, 298(5596):1179–81. doi: 10.1126/science.1079329.

Wüst, G., 1961. On the vertical circulation of the Mediterranean Sea. *Journal of Geophysical Research*, 66(10):3261. doi: 10.1029/JZ066i010p03261.

Zodiatis, G., 1993. Circulation of the cretan sea-water masses (eastern mediterranean-sea). *Oceanologica acta*, 16:107–114.

Zodiatis, G., P. Drakopoulos, S. Brenner, and S. Groom, 2005. Variability of the Cyprus warm core Eddy during the CYCLOPS project. *Deep Sea Research Part II: Topical Studies in Oceanography*, 52(22-23):2897–2910. doi: 10.1016/j.dsr2.2005.08.020.

Zodiatis, G., A. Theodorou, and A. Demetropoulos, 1998. Hydrography and circulation south of Cyprus in late summer 1995 and in spring 1996. *Oceanologica Acta*, 21(3):447–458. doi: 10.1016/S0399-1784(98)80029-7.

Appendices

A Supplementary Figures for Chapter 3

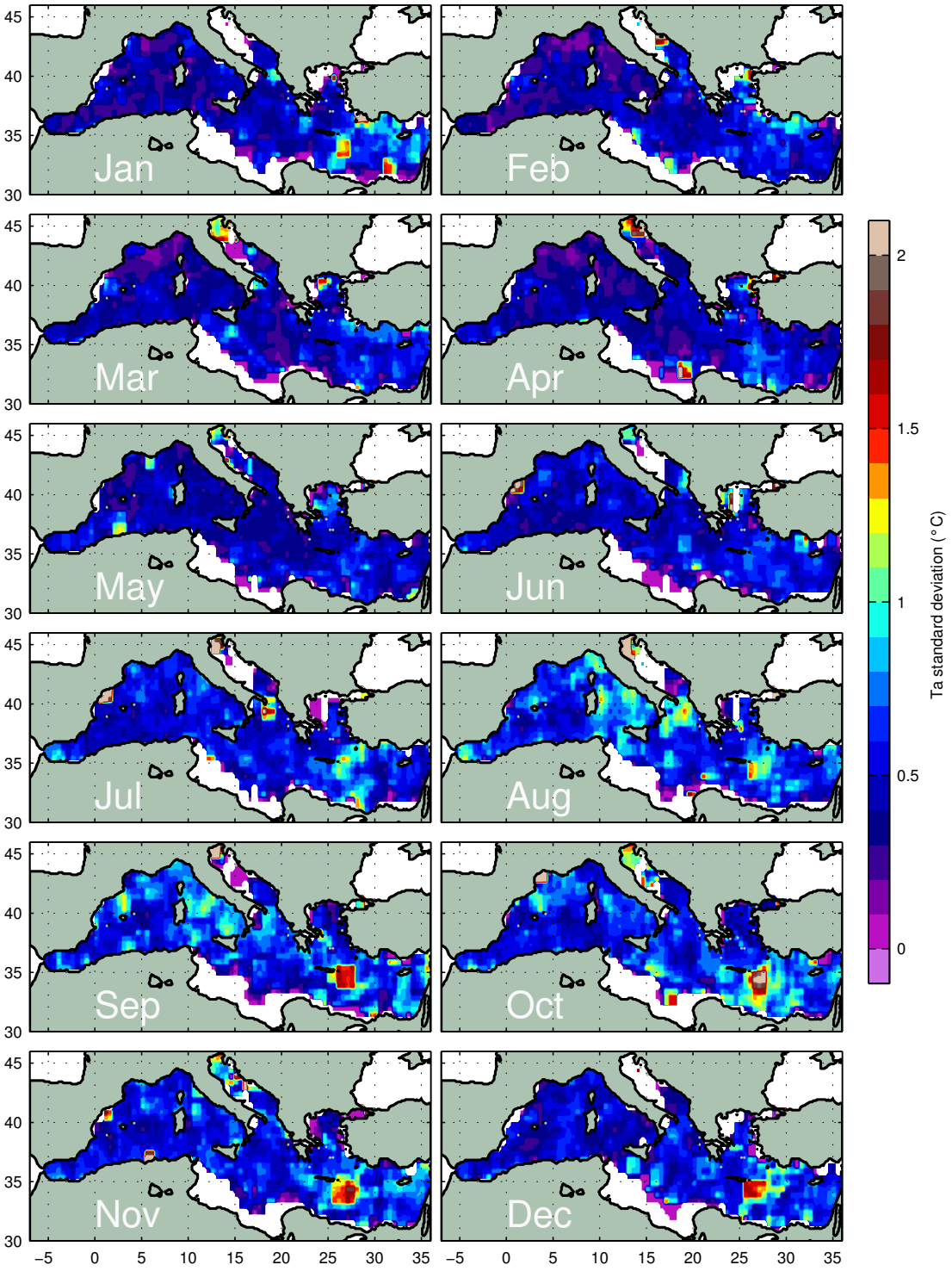

Figure A.1: Maps of the standard deviation associated to the mesh box averages of the upper-ocean temperature T_a shown on figure 3.10.

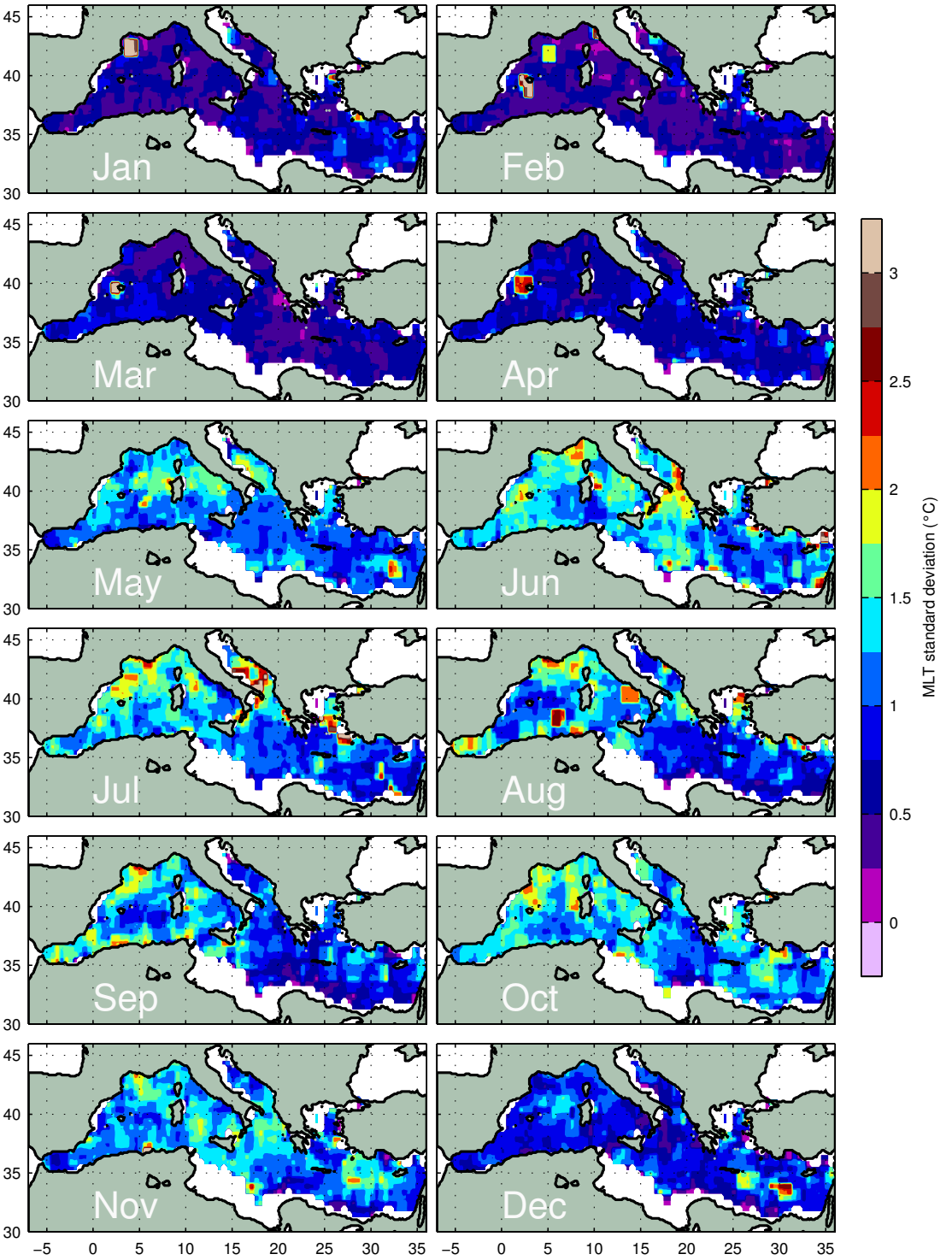

Figure A.2: Maps of the standard deviation associated to the mesh box averages of the mixed layer temperature shown on figure 3.11.

B Enhancing the Comprehension of Mixed Layer Depth Control on the Mediterranean Phytoplankton Phenology, Lavigne H. et al., 2013 (doi: 10.1002/jgrc.20251)

JOURNAL OF GEOPHYSICAL RESEARCH: OCEANS, VOL. 118, 1–15, doi:10.1002/jgrc.20251, 2013

Enhancing the comprehension of mixed layer depth control on the Mediterranean phytoplankton phenology

Héloïse Lavigne,[1] Fabrizio D'Ortenzio,[1] Christophe Migon,[1] Hervé Claustre,[1] Pierre Testor,[2] Maurizio Ribera d'Alcalà,[3] Rosario Lavezza,[3] Loïc Houpert,[4] and Louis Prieur[1]

Received 10 February 2013; revised 3 May 2013; accepted 22 May 2013.

[1] Phytoplankton phenology is primarily affected by physical forcing. However, its quantification is far from being completely understood. Among the physical forcing factors, the mixed layer depth (MLD) is considered to have the strongest impact on phytoplankton dynamics, and consequently, on their phenology. The role of MLD variations in shaping the phytoplankton phenology was explored in the Mediterranean Sea, a basin displaying contrasting phenological regimes. A database of MLD estimations was merged with ocean color chlorophyll concentrations ($[Chl]_{SAT}$) to generate concomitant annual MLD and $[Chl]_{SAT}$ cycles. Several indices were calculated to quantitatively analyze these cycles. The relevance of indices summarizing the temporal difference between main characteristics of MLD and $[Chl]_{SAT}$ cycles was emphasized. As previously observed, two dominant phenological regimes coexist in the Mediterranean Sea. The first is marked by a typical spring bloom, as in temperate regions. The second displays a low seasonality and an absence of an intense $[Chl]_{SAT}$ peak as in subtropical areas. The MLD is shown to play a key role in determining the dominant phenological regime in a given area. Results also show that regions having low seasonality display concomitant MLD and $[Chl]_{SAT}$ maxima, whereas $[Chl]_{SAT}$ peaks are generally observed 30 days after MLD peaks in regions with strongest seasonality. Over the whole basin, $[Chl]_{SAT}$ increase starts 1 month after the initiation of MLD deepening. Finally, after examining the impact of MLD on light and nutrient availability for phytoplankton, mechanisms were proposed to explain the time lags between MLD and $[Chl]_{SAT}$ increase and MLD and $[Chl]_{SAT}$ maxima.

Citation: Lavigne, H., F. D'Ortenzio, C. Migon, H. Claustre, P. Testor, M. Ribera d'Alcalà, R. Lavezza, L. Houpert, and L. Prieur (2013), Enhancing the comprehension of mixed layer depth control on the Mediterranean phytoplankton phenology, *J. Geophys. Res. Oceans*, *118*, doi:10.1002/jgrc.20251.

1. Introduction

[2] Characterizing the oceanic phytoplankton phenology is a critical step to identify major alterations in the functioning of oceanic ecosystems and to further connect these alterations to global or local environmental changes. As indicated in a recent review [*Ji et al*., 2010], the description of the oceanic phytoplankton phenology implies the identification (in terms of date, duration, and magnitude) of the main steps in the temporal evolution of key parameters of an ocean ecosystem (i.e., chlorophyll-a, phytoplankton species compositions, zooplankton abundances, etc.). Linking these key episodes to environmental conditions could strongly improve our capability to identify future trends in marine ecosystem dynamics.

[3] However, until recently, the lack of data hinders a broad and global analysis of phytoplankton ocean phenology, except on some areas (i.e., Hawaii Ocean Time series (HOT) and Bermuda Atlantic Time Series (BATS)) where data are available. Satellite ocean color remote sensing, generating global and repeated observations of the ocean surface chlorophyll concentration (a proxy for phytoplankton biomass) induced a fresh impetus in the study of phytoplankton phenology. Indeed, despite the limits of the ocean color data (i.e., cloud coverage, surface observation, algorithmic issues, variation in carbon to chlorophyll ratio) numerous analyses used satellite observations of surface

Additional supporting information may be found in the online version of this article.

[1]Laboratoire d'Oceanographie de Villefranche, Université Pierre et Marie Curie and CNRS, UMR 7093, Villefranche-sur-Mer, France.
[2]Laboratoire d'Oceanographie et du Climat: Expérimentations et Approches Numériques, Université Pierre et Marie Curie, Institut Pierre Simon Laplace et CNRS, UMR 7159, Paris, France.
[3]Stazione Zoologica A. Dohrn, Laboratorio di Oceanografia Biologica, Naples, Italy.
[4]Centre de Formation et de Recherche sur les Environnements Méditerranéens, Université de Perpignan Via Domicia et CNRS, UMR 5110, Perpignan, France.
[5]Laboratoire d'Oceanographie de Villefranche, Université Pierre et Marie Curie et CNRS, UMR 7093, Villefranche-sur-Mer, France.

Corresponding author: H. Lavigne, Laboratoire d'Océanographie de Villefranche, Quai de la Darse BP08, FR-06238 Villefranche sur Mer CEDEX, France. (lavigne@obs-vlfr.fr)

2169-9275/13/10.1002/jgrc.20251

C Impact of Open-Ocean Convection on Particle Fluxes and Sediment Dynamics in the Deep Margin of the Gulf of Lions, Stabholz M. et al., 2012 (doi:10.5194/bg-10-1097-2013)

Biogeosciences, 10, 1097–1116, 2013
www.biogeosciences.net/10/1097/2013/
doi:10.5194/bg-10-1097-2013

Biogeosciences Open Access

Impact of open-ocean convection on particle fluxes and sediment dynamics in the deep margin of the Gulf of Lions

M. Stabholz[1,2], X. Durrieu de Madron[1], M. Canals[2], A. Khripounoff[3], I. Taupier-Letage[4], P. Testor[5], S. Heussner[1], P. Kerhervé[1], N. Delsaut[1], L. Houpert[1], G. Lastras[2], and B. Dennielou[6]

[1]CEFREM, CNRS, Université de Perpignan Via Domitia, UMR 5110, 52 avenue Paul Alduy, 66860 Perpignan, France
[2]GRC Geociències Marines, Departament d'Estratigrafia, Paleontologia i Geociències Marines, Universitat de Barcelona, C/Martí i Franqués, s/n, 08028 Barcelona, Spain
[3]IFREMER, Département EEP/LEP, Centre de Bretagne BP70, 29280 Plouzané Cedex, France
[4]Aix-Marseille Université, Université du Sud Toulon-Var, CNRS/INSU, IRD, MIO, UMR 6117, UM 110, 83507 La Seyne sur Mer, France
[5]LOCEAN, CNRS, IRD, Université Pierre et Marie Curie, MNHN, UMR 7159, 4 place Jussieu, 75252 Paris, France
[6]IFREMER, Unité de Recherche Géosciences Marines, BP70, 29280 Plouzané Cedex, France

Correspondence to: M. Stabholz (marionstabholz@hotmail.com)

Received: 1 August 2012 – Published in Biogeosciences Discuss.: 18 September 2012
Revised: 7 January 2013 – Accepted: 20 January 2013 – Published: 19 February 2013

Abstract. The deep outer margin of the Gulf of Lions and the adjacent basin, in the western Mediterranean Sea, are regularly impacted by open-ocean convection, a major hydrodynamic event responsible for the ventilation of the deep water in the western Mediterranean Basin. However, the impact of open-ocean convection on the flux and transport of particulate matter remains poorly understood. The variability of water mass properties (i.e., temperature and salinity), currents, and particle fluxes were monitored between September 2007 and April 2009 at five instrumented mooring lines deployed between 2050 and 2350-m depth in the deepest continental margin and adjacent basin. Four of the lines followed a NW–SE transect, while the fifth one was located on a sediment wave field to the west. The results of the main, central line SC2350 ("LION") located at 42°02.5′ N, 4°41′ E, at 2350-m depth, show that open-ocean convection reached mid-water depth (≈ 1000-m depth) during winter 2007–2008, and reached the seabed (≈ 2350-m depth) during winter 2008–2009. Horizontal currents were unusually strong with speeds up to 39 cm s^{-1} during winter 2008–2009. The measurements at all 5 different locations indicate that mid-depth and near-bottom currents and particle fluxes gave relatively consistent values of similar magnitude across the study area except during winter 2008–2009, when near-bottom fluxes abruptly increased by one to two orders of magnitude. Particulate organic carbon contents, which generally vary between 3 and 5 %, were abnormally low (≤ 1 %) during winter 2008–2009 and approached those observed in surface sediments (≈ 0.6 %). Turbidity profiles made in the region demonstrated the existence of a bottom nepheloid layer, several hundred meters thick, and related to the resuspension of bottom sediments. These observations support the view that open-ocean deep convection events in the Gulf of Lions can cause significant remobilization of sediments in the deep outer margin and the basin, with a subsequent alteration of the seabed likely impacting the functioning of the deep-sea ecosystem.

1 Introduction

Albeit the deep-sea is the largest ecosystem on Earth, not much is known about how it is affected by changes in environmental conditions controlling the cycling of biogeochemical compounds, the distribution of deep-sea habitats or the functioning of ecosystems. Dense water convection represents, among physical processes influencing circulation in the deep-sea, one of the few linking the surface ocean to the deep ocean and, ultimately, to the seabed. Dense water formation, which can occur in both coastal areas and open sea regions, and the subsequent export of newly formed

D Deep-Sea Bioluminescence Blooms after Dense Water Formation at the Ocean Surface, Tamburini C. et al., 2013 (doi:10.1371/journal.pone.0067523)

OPEN ACCESS Freely available online

PLOS ONE

Deep-Sea Bioluminescence Blooms after Dense Water Formation at the Ocean Surface

Christian Tamburini[1,2]*, Miquel Canals[3], Xavier Durrieu de Madron[4], Loïc Houpert[4], Dominique Lefèvre[1,2], Séverine Martini[1,2], Fabrizio D'Ortenzio[5], Anne Robert[1,2], Pierre Testor[6], Juan Antonio Aguilar[7], Imen Al Samarai[8], Arnaud Albert[9], Michel André[10], Marco Anghinolfi[11], Gisela Anton[12], Shebli Anvar[13], Miguel Ardid[14], Ana Carolina Assis Jesus[15], Tri L. Astraatmadja[15¤a], Jean-Jacques Aubert[8], Bruny Baret[16], Stéphane Basa[17], Vincent Bertin[8], Simone Biagi[18,19], Armando Bigi[20], Ciro Bigongiari[7], Claudio Bogazzi[15], Manuel Bou-Cabo[14], Boutayeb Bouhou[16], Mieke C. Bouwhuis[15], Jurgen Brunner[8¤b], José Busto[8], Francisco Camarena[14], Antonio Capone[21,22], Christina Cârloganu[23], Giada Carminati[18,19¤c], John Carr[8], Stefano Cecchini[18,24], Ziad Charif[8], Philippe Charvis[25], Tommaso Chiarusi[18], Marco Circella[26], Rosa Coniglione[27], Heide Costantini[8,11], Paschal Coyle[8], Christian Curtil[8], Patrick Decowski[15], Ivan Dekeyser[1,2], Anne Deschamps[25], Corinne Donzaud[16,28], Damien Dornic[7,8], Hasankiadeh Q. Dorosti[29], Doriane Drouhin[9], Thomas Eberl[12], Umberto Emanuele[7], Jean-Pierre Ernenwein[8], Stéphanie Escoffier[8]*, Paolo Fermani[21,22], Marcelino Ferri[14], Vincenzo Flaminio[20,30], Florian Folger[12], Ulf Fritsch[12], Jean-Luc Fuda[1,2¤d], Salvatore Galatà[8], Pascal Gay[23], Giorgio Giacomelli[18,19], Valentina Giordano[27], Juan-Pablo Gómez-González[7], Kay Graf[12], Goulven Guillard[23], Garadeb Halladjian[8], Gregory Hallewell[8], Hans van Haren[31], Joris Hartman[15], Aart J. Heijboer[15], Yann Hello[25], Juan Jose Hernández-Rey[7], Bjoern Herold[12], Jurgen Hößl[12], Ching-Cheng Hsu[15], Marteen de Jong[15¤a], Matthias Kadler[32], Oleg Kalekin[12], Alexander Kappes[12], Uli Katz[12], Oksana Kavatsyuk[29], Paul Kooijman[15,33,34], Claudio Kopper[12], Antoine Kouchner[16], Ingo Kreykenbohm [32], Vladimir Kulikovskiy[11,35], Robert Lahmann[12], Patrick Lamare[13], Giuseppina Larosa[14], Dario Lattuada[27], Gordon Lim[15,34], Domenico Lo Presti[36,37], Herbert Loehner[29], Sotiris Loucatos[38], Salvatore Mangano[7], Michel Marcelin[17], Annarita Margiotta[18,19], Juan Antonio Martinez-Mora[14], Athina Meli[12], Teresa Montaruli[26,39], Luciano Moscoso[16,38†], Holger Motz[12], Max Neff[12], Emma nuel Nezri[17], Dimitris Palioselitis[15], Gabriela E. Păvălaş[40], Kevin Payet[38], Patrice Payre[8], Jelena Petrovic[15], Paolo Piattelli[27], Nicolas Picot-Clemente[8], Vlad Popa[40], Thierry Pradier[41], Eleonora Presani[15], Chantal Racca[9], Corey Reed[15], Giorgio Riccobene[27], Carsten Richardt[12], Roland Richter[12], Colas Rivière[8], Kathrin Roensch[12], Andrei Rostovtsev[42], Joaquin Ruiz-Rivas[7], Marius Rujoiu[40], Valerio G. Russo[36,37], Francisco Salesa[7], Augustin Sánchez-Losa[7], Piera Sapienza[27], Friederike Schöck[12], Jean-Pierre Schuller[38], Fabian Schussler[38], Rezo Shanidze[12], Francesco Simeone[21,22], Andreas Spies[12], Maurizio Spurio[18,19], Jos J. M. Steijger[15], Thierry Stolarczyk[38], Mauro G. F. Taiuti[11,43], Simona Toscano[7], Bertrand Vallage[38], Véronique Van Elewyck[16], Giulia Vannoni[38], Manuela Vecchi[8], Pascal Vernin[38], Guus Wijnker[15], Jorn Wilms[32], Els de Wolf[15,34], Harold Yepes[7], Dmitry Zaborov[42], Juan De Dios Zornoza[7], Juan Zúñiga[7]

1 Aix Marseille Université, CNRS/INSU, IRD, Mediterranean Institute of Oceanography (MIO), UM 110, Marseille, France, **2** Université de Toulon, CNRS/INSU, IRD, Mediterranean Institute of Oceanography (MIO), UM 110, La Garde, France, **3** GRC Geociències Marines, Departament d'Estratigrafia, Paleontologia i Geociències Marines, Facultat de Geologia, Universitat de Barcelona, Campus de Pedralbes, Barcelona, Spain, **4** Université de Perpignan, CNRS-INSU, CEFREM UMR5110, Perpignan, France, **5** Université Pierre & Marie Curie, CNRS-INSU, LOV UMR7093, Villefranche-sur-mer, France, **6** Université Pierre & Marie Curie, CNRS-INSU, Institut Pierre Simon Laplace, LOCEAN UMR 7159, Paris, France, **7** IFIC – Instituto de Física Corpuscular, Edificios Investigación de Paterna, CSIC – Universitat de València, Apdo. de Correos, Valencia, Spain, **8** CPPM – Aix-Marseille Université, CNRS/IN2P3, Marseille, France, **9** GRPHE – Institut universitaire de technologie de Colmar, Colmar, France, **10** Technical University of Catalonia, Laboratory of Applied Bioacoustics, Barcelona, Spain, **11** INFN – Sezione di Genova, Genova, Italy, **12** Friedrich-Alexander-Universität Erlangen-Nürnberg, Erlangen Centre for Astroparticle Physics, Erlangen, Germany, **13** Direction des Sciences de la Matière – Institut de recherche sur les lois fondamentales de l'Univers – Service d'Electronique des Détecteurs et d'Informatique, CEA Saclay, Gif-sur-Yvette, France, **14** Institut d'Investigació per a la Gestió Integrada de les Zones Costaneres (IGIC) – Universitat Politècnica de València, Gandia, Spain, **15** Nikhef, Amsterdam, The Netherlands, **16** APC, Université Paris Diderot, CNRS/IN2P3, CEA/IRFU, Observatoire de Paris, Sorbonne Paris Cité, Paris, France, **17** Aix Marseille Université, CNRS, LAM (Laboratoire d'Astrophysique de Marseille) UMR 7326, Marseille, France, **18** INFN – Sezione di Bologna, Bologna, Italy, **19** Dipartimento di Fisica dell'Università, Bologna, Italy, **20** INFN – Sezione di Pisa, Pisa, Italy, **21** INFN -Sezione di Roma, Roma, Italy, **22** Dipartimento di Fisica dell'Università La Sapienza, Roma, Italy, **23** Clermont Université, Université Blaise Pascal, CNRS/IN2P3, Laboratoire de Physique Corpusculaire, IN2P3-CNRS, Clermont-Ferrand, France, **24** INAF-IASF, Bologna, Italy, **25** Géoazur – Université de Nice Sophia-Antipolis, CNRS/INSU, IRD, Observatoire de la Côte d'Azur and Université Pierre et Marie Curie, Villefranche-sur-Mer, France, **26** INFN – Sezione di Bari, Bari, Italy, **27** INFN – Laboratori Nazionali del Sud (LNS), Catania, Italy, **28** Université Paris-Sud, Orsay, France, **29** Kernfysisch Versneller Instituut (KVI), University of Groningen, Groningen, The Netherlands, **30** Dipartimento di Fisica dell'Università Pisa, Italy, **31** Royal Netherlands Institute for Sea Research (NIOZ), Texel, The Netherlands, **32** Dr. Remeis Sternwarte & ECAP, Bamberg, Germany,

33 Universiteit Utrecht, Faculteit Betawetenschappen, Utrecht, The Netherlands, **34** Universiteit van Amsterdam, Instituut voor Hoge-Energie Fysika, Amsterdam, The Netherlands, **35** Moscow State University, Skobeltsyn Institute of Nuclear Physics, Moscow, Russia, **36** INFN – Sezione di Catania, Catania, Italy, **37** Dipartimento di Fisica ed Astronomia dell'Università, Catania, Italy, **38** Direction des Sciences de la Matière – Institut de recherche sur les lois fondamentales de l'Univers – Service de Physique des Particules, CEA Saclay, Gif-sur-Yvette, France, **39** University of Wisconsin – Madison, Madison, Wisconsin, United States of America, **40** Institute for Space Sciences, Bucharest, Romania, **41** IPHC-Institut Pluridisciplinaire Hubert Curien – Université de Strasbourg et CNRS/IN2P3, Strasbourg, France, **42** ITEP – Institute for Theoretical and Experimental Physics, Moscow, Russia, **43** Dipartimento di Fisica dell'Università, Genova, Italy

Abstract

The deep ocean is the largest and least known ecosystem on Earth. It hosts numerous pelagic organisms, most of which are able to emit light. Here we present a unique data set consisting of a 2.5-year long record of light emission by deep-sea pelagic organisms, measured from December 2007 to June 2010 at the ANTARES underwater neutrino telescope in the deep NW Mediterranean Sea, jointly with synchronous hydrological records. This is the longest continuous time-series of deep-sea bioluminescence ever recorded. Our record reveals several weeks long, seasonal bioluminescence blooms with light intensity up to two orders of magnitude higher than background values, which correlate to changes in the properties of deep waters. Such changes are triggered by the winter cooling and evaporation experienced by the upper ocean layer in the Gulf of Lion that leads to the formation and subsequent sinking of dense water through a process known as "open-sea convection". It episodically renews the deep water of the study area and conveys fresh organic matter that fuels the deep ecosystems. Luminous bacteria most likely are the main contributors to the observed deep-sea bioluminescence blooms. Our observations demonstrate a consistent and rapid connection between deep open-sea convection and bathypelagic biological activity, as expressed by bioluminescence. In a setting where dense water formation events are likely to decline under global warming scenarios enhancing ocean stratification, *in situ* observatories become essential as environmental sentinels for the monitoring and understanding of deep-sea ecosystem shifts.

Citation: Tamburini C, Canals M, Durrieu de Madron X, Houpert L, Lefèvre D, et al. (2013) Deep-Sea Bioluminescence Blooms after Dense Water Formation at the Ocean Surface. PLoS ONE 8(7): e67523. doi:10.1371/journal.pone.0067523

Editor: John Murray Roberts, Heriot-Watt University, United Kingdom

Received December 25, 2012; **Accepted** May 20, 2013; **Published** July 10, 2013

Funding: This work was partially funded by the ANR-POTES program (ANR-05-BLAN-0161-01), ANTARES-Bioluminescence project (INSU-IN2P3), AAMIS project (Univ. Méditerranée), EC2CO Biolux project (CNRS INSU), Excellence Research Groups (2009-SGR-1305, Generalitat de Catalunya), EuroSITES (FP7-ENV-2007-1-202955), MARINERA-REDECO (CTM2008-04973-E/MAR), HERMIONE (FP7-ENV-2008-1-226354), KM3NeT-PP (212525), ESONET NoE (FP6- GOCE-036851), DOS MARES (CTM2010-21810-C03-01) and CONSOLIDER-INGENIO GRACCIE (CSD2007-00067) projects. SM was granted a MERNT fellowship (Ministry of Education, Research and Technology, France). LH acknowledges the support of the Direction Générale de l'Armement (supervisor: Elisabeth Gibert-Brunet). The authors also acknowledge the financial support of the funding agencies: CNRS, CEA, ANR, FEDER fund and Marie Curie Program, Régions Alsace and Provence-Alpes-Côte d'Azur, Département du Var and Ville de La Seyne-sur-Mer, France; BMBF, Germany; INFN, Italy; FOM and NWO, the Netherlands; Council of the President of the Russian Federation for young scientists and leading scientific schools supporting grants, Russia; ANCS, Romania; MICINN (FPA2009-13983-C02-01), PROMETEO (2009/026) and MultiDark (CSD2009-00064). The funders had no role in study design, data collection and analysis, decision to publish, or preparation of the manuscript.

Competing Interests: The authors have declared that no competing interests exist.

* E-mail: christian.tamburini@univ-amu.fr (CT); escoffier@cppm.in2p3.fr (SE)

¤a Current address: University of Leiden, Leiden, The Netherlands
¤b Current address: DESY, Zeuthen, Germany
¤c Current address: University of California Irvine, Irvine, California, United States of America
¤d Current address: IRD – Centre de Nouméa, Noumea, Nouvelle-Calédonie

† Deceased.

Introduction

The deep-sea ecosystem is unique because of its permanent darkness, coldness, high pressure and scarcity of carbon and energy to sustain life. Most of its biological activity relies on the arrival of carbon in the form of organic matter from surface waters. Ninety percent of the numerous pelagic organisms that inhabit the deep ocean are capable of emitting light [1] through the chemical process of bioluminescence, which appears to be the most common form of communication in this remote realm [1,2,3]. Deep-sea bioluminescence is also viewed as an expression of abundance and adaptation of organisms to their environment [4]. Marine bioluminescent organisms include a variety of distinct taxa [4]. When stimulated mechanically or electrically, eukaryotic bioluminescent organisms emit erratic luminous flashes, and also spontaneous flashes to attract prey and mates for recognition of congeners or for defence purposes [1,3,4]. In contrast, luminescent bacteria are unaffected by mechanical stimulation and can glow continuously for many days under specific growth conditions [5,6]. Bioluminescent bacteria occur in marine waters as free-living forms, symbionts in luminous organs of fishes and crustaceans and attached to marine snow aggregates sinking through the water column [5,7]. During micro-algae blooms, strong bioluminescence produced by colonies of bacteria could even lead to spectacular marine phenomena such as "milky seas" in surface waters [6].

Bioluminescence sources have been observed and quantified over the last three decades using a variety of observational platforms and instruments such as manned submersibles [1] and autonomous underwater vehicles [8], *in situ* high sensitivity cameras [9,10], underwater photometers [7,11,12], and remote satellite imagery [6]. In most cases, deep–sea bioluminescence is triggered and observed after external mechanical stimulation using, for instance, pumped flows through turbulence-generating grids [13] or downward moving grids that collide with the

E Sediment transport along the Cap de Creus Canyon flank, Martín J. et al., 2013 (doi:10.5194/bg-10-3221-2013)

Biogeosciences, 10, 3221–3239, 2013
www.biogeosciences.net/10/3221/2013/
doi:10.5194/bg-10-3221-2013

Biogeosciences Open Access

Sediment transport along the Cap de Creus Canyon flank during a mild, wet winter

J. Martín[1], X. Durrieu de Madron[2], P. Puig[1], F. Bourrin[2], A. Palanques[1], L. Houpert[2], M. Higueras[2], A. Sanchez-Vidal[3], A. M. Calafat[3], M. Canals[3], S. Heussner[2], N. Delsaut[2], and C. Sotin[2]

[1]Institut de Ciències del Mar (CSIC), Passeig Marítim de la Barceloneta 37–49, 08003 Barcelona, Spain
[2]CEFREM, CNRS-Université de Perpignan, Via Domitia, 52 avenue Paul Alduy, 66860 Perpignan, France
[3]GRC Geociències Marines, Departament d'Estratigrafia, Paleontologia i Geociències Marines, Facultat de Geologia, Universitat de Barcelona, Campus de Pedralbes, Martí i Franquès s/n, 08028 Barcelona, Spain

Correspondence to: J. Martín (jmartin@icm.csic.es)

Received: 28 November 2012 – Published in Biogeosciences Discuss.: 14 December 2012
Revised: 2 April 2013 – Accepted: 19 April 2013 – Published: 14 May 2013

Abstract. Cap de Creus Canyon (CCC) is known as a preferential conduit for particulate matter leaving the Gulf of Lion continental shelf towards the slope and the basin, particularly in winter when storms and dense shelf water cascading coalesce to enhance the seaward export of shelf waters. During the CASCADE (CAscading, Storm, Convection, Advection and Downwelling Events) cruise in March 2011, deployments of recording instruments within the canyon and vertical profiling of the water column properties were conducted to study with high spatial-temporal resolution the impact of such processes on particulate matter fluxes. In the context of the mild and wet 2010–2011 winter, no remarkable dense shelf water formation was observed. On the other hand, the experimental setup allowed for the study of the impact of E-SE storms on the hydrographical structure and the particulate matter fluxes in the CCC. The most remarkable feature in terms of sediment transport was a period of dominant E-SE winds from 12 to 16 March, including two moderate storms (maximum significant wave heights = 4.1–4.6 m). During this period, a plume of freshened, relatively cold and turbid water flowed at high speeds along the southern flank of the CCC in an approximate depth range of 150–350 m. The density of this water mass was lighter than the ambient water in the canyon, indicating that it did not cascade off-shelf and that it merely downwelled into the canyon forced by the strong cyclonic circulation induced over the shelf during the storms and by the subsequent accumulation of seawater along the coast. Suspended sediment load in this turbid intrusion recorded along the southern canyon flank oscillated between 10 and 50 mg L^{-1}, and maximum currents speeds reached values up to 90 cm s^{-1}. A rough estimation of 10^5 tons of sediment was transported through the canyon along its southern wall during a 3-day-long period of storm-induced downwelling. Following the veering of the wind direction (from SE to NW) on 16 March, downwelling ceased, currents inside the canyon reversed from down- to up-canyon, and the turbid shelf plume was evacuated from the canyon, most probably flowing along the southern canyon flank and being entrained by the general SW circulation after leaving the canyon confinement. This study highlights that remarkable sediment transport occurs in the CCC, and particularly along its southern flank, even during mild and wet winters, in absence of cascading and under limited external forcing. The sediment transport associated with eastern storms like the ones described in this paper tends to enter the canyon by its downstream flank, partially affecting the canyon head region. Sediment transport during these events is not constrained near the seafloor but distributed in a depth range of 200–300 m above the bottom. Our paper broadens the understanding of the complex set of atmosphere-driven sediment transport processes acting in this highly dynamic area of the northwestern Mediterranean Sea.

1 Introduction

Continental margins are transitional areas between the land masses and the open sea where inputs of particulate matter

F Bottom Nepheloid Layers and Dense Shelf Water Cascading, Puig P. et al., 2012 (doi:10.1016/j.pocean.2012.10.003)

Progress in Oceanography 111 (2013) 1–23

Contents lists available at SciVerse ScienceDirect

Progress in Oceanography

journal homepage: www.elsevier.com/locate/pocean

Thick bottom nepheloid layers in the western Mediterranean generated by deep dense shelf water cascading

Pere Puig [a,*], Xavier Durrieu de Madron [b], Jordi Salat [a], Katrin Schroeder [c], Jacobo Martín [a], Aristomenis P. Karageorgis [d], Albert Palanques [a], François Roullier [e], José Luis Lopez-Jurado [f], Mikhail Emelianov [a], Thierry Moutin [g], Loïc Houpert [b]

[a] Institut de Ciències del Mar (CSIC), Passeig Marítim de la Barceloneta, 37-49, 08003 Barcelona, Spain
[b] CEFREM, UMR 5110 CNRS-UPVD, 52 Avenue Paul Alduy, 66860 Perpignan Cedex, France
[c] CNR – National Research Council of Italy, ISMAR – Marine Sciences Institute, Forte Santa Teresa, 19032 Pozzuolo di Lerici, Italy
[d] Hellenic Centre for Marine Research, 46.7 km Athens-Sounio Avenue, 19013 Anavyssos, Greece
[e] Laboratoire d'Océanographie de Villefranche (LOV), Université Pierre et Marie Curie, Paris 6, 06230 Villefranche-sur-Mer, France
[f] Centro Oceanográfico de Baleares, Instituto Español de Oceanografía, Muelle de Poniente s/n, 0715 Palma de Mallorca, Spain
[g] Aix-Marseille Université, Université du Sud Toulon-Var, CNRS/INSU, IRD, MIO, UM 110, 13288, Marseille, Cedex 09, France

ARTICLE INFO

Article history:
Received 28 October 2011
Received in revised form 25 September 2012
Accepted 1 October 2012
Available online 17 October 2012

ABSTRACT

The analysis of a compilation of deep CTD casts conducted in the western Mediterranean from 1998 to 2011 has documented the role that dense water formation, and particularly deep dense shelf water cascading off the Gulf of Lions, plays in transporting suspended particulate matter from the coastal regions down to the basin. Deep CTD casts reveal that after the 1999 and 2005–2006 deep cascading events the Western Mediterranean Deep Water (WMDW) was characterized by the presence of a thick bottom nepheloid layer (BNL) that corresponded in thickness with a thermohaline anomaly generated by the mixture of dense waters formed by deep convection in the open sea and by deep cascading. This BNL can be hundreds of meters thick and in the central part of the basin usually exhibits suspended sediment concentrations of <0.1 mg/l above background levels, reaching higher concentrations close to the continental rise, with near-bottom peaks >1 mg/l. After winter 1999 the BNL spread from the Gulf of Lions and the Catalan margin over the northwestern Mediterranean basin, reaching west of the Balearic Islands and the Ligurian Sea, while after winters 2005–2006 the BNL covered the entire western Mediterranean basin. Thickness and concentration of the BNL tend to diminish with time but this trend is highly dependent on the volume of dense water generated, both by convection and cascading. After winter 1999 the BNL signal vanished in one year, but after winters 2005–2006 it lasted for longer and the turbidity signal can still be distinguished at present (2011). Particle size distribution in the BNL reveals the presence of large aggregates up to 1 mm in size formed by a mixture of single particles with the same bimodal grain size distribution as the surface sediments found in the northwestern Mediterranean slope and basin. Results presented in this paper highlight the fact that the WMDW can be periodically affected by the arrival of new dense waters loaded with suspended particles mainly introduced by resuspension processes during major cascading events, being a key process that could ultimately affect deep-sea biogeochemical cycles in the western Mediterranean.

1. Introduction

Suspended particles in the oceans play a key role as extractors from, transporters through and sources to the water column of many major and minor elements, being responsible for maintaining most oceanic chemical concentrations (Biscaye and Eittreim, 1977; Eisma, 1993). Particles are introduced into the ocean by biological production, rivers, glaciers, wind and bottom sediments resuspension. Biological, chemical and gravitational processes then act to remove particles from the water column. These removal mechanisms, however, occur on much shorter time scales than the formation, movement or mixing of oceanic water masses, and therefore, particles do not act as pure conservative tracers of water masses, but their presence and concentration can indicate the location and intensity of oceanographic processes, particularly those involving the resuspension of sediments due to strong bottom currents, and can be used as tracers of water motions (McCave, 1986; Gardner et al., 1990). The redistribution of particulate matter has important implications for understanding and quantitatively modeling biogeochemical processes in the oceans. In the open ocean, surface production is generally the most significant source of

* Corresponding author. Tel.: +34 93 2309518.
E-mail address: ppuig@icm.csic.es (P. Puig).

0079-6611/$ - see front matter © 2012 Elsevier Ltd. All rights reserved.
http://dx.doi.org/10.1016/j.pocean.2012.10.003

G Interaction of dense shelf water cascading and open-sea convection in the northwestern Mediterranean during winter 2012, Durrieu de Madron X. et al., 2013 (doi: 10.1002/grl.50331)

GEOPHYSICAL RESEARCH LETTERS, VOL. 40, 1–7, doi:10.1002/grl.50331, 2013

Interaction of dense shelf water cascading and open-sea convection in the northwestern Mediterranean during winter 2012

X. Durrieu de Madron,[1] L. Houpert,[1] P. Puig,[2] A. Sanchez-Vidal,[3] P. Testor,[4] A. Bosse,[4] C. Estournel,[5] S. Somot,[6] F. Bourrin,[1] M. N. Bouin,[7] M. Beauverger,[4] L. Beguery,[8] A. Calafat,[3] M. Canals,[3] C. Cassou,[9] L. Coppola,[10] D. Dausse,[4] F. D'Ortenzio,[10] J. Font,[2] S. Heussner,[1] S. Kunesch,[1] D. Lefevre,[11] H. Le Goff,[4] J. Martín,[2] L. Mortier,[4] A. Palanques,[2] and P. Raimbault[11]

Received 2 January 2013; revised 4 March 2013; accepted 6 March 2013.

[1] The winter of 2012 experienced peculiar atmospheric conditions that triggered a massive formation of dense water on the continental shelf and in the deep basin of the Gulf of Lions. Multiplatforms observations enabled a synoptic view of dense water formation and spreading at basin scale. Five months after its formation, the dense water of coastal origin created a distinct bottom layer up to a few hundreds of meters thick over the central part of the NW Mediterranean basin, which was overlaid by a layer of newly formed deep water produced by open-sea convection. These new observations highlight the role of intense episodes of both dense shelf water cascading and open-sea convection to the progressive modification of the NW Mediterranean deep waters. **Citation:** Durrieu de Madron, X., et al. (2013), Interaction of dense shelf water cascading and open-sea convection in the northwestern Mediterranean during winter 2012, *Geophys. Res. Lett.*, *40*, doi:10.1002/grl.50331.

1. Introduction

[2] Dense shelf water cascading and open-sea convection coexist in a few regions around the world such as the Mediterranean (Gulf of Lions, Adriatic Sea, Aegean Sea) [*CIESM*, 2009], the East/Japan Sea [*Kim et al*., 2008], and Greenland Sea [*Quadfasel et al*., 1988]. However, interplay between both types of processes on the deep water mass characteristics is still poorly documented.

[3] In the Gulf of Lions (GoL), dense water formation shows a high interannual variability. It is mostly produced by surface cooling and evaporation due to cold and dry northern winds, and preconditioning of the water column. Dense shelf water overflowing the shelf edge occasionally cascades down to more than 2000 m, resulting in the apparition of fresher and colder bottom water in the basin [*Canals et al*., 2006; *Font et al*., 2007]. Open-sea convection involves a progressive deepening of the upper ocean mixed layer, which first reaches the warmer and saltier underlying Levantine Intermediate Water and eventually extends all the way down to the bottom, should the atmospheric forcing be intense enough [*L'Heveder et al*., 2012].

[4] Although open-sea convection is the main mechanism for the renewal of the Western Mediterranean Deep Water (WMDW), the influence of dense shelf water cascading has been suggested by several studies. Analysis of historical temperature-salinity profiles from the late 1960s suggested mixing of deep cascading and convection dense waters, with a subdecadal recurrence [*Béthoux et al*., 2002], the winters 2005 and 2006 being the last major events [*Puig et al*., 2013].

[5] Here we present a comprehensive set of hydrological and hydrodynamical observations collected during the winter and summer 2012 that provide new insights on the propagation and mixing of both type of the dense shelf waters, and their influence on the modification of the WMDW, as a new step in the Western Mediterranean Transition that started in 2005 [*CIESM*, 2009].

2. Data and Methods

[6] Six mooring lines and two surface buoys constituted the observational design (Figure 1a). Three moorings were located at 1000 m depth in canyons at the NE (Planier, PLC) and SW ends (Lacaze-Duthiers, LDC; Cap de Creus, CCC) of the GoL margin, and three others between 1900–2500 m depth on the Catalan continental slope (HC, FOFA) and GoL basin (LION). Two meteorological buoys were located on the GoL inner shelf of the (POEM), and in the basin (MF-LION).

[7] All the lines were equipped with current meters between 20 and 45 m above bottom, and the deepest ones

[1]CEFREM, CNRS-Université de Perpignan, 52 avenue Paul Alduy, 66860, Perpignan, France.
[2]ICM-CSIC, Passeig Marítim de la Barceloneta, 37-49, 08003, Barcelona, Spain.
[3]GRC-GM, Universitat de Barcelona, Martí i Franquès s/n, 08028, Barcelona, Spain.
[4]LOCEAN/IPSL, CNRS-Université de Paris 6, 4 Place Jussieu, 75005, Paris, France.
[5]LA, CNRS-Université de Toulouse, 14 avenue Edouard Belin, 31400, Toulouse, France.
[6]CNRM-GAME, Météo France - CNRS, 42 avenue Coriolis, 31057, Toulouse, France.
[7]CMM, Météo-France, 13 rue du Chatellier, 29604, Brest, France.
[8]DT-INSU, CNRS, Zone portuaire de Breguaillon, 83507, La Seyne/mer, France.
[9]CERFACS/CNRS, 42 avenue Gaspard Coriolis, 31057, Toulouse, France.
[10]LOV, CNRS-Université de Paris 6, Observatoire océanographique, 06234, Villefranche/mer, France.
[11]MIO, CNRS-Université de la Méditerranée, Campus de Luminy, 13288, Marseille, France.

Corresponding author: X. Durrieu de Madron, CEFREM, CNRS-Université de Perpignan, 52 ave. Paul Alduy, 66860 Perpignan, France. (demadron@univ-perp.fr)

0094-8276/13/10.1002/grl.50331